
# Non-Invasive Microwave-Based Sensor System for Monitoring Hydration Levels in Patients with Electromagnetic Waves

Innocent Lubangakene BEng(Hons) MIET

A thesis is submitted in fulfilment of the requirements of London Metropolitan University for the degree of Doctor of Philosophy

**July 2025**

## Acknowledgments

My heartfelt thanks go to my supervisors, Prof Bal Virdee and Dr. Pancham Shukla, for their expert guidance, support, and encouragement. I also thank London Metropolitan University specifically the school of Computing and Digital Media for providing the resources and academic environment essential for my research.

To my colleagues, friends, and family, thank you for your unwavering support, understanding, and motivation. Your presence made this journey possible and meaningful.

## Abstract

This thesis presents the design, development, and experimental validation of a novel, non-invasive microwave-based biosensor system for real-time hydration monitoring. Addressing a critical need in clinical and wearable health technology, the research explores the use of dielectric properties of human tissues, particularly at microwave frequencies, to detect variations in tissue water content as a proxy for hydration status. Building on prior work from the London Met University Rescaling project, which introduced BaFe-inclusion-based microstrip patch sensors/antennas for enhanced electromagnetic sensitivity, this thesis extends to that concept by developing and optimizing a ferrite-loaded H-slot microstrip patch antenna for non-invasive hydration diagnosis. The sensor operates around 2.2 GHz in the ISM band, ensuring safe, low-power interaction with the human body.

The system integrates the antenna with a portable vector network analyser (NanoVNA) and a Raspberry Pi running custom Python software for signal processing, visualization, and classification. Extensive human subject testing (N = 425 measurements) demonstrated the sensor's ability to distinguish between hypohydrated, euhydrated, and hyperhydrated states using reflection coefficient ($S_{11}$) thresholds. Experimental results showed strong agreement with simulation predictions, confirming the inverse relationship between tissue hydration and reflected microwave power. The system achieved high sensitivity, dynamic range, and robustness across varying users and conditions, with minimal influence from confounding factors such as age or sex.

The work validates the feasibility of using reflection coefficient analysis for real-time, non-invasive hydration tracking and paves the way for personalized, continuous health monitoring diagnosis. Specifically, this novel non-invasive approach represents a substantial advancement in the general field of biomedical science by enabling instantaneous hydration status estimation within seconds eliminating the delays, invasiveness, and inaccuracies associated with conventional methods such as blood osmolality testing, urine analysis, or bioelectrical impedance. This rapid and reliable assessment capability provides a new paradigm for clinical diagnostics, sports science, and remote health monitoring, demonstrating how electromagnetic-based sensing can deliver precise physiological insights without discomfort or laboratory dependence.

# Table of Contents

## List of Figures

## List of Tables

# 1. Introduction

## 1.1. Background of the Study

Maintaining an optimal hydration status is critical to human health, particularly in the management of chronic conditions such as heart failure, kidney disease, and heat-related illnesses [1]. Dehydration remains a significant contributor to morbidity and mortality, especially among the elderly, infants, and patients in intensive care units. Traditional methods of hydration assessment such as Blood Urea Nitrogen (BUN), serum osmolality, urine output monitoring, and body weight fluctuations although clinically validated, often rely on invasive, intermittent, or patient-dependent measurements that do not support continuous or real-time tracking [2]. These limitations underscore the urgent need for advanced, non-invasive technologies capable of providing precise, real-time monitoring of hydration status [3].

Recent technological advances have opened new frontiers in biomedical sensing, with electromagnetic (EM) wave-based techniques particularly in the microwave frequency range emerging as promising candidates for non-invasive hydration monitoring [4]. Microwave sensing operates on the principle of dielectric contrast, leveraging the distinct dielectric properties of water-rich tissues in comparison to other biological substrates such as fat, bone, and muscle [5]. Because water exhibits high permittivity ($\varepsilon_r$) and dielectric loss ($\sigma$), at microwave frequencies, even subtle changes in tissue water content can be detected via alterations in signal propagation, reflection, or absorption [6][7].

The potential capability of microwave-based sensors to detect changes in tissue dielectric properties due to hydration status opens a compelling avenue for the development of wearable, skin-conformal, or implantable devices. These systems will be designed to include a microwave transmitter, receiver, and planar antenna structure embedded in flexible materials, thereby enabling continuous, unobtrusive, and patient-friendly monitoring [6]. The dielectric mismatch between tissues and water allows microwave signals to penetrate skin and muscle and return quantifiable information correlated to hydration dynamics [8][9].

Several studies have explored the potential use of microwave-based sensors for monitoring hydration levels [6]-[12][30]. These systems in these studies were designed to typically consist of a microwave transmitter, receiver, and antenna that are placed near the skin. The transmitted microwave signal interacts with the skin and underlying tissues, and the reflected or transmitted signal is measured and analysed to determine the water content. The interaction between the

microwave signals and the water content in the body is the fundamental principle behind these hydration monitoring systems. By analysing the changes in the reflected or transmitted microwave signals, the sensors can quantify the water content in the targeted tissue regions, providing healthcare professionals with valuable insights into a patient's hydration status [10].

Microwave-based hydration monitoring potentially offer several advantages over traditional methods. These sensors will be able to provide continuous, real-time measurements of hydration levels without the need for invasive procedures or laboratory tests. This can be particularly useful for patients with chronic conditions, such as heart failure or kidney disease, where maintaining proper fluid balance is critical. Furthermore, these sensors can be integrated into wearable or skin-mounted devices, enabling remote monitoring and early detection of dehydration or fluid overload [11]. This will help healthcare professionals closely track a patient's hydration status and make timely interventions to manage fluid balance, ultimately improving patient outcomes and quality of life [12]. Additionally, the ability to continuously monitor hydration levels can aid in the management of various medical conditions where fluid balance is a key factor, such as congestive heart failure, renal diseases, and dehydration-related illnesses [14].

In terms of the frequency range of interest, the 2.45 GHz Industrial, Scientific, and Medical (ISM) band has become a focal point for microwave biosensing due to its regulatory acceptability, compact antenna requirements, and pronounced interaction with water molecules [15]. These attributes make it ideal for the realization of wearable hydration monitors that can operate in real time without the need for invasive sampling or manual input.

In clinical scenarios, the utility of such technology is significant. For example, in perioperative care, subtle shifts in fluid balance can be detected early; in geriatrics, home-based hydration monitoring can reduce emergency admissions due to dehydration. In sports science, athletes can receive feedback on hydration status in real-time to optimize performance and recovery. These cross-sector benefits reinforce the necessity to further explore and validate microwave-based systems.

Although there have been promising advances, microwave hydration sensors are still primarily confined to prototype development and early-stage clinical testing. Key challenges including precise calibration, sensitivity to individual physiological differences (such as skin thickness and adipose tissue), susceptibility to electromagnetic interference, and regulatory hurdles must be addressed before these systems can be adopted in clinical settings.

This thesis offers significant potential to drive progress in this area by tackling these critical barriers. Through the integration of sophisticated biosensor simulation, computational modelling, prototype design and experimental validation, the research provides innovative approaches to improve the accuracy, reliability, and clinical viability of non-invasive hydration monitoring. By addressing current limitations, this work lays an important foundation for the future translation of microwave-based sensing technologies into real-world healthcare application

## 1.2. Problem Statement

Hydration plays a pivotal role in physiological homeostasis, impacting cardiovascular performance, thermoregulation, renal function, and cognitive processes [1]. The clinical assessment of hydration status is especially critical in managing patients with comorbidities such as heart failure, kidney dysfunction, sepsis, and electrolyte imbalance. Despite its clinical importance, there is still not universally accepted, non-invasive, and reliable method for continuous real-time hydration monitoring. [16] Current diagnostic approaches are often indirect, episodic, or invasive such as haematological analysis, urine-specific gravity, bioelectrical impedance, and body mass fluctuations none of which are suitable for continuous, in-situ monitoring.

Current techniques present several fundamental limitations:

- Invasiveness and patient discomfort: Blood draws and catheterisation, while accurate are invasive and unsuitable for frequent use or vulnerable populations [17].
- Environmental and physiological variability: Factors such as temperature, medication, physical activity may affect readings obtained through the traditional methodologies.
- Clinical latency: Urine output, body weight and laboratory testing provide only snapshot assessments, often missing critical changes in hydration dynamics.

Furthermore, while electrical bioimpedance methods offer a degree of non-invasiveness, their accuracy deteriorates in patients with fluid shifts (e.g., edema, third-spacing), which are common in critically ill or elderly populations [18]. They are also less suitable for continuous or ambulatory monitoring.

The emergency of microwave-based sensing technologies offers a theoretically robust alternative, exploiting the dielectric contrast between water and biological tissues to non-invasively infer hydration status. However, practical implementations of such systems face numerous barriers:

- Calibration complexity: Inter-subject variability in skin thickness, fat content, and tissue composition significantly affects dielectric response, complicating signal interpretation.
- Hardware integration challenges: Designing antennas and transmission modules that are simultaneously biocompatible, flexible, energy-efficient, and sensitive to hydration-linked dielectric changes remains a formidable engineering task.
- Regulatory and clinical translation barriers: Most microwave biosensors have yet to undergo large-scale clinical trials and face regulatory scrutiny in safety, signal exposure limits (e.g., Specific Absorption Rate, SAR), and electromagnetic compatibility.

Consequently, despite a compelling theoretical foundation, microwave-based hydration monitoring systems remain underutilized and largely unvalidated in mainstream clinical practice [19]**.** This gap represents a critical barrier to advancing precision hydration management across multiple medical domains. Without a validated, real-time, non-invasive tool, clinicians are left to rely on reactive rather than proactive interventions, which can lead to delays in care, increased morbidity, and higher healthcare costs**.**

The core problem addressed in this thesis is therefore the design, optimization, and preliminary validation of a microwave-based hydration sensor system operating within a clinically viable frequency band (specifically, the 2.45 GHz ISM band), with a focus on overcoming the current barriers to implementation namely, sensitivity, calibration robustness, integration feasibility, and signal interpretation accuracy.

## 1.3. Aim and Objectives of the Thesis

The primary aim of this research is to design, implement, and evaluate a non-invasive microwave-based sensor system for real-time monitoring of hydration levels in human subjects**.** The study seeks to leverage the dielectric properties of biological tissues, particularly the high permittivity and conductivity of water, to enable accurate, continuous hydration assessment using microwave-frequency electromagnetic waves specifically centred at the 2.45 GHz ISM band.

The goal is to develop a clinically relevant, miniaturized, wearable sensing platform that can be deployed in healthcare, sports, and remote-monitoring contexts to enable early detection of dehydration and aid in fluid management decision-making.

### 1.3.1. Objectives of the Thesis

To achieve the aim of the thesis, the research is guided by the following specific objectives:

I. ***To characterize the dielectric behaviour of hydrated and dehydrated biological tissues*:** One of the key objectives of this study is to quantify how variations in tissue hydration alter its permittivity ($\varepsilon_r$) and conductivity ($\sigma$) at microwave frequencies of interest $f_r =$ 2.45 GHz. This will be achieved using numerical electromagnetic modelling techniques such as Finite-Difference Time-Domain (FDTD) or Finite Element Method (FEM) on highly specialised simulations tools like Microwave CST to simulate tissue-sensor interactions. The models will incorporate realistic dielectric properties of biological tissues at different hydration levels, enabling analysis of how these variations influence electromagnetic field distribution and sensor response. By performing parametric simulations and analysing resulting changes in reflection, transmission, and absorption characteristics, the objective is to establish a clear quantitative relationship between tissue hydration and its dielectric behaviour, which is critical for the design and optimization of non-invasive microwave-based diagnostic tools.

II. ***To design and fabricate a compact microwave-based hydration sensor prototype*:** Another objective is to develop and optimize a sensor architecture tailored for non-invasive tissue characterization, focusing on key design parameters such as antenna geometry, substrate material, and packaging. The goal is to ensure efficient electromagnetic coupling with biological tissue while maintaining structural integrity, biocompatibility, and ease of integration into wearable or portable systems. Additionally, the appropriate operating frequency range centred around 2.45 GHz will be selected based on factors including penetration depth, dielectric sensitivity to hydration changes, and compliance with ISM (Industrial, Scientific, and Medical) band regulations. This objective supports the creation of a reliable and practical sensing platform for continuous, non-invasive monitoring.

III. ***To evaluate the sensor's sensitivity and specificity to hydration-related dielectric changes*:** conduct controlled experiments using tissue phantoms and in-vitro or ex-vivo biological samples to validate the sensor's performance under realistic conditions. These experiments will involve systematic variation of tissue hydration levels to mimic physiological changes, enabling calibration and benchmarking of the sensor's sensitivity. Key electromagnetic parameters including signal reflection ($S_{11}$), transmission ($S_{21}$), and phase shifts will be measured using a Vector Network Analyser (VNA) to assess the interaction between the sensor and the biological medium. The collected data will be

analysed to extract reliable hydration metrics, establishing the correlation between dielectric responses and water content, and thereby supporting the development of accurate, non-invasive hydration monitoring techniques.

IV. ***To develop signal processing algorithms for hydration level estimation:*** Apply feature extraction techniques to the sensor response data, focusing on parameters such as resonance frequency shift $f_r$ , return-loss (dB), and phase response. These features will be used to characterize the dielectric behaviour of tissues across varying hydration levels, enabling the development of reliable indicators for hydration assessment. To enhance measurement accuracy and adaptability across individuals and usage scenarios, an adaptive filtering algorithm will be integrated into the system. This will support robust calibration and personalization by compensating for variations due to sensor placement, tissue heterogeneity, or environmental factors, ultimately improving the consistency and reliability of the non-invasive hydration sensing platform.

V. ***To validate the accuracy and reproducibility of the microwave sensor system against clinical gold standards:*** Another key objective is to compare microwave-derived hydration estimates with established clinical and laboratory methods such as bioimpedance spectroscopy, urine osmolality, and blood serum tests across a range of hydration states. This comparative analysis will help validate the accuracy and clinical relevance of the microwave sensing approach. Experimental trials will be conducted involving multiple subjects and repeated measurements to assess the system's repeatability and inter-subject variability. These trials will provide critical insights into the robustness, reliability, and generalizability of the sensor across diverse physiological conditions, supporting its potential for real-world, non-invasive hydration monitoring applications.

VI. ***To assess the sensor's potential for use in clinical, home-based, and athletic environments:*** The final objective is to evaluate the usability, reliability, and real-world performance of the developed sensor system through simulated or early-stage field deployments. This includes assessing user interaction, setup simplicity, data acquisition stability, and system responsiveness under practical conditions that mimic everyday use. Feedback from these deployments will inform design refinements and highlight any limitations in functionality or user experience. Additionally, potential barriers to regulatory approval such as safety, electromagnetic exposure limits, and data accuracy

requirements will be identified. A roadmap for clinical integration will be developed by mapping the sensor's alignment with medical device regulations, certification processes, and potential application areas within healthcare settings, paving the way for future translation into clinical practice.

Each objective contributes to establishing a proof-of-concept, clinically relevant, and technically feasible hydration monitoring system based on microwave sensing. Together, they support the advancement of non-invasive biosensing technologies in next-generation healthcare.

## 1.4. Research Questions

To guide the investigation into the design, development, and application of microwave-based hydration monitoring systems, this study seeks to address the following core research questions:

***Primary Research Question***

1. Can a microwave-based, non-invasive sensor operating at 2.45 GHz accurately and reliably detect variations in human tissue hydration levels in real-time?

***Secondary Research Questions***

1. How do variations in tissue hydration affect the dielectric properties or permittivity ($\varepsilon_r$) and conductivity ($\sigma$) of human skin, muscle, and subcutaneous tissue at microwave frequencies?
2. What is the optimal microwave sensor design including antenna geometry, substrate material, and operating frequency for sensitive, non-invasive detection of hydration changes in biological tissue?
3. How do microwave signal parameters (e.g., S-parameters, resonance frequency, return loss) correlate with hydration level changes across different physiological states or individuals?
4. What are the performance benchmarks (e.g., sensitivity, specificity, repeatability) of the microwave hydration sensor compared to traditional hydration assessment techniques (bioimpedance, serum osmolality, etc.)?
5. How can signal processing and programming techniques be applied to enhance the accuracy, personalization, and real-time capability of hydration level estimation using microwave data?
6. To what extent can the developed sensor system be integrated into a wearable platform without compromising data quality, user comfort, or regulatory compliance?

7. What are the clinical, operational, and ethical considerations required to transition this technology from laboratory prototypes to practical deployment in healthcare or remote monitoring settings?

These research questions serve as a blueprint for the empirical, theoretical, and design investigations throughout the thesis. They are aligned with the broader objectives of enhancing the accuracy, usability, and translational potential of microwave-based biosensing systems in personalized and preventive medicine.

## 1.5. Research Hypothesis

This research is built upon the theoretical premise that microwave electromagnetic waves are highly sensitive to variations in the water content of biological tissues due to the distinct dielectric properties of water compared to other soft tissues. As such, changes in hydration status will induce measurable shifts in the dielectric response, which can be captured and analysed by a well-designed microwave sensing system.

The core hypothesis guiding this research is as follows:

***Primary Hypothesis:***

**$H_1$**: A microwave-based sensor operating at the 2.45 GHz ISM band can detect and quantify changes in human tissue hydration levels in real time by measuring variations in dielectric properties, with accuracy and reliability comparable to conventional hydration assessment methods.

***Supporting Hypotheses:***

**$H_11$:** Variations in hydration status induce statistically significant changes in the tissue's complex permittivity (both real and imaginary components) at microwave frequencies.

**$H_12$:** A microwave antenna array designed with specific substrate properties and geometries can achieve sufficient sensitivity to hydration-induced dielectric changes in skin and subcutaneous tissues.

**$H_13$:** Signal parameters such as $S_{11}$ (return-loss) and resonance frequency shift are strongly correlated ($r > 0.85$) with standardized hydration markers (e.g., body weight change, urine osmolality, bioimpedance).

**$H_I4$:** Signal calibration through individualized machine learning algorithms enhances detection sensitivity and reduces variability across different patient morphologies.

**$H_I5$:** The final sensor system can be miniaturized and embedded into a wearable device without compromising the quality or interpretability of hydration data.

These hypotheses will be tested using a combination of simulation-based modelling, artificial experiments, human-subject trials, and cross-validation against clinical reference methods. The outcomes will determine the viability of microwave-based hydration sensing as a mainstream tool for medical diagnostics and remote health monitoring.

## 1.6. Significance of the Study

Hydration status is a critical physiological parameter influencing systemic health, yet current clinical methodologies lack the capacity for continuous, real-time, and non-invasive monitoring. This research addresses a substantial clinical and technological gap by advancing a novel approach for non-invasive microwave-based hydration sensing, with the potential to transform fluid monitoring paradigms in both acute and chronic care settings.

### 1.6.1. Clinical and Healthcare Relevancy

***Remote and Preventive Monitoring:*** The system enables real-time tracking of hydration in high-risk groups (e.g., elderly, athletes, post-operative patients), reducing reliance on reactive interventions. This aligns with global healthcare trends toward telemedicine, home-based care, and preventive diagnostics.

***Non-Invasive Patient Management:*** By eliminating the need for needles, urine samples, or specialized laboratory equipment, the system increases patient compliance and reduces the burden on healthcare infrastructure.

***Chronic Disease Monitoring:*** Patients with renal insufficiency, heart failure, or diabetes often require fluid management. Continuous hydration assessment using a wearable microwave sensor can guide early interventions, medication adjustments, and fluid therapy, potentially preventing adverse events and hospitalizations.

### 1.6.2. Scientific and Technical Significance

***Electromagnetic-tissue interaction Modelling:*** This study contributes to the quantitative understanding of how hydration levels influence dielectric properties of biological tissues at

microwave frequencies, particularly around the 2.45 GHz band. These insights provide a foundation for advancing electromagnetic-based biosensing systems.

***Sensor Innovation:*** The proposed sensor architecture leverages unique materials, antenna miniaturization, and low-power microwave circuitry to enable a wearable, patient-conformable sensing platform. By optimizing sensor geometry and dielectric coupling, this work contributes to the next generation of precision bioelectronics.

***Signal Processing and Classification:*** This research introduces advanced signal processing to extract hydration-relevant features from complex microwave data. These methodologies enhance the accuracy, specificity, and adaptability of biosensors in dynamic, real-world environments.

## 1.7. Scope of the Study

***Sensor Frequency Range:*** The study is confined to the 2.45 GHz ISM band, selected for its balance between tissue penetration depth, sensitivity to water, and regulatory approval for biomedical use. While other frequencies exist in the microwave spectrum (e.g., 1–10 GHz), only this frequency is explored in the physical sensor development.

***Biological Focus:*** The sensor is optimized for use on peripheral anatomical sites, such as the forearm or upper chest regions accessible for surface sensing and known to reflect systemic hydration changes. Deep-organ hydration (e.g., intracranial or pulmonary) is not addressed.

***Target Population:*** Experimental trials will focus on healthy adult volunteers and artificial biological biomarkers (sweat). While the long-term goal includes deployment in clinical populations (e.g., elderly, patients with kidney failure), those groups are beyond the scope of this prototype validation phase.

***Validation Methods:*** Sensor accuracy will be assessed by comparing its output to standard hydration metrics such as bioimpedance spectroscopy, urine specific gravity, and controlled body mass changes. Advanced biomarkers (e.g., serum osmolality, isotopic dilution) are acknowledged but not implemented.

***Device Design:*** The study focuses on developing a proof-of-concept wearable sensor. While the potential for full miniaturization and wireless transmission is discussed, only wired or semi-standalone configurations will be physically fabricated in this phase due to time and cost limitations.

***Data Analysis Techniques:*** Signal analysis will use classical electromagnetic theory alongside programming classification algorithms for personalized calibration and hydration prediction. However, machine learning and deep learning models requiring large datasets are not implemented at this stage.

### 1.7.1. Delimitations of the Study

The sensor is not intended for invasive deployment, nor is it tested inside body cavities or under surgical conditions.

Longitudinal studies tracking hydration over days or weeks are not conducted. Validation is limited to controlled, acute hydration/dehydration states.

The study does not include regulatory certification processes (e.g., CE marking, FDA clearance), though safety and compliance standards (SAR, EMC) are referenced.

Only one frequency band is investigated in practice, though broader frequency sweeps may be simulated.

**References**


1. M.-E. Roumelioti *et al.*, "Fluid Balance Concepts in medicine: Principles and practice," *World J. Nephrol.*, 2018 [Online]. Available: https://www.wjgnet.com/2220-6124/full/v7/i1/1.htm
2. A. Tahar, H. Zrour, S. Dupont, and A. Pozdzik, "Non-invasive approaches to hydration assessment: a literature review," *Urolithiasis*, vol. 52, no. 1, Sep. 2024, doi: 10.1007/s00240-024-01630-y.
3. N. L. Kazanskiy, S. N. Khonina, and M. A. Butt, "A review on flexible wearables – Recent developments in non-invasive continuous health monitoring," *Sens. Actuators A Phys.*, vol. 366, p. 114993, Feb. 2024, doi: 10.1016/j.sna.2023.114993.
4. R. Pethig, "IOPscience," *Clin. Phys. Physiol. Meas.*, [Online]. Available: https://iopscience.iop.org/article/10.1088/0143-0815/8/4A/002
5. C. Gabriel and A. Peyman, "Dielectric Properties of Biological Tissues; Variation with Age," in *Conn's Handbook of Models for Human Aging*, 2nd ed., J. L. Ram and P. M. Conn, Eds. Academic Press, 2018, pp. 939–952, doi: 10.1016/B978-0-12-811353-0.00069-5.
6. B. C. Besler and E. C. Fear, "Microwave Hydration Monitoring: System Assessment Using Fasting Volunteers," *Sensors*, vol. 21, no. 21, p. 6949, Oct. 2021, doi: 10.3390/s21216949.
7. A. Kandwal *et al.*, "A comprehensive review on electromagnetic wave based non-invasive glucose monitoring in microwave frequencies," *Heliyon*, vol. 10, no. 18, p. e37825, Sep. 2024, doi: 10.1016/j.heliyon.2024.e37825.
8. A. J. Bandodkar, W. J. Jeang, R. Ghaffari, and J. A. Rogers, "Wearable Sensors for Biochemical Sweat Analysis," *Annu. Rev. Anal. Chem.*, vol. 12, no. 1, p. 1, Feb. 2019, doi: 10.1146/annurev-anchem-061318-114910.
9. J. C. Lin, "Microwave Property of Biological Materials," *Springer eBooks*, pp. 73–96, Jan. 2021, doi: 10.1007/978-3-030-64544-1_4.

10. D. C. Garrett and E. C. Fear, “Feasibility Study of Hydration Monitoring Using Microwaves–Part 1: A Model of Microwave Property Changes with Dehydration,” *IEEE J. Electromagn., RF Microwaves Med. Biol.*, vol. 3, no. 4, pp. 292–299, Dec. 2019, doi: 10.1109/JERM.2019.2911849.
11. D. V. Solovei, J. Žák, P. Majzlíková, J. Sedláček, and J. Hubálek, “Chemical Sensor Platform for Non-Invasive Monitoring of Activity and Dehydration,” *Sensors*, Jan. 2015, doi: 10.3390/s150101479.
12. S. Krishnan *et al.*, “Wireless, Battery-Free Epidermal Electronics for Continuous, Quantitative, Multimodal Thermal Characterization of Skin,” *Small*, Oct. 2018, doi: 10.1002/smll.201803192.
13. W. Dawsmith, N. Ohtani, R. Donnan, M. Naftaly, R. A. Dudley, and T. T. Chowdhury, “Microwave Frequency Dependent Dielectric Properties of Blood as a Potential Technique to Measure Hydration,” *IEEE Access*, vol. 12, pp. 44940–44948, 2024, doi: 10.1109/ACCESS.2020.2977432.
14. S. Siyoucef, R. Al-Aslani, M. Adnane, T.-M. Laleg-Kirati, and T. Y. Al-Naffouri, “Internet of medical things for non-invasive and non-contact dehydration monitoring away from the hospital: state-of-the-art, challenges and prospects,” *arXiv*, 2024. [Online]. Available: https://arxiv.org/abs/2412.17813
15. C. Origlia, D. O. Rodriguez-Duarte, J. A. Tobon, J.-C. Bolomey, and F. Vipiana, “Review of Microwave Near-Field Sensing and Imaging Devices in Medical Applications,” *Sensors*, vol. 24, no. 14, p. 4515, Jul. 2024, doi: 10.3390/s24144515.
16. V. L. Bartlett, S. S. Dhruva, N. D. Shah, P. Ryan, and J. S. Ross, “Feasibility of Using Real-World Data to Replicate Clinical Trial Evidence,” *JAMA Netw. Open*, vol. 2, no. 10, p. e1912869, Oct. 2019, doi: 10.1001/jamanetworkopen.2019.12869.
17. K. Suehiro, A. Joosten, L. S. Murphy, *et al.*, “Accuracy and precision of minimally invasive cardiac output monitoring in children: a systematic review and meta-analysis,” *J. Clin. Monit. Comput.*, vol. 30, pp. 603–620, 2016, doi: 10.1007/s10877-015-9757-9.
18. M. Y. Jaffrin and H. Morel, “Body fluid volumes measurements by impedance: A review of bioimpedance spectroscopy (BIS) and bioimpedance analysis (BIA) methods,” *Med. Eng. Phys.*, vol. 30, no. 10, pp. 1257–1269, 2008.
19. M. Baghelani, Z. Abbasi, M. Daneshmand, and P. E. Light, “Noninvasive Microwave Sensor for Real-Time Continuous Dehydration Monitoring,” *IEEE Sens. J.*, vol. 24, no. 7, pp. 9959–9969, Apr. 2024, doi: 10.1109/JSEN.2024.3362702.

# 2. Dielectric Theory, Characterization and Permittivity Measurements

The main theme of this chapter is to evaluate dielectric characteristics of biological tissue with a primary emphasis on human biological tissues. The initial subchapter will introduce the theory of dielectric materials when investigating their interaction with electric and magnetic fields. This theoretical foundation will set precedence for understanding how biological tissues behave under various electromagnetic conditions. By establishing this theoretical groundwork, subsequent sections will provide a comprehensive analysis of the dielectric properties, enabling a deeper insight into their practical application for non-invasive hydration monitoring.

The chapter will conclude with a summary of the diverse methodologies employed for dielectric measurements. The section will not only provide a wholistic overview of the various techniques but to also justify selection of open-ended coaxial probe measurements and reflection based microstrip biosensor for the research done within this thesis. A discussion of these methods will include their accuracy, sensitivity, and suitability for in vivo and in vitro non-invasive hydration sensing, offering a critical evaluation of why they are optimal for the thesis objectives. Finally, potential challenges and limitations of dielectric measurement techniques will be addressed to provide a balanced perspective on the research findings.

## 2.1 Dielectric Materials

In a vacuum, the relationship between electric flux density $D$ (C/$m^2$) and the electric field $E$ (V/m) is expressed through the constitutive equation:

$$D = \varepsilon_o E \tag{2.0}$$

Here $\varepsilon_0$ is the permittivity of free space (vacuum), which has a value of approximately:

$$\varepsilon_o = 8.854 \times 10^{-12}\ (F/m)$$

Equation (2.0) states that in a vacuum, the electric flux density $D$ is directly proportional to the electric field $E$ through the vacuum permittivity constant $\varepsilon_0$. In isotropic mediums, this relationship includes the material's relative permittivity $\varepsilon_r$ resulting into Equation (2.1) [1]:

$$D = \varepsilon_o \varepsilon_r E \tag{2.1}$$

Here $\varepsilon_r$ is the permittivity of the medium, which depends on the material's susceptibility $\chi$. The permittivity $\varepsilon_r$ is related to the vacuum permittivity $\varepsilon_o$ and the electric susceptibility $\chi$ by the following Equation [2]:

$$\varepsilon = \varepsilon_o(1 + \chi) \quad (1.2)$$

The electric susceptibility $\chi$ measures the material's ability to be polarised under an electric field. Polarization refers to the alignment of electric dipoles within the material when exposed to an external electromagnetic field, which influences the overall electric flux density *D* within the dielectric [3]. All dielectric materials exhibit a phenomenon called polarization, which is the arrangement of bound charges within the material is response to an external electric field. When an external field is applied to a dielectric material, the positive and negative charges within the material experience a slight displacement in opposite directions. Since bound charges cannot move freely, they shift marginally from their equilibrium positions, creating a localised charge imbalance. This displacement either induces the formation of new electric diploes or alters the orientation of existing ones, resulting in net polarisation within the material [4]. This polarisation enhances the material's capacity to store electrical energy and is described by the polarization vector equation:

$$P = \varepsilon_o \chi E \quad (2.3)$$

The electric flux density can be expressed as [5]:

$$D = \varepsilon_o E = \varepsilon_o(1 + \chi)E = \varepsilon_0 E + P \quad (2.4)$$

The dielectric permittivity of a material is commonly considered in the form of relative permittivity. Relative permittivity is a dimensionless quantity defined as the ratio of the permittivity of material to the permittivity of free space [6].

$$\varepsilon_r = \frac{\varepsilon}{\varepsilon_o} \quad (2.5)$$

This normalisation process simplifies the comparison of a material's dielectric properties relative to those of a vacuum. As a result, the relative permittivity provides a standardised reference, allowing for a clearer and more meaningful assessment of a material's dielectric behaviour.

Equations (2.0 to 2.5) apply to the most basic categories of materials, which exhibit properties such as homogeneity, isotropy, linearity and independence from frequency. However, not all materials conform to these idealised characteristics. In inhomogeneous materials, permittivity varies across different regions, making the analysis more complex due to its spatial dependence [7]. Similarly, anisotropic materials introduce another level of intricacy, as their permittivity is direction-dependent, meaning their response changes based on the orientation of the applied electric field. This directional variation necessitates a more detailed evaluation of how material

interacts with electric fields in different orientations [8]. Nonlinear materials further complicate the analysis since their permittivity is not constant but varies as a function of the electric field's strength [9]. This nonlinearity implies that the material's response shifts depending on the intensity of the applied field, requiring additional considerations in calculations and modelling. Additionally, while most materials exhibit some degree of frequency-dependent permittivity, this variation is not always significant. When the permittivity remains relatively stable across the relevant frequency range, the material can be treated as frequency-independent for practical purposes. However, in cases where the permittivity changes considerably with frequency (dispersive materials). Its dependence must be accounted for in the analysis.

It is crucial to note that permittivity is a complex value with a real and imaginary part. This is expressed by

$$\hat{\varepsilon}_r = \varepsilon_r' - j\varepsilon_r^{"} \tag{2.6}$$

In this thesis, the term "permittivity" is employed to specifically refer to the complex permittivity denoted by $\hat{\varepsilon}$, in the context of normalization to a dimensionless quantity, the term "permittivity" is equivalent to the complex relative permittivity $\hat{\varepsilon}_r$. To better understand the electromagnetic wave propagation and material behaviour, the complex permittivity equation is inserted into Maxwell's fourth equation:

$$\nabla \times H = j\omega D + J$$

$$\nabla \times H = j\omega\varepsilon_0\varepsilon_r E + \sigma_s E$$

or $$\nabla \times H = j\omega\varepsilon_{eff} E$$

where $$\varepsilon_{eff} = \varepsilon_0\varepsilon_r' - j\left(\varepsilon_0\varepsilon_r^{"} - j\frac{\sigma_s}{\omega}\right)$$

$$\nabla \times H = j\omega\left(\varepsilon_0\varepsilon_r' - j\varepsilon_0\varepsilon_r^{"} - j\frac{\sigma_s}{\omega}\right)E \tag{2.7}$$

Where $H$ is the magnetic field strength, $\omega = 2\pi f$ is the angular frequency, $J$ is the total current density and $\sigma_s$ is the static conductivity**.**

In the context of electromagnetic wave propagation and material behaviour, Equation (2.7) showcases the interaction between the imaginary and real components of complex permittivity. It is noted that the real component represents how the material stores electrical energy while the imaginary part $\varepsilon_r^{"}$ and the static conductivity $\sigma_s$, describes energy absorption and losses in the material. Two distinct types of losses are present; the first represents the dielectric damping in

the material and the second represents the losses due to the static conductivity $\sigma_s$. Static conductivity is comprised of various conduction mechanisms, but ionic conductivity is the most common [10]. Ionic conductivity occurs when charged particles, such as ions in a dielectric material migrate under an applied electric field, leading to energy dissipation. Researchers usually quantify these losses using metrics such as the loss tangent or loss factor [11].

$$tan_{\delta} = \frac{\varepsilon_r^{"}}{\varepsilon_r'} \tag{2.8}$$

Where $\delta$ is the loss angle. This loss factor is a quotient of energy lost per cycle against energy stored per cycle. To better illustrate the complex permittivity, it is represented in a complex plane, where the real and imaginary components exhibit a 90° phase shift as shown in Figure 2.1.

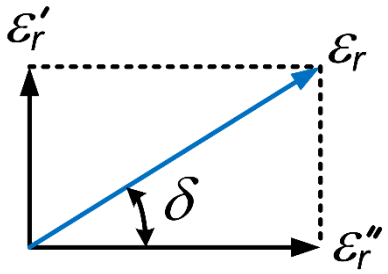


*Figure 2.1: Complex permittivity in a complex plane.*

Complex permittivity can be illustrated by plotting the real and imaginary components as functions of frequency. However, given that the conductivity $\sigma_s$ is linked with the imaginary part of relative permittivity through $\sigma_s = \omega\varepsilon_0\varepsilon_r^{"}$, it is uncommon to see plots of real part of relative permittivity and equivalent conductivity [12]. In such cases, the conductivity is the sum of all loss mechanisms: ionic and dielectric. The resulting conductivity profile provides an in-depth view of how energy dissipates within the material as a function of frequency. It must be noted that this behaviour varies significantly depending on the specific material properties and the frequency range under consideration.

As shown in Figure 2.2 frequency dispersion occurs around the resonant frequency, often referred to as relaxation frequency $f_{rel}$. This is where $\varepsilon_r'$ and $\varepsilon^{"} and\ \varepsilon'$ exhibit distinct behaviours as the frequency varies. Real materials such as biological tissues exhibit multiple resonant frequencies, each intricately linked to distinct polarization mechanisms. These phenomena are comprehensively discussed in the next chapter.

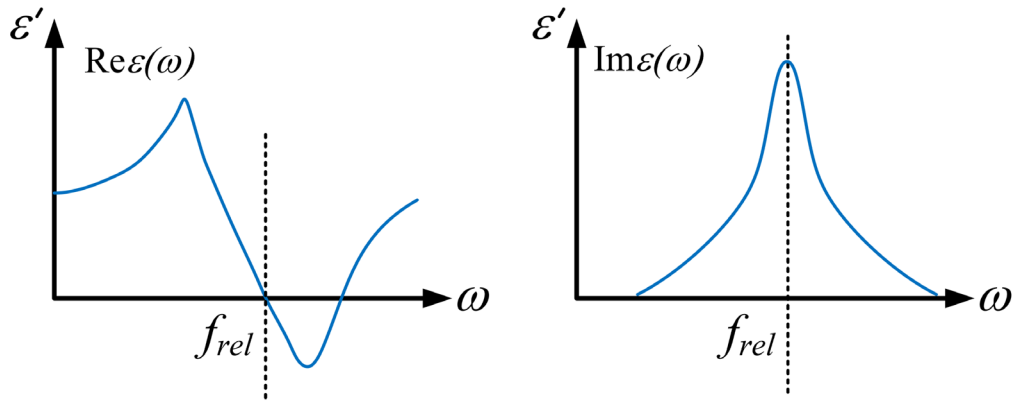


*Figure 2.2: Real and imaginary part of permittivity as a function of frequency.*

## 2.2 Dielectric relaxations

Dielectric relaxation is fundamental in understanding the behaviour of polar and non-polar materials under the influence of an external electric field [4][13]. It describes the delay in the response of a dielectric medium to change in an applied electric field, which arises due to the inherent time-dependent polarization processes within the material. The polarization dynamic depends on several factors, including the nature of bound charges and the internal structure of the dielectric [14]. Within a dielectric, electric charges remain bound they cannot move independently over very short distances.

The relaxation of dielectric materials is characterized by the complex dielectric function, which encompasses both permittivity (ε′) and dielectric loss (ε″), describing the storage and dissipation of electrical energy, respectively [15]. The frequency-dependent nature of dielectric relaxation is often modelled using empirical and theoretical approaches, such as the Debye, Cole-Cole, Cole-Davidson, and Havriliak-Negami models [16][17]. These models help in elucidating the microscopic mechanisms governing polarization and relaxation in different types of materials, including biological tissues, and composite materials. The mechanisms responsible for dielectric relaxation include dipolar orientation, ionic conduction, interfacial (Maxwell-Wagner-Sillars) polarization, and quantum mechanical effects in specific systems. Each mechanism contributes uniquely to a material's overall dielectric response, depending on factors such as temperature, frequency, composition, and structural properties.

### 2.2.1 Dielectric relaxation models

The Debye model, shown in Figure 2.3, is a well-known equivalent material model for a single layer lossy material. The Debye model assumes that the medium is comprised of uniform polar

molecules that rotate without mutual interaction leading to a single relaxation time [18]. It is expressed as follows:

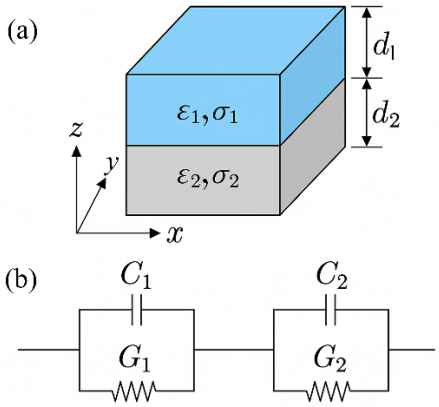


*Figure 2.3: Two-layered model of a dielectric material adapted from [18].*

$$\varepsilon^*(\omega) = \varepsilon' - j\varepsilon'' = \varepsilon_\infty + \frac{\varepsilon_s - \varepsilon_\infty}{1 + j\omega\tau} \qquad (2.9)$$

Where $\varepsilon'$ is the real part of the complex dielectric constant, $\varepsilon''$ is the imaginary part of the complex dielectric constant, $\varepsilon_s$ is the dielectric constant at low frequencies, $\varepsilon_\infty$ is the dielectric constant at very high frequencies, $\omega$ is the angular frequency, and $\tau$ is the time constant, and also called relaxation factor.

The Debye model provides a fundamental description of dipolar relaxation in dielectrics, if the polarization relaxes exponentially with a single relaxation time τ. This model is particularly useful for materials where a single relaxation process dominates, such as certain polar liquids and polymers. The term represents the dielectric dispersion, which indicates the extent of frequency-dependent variation in the permittivity.

One of the key implications of the Debye model is that it predicts a symmetric distribution of relaxation times, making it ideal for simple molecular systems. However, in real materials, deviations from the ideal Debye behaviour are often observed due to molecular interactions, structural heterogeneities, and the presence of multiple relaxation mechanisms [18]. These deviations necessitate the use of extended models such as the Cole-Cole, Cole-Davidson, and Havriliak-Negami models, which introduce additional empirical parameters to account for non-ideal relaxation behaviour.

The loss tangent, defined as $tan_\delta = \frac{\varepsilon_r''}{\varepsilon_r'}$, is an important parameter derived from the Debye model and provides insight into the dissipation of energy within the dielectric material. This is

particularly relevant in applications involving microwave absorption, energy storage, and dielectric spectroscopy, where optimizing the dielectric response is critical.

The Cole-Cole model was introduced as an empirical model that better fits the dielectric relaxation in polymers which have broader dispersion curves and lower maximum loss [19]:

$$\varepsilon^*(\omega) = \varepsilon' - j\varepsilon'' = \varepsilon_\infty + \frac{\varepsilon_s - \varepsilon_\infty}{1 + (j\omega\tau)^{1-\alpha}} \tag{2.10}$$

Where $\alpha$ is a number between 0 and 1. When the exponent parameter $\alpha$ equals 1, the Cole-Cole model reduces to the Debye model. When $\alpha$ is less than 1, the relaxation is stretched, extending over a broader range of frequencies than Debye relaxation. This flexibility makes the Cole-Cole model applicable to a wide range of materials with different dielectric properties.

The Cole-Davidson model extends the Debye model by incorporating asymmetric broadening of the relaxation spectrum [20]. It is given by

$$\varepsilon^*(\omega) = \varepsilon' - j\varepsilon'' = \varepsilon_\infty + \frac{\varepsilon_s - \varepsilon_\infty}{1 + (j\omega\tau)^{\beta}} \tag{2.11}$$

Where β ($0 < \beta \leq 1$) is an empirical parameter that accounts for asymmetric broadening of the relaxation time distribution. The Cole-Davidson model is particularly useful for describing materials in which the relaxation process is skewed towards longer relaxation times.

The most general form of dielectric relaxation is described by the Havriliak-Negami model which is a combination of Cole-Cole and Cole-Davidson models [21]. It is expressed as:

$$\varepsilon^*(\omega) = \varepsilon' - j\varepsilon'' = \varepsilon_\infty + \frac{\varepsilon_s - \varepsilon_\infty}{1 + (j\omega\tau)^{(1-\alpha)\beta}} \tag{2.12}$$

Where $\alpha (0 \leq \alpha \leq 1)$ and $\beta (0 \leq \beta \leq 1)$ are empirical parameters. The model accounts for both symmetric and asymmetric broadening of the relaxation spectrum, making it the most flexible model for describing dielectric relaxation in complex materials.

### 2.2.2 Dielectric Polarization mechanisms

Dielectric polarization refers to the response of a material to an external electric field, resulting in the formation of dipole moments [22]. Several polarization mechanisms contribute to the overall dielectric response of a material depending on the frequency of the applied electric field. The precise permittivity value is dependent on these polarization mechanisms which include

electronic, ionic, dipolar and atomic polarization [23]. Their approximate frequency range and effect on both real and imaginary part of the permittivity is shown in Figure 2.4.

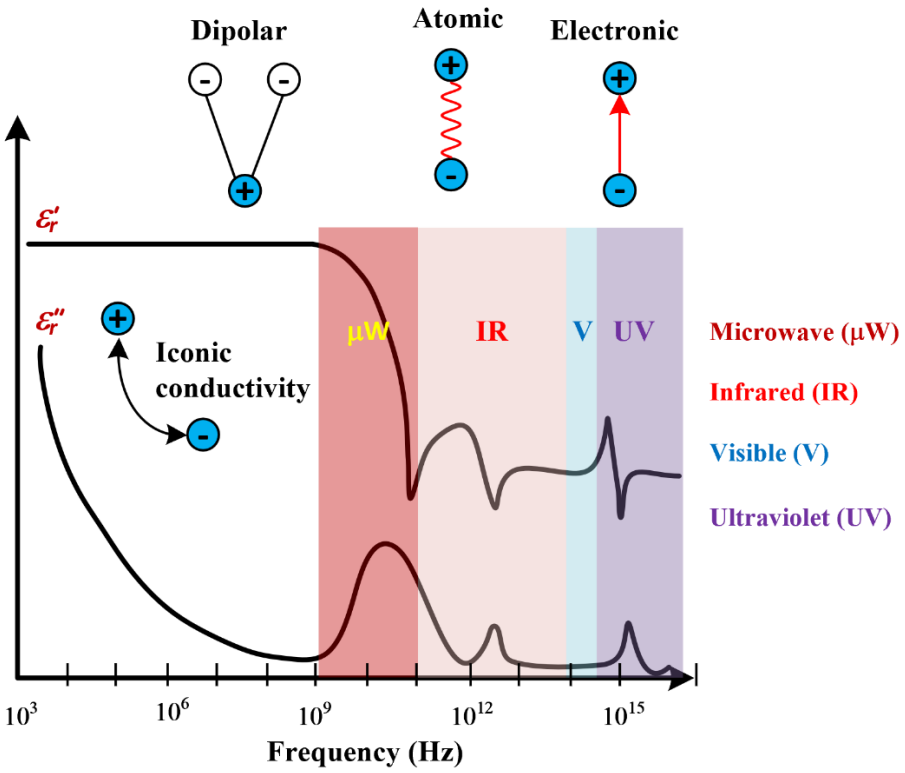


*Figure 2.4: Dielectric polarization mechanisms [23].*

At low frequencies ($10^3$ - $10^6$ Hz), the dominant contribution to dielectric behaviour is ionic conductivity. Mobile charge carriers (ions) migrate under an applied electric field, leading to a significant imaginary component ($\varepsilon''$) due to resistive losses. The process is essential in electrolytes, ionic conductors and biological tissues where charge transport plays a role in functionality [24].

In microwave frequency range (~$10^9$ Hz), dipolar polarization becomes significant. This happens when molecular dipoles attempt to align with the oscillating electric field. The effectiveness of dipolar alignment is frequency-dependent, with a characteristic relaxation beyond which the dipoles cannot reorient fast enough. This relaxation leads to a decline in $\varepsilon'$ and a peak in $\varepsilon''$ associated with energy dissipation [23].

At frequencies approaching the infrared (IR) region (~$10^{12}$ Hz), atomic polarization mechanisms dominate. This effect arises from the displacement of atoms or ions within the crystal lattice under an external electric field. The vibrational resonance of atoms within a material leads to strong

dielectric absorption, with sharp features in both $\varepsilon'$ and $\varepsilon''$. This process is critical in phonon-mediated interactions and optical phonon applications in semiconductors.

At even higher frequencies ($10^{15}$ Hz), electronic polarization is the primary response mechanism. Here, the applied electric field influences the electron cloud surrounding the atomic nucleus, causing a shift in charge distribution. This effect is nearly instantaneous compared to lower-frequency polarization processes. In the ultraviolet (UV) region, resonance phenomena may lead to characteristic absorption peaks.

### 2.2.3 Relaxation Regions in Biological Tissue

When investigating human biological tissue, identifying electrical boundaries is important for understanding the dielectric properties of biological structures [25]. Hanninen et al examined that these boundaries are primarily defined by cell membranes, which act as critical interfaces between intracellular and extracellular environments. Composed of a phospholipid bilayer, cell membranes possess inherent electrical resistance and capacitance, influencing how tissues respond to external electric fields [26].

When an external field is applied to biological tissues, various polarization mechanisms occur, leading to distinct dielectric dispersion regions. These relaxation regions α, β, γ, and δ dispersions reflect different frequency-dependent responses of biological matter. Each dispersion is associated with specific physiological processes, such as ion mobility, macromolecular interactions, and water content [27].

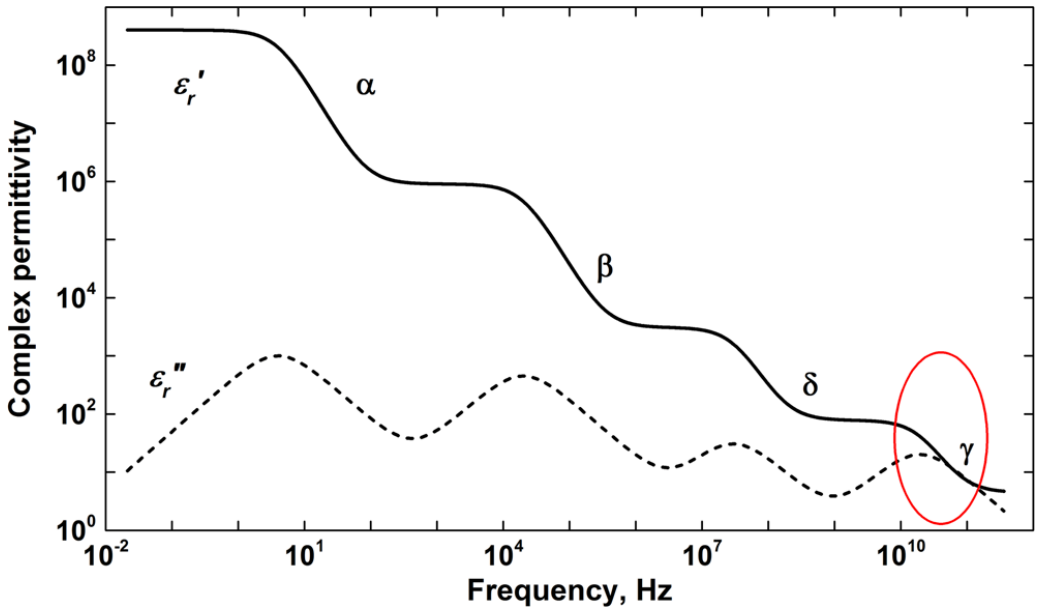


*Figure 2.5: Schematic diagram showing relaxation regions (α, β, γ, and δ) of biological tissue.*

For non-invasive hydration monitoring, the frequency region of interest is 2.45 GHz, which falls within the Industrial, Scientific, and Medical (ISM) band. This frequency lies within the δ-dispersion region (see Figure 2.5), which is one of the critical frequency ranges in the dielectric spectrum of biological tissues. In this region, typically spanning from a few hundred MHz to several GHz, the dielectric response is primarily governed by the relaxation dynamics of free and loosely bound water molecules. Specifically, at 2.45 GHz a frequency commonly used in microwave and biomedical applications the dielectric properties of biological tissues are especially sensitive to the rotational relaxation of dipolar water molecules, particularly free water [28].

The δ-dispersion region is distinguished from other dispersion regions ($\alpha$ and $\beta$) by its association with molecular-level interactions, especially the reorientation of water molecules in response to an applied alternating electromagnetic field. Unlike the α-dispersion region, which is dominated by ionic diffusion and interfacial polarization, or the β-dispersion region, associated with polarization of cellular membranes and macromolecules, δ-dispersion is strongly modulated by water content and the physicochemical state of water within the tissue matrix [29].

Given that hydration levels directly influence the proportion of free versus bound water in biological tissues, monitoring the dielectric properties at 2.45 GHz provides a powerful non-invasive approach for assessing tissue hydration. In this frequency range, changes in water content leads to measurable variations in the complex permittivity, particularly the real part (dielectric constant) and the imaginary part (dielectric loss), which reflect the ability of tissues to store and dissipate electric energy, respectively [30].

Moreover, this frequency aligns well with the Debye relaxation model of water, where the characteristic relaxation time of free water molecules corresponds to maximum dielectric loss at approximately 2.5 GHz at room temperature [31][32]. Thus, operating at or near 2.45 GHz enables the detection of minute shifts in dielectric properties, making it highly sensitive and reliable for quantifying hydration status, especially in clinical diagnostics, physiological monitoring, and bioimpedance applications.

In summary, the choice of 2.45 GHz within the δ-dispersion region is not arbitrary but theoretically grounded and empirically validated. It exploits the intrinsic dielectric behaviour of water, which is a dominant constituent of biological tissues and a key indicator of hydration. This

provides a robust and physiologically relevant basis for developing dielectric spectroscopy tools aimed at real-time, non-invasive hydration monitoring.

## 2.3 Dielectric Measurement Methods

The measurement of dielectric properties is fundamental to understanding the electrical behaviour of materials, particularly their ability to store and dissipate electric energy. These properties are crucial in biomedical applications. Dielectric measurements can be conducted over a wide range of frequencies, from millihertz (mHz) to terahertz (THz), depending on the material characteristics and the intended application [33]. Various methodologies have been developed to assess these properties accurately, each suited to specific frequency ranges. All the various methods have their own advantages and disadvantages, so it is essential to have a comprehensive study of the different techniques to provide a confident selection of a suitable measurement method for potential non-invasive hydration monitoring in biological tissue. The subsequent subchapters will briefly define several of the most common methods for dielectric spectroscopy, which include transmission methods, free space methods, resonant methods and open-ended coaxial probe.

### 2.3.1 Resonant Methods

Resonant techniques form a significant category of dielectric measurement methods, known for their high precision and sensitivity (Figure 2.5). These characteristics make them highly effective in dielectric measurement applications [34]. The underlying principle of resonant measurements lies in their ability to exploit resonance phenomena in dielectric materials. Dielectric resonators or structures used for these measurements are precisely tuned to a resonance condition, which provides critical information about the properties of the material [35].

One major advantage of resonant measurements is that, in many cases, it is sufficient to measure the resonance frequency to accurately assess the permittivity of the material, eliminating the need to determine the sample volume. This feature enhances the efficiency and accuracy of the technique. There are many different types of resonators and structures used for resonant dielectric measurements [36]. These resonators are suitable for both solid and liquid samples and operate across an extensive frequency range, from a few kilohertz to hundreds of gigahertz.

Another common type is the microstrip resonator [37]. These resonators are widely available as commercially produced accessories, particularly for bench-top vector network analysers, but they

are also relatively easy to fabricate. In this approach, small samples are plated onto the microstrip, and measurements are typically conducted in a probe-station.

Recent research has focused on more advanced resonators, such as split-ring resonators and dielectric resonators loaded into waveguides built using substrate integrated waveguide (SIW) technology [38]. The latter is particularly intriguing due to its capability for non-invasive measurements of solid samples. Additionally, it operates in the X-band at room temperature, making it a promising approach for practical applications.

This thesis will also investigate the integration of magnetic ferrite materials within microstrip patch antenna structures as a potential non-invasive method for hydration monitoring in biological tissues (refer to Chapter 5). The incorporation of ferrite materials is anticipated to influence the electromagnetic properties of the antenna, particularly its resonant behaviour, thereby enabling sensitive detection of variations in tissue dielectric properties associated with hydration levels. By exploiting resonant sensing techniques, this study aims to improve the precision and reliability of dielectric measurements in biomedical contexts. The proposed approach represents a novel intersection of antenna engineering and biomedical sensing, offering a promising pathway toward the development of compact, cost-effective, and non-invasive diagnostic tools for real-time hydration assessment in clinical and health-monitoring applications.

### 2.3.2 Transmission methods

This methodology involves the propagation of an electromagnetic wave through a transmission line that encapsulates the Material under test (MUT) [39] (see Figure 2.5). As the electromagnetic wave travels through the transmission line, it experiences reflection and transmission at points of discontinuity. These disruptions are caused by changes in impedance of the line, which in turn, are caused by changes in permittivity of the material within the line. The transmitted ($S_{21}$) and reflected ($S_{11}$) signals are then measured using a vector network analyser. The complex permittivity of the material is then calculated from the amplitude and phase of these waves. Using classification algorithms, the permittivity and permeability can be computed from the measured scattering parameters [39]. The extraction process involves solving the inverse problem using transmission line theory and material characterization models, such as Nicolson-Ross-Weir (NRW), Short-Open Calibration [40]. Furthermore, environmental factors such as temperature, humidity, and frequency-dependent variations are considered to ensure precision in measurement. The experimental setup may also incorporate calibration procedures, including Thru-Reflect-Line (TRL) or Short-Open-Load-Through (SOLT) calibration, to minimize errors and improve

repeatability. This methodology finds applications in various fields, including non-destructive material testing, biomedical sensing, microwave engineering, and metamaterial research, where precise electromagnetic characterization is crucial.

### 2.3.3 Free Space Methods

The free-space method is a non-contact and non-destructive technique for measuring the permittivity of materials (Figure 2.5). This approach involves transmitting an electromagnetic wave through free space and directing it toward the Material Under Test (MUT). The interaction between the incident wave and the material results in reflection, transmission, and absorption effects, which are influenced by the material's electromagnetic properties [41][42].

To capture these effects, the transmitted and reflected waves are measured using a pair of antennas positioned on either side of the MUT. These antennas are connected to a Vector Network Analyzer (VNA), which records the scattering parameters ($S_{11}$) for reflection and $S_{21}$) for transmission). The amplitude and phase information of these signals are then used to extract the complex permittivity ( $\varepsilon$)and permeability ($\mu$ )of the material. To ensure precise measurements, calibration techniques such as Thru-Reflect-Line (TRL), Short-Open-Load-Through (SOLT), and Free-Space Time-Gating are often applied to eliminate unwanted reflections, diffraction, and environmental interferences [43]. The method is well-suited for characterizing dielectric and composite materials over a broad frequency range, particularly in the microwave and millimetre-wave spectrum.

The free-space method holds significant potential in biomedical applications, particularly for non-invasive tissue assessment by leveraging the unique dielectric properties of biological tissues across different frequencies [44]. This technique enables tissue characterization, aiding in cancer detection and wound healing monitoring by differentiating between healthy and diseased tissues. It also facilitates microwave imaging and early cancer diagnosis, particularly in breast cancer screening, as a safer alternative to ionizing radiation-based mammography. Additionally, free-space measurements can be explored for continuous glucose monitoring in diabetic patients and hydration assessment for conditions such as dehydration, burn severity, and edema. The method also supports the development of wireless and implantable sensors for monitoring physiological signals like EEG, ECG, and wound healing progress. Key advantages include its non-contact, non-destructive nature, wide frequency range for optimized tissue characterization, and potential for remote sensing, reducing reliance on invasive procedures. As research advances, this method

is poised to play a crucial role in biomedical diagnostics, wearable health monitoring, and medical imaging, contributing to the future of biomedical engineering and patient care.

### 2.3.4 Open Ended Coaxial Probe Method

The OECP technique (Figure 2.6) is based on the reflection of electromagnetic waves from a coaxial probe in contact with a material [45]. When the probe is placed against biological tissue, a fraction of the incident wave is reflected while another portion penetrates the material. The reflection coefficient ($S_{11}$) is measured using a Vector Network Analyzer (VNA), from which the complex permittivity of the material is extracted [46]. The dielectric properties provide insights into tissue hydration, ion mobility, and molecular interactions.

The open-ended coaxial probe (OECP) method, a widely adopted technique in material characterization, offers a direct and reliable means of measuring the complex permittivity of biological tissues. The dielectric constant ($\varepsilon'$) and loss factor ($\varepsilon''$) of tissues are intrinsically linked to their water content, ionic concentration, and structural composition [47]. Given that water exhibits significant dielectric dispersion within the microwave frequency range, this study focuses on 2.45 GHz a frequency extensively utilized in both biomedical diagnostics and industrial microwave applications. One of the central research questions and objectives of this thesis is to evaluate the efficacy of the OECP method as a proof-of-concept tool for non-invasive hydration monitoring by establishing a quantifiable and reproducible correlation between tissue hydration levels and their corresponding dielectric properties.

The research will include rigorous experimental validation using a range of test samples, including artificial sweat solutions (refer to Chapter 4), ex vivo biological tissues, and in vivo human skin measurements. The experimental setup features a precision-calibrated OECP system interfaced with a Vector Network Analyzer (VNA) operating at 2.45 GHz to ensure high-fidelity permittivity measurements across samples with controlled hydration states.

To enhance the interpretability and predictive capabilities of the dielectric measurements, classification algorithms will be investigated for their potential to accurately distinguish between hydration levels based on permittivity data.

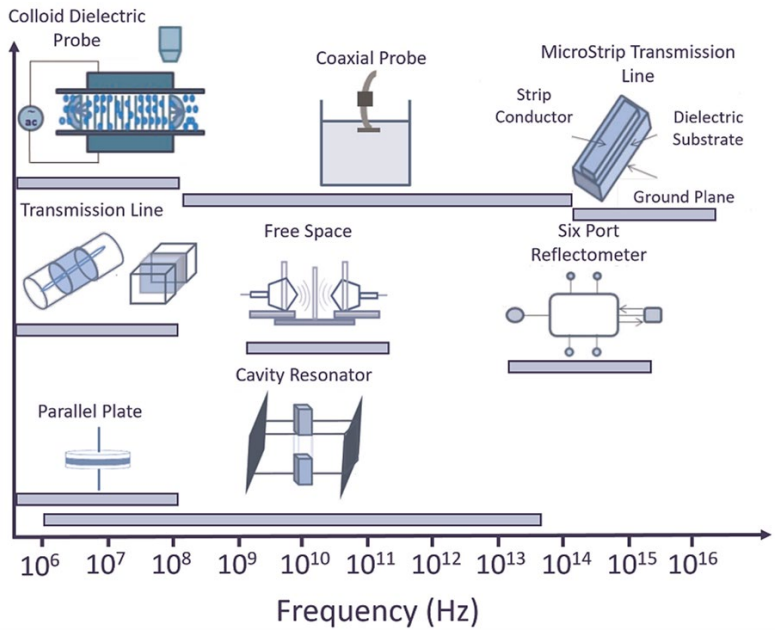


*Figure 2.6: Techniques for characterizing dielectric properties across a wide frequency range [23].*

## References


1. K. Zhang and D. Li, Electromagnetic Theory for Microwaves and Optoelectronics. Berlin; New York: Springer, 2008.
2. D. V. Matyushov, "Dielectric susceptibility of water in the interface," J. Phys. Chem. B, vol. 125, no. 30, pp. 8282–8293, Jul. 2021, doi: 10.1021/acs.jpcb.1c03720.
3. I. Sinev, et al., "Polarization control over electric and magnetic dipole resonances of dielectric nanoparticles on metallic films," Laser Photon. Rev., vol. 10, no. 5, pp. 799–806, 2016.
4. C. Gabriel, "Dielectric properties of biological materials," Bioeng. Biophys. Aspects Electromagn. Fields, 2018, pp. 87–136.
5. T. Yin, C.-F. Wang, K. Xu, Y. Zhou, Y. Zhong, and X. Chen, "Electric flux density learning method for solving 3-D electromagnetic scattering problems," IEEE Trans. Antennas Propag., vol. 70, no. 7, pp. 5144–5155, Jul. 2022, doi: 10.1109/TAP.2022.3145486.
6. M. S. Venkatesh and G. S. V. Raghavan, "An overview of dielectric properties measuring techniques," Can. Biosyst. Eng., vol. 47, no. 7, pp. 15–30, 2005.
7. J. Ramírez-González, D. C. Sinclair, and A. R. West, "Impedance and dielectric spectroscopy of functional materials: a critical evaluation of the two techniques," J. Electrochem. Soc., vol. 170, no. 11, p. 116504, Nov. 2023, doi: 10.1149/1945-7111/ad09fa.
8. C. Zheng, et al., "A two-directional vibrational probe reveals different electric field orientations in solution and an enzyme active site," Nat. Chem., vol. 14, no. 8, pp. 891–897, 2022, doi: 10.1038/s41557-022-00937-w.
9. T. Linde, J. T. Loh, S. Kornhuber, K. Backhaus, S. Schlegel, and S. Großmann, "Implications of nonlinear material parameters on the dielectric loss under harmonic distorted voltages," Energies, vol. 14, no. 3, p. 663, 2021, doi: 10.3390/en14030663.
10. A. Abdelmalik, J. Fothergill, and S. Dodd, "Electrical conduction and dielectric breakdown characteristics of alkyl ester dielectric fluids obtained from palm kernel oil," IEEE Trans.

Dielectr. Electr. Insul., vol. 19, no. 5, pp. 1623–1632, Oct. 2012, doi: 10.1109/TDEI.2012.6311509.
11. V. V. Shcherbakov, et al., "Dielectric characteristics, electrical conductivity and solvation of ions in electrolyte solutions," Materials, vol. 14, no. 19, p. 5617, 2021.
12. J. Baker-Jarvis and S. Kim, "The interaction of radio-frequency fields with dielectric materials at macroscopic to mesoscopic scales," J. Res. Natl. Inst. Stand. Technol., vol. 117, pp. 1–60, Feb. 2012, doi: 10.6028/jres.117.001.
13. Y. Feldman, Y. A. Gusev, and M. A. Vasilyeva, "Dielectric relaxation phenomena in complex systems," Kazan Fed. Univ., Inst. Phys., 2012.
14. Dielectric Polarization and Bound Charges, [online] https://web2.ph.utexas.edu/~vadim/Classes/2024s-u/bound.pdf?utm_source=chatgpt.com
15. C. Steiner, et al., "Determination of the dielectric properties of storage materials for exhaust gas aftertreatment using the microwave cavity perturbation method," Sensors, vol. 20, no. 21, p. 6024, 2020, doi: 10.3390/s20216024.
16. S. Holm, "Time domain characterization of the Cole-Cole dielectric model," J. Electr. Bioimpedance, vol. 11, no. 1, p. 101, 2020, doi: 10.2478/joeb-2020-0015.
17. E. Barelli, "Dielectric relaxation in biological materials," 2015.
18. R. H. Cole, "Dielectric absorption in polar media and the local field," J. Chem. Phys., vol. 6, no. 7, pp. 385–391, 1938.
19. T. P. Iglesias, G. Vilão, and J. C. R. Reis, "An approach to the interpretation of Cole–Davidson and Cole–Cole dielectric functions," J. Appl. Phys., vol. 122, no. 7, 2017.
20. Y. Feldman, A. Puzenko, and Y. Ryabov, "Non-Debye dielectric relaxation in complex materials," Chem. Phys., vol. 284, no. 1-2, pp. 139–168, 2002.
21. A. S. Elwakil, A. A. Al–Ali, and B. J. Maundy, "Extending the double-dispersion Cole–Cole, Cole–Davidson and Havriliak–Negami electrochemical impedance spectroscopy models," Eur. Biophys. J., vol. 50, no. 6, pp. 915–926, 2021.
22. B. Quan, et al., "Dielectric polarization in electromagnetic wave absorption: Review and perspective," J. Alloys Compd., vol. 728, pp. 1065–1075, 2017, doi: 10.1016/j.jallcom.2017.09.082.
23. D. El Khaled, et al., "Dielectric spectroscopy in biomaterials: Agrophysics," Materials, vol. 9, p. 310, 2016, doi: 10.3390/ma9050310.
24. A. Alsoud, et al., "Study of the dielectric properties, relaxation mechanisms and electrical conduction mechanisms of epoxy/α iron oxide nanocomposites," J. Alloys Compd., 2025, Art. no. 179806, doi: 10.1016/j.jallcom.2025.179806.
25. G. B. Furman, V. M. Meerovich, and V. L. Sokolovsky, "Correlation of transverse relaxation time with structure of biological tissue," J. Magn. Reson., vol. 270, pp. 7–11, 2016.
26. N. E. Hänninen, et al., "Relaxation anisotropy of quantitative MRI parameters in biological tissues," Sci. Rep., vol. 12, p. 12155, 2022, doi: 10.1038/s41598-022-15773-8.
27. C. Gabriel, "Dielectric properties of biological materials," Bioeng. Biophys. Aspects Electromagn. Fields, 2018, pp. 87–136.
28. S. Romanenko, et al., "The interaction between electromagnetic fields at megahertz, gigahertz and terahertz frequencies with cells, tissues and organisms: risks and potential," J. R. Soc. Interface, vol. 14, no. 137, 2017, doi: 10.1098/rsif.2017.0585.
29. C. Galindo, et al., "The effect of ionic redistributions on the microwave dielectric response of cytosol water upon glucose uptake," Eur. Biophys. J., vol. 53, pp. 183–192, 2024, doi: 10.1007/s00249-024-01708-w.

30. A. Kordić and A. Šarolić, “Dielectric spectroscopy shows a permittivity contrast between meningioma tissue and brain white and gray matter,” Cancers, vol. 15, no. 16, p. 4153, 2023, doi: 10.3390/cancers15164153.
31. P. M. Meaney, A. P. Gregory, J. Seppälä, and T. Lahtinen, “Open-ended coaxial dielectric probe effective penetration depth determination,” IEEE Trans. Microw. Theory Tech., vol. 64, no. 3, pp. 915–923, Mar. 2016, doi: 10.1109/TMTT.2016.2519027.
32. U. Kaatze, “Dielectric relaxation of water,” Dielectric relaxation in biological systems, V. Raicu and Y. Feldman, Eds. 2015, pp. 189–220.
33. V. Artemov and V. Artemov, “The interaction of electromagnetic waves with water,” The Electrodynamics of Water and Ice, 2021, pp. 51–104.
34. L. Li, J. Y. Zhu, and X. M. Chen, “Measurement error of temperature coefficient of resonant frequency for microwave dielectric materials by $TE_{01}\delta$-mode resonant cavity method,” IEEE Trans. Microw. Theory Tech., vol. 64, no. 11, pp. 3781–3786, Nov. 2016, doi: 10.1109/TMTT.2016.2601928.
35. C. Guo, R. Liu, X. Chen, G. Mavko, and Z. He, “An ultra-wideband measurement method for the dielectric property of rocks,” IEEE Geosci. Remote Sens. Lett., vol. 16, no. 6, pp. 874–878, Jun. 2019, doi: 10.1109/LGRS.2018.2886416.
36. H. N. Morales-Lovera, et al., “Microstrip sensor and methodology for the determination of complex anisotropic permittivity using perturbation techniques,” Sci. Rep., vol. 12, no. 1, p. 2205, Feb. 2022, doi: 10.1038/s41598-022-06259-8.
37. Z. U. Islam, A. Bermak, and B. Wang, “A review of microstrip patch antenna-based passive sensors,” Sensors, vol. 24, no. 19, p. 6355, Sep. 2024, doi: 10.3390/s24196355.
38. N. S. Khair, et al., “Substrate-integrated waveguide (SIW) microwave sensor theory and model in characterising dielectric material: A review,” Sensors Int., vol. 4, p. 100244, 2023, doi: 10.1016/j.sintl.2023.100244.
39. F. S. Malan, “Study of moisture in concrete utilizing the effect on the electromagnetic fields at UHF frequency on an embedded transmission line,” PhD thesis, 2002.
40. K.-P. Latti, M. Kettunen, J.-P. Strom, and P. Silventoinen, “A review of microstrip T-resonator method in determining the dielectric properties of printed circuit board materials,” IEEE Trans. Instrum. Meas., vol. 56, no. 5, pp. 1845–1850, Oct. 2007, doi: 10.1109/TIM.2007.903587.
41. Z. Wang and W. Che, “In-vitro and in-vivo techniques to measure the dielectric constant of biological tissues at microwave frequencies,” Proc. Int. Conf. Microw. Millim. Wave Technol., Nanjing, 2008, pp. 922–925, doi: 10.1109/ICMMT.2008.4540556.
42. R. Zajicek, T. Smejkal, L. Oppl, and J. Vrba, “Waveguide probes for complex permittivity measurement,” Proc. 14th Conf. Microw. Techn., Prague, Czech Republic, 2008, pp. 1–4, doi: 10.1109/COMITE.2008.4569903.
43. P. Mehrotra, B. Chatterjee, and S. Sen, “EM-wave biosensors: A review of RF, microwave, mm-wave and optical sensing,” Sensors, vol. 19, no. 5, p. 1013, 2019.
44. Z. Akhter and M. J. Akhtar, “Free-space time domain position insensitive technique for simultaneous measurement of complex permittivity and thickness of lossy dielectric samples,” IEEE Trans. Instrum. Meas., vol. 65, no. 10, pp. 2394–2405, Oct. 2016.
45. W. J. Ellison and J.-M. Moreau, “Open-ended coaxial probe: model limitations,” IEEE Trans. Instrum. Meas., vol. 57, no. 9, pp. 1984–1991, Sep. 2008, doi: 10.1109/TIM.2008.917683.
46. P. M. Meaney, A. P. Gregory, J. Seppälä, and T. Lahtinen, “Open-ended coaxial dielectric probe effective penetration depth determination,” IEEE Trans. Microw. Theory Tech., vol. 64, no. 3, pp. 915–923, Mar. 2016, doi: 10.1109/TMTT.2016.2519027.

# 3. Permittivity of Biological Tissues

Over the past decades, extensive research has led to the development of several comprehensive permittivity databases, cataloguing the electromagnetic characteristics of different biological tissues across a wide frequency spectrum [1] [2]. These databases serve as fundamental references for computational modelling, bioelectromagnetic research, and the development of medical devices [3]-[5]. However, despite their vast and expansive nature, significant knowledge gaps persist, particularly in the characterization of tissues exhibiting intrinsic anisotropy or structural complexity such as the human body.

One such gap exists in the accurate characterization of multilayered biological tissues, such as human skin and the wrist region, where the heterogeneous composition including the epidermis, dermis, hypodermis, and underlying vascular structures creates a non-uniform dielectric response [6]. The presence of varying hydration levels, collagen fibre orientation, and interstitial fluid dynamics further complicates the dielectric behaviour of these tissues [7]. Current permittivity databases often overlook these complexities, as most measurements are derived from homogeneous tissue samples or assume isotropic behaviour [4][5]. Consequently, there is a pressing need for high-resolution, frequency-dependent permittivity data that accounts for the layered and anisotropic properties of complex biological tissues. However, addressing this need falls outside the scope of this thesis.

In addition to database limitations, the practical measurement of biological tissue permittivity presents significant experimental challenges. Accurate real-time acquisition of dielectric properties is influenced by factors such as probe-tissue contact consistency, measurement frequency range, temperature variations, and the inherent dynamic nature of biological tissues [8]. Techniques such as open-ended coaxial probes, transmission line methods, and resonant cavity techniques are commonly employed to measure tissue permittivity. However, each method has limitations regarding spatial resolution, penetration depth, and sensitivity to environmental variations. The intricacies of in vivo measurements further compound these challenges, as physiological conditions such as blood flow, metabolic activity, and external influences (e.g., ambient humidity) introduce variability in permittivity readings.

This chapter aims to critically evaluate the most prominent databases available for biological tissue permittivity, identifying their strengths and limitations in the context of complex, multilayered tissues. Furthermore, it will explore the methodological aspects of measuring the

dielectric properties of biological tissues, addressing the inherent challenges associated with real-time acquisition. The theoretical permittivity values obtained from this chapter will serve as a benchmark for developing a robust classification framework for hydration readings in chapter 4 and 5 respectively.

### 3.1. Common Sources for Permittivity of Biological Tissues

The most prevalent reference of the permittivity values of biological tissues is a three-part research study studied by Gabriel and her team who performed frequency dependent measurements from 10 Hz to 20 GHz [9]. This study demonstrates that the four pole Cole-Cole model of the real and imaginary part which best matches the measurement results for a particular tissue. The four-pole model was chosen simply because each pole corresponds to one of the four dispersion mechanisms (biological relaxation regions in biological tissues) in subchapter 2.2.3. The final equation for the complex permittivity of each tissue is given by [10]:

$$\varepsilon_r = \varepsilon_\infty + \sum_{n=1}^{4} \frac{\varepsilon_{sn} - \varepsilon_\infty}{1 + (j\omega\tau_n)^{1-\alpha_n}} + \frac{\sigma_s}{j\omega\varepsilon_o} \tag{3.1}$$

Where the parameters are:

$\varepsilon_\infty$: High-frequency (optical) permittivity — the value of permittivity as $\omega \to \infty$.

$\varepsilon_{sn}$: Static permittivity for the $n^{th}$ relaxation process.

$\tau_n$: Relaxation time for the $n^{th}$ process — indicates how fast polarization responds.

$\alpha_n$: Distribution parameter ($0 \leq \alpha_n \leq 1$) — describes broadening of relaxation.

$j$: Imaginary unit, where $j = \sqrt{(-1)}$.

$\omega$: Angular frequency ($\omega = 2\pi f$), with $f$ being the frequency.

$\sigma_s$: Static (DC) conductivity — accounts for conduction loss at low frequencies.

$\varepsilon_o$: Vacuum permittivity (approximately $8.854 \times 10^{-12}$ F/m).

Although the four pole Cole-Cole model is very effective in representing frequency-dependent permittivity of biological tissues, it has several limitations. One of major concerns is that the model is purely empirical which implies that it is derived from experimental data and not first-principle approach. As a result, it does not entirely account for the underlying biophysical interactions at a molecular level. This can result in inaccuracies when applying the model outside the measured frequency range or to tissues with highly heterogeneous structures.

Another critical limitation is its lack of direct correlation with temperature variations. Biological tissues exhibit significant dielectric property changes with temperature fluctuations due to factors such as increased ionic mobility, changes in tissue hydration and alterations in molecular relaxation dynamics [11]. However, the standard four pole Cole-Cole model does not factor in temperature as a parameter, implying that it cannot dynamically adjust permittivity values based on thermal conditions. This can introduce inaccuracies in the potential applications of non-invasive hydration monitoring in biological tissues.

To compensate for the limitations of the four-pole Cole-Cole model, several databases have been established to provide comprehensive permittivity measurements for various biological tissues across the frequency range of interest. Among these, the IT'IS Foundation (Foundation for Research on Information Technologies in Society) has developed one of the most extensive dielectric property databases [3]. This resource builds upon the well-known Gabriel dataset, expanding the number of biological tissues included and refining the measurement techniques used to capture their dielectric properties. The IT'IS database also incorporates predictive models, allowing researchers to estimate tissue properties across a broader frequency spectrum. Unlike the Gabriel dataset, which remains static and is based on a fixed set of measurements, the IT'IS database is continuously updated with new experimental findings and computational advancements, ensuring that it reflects the most current understanding of tissue permittivity.

One potential application of these dielectric property datasets is the investigation of complex, multilayered biological tissues, such as those found around the human wrist region. The wrist is composed of multiple layers of varying tissue types, including skin, fat, muscle, tendons, and blood vessels, each exhibiting distinct dielectric properties. Due to this structural complexity, accurate permittivity readings in this region can serve as an indicator to distinguish between hydrated and dehydrated biological tissue.

This research aims to perform dielectric measurements within the 2.45 GHz ISM (Industrial, Scientific, and Medical) band, widely utilized in wireless communication and biomedical sensing. At this frequency, the dipole effect of water molecules leads to a significant dielectric contrast between hydrated and dehydrated tissues, enhancing sensitivity in tissue characterization.

### 3.2. Dielectric Properties of Multilayered Tissue Around the Human Wrist

Biological tissues in the wrist including skin, fat (adipose), muscle, tendon, and bone have frequency-dependent dielectric properties characterized by their relative permittivity ($\varepsilon_r$),

electrical conductivity ($\sigma$), and loss tangent ($tan\delta$) [12]-[14]. The relative permittivity $\varepsilon_r$ describes a tissue's ability to store electric energy (polarization), while conductivity ($\sigma$) represents the ability to conduct electric current (loss through ionic movement). The loss tangent ($tan\delta$) is the ratio of the dissipative loss to the energy stored, indicating how lossy the tissue is. These properties vary strongly with frequency due to different polarization mechanisms in the tissues. In general, low frequencies (kHz range and below) induce interfacial and ionic polarization (α-dispersion) yielding very high permittivity and low effective conductivity, mid-range frequencies (kHz–MHz, $\beta$-dispersion) see a drop in permittivity as cell membranes and proteins relax, and high frequencies (tens of MHz to GHz, γ-dispersion) engage water dipole orientation  permittivity tends to decrease while conductivity rises [15][16]. For example, above ~50 MHz (entering the γ-dispersion), the real part of muscle permittivity measurably decreases with increasing frequency as bound water relaxes, whereas at very low frequencies permittivity can be extremely high (due to Maxwell–Wagner polarization) (detailed explanation in subchapter 2.2.3) [17][18].

### 3.2.1 Anatomical Composition of the Wrist Region

The wrist comprises several distinct tissue layers each with unique dielectric properties that influences their interaction with electromagnetic fields.

***Skin (Epidermis and Dermis):*** Skin is a layered tissue with an outer stratum corneum (dry, low-water content) and deeper dermis (high-water content) [19]. Its dielectric properties reflect this composite structure. At radio- and microwave frequencies the bulk skin permittivity is relatively high, as shown in Figure 3.1, because of the hydrated layers beneath the surface. For example, human dry skin has $\varepsilon_r$ on the order of 30–40 at microwave frequencies; at 2.4 GHz a measured value is $\varepsilon_r$ = 38 with conductivity $\sigma \approx 1.46\ (\mathrm{S}/m)$ . At a lower frequency of 300 MHz, skin's permittivity is higher (around 50) with $\sigma \approx 0.64\ (\mathrm{S}/m)$. The loss tangent of skin in this range is moderately high (e.g. ~0.77 at 300 MHz), indicating significant dielectric loss due to ionic conductivity. The dry stratum corneum has a much lower permittivity and adds extra dispersion at low frequencies (below MHz), so "wet" skin (hydrated) exhibits slightly higher effective permittivity and conductivity than dry skin.

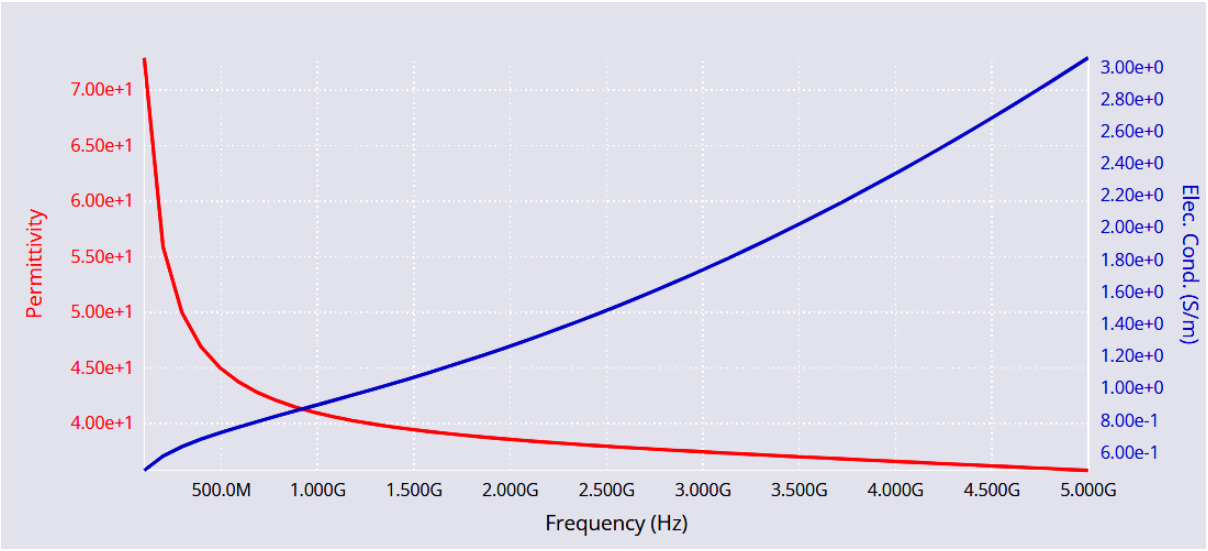


*Figure 3.1: Dielectric properties for skin from 100MHz to 5GHz adapted from the IT'IS database [3].*

***Adipose (Fat) Tissue***: Fat (subcutaneous adipose tissue) has a very low water content, so it exhibits much lower permittivity and conductivity than other tissues. Its dielectric properties are relatively stable across frequency (with weaker dispersion) because there is little polar water to contribute [20]. At 2.4 GHz, human fat has $\varepsilon_r \approx 5.3$ and $\sigma \approx 0.11$ $(S/m)$ [3]. Even at a lower frequency like 300 MHz, the permittivity is only on the order of 5–6 (e.g. $\varepsilon_r \approx 5.3$, $\sigma \approx 0.11$ $(S/m)$ at 300 MHz). The low permittivity and conductivity of fat yield a small loss tangent (tan δ ~0.15–0.4 in the MHz–GHz range), as shown in Figure 3.2, meaning fat is a good dielectric with minimal energy absorption relative to stored energy. Because of its low polarizability, fat shows much smaller variation with frequency, there is a minor increase in $\varepsilon_r$ at very low frequencies due to residual bound charges, but overall fat remains the lowest-permittivity tissue in the wrist [20]. Its low dielectric constant and loss make fat a contrast agent of sorts: interfaces between fat and high-water tissues (muscle or skin) cause strong impedance contrasts to electromagnetic waves.

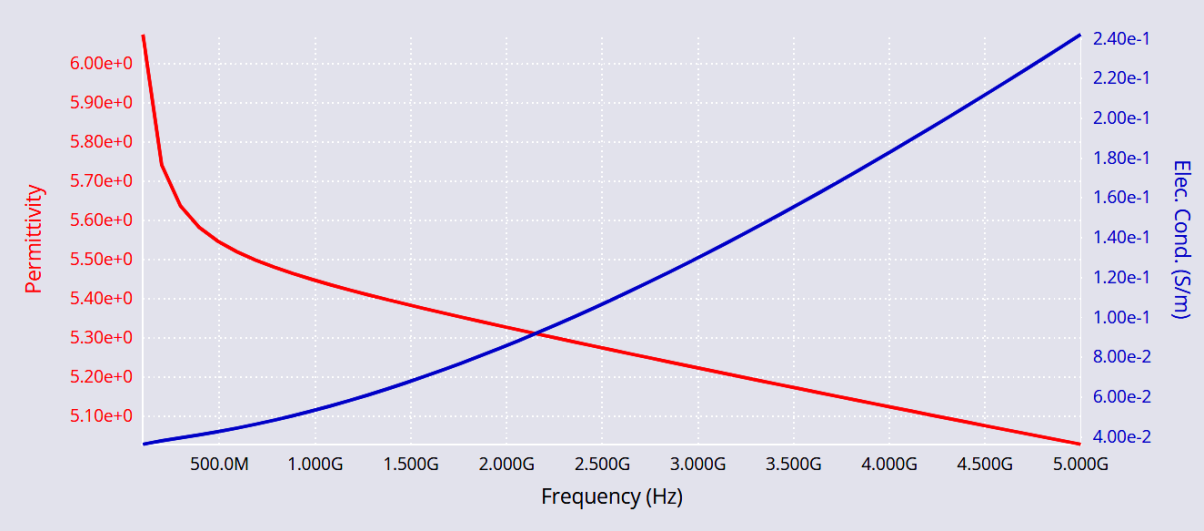


*Figure 3.2: Dielectric tissue frequency chart of fat tissue from 100 MHz to 5 GHz adapted from the IT'IS database [3].*

***Muscle:*** Muscle is a high-water, high-electrolyte tissue and thus has one of the highest permittivity and conductivities among wrist tissues [3]. In the low-frequency limit, muscle's effective permittivity can reach into the thousands (due to charges accumulating at cell membranes), but as frequency increases into the MHz range, the permittivity drops dramatically (*β-dispersion*) and stabilizes in the tens at RF/microwave frequencies. For example, at 300 MHz muscle has a $\varepsilon_r \approx 58$ and , $\sigma \approx 0.77$ $(\mathrm{S}/m)$. By 2.4 GHz falls to $\varepsilon_r \approx 52 - 53$ while $\sigma$ rises to ≈1.7S/m, reflecting the approach to the water dipole relaxation region. Muscle's loss tangent is relatively high in the lower RF range (≈ 0.79 at 300 MHz indicating nearly as much energy lost as stored) but tends to decrease at microwave frequencies (e.g. tan δ on the order of 0.25 at a few GHz), since $\varepsilon_r$ drops and the phase lag due to dipolar loss is somewhat lower, as shown in Figure 3.3. The high ionic content in muscle means conductivity increases with frequency (up to the point of the water relaxation): experimentally, beyond ~50–100 MHz muscle permittivity decreases while conductivity increases due to ionic and dipolar losses [21].

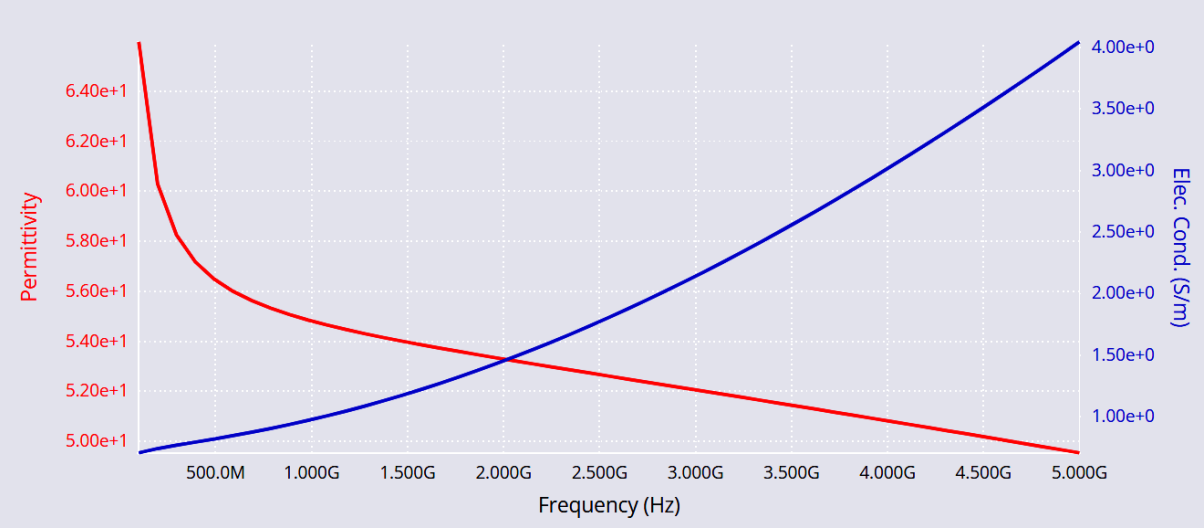


*Figure 3.3: Tissue frequency chart for muscle from 100 MHz to 5 GHz adapted from IT'IS database [3].*

***Tendon:*** Tendons in the wrist (e.g. connecting forearm muscles to the hand) are composed primarily of collagen fibres with moderate water content. Consequently, tendon's dielectric properties are intermediate between those of water-rich muscle and water-poor fat or bone [22]. Tendons do exhibit frequency-dependent behaviour (they have bound water that contributes to dispersions), but due to their lower water fraction, their permittivity is markedly lower than muscles at a given frequency. Literature data and models indicate that at radio frequencies, tendon's relative permittivity is on the order of a few tens [9][13]. For instance, around the 100 kHz–1 MHz range, tendon permittivity may still be high (several hundred) due to interfacial polarization, but by ~100 MHz and above, it likely falls into the few tens. While specific measurements in tendon are less common, one parametric model gives an estimated high-frequency permittivity ~4 and multiple dispersion contributions totalling $\Delta\varepsilon{\sim}100+$ across lower frequencies implying, for example, a mid-range $\varepsilon_r \approx 20-40$ at MHz frequencies [3]. Conductivity of tendon is relatively low (e.g. modelled static $\sigma \approx 0.03\,(\mathrm{S}/m)$, rising with frequency), so its loss tangent is moderate, as shown in Figure 3.4. In practical terms, tendon tissue in the wrist can be seen as a dielectric with moderate permittivity and low loss, acting more insulating than muscle but not as much as fat. It helps form a transition layer for electromagnetic waves between muscle and bone.

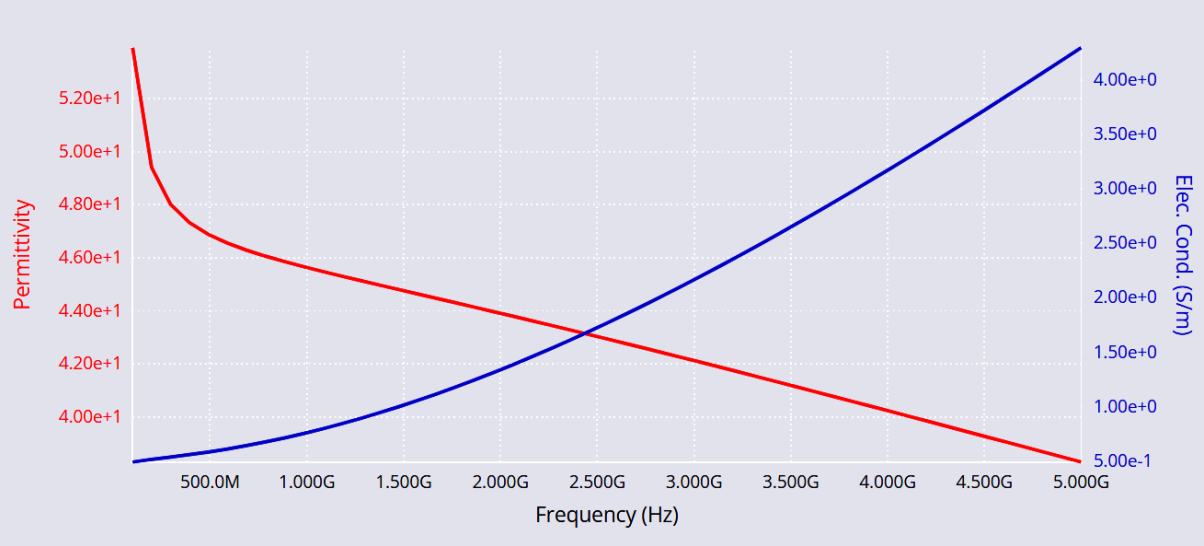


*Figure 3.4: Tissue frequency chart for tendon/ligament from 100 MHz to 5 GHz adapted from IT'IS database [3].*

***Bone:*** Bone (in the context of the wrist, primarily cortical bone of the forearm and carpal bones) has very low water content (on the order of 15–25% for cortical bone) [21]. As a result, bone's dielectric constant is quite low, and it behaves more like a dielectric solid with higher resistivity. As shown in Figure 3.5, at 2.4 GHz, human cortical bone is reported with $\varepsilon_r \approx 11.3$ and $\sigma \approx 0.40$ $(S/m)$. At 300 MHz, bone's permittivity is only slightly higher (~13.4) while conductivity is much lower (~0.08 S/m). This indicates that bone's conductivity increases strongly with frequency in the RF range (as capacitive coupling through its small water fraction improves) [23]. The loss tangent of cortical bone is relatively low (tan δ ≈0.37 at 300 MHz, dropping to roughly 0.26 at microwave frequencies based on the above values), meaning bone is comparatively low loss. Cancellous (spongy) bone, found in the ends of long bones and vertebrae, contains more marrow and fluid; it therefore has a slightly higher permittivity than cortical bone. For example, cancellous bone permittivity can be a few units higher than cortical across frequencies. Overall, bone in the wrist presents a small dielectric constant and low conductivity, making it the most electrically insulative of the major tissues [24]. Its dielectric properties vary less with frequency (largely lacking the strong dispersions of high-water tissues), though at very high frequencies (>1 GHz) the remaining bound water's dipolar relaxation will still cause some decrease in $\varepsilon_r$.

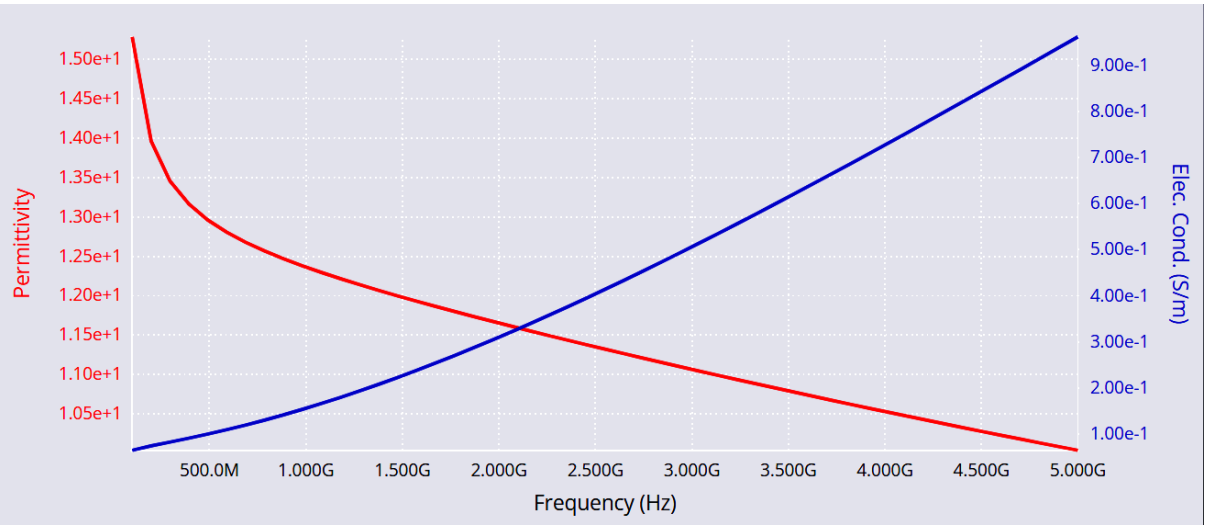


*Figure 3.5: Tissue frequency chart for bone from 100 MHz to 5 GHz for cortical bone tissue [3].*

### 3.2.2 Frequency-Dependent Trends Summary

Across all these tissues, a common trend is that higher water and electrolyte content yields higher permittivity and conductivity at a given frequency [25][3] [. Muscle and skin (rich in water) have the highest $\varepsilon_r$ and $\sigma$, while fat and cortical bone (water-poor) have the lowest. As frequency increases from kHz to GHz, relative permittivity $\varepsilon_r$ tends to decrease (especially for high-water tissues) because various polarization mechanisms "freeze out" or saturate at their characteristic relaxation frequencies. Conversely, conductivity tends to increase with frequency in biological tissues (up to the point of ionic dispersion), since higher-frequency fields can overcome capacitive barriers and cause more charge carriers to oscillate [26]. These frequency dispersions in tissues are well characterized by multi-pole Cole–Cole models (Chapter 2). For example, the classic Gabriel studies identified three main dispersion regions: *α-dispersion* below ~10 kHz (ionic diffusion, cell membrane charging), *β-dispersion* from ~10 kHz to ~100 MHz (cellular Maxwell–Wagner polarization, large drop in $\varepsilon_r$, and *γ-dispersion* from ~100 MHz up to ~100 GHz (dipolar relaxation of water) [9]. In the context of the wrist, this means a tissue like muscle might have $\varepsilon_r$ in the thousands at 1 kHz, dropping to ~100 by a few MHz, ~60 at 100 MHz, and ~50 at 1 GHz. Low-water tissues (fat, bone) show much smaller changes e.g. fat stays near $\varepsilon_r \approx 5$ across the MHz–GHz range. The loss tangent generally peaks in the mid-frequency ranges where permittivity is still moderately high while significant conduction has begun, for many tissues this frequency range is in the tens to hundreds of MHz. At higher microwave frequencies, $\tan\delta$ can become lower in some tissues as $\varepsilon_r$ diminishes, though

ultimately at extremely high frequencies (tens of GHz) water losses cause another increase in loss.

### 3.3 Modelling Wrist Tissue to Approximate Combined Permittivity

This section presents an analytical approach to approximating the effective permittivity of wrist tissues around the 2.45 GHz frequency band. Using the data from IT'IS database on dielectric properties of biological tissues, an equivalent permittivity model is determined in [3] through effective medium approximations.

Figure 3.6 shows the multiple tissue layers, each contributing to the overall permittivity $\varepsilon_r$. The dielectric properties of these tissues at our frequency of interest 2.45 GHz obtained from the IT'IS database are summarised in Table 3.1. It should be noted that these values show significant variation among the different tissues, requiring a good homogenization technique to estimate the combined permittivity.

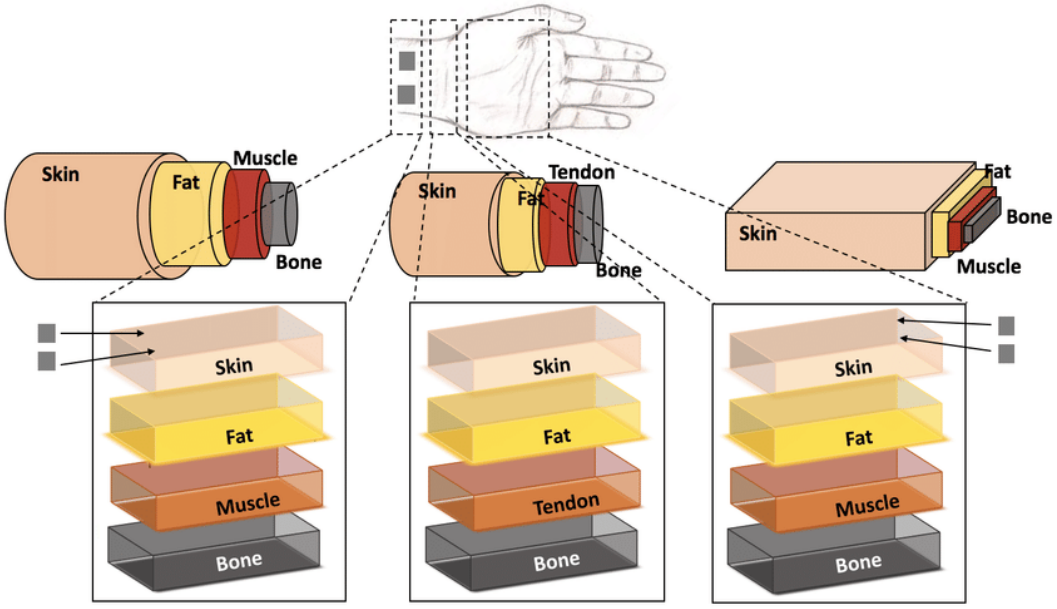


*Figure 3.6:Cross sectional approximation of human hand wrist for non-invasive hydration monitoring referenced from [27].*

Human wrist tissue is a heterogeneous mixture of skin, muscle, fat, bone, blood, and other constituents, each with different dielectric properties. These differences stem largely from varying water content; for example, low-water-content tissues like fat and cortical bone have much lower permittivity than high-water-content tissues such as muscle or blood [28]. It is useful to approximate the wrist region as a homogeneous medium with an effective permittivity that represents the bulk response of the composite tissue. This requires a theoretical model to "mix"

the permittivity of the components. One widely used approach is the Bruggeman effective medium model, a classical mixing rule from electromagnetic Effective Medium Theory (EMT) [29]. The model predicts macroscopic properties (like dielectric constant or conductivity) of composites from their constituents. It is often called a symmetric mixing rule because, unlike some other models, it does not distinguish a specific host medium – all phases are treated equally, weighted only by their volume fraction **[**30**]**. In practical terms, this means the environment and inclusions are not assigned different roles; each component of the mixture contributes on an equal footing in the self-consistent determination of the effective permittivity. This symmetry is advantageous for biological tissues, which are complex mixtures without a clear "background" medium [31].

Table 3.2: Dielectric properties of wrist tissues at 2.45 GHz

| Tissue | Relative Permittivity ($\boldsymbol{\varepsilon_r}$) | Conductivity ($\boldsymbol{\sigma}$, S/m) | Density $\left(\boldsymbol{kg^3/m}\right)$ | Approx. Thickness (mm) | Volume fraction (%) |
|---|---|---|---|---|---|
| **Skin** | 38.0 | 1.46 | 1109 | 1.5-2.5 | 10 |
| **Fat** | 5.3 | 0.11 | 911 | 2-4 | 15 |
| **Muscle** | 52.7 | 1.73 | 1040 | 10-15 | 40 |
| **Bone (Cortical)** | 12.5 | 0.28 | 1810 | 3-5 | 25 |
| **Blood** | 61.0 | 1.85 | 1060 | <1 | 10 |

Given that wrist tissues are not purely dispersed, the Bruggeman model is more appropriate [32]:

$$f_i \frac{\varepsilon_1 - \varepsilon_{eff}}{\varepsilon_1 + 2\varepsilon_{eff}} + f_{i+1} \frac{\varepsilon_2 - \varepsilon_{eff}}{\varepsilon_2 + 2\varepsilon_{eff}} + f_n \frac{\varepsilon_n - \varepsilon_{eff}}{\varepsilon_n + 2\varepsilon_{eff}} = 0 \qquad (3.2)$$

Where: $\varepsilon_{eff}$ is the effective permittivity, $\varepsilon_i$ is permittivity of the tissue layer *i* and $f_i$ is the volume fraction of tissue $i^{\text{th}}$ layer

The effective permittivity $\left(\varepsilon_{eff}\right)$of the wrist's typical cross-section was determined using the Bruggeman Equation (3.2), a widely used model for heterogeneous dielectric mixtures [32][33]. The wrist was considered as a composite material with five primary components, as shown in see Table 1 constituted from: skin (10%), fat (15%), muscle (40%), bone (25%), and blood (10%) [34]. Each component has a known permittivity ≈38 for skin, ≈ 5.3 for fat, ≈52.7 for muscle, ≈12.5 for bone, and ≈61 for blood [3]. By applying these volume fractions and permittivity values into the Bruggeman Equation (3.2), we solved the nonlinear equation numerically using the fsolve function. The computation yielded an effective permittivity of approximately 29.72,

representing the overall dielectric behaviour of the wrist's cross-section based on its composition. This result is particularly significant, as it establishes a benchmark for assessing hydration status in controlled studies discussed in the next chapter. By providing a reliable reference point, this value will aid in distinguishing variations in tissue hydration, enhancing the accuracy of classification models and improving the interpretation of EM-based measurements in future analysis.

**References**


1. A. Matković et al., "Complex permittivity of ex-vivo human, bovine and porcine brain tissues in the microwave frequency range," Diagnostics, vol. 12, no. 11, p. 2580, Oct. 2022, doi: 10.3390/diagnostics12112580.
2. M. Ibrani, L. Ahma, and E. Hamiti, "The age-dependence of microwave dielectric parameters of biological tissues," Microwave Materials Characterization, InTech, Nov. 2012, doi: 10.5772/51400.
3. IT'IS Foundation, "Dielectric properties," [Online]. Available: https://itis.swiss/virtual-population/tissue-properties/database/dielectric-properties.
4. Schmid & Partner Engineering AG, "Dielectric Material Database," [Online]. Available: https://speag.swiss/news-events/news/measurement/dielectric-material-database/.
5. CNR-IFAC, "Dielectric properties of body tissues: Home Page," [Online]. Available: http://niremf.ifac.cnr.it/tissprop/.
6. S. I. Alekseev and M. C. Ziskin, "Human skin permittivity determined by millimeter wave reflection measurements," Bioelectromagnetics, vol. 28, no. 5, pp. 331–339, 2007, doi: 10.1002/bem.20308.
7. M. Granke et al., "The role of water compartments in the material properties of cortical bone," Calcif. Tissue Int., vol. 97, no. 3, pp. 292–307, 2015, doi: 10.1007/s00223-015-9977-5.
8. X. Wang et al., "High-resolution probe design for measuring the dielectric properties of human tissues," BioMed Eng OnLine, vol. 20, p. 86, 2021, doi: 10.1186/s12938-021-00924-1.
9. C. Gabriel et al., "The dielectric properties of biological tissues: I. Literature survey," Phys. Med. Biol., vol. 41, no. 11, pp. 2231–2249, 1996, doi: 10.1088/0031-9155/41/11/001.
10. L. Zhang, Y. Pang, L. Ding, and G. Li, "The Cole-Cole model of porcine activity tissues in radio frequency," in Proc. Int. Congr. Image Signal Process., BioMed. Eng. Inform., Shanghai, China, 2017, pp. 1–5, doi: 10.1109/CISP-BMEI.2017.8302246.
11. K. R. Foster and H. P. Schwan, "Dielectric properties of tissues," in CRC Handbook of Biological Effects of Electromagnetic Fields, 3rd ed., CRC Press, 2019, pp. 27–96.
12. D. B. Rodrigues et al., "Dielectric properties measurements of brown and white adipose tissue in rats from 0.5 to 10 GHz," Biomed. Phys. Eng. Express, vol. 2, no. 2, 025005, 2016, doi: 10.1088/2057-1976/2/2/025005.
13. S. Gabriel et al., "The dielectric properties of biological tissues: I. Literature survey," [Online]. Available: https://www.researchgate.net/publication/14269211_The_dielectric_properties_of_biological_tissues_I_Literature_survey.

14. O. Kangasmaa et al., "Estimating human fat and muscle conductivity from 100 Hz to 1 MHz using measurements and modelling," Bioelectromagnetics, vol. 46, no. 1, p. e22541, 2025, doi: 10.1002/bem.22541.
15. E. Porter, A. L. Gioia, A. Santorelli, and M. O'Halloran, "Modeling of the dielectric properties of biological tissues within the histology region," IEEE Trans. Dielectr. Electr. Insul., vol. 24, no. 5, pp. 3290–3301, Oct. 2017, doi: 10.1109/TDEI.2017.006690.
16. J. Zimmermann and U. van Rienen, "Ambiguity in the interpretation of the low-frequency dielectric properties of biological tissues," Bioelectrochemistry, vol. 140, p. 107773, 2021, doi: 10.1016/j.bioelechem.2021.107773.
17. D. El Khaled et al., "Dielectric spectroscopy in biomaterials: Agrophysics," Materials, vol. 9, no. 5, p. 310, 2016, doi: 10.3390/ma9050310.
18. F. D. Tehrani et al., "Tutorial on impedance and dielectric spectroscopy for single-cell characterisation on microfluidic platforms: theory, practice, and recent advances," Lab Chip, vol. 25, no. 5, pp. 837–855, Feb. 2025, doi: 10.1039/d4lc00882k.
19. W. Lopez-Ojeda et al., "Anatomy, Skin (Integument)," StatPearls, [Online]. Available: https://www.ncbi.nlm.nih.gov/books/NBK441980/.
20. B. Mittal, "Subcutaneous adipose tissue & visceral adipose tissue," Indian J. Med. Res., vol. 149, no. 5, pp. 571–573, 2019, doi: 10.4103/ijmr.IJMR_1910_18.
21. D. Werber, A. Schwentner, and E. Biebl, "Investigation of RF transmission properties of human tissues," Adv. Radio Sci., vol. 4, pp. 357–360, 2006, doi: 10.5194/ars-4-357-2006.
22. I. Tresoldi et al., "Tendon's ultrastructure," Muscles Ligaments Tendons J., vol. 3, no. 1, pp. 2–6, May 2013, doi: 10.11138/mltj/2013.3.1.002.
23. M. Cervantes et al., "Low-frequency electrical conductivity of trabecular bone: insights from in silico modeling," Mathematics, vol. 11, no. 4038, 2023, doi: 10.3390/math11194038.
24. J. D. Currey, "The structure and mechanics of bone," J. Mater. Sci., vol. 47, pp. 41–54, 2012.
25. R. Pethig, "Dielectric properties of body tissues," Clin. Phys. Physiol. Meas., vol. 8, no. 4A, pp. 5, 1987.
26. W. Kuang and S. O. Nelson, "Low-frequency dielectric properties of biological tissues: a review with some new insights," 1998.
27. W. J. Tomlinson et al., "Secure on-skin biometric signal transmission using galvanic coupling," Proc. IEEE INFOCOM, Paris, France, 2019, pp. 1135–1143, doi: 10.1109/INFOCOM.2019.8737540.
28. N. AlSawaftah et al., "Microwave Imaging for Early Breast Cancer Detection: Current State, Challenges, and Future Directions," J. Imaging, vol. 8, no. 5, p. 123, Apr. 2022, doi: 10.3390/jimaging8050123.
29. J. Sancho-Parramon et al., "Effective medium models for metal-dielectric composites: an analysis based on the spectral density theory," Proc. SPIE, vol. 5963, 596320, Oct. 2005, doi: 10.1117/12.625125.
30. M. J. Cervantes et al., "Low-frequency electrical conductivity of trabecular bone: insights from in silico modeling," Mathematics, vol. 11, p. 4038, 2023, doi: 10.3390/math11194038.
31. J. Wang et al., "THz sensing of human skin: A review of skin modeling approaches," Sensors, vol. 21, p. 3624, 2021, doi: 10.3390/s21113624.
32. S. M. Puranik, A. C. Kumbharkhane, and S. C. Mehrotra, "The static permittivity of binary mixtures using an improved Bruggeman model," J. Mol. Liq., vol. 59, no. 2-3, pp. 173–177, 1994.

33. X. Ji and S. Zhou, "Variational approach to concentration dependent dielectrics with the Bruggeman model: Theory and numerics," Commun. Math. Sci., vol. 17, no. 7, pp. 1949–1974, 2019.
34. T. Gerhalter et al., "Acute changes in extracellular volume fraction in skeletal muscle monitored by 23Na NMR spectroscopy," Physiol. Rep., vol. 5, no. 16, e13380, 2017, doi: 10.14814/phy2.13380.

## 4. Preliminary Studies on Permittivity Measurements Using Open Ended Coaxial Probe

This chapter investigates how measurements of biological tissue permittivity ($\varepsilon$) relate to hydration levels using the open-ended coaxial probe (OECP) method. This method operates by analysing the reflection coefficient at the probe-sample interface, enabling the assessment of tissue hydration without invasive procedures.

The study began with an initial investigation into the permittivity of artificial sweat to establish a benchmark for hydration assessment. By systematically measuring the permittivity response of artificial sweat samples at 2.45 GHz, the study provided a controlled reference to understand how varying hydration levels influence dielectric properties. The results from this phase were crucial in differentiating between intrinsic tissue hydration changes and surface hydration effects, forming the basis for the subsequent human tissue measurements.

Building on these findings, an extensive experimental study was conducted on over 200 participants under controlled conditions to examine the relationship between hydration levels and the dielectric properties of human skin. The primary focus remained on the 2.45 GHz Industrial, Scientific, and Medical (ISM) band due to its strong interaction with water molecules and its widespread use in biomedical and communication applications. Permittivity measurements were performed using a calibrated OECP setup to ensure accurate extraction of dielectric properties, with experiments designed to systematically vary skin hydration levels through controlled exposure to different environmental conditions and hydration states.

Hydration-dependent permittivity changes were analysed by exposing participants to dry and humid environments, applying hydrating agents, and measuring before and after physical activity. Results demonstrated a strong correlation between increased skin hydration and lower permittivity values at 2.45 GHz, highlighting the sensitivity of this frequency band to water content in biological tissues. To ensure accuracy, the experimental setup incorporated rigorous calibration protocols using standard reference liquids and tissue phantoms. Open, short, and matched load impedance standards were employed to eliminate systematic measurement errors, while consistent probe-to-skin contact pressure was maintained to minimize mechanical inconsistencies.

The findings of this study confirm that the 2.45 GHz ISM band is highly effective for hydration monitoring due to its strong interaction with water molecules. Additionally, the artificial sweat study provided a valuable reference for quantifying hydration levels based on permittivity

changes, contributing to the development of a benchmark for future hydration assessment techniques.

## 4.1. Microwave Measurements

In a coaxial probe at gigahertz frequencies, both the voltage and the current wave comprise of two components, the incident propagating wave towards the load (open end) and the reflected wave propagating towards the generator. The reflected wave arises when the incident wave is reflected from the open end of the coaxial probe. The voltage reflection coefficient Γ at the point of open end is defined as the ratio of the reflected voltage phasor V and the incident voltage phasor $V_+$:

$$\Gamma = \frac{V_-(z)}{V_+(z)} = \frac{Z - Z_0}{Z + Z_0} \tag{4.1}$$

Since Γ is a complex quantity, it provides both magnitude and phase information about the reflection occurring at the probe interface. The reflection coefficient is linked to the impedance at the measurement point through Equation (4.1), where $Z$ is the unknown impedance (Ω) at the probe surface and $Z_0$ is the characteristic impedance of the coaxial transmission line, typically 50 Ω. For an open-ended coaxial probe, the impedance at the tip approaches infinity, leading to nearly total reflection ($\Gamma \approx 1$). However, when the probe is in contact with a material, Γ depends on the material's permittivity and permeability.

### 4.1.1. Input Impedance and Reflection Coefficient at the VNA port

In analysing the reflection properties, as shown in Figure 4.1, the origin of the axis is at the open end of the probe, and the positive direction of the axis extends from the open end towards the generator, i.e., the Vector Network Analyzer (VNA). The relationship between the input impedance $Z_i$ and the input reflection coefficient $\Gamma_i$ at the VNA port is given by Equation (4.2):

$$Z_i = Z_0 \frac{1 + \Gamma_i}{1 - \Gamma_i} \quad \text{or} \quad \Gamma_i = \frac{Z_0 - Z_i}{Z_0 + Z_i} \tag{4.2}$$

Whereas the input admittance and reflection coefficient at the same point on the transmission line are related with the following equation:

$$Y_i = Y_0 \frac{1 - \Gamma_i}{1 + \Gamma_i} \quad \text{or} \quad \Gamma_i = \frac{Y_0 - Y_i}{Y_0 + Y_i} \tag{4.3}$$

$Z_o$ and $Y_o$ denote the characteristic impedance and the admittance, respectively, of the transmission line and the VNA. By combining Equations (4.1, 4.2 & 4.3) we can deduce the

complex permittivity from the measured reflection coefficient. The coaxial probe cannot be considered an ideal transmission line as there is additional unaccounted reflections and losses that arise from probe imperfections, discontinuities, and interactions with the surrounding environment. These factors introduce measurement uncertainties that must be accounted for through calibration techniques, correction models, or empirical adjustments to ensure accurate permittivity extraction.

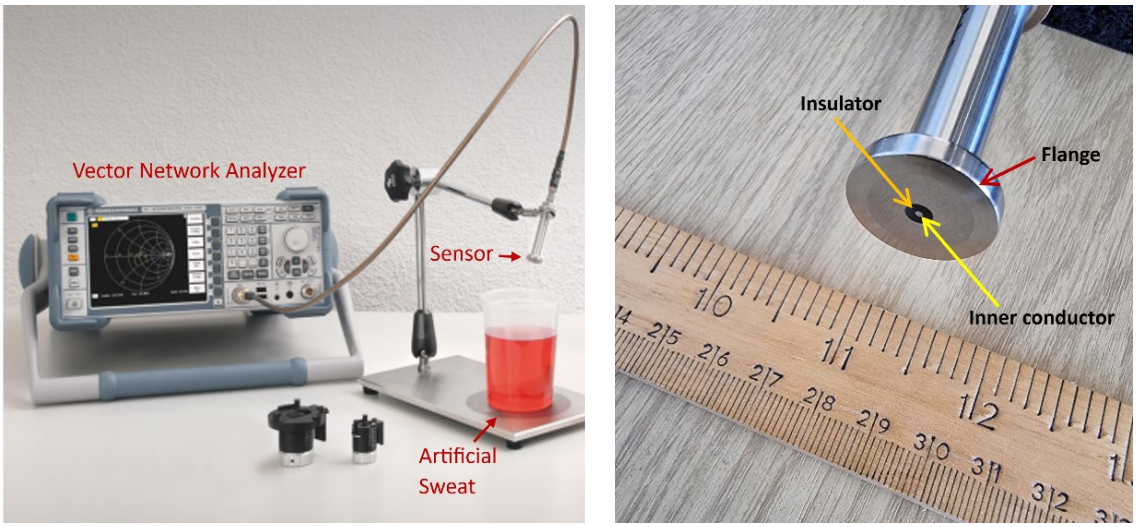


(a) (b)

*Figure 4.1: (a) Experimental setup showing OECP method inserted in a solution of artificial sweat to measure its permittivity, (b) close view of the 3.5 mm DAK probe sensor.*

## 4.2. Experimental Setup and Calibration Procedures

### 4.2.1. Instrumentation

All measurements were performed using a SPEAG Dielectric Assessment Kit (DAK) 3.5 mm coaxial probe connected to a Vector Network Analyzer (VNA), as shown in Figure 4.1. The DAK 3.5 mm probe is a high-precision, open-ended coaxial sensor designed to operate across a frequency range of 400 MHz to 11 GHz, including the relevant ISM band at 2.4–2.5 GHz. The probe was connected to the VNA via a coaxial cable, with the VNA sourcing a swept-frequency signal and recording the reflection coefficient $S_{11}$ at the probe tip. To ensure accurate measurements, the VNA was calibrated in advance using standard open, short, and load references in accordance with the manufacturer's guidelines. This calibration ensured that the measured $S_{11}$ accurately reflected the probe tip impedance without systematic errors. Prior to each measurement set, the system's calibration was verified by measuring known references such

as open-circuit air and standard liquids like deionized water or saline solutions with known permittivity.

A custom artificial sweat solution was prepared (see Section 4.4 for details) and poured into a small glass beaker, with approximately 50 ml of sample per measurement. The coaxial probe was carefully immersed in the liquid, ensuring that the aperture was fully submerged without touching the container walls. Measurements were conducted at room temperature, which was monitored throughout, as permittivity is sensitive to temperature variations.

After each frequency sweep, the probe was rinsed with deionized water and gently dried, while the beaker was also cleaned to prevent cross-contamination between samples. The Vector Network Analyzer (VNA) was configured to sweep from 0.4 GHz to 11 GHz, collecting complex $S_{11}$ values at 212 frequency points. For each artificial sweat sample, three sweeps were performed and averaged to enhance measurement reliability.

As shown in Figure 12, the measurement setup included the VNA, coaxial probe, and a beaker containing the artificial sweat sample. Before recording, the probe was allowed to stabilize, and care was taken to eliminate bubbles or air gaps at the probe tip, which could affect readings. The DAK software was used to convert the measured $S_{11}$ into the real ($\varepsilon'$) and imaginary ($\varepsilon''$) components of permittivity across the frequency range. Conductivity was also derived from $\varepsilon''$, as described in Chapter 2. The resulting permittivity spectra were saved for subsequent analysis and modelling.

### 4.2.2. Calibration

Accurate calibration was essential throughout both the artificial sweat and human skin measurements. The coaxial probe was initially calibrated using standard references—air, short, and a deionized water solution as known loads to correct for systematic errors.

Biological tissue measurements presented additional challenges. For instance, the slightly rough surface of the skin and the potential for small air gaps could introduce measurement inaccuracies. To mitigate these issues, gentle pressure was applied to ensure full contact between the probe and the skin. In some preliminary trials, a drop of saline was used as a coupling medium; however, final measurements were conducted under dry-contact conditions to better reflect real-world, wearable use cases.

Measurement repeatability was verified by taking multiple readings at the same skin site. If the variance exceeded 5%, the system calibration was re-checked and the measurement repeated. For liquid measurements using artificial sweat, the equipment's noise floor and dynamic range-imposed limitations, especially at the extremes of the frequency band. Consequently, the most reliable data were obtained in the mid-frequency range (~0.5–6 GHz), and results are primarily emphasized within this range.

For single-frequency measurements on the wrist, calibration drift over time was monitored by periodically re-measuring a reference phantom. Any inconsistencies such as slight shifts in baseline reflection due to cable flexing were corrected by re-calibrating the probe. These measures ensured high accuracy and consistency across all permittivity measurements, providing a robust foundation for analysing hydration effects.

## 4.3. Artificial Sweat Study and its Role in Hydration Assessment

### 4.3.1. Introduction

Sweat evaporation is essential to regulate heat generated within humans. Sweat contains important biomarkers that can give insight into the health of people. One technique to analyze sweat is by measuring its permittivity. Permittivity can be determined by analyzing the electromagnetic wave interaction with biological tissues. This information is now being exploited in the development of healthcare wearable non-invasive diagnostic tools [1-7]. Sweat can be used to track physiological biomarkers including drugs, potassium, sodium, calcium, chlorine, lactic acid, glucose, ammonia, ethanol, urea, cortisol, and various neuropeptides and cytokines. The health condition of people is reflected in the concentration of sweat. In fact, the alcohol concentration in sweat correlates with the level of alcohol in the blood, and the level of urea in the sweat informs the condition of the kidney. The sweat of people with cystic fibrosis has high levels of chlorine. Also, calcium indicates the condition of the cardiovascular system and other important functions of the body [8].

Old people in hospitals and care homes as well as people on strong medication can lose the sensation of thirst. Infants too are unable to tell when they are thirsty. Old people and infants are at an increased risk of dehydration, which has potentially serious health consequences. Hydration is important to maintain the overall health and cognition of individuals [9]. When optimal hydration is not maintained, thermoregulatory stress, hyperosmolality, and other biophysical conditions can impair. In fact, mild dehydration of -1% to -2% of body mass can

significantly compromise alertness and cognitive responses and affects performance [10]. Chronic dehydration can increase the risk of infection, particularly of the urinary tract. Moreover, the kidneys and other major organs that receive decreased blood flow are in danger of failure. The status of the hydration can be monitored through sweat.

The advances made over recent years in the field of bioelectronics and electromagnetic engineering have made it now possible to apply this technology for application in the development of non-invasive biosensors for healthcare monitoring [4], [5]. Wearable biosensors therefore have great potential for personal real time point of care diagnostics of body sweat. A controlled standardized test medium is therefore needed to calibrate such biosensors based on artificial sweat that is an analogue of real perspiration excreted by eccrine glands. Different formulations of artificial sweat have been reported in literature where the major components are sodium chloride (NaCl), potassium chloride (KCL), urea and lactic acid [7], [11].

The measurement of properties of perspiration, real and artificial, have been studied in both in-vivo and ex-vivo. Permittivity of sweat collected from different parts of the body has reported in [3]. The authors used a phasemeter to measure transmission coefficient of sweat to calculate its permittivity across a frequency range of 300 MHz to 3 GHz. Investigated in [12] is the permittivity of NaCl and KCL solutions over a temperature of between 10˚C and 60˚C and concentrations levels ranging from 0.001-5 mol/L between frequency band of 100 MHz to 40 GHz. The permittivity of aqueous solutions of NaCl is measured in the millimetre-wave band between 26 GHz and 110 GHz and at a temperature range between 0˚C and 25˚C in [13]. Dielectric properties of aqueous solutions of NaCl, KCL, urea and lactic acid simulating sweat are reported in [6] where the complex dielectric permittivity was studied across 1 GHz to 20 GHz at room temperature of 23˚C of ionic solutions of 0.01-1.7 mol/L concentrations. The above studies, however, fail to investigate the frequency dependency variation with change in concentration of metabolites (NaCl, KCL, Lactic acid & Urea) contained in sweat.

This study presents the empirical results of the permittivity and conductivity of artificial sweat metabolite of different concentrations as a function of frequency. The artificial sweat was constituted from a formulation of NaCl, KCL, lactic acid and urea. The permittivity and conductivity parameters were measured over a frequency range of between 400 MHz and 11 GHz.

### 4.3.2. Materials and Methods

Artificial sweat used in the study was synthesized according to the EN1811:2011 European Standard [14]. Table 4.2 lists the aqueous solutions that were prepared to synthesize perspiration. The recipe consisted of dissolving 0.5% of NaCl, 0.1% of KCL, 0.1% of lactic acid and 0.1% of Urea.

Five solutions were synthesized with different concentrations of metabolites and minerals. These solutions covered the perspiration concentration spectrum found in humans under different hydration states. Aqueous solution representing diluted sweat was prepared by dissolving 2.5g of NaCl, 0.5g of KCl, 0.5g of lactic acid and 0.5g of Urea in one litre of distilled water. Over diluted solution comprised 1.25g of NaCl, 0.25g of KCl, 0.25g of lactic acid and 0.25g of urea dissolved in one litre of distilled water. In the case of concentrated sweat the percentage of metabolites and minerals dissolved in one litre of distilled water were, i.e., 10g of NaCl, 2g of KCl, 2g of lactic acid and 2g of urea. Lastly, to account for over-concentrated sweat, 20g of NaCl, 4g of KCl, 4g of lactic acid and 4g of urea mixed in one litre of distilled water. The pH level of all artificial sweat solutions was made to be consistent with real sweat, i.e., 6.00±0.05.

Table 4.1: Artificial sweat solution under test

| **Base Component** | **Concentration of Components (g/L)** | | | | |
|---|---|---|---|---|---|
| | Over-concentrated (4%) | Concentrated (2%) | Standard (1%) | Diluted (0.5%) | Over-diluted (0.25%) |
| **NaCl** | 20g | 10g | 5g | 2.5g | 1.25g |
| **KCl** | 4g | 2g | 1g | 0.5g | 0.25g |
| **Urea** | 4g | 2g | 1g | 0.5g | 0.25g |
| **Lactic acid** | 4g | 2g | 1g | 0.5g | 0.25g |

### 4.3.3. Experimental Setup

The real part of the permittivity and conductivity of the artificial sweat solutions were measured using a high-precision measurement coaxial probe by SPEAG over a wide frequency range from 0.4 GHz to 11 GHz. The coaxial probe was connected to a vector network analyzer (VNA) to measure the complex reflection coefficient ($S_{11}$), as shown in Figure 4.2. Before the measurements were taken the probe was first calibrated according to SPEAG's high-quality standards. The electromagnetic (EM) fields at the probe end penetrate the artificial sweat solution under test and the reflected signal was measured with the VNA. The reflected signal

was converted to the complex permittivity of the artificial sweat using Nicholson-Ross-Weir method using [15, 16]:

$$\varepsilon_r = \mu_r \left(\frac{1-\Gamma}{1+\Gamma}\right)^2 \left(1 - \frac{\lambda_o^2}{\lambda_c^2}\right) + \frac{1}{\mu_r}\left(\frac{\lambda_0}{\lambda_c}\right)^2 \quad (4.4)$$

$$\sigma = \omega \varepsilon_o \varepsilon_r'' \quad (4.5)$$

Where $\varepsilon_r$ is the relative permittivity, $\mu_r$ is the relative permeability, Γ is the reflection coefficient, $\lambda_o$ is the wavelength in the sample, $\lambda_c$ is the cut-off wavelength of the coaxial probe, $\sigma$ is the electric conductivity, $\varepsilon_o$ is the vacuum permittivity, and $\varepsilon_r''$ is imaginary part of the relative permittivity.

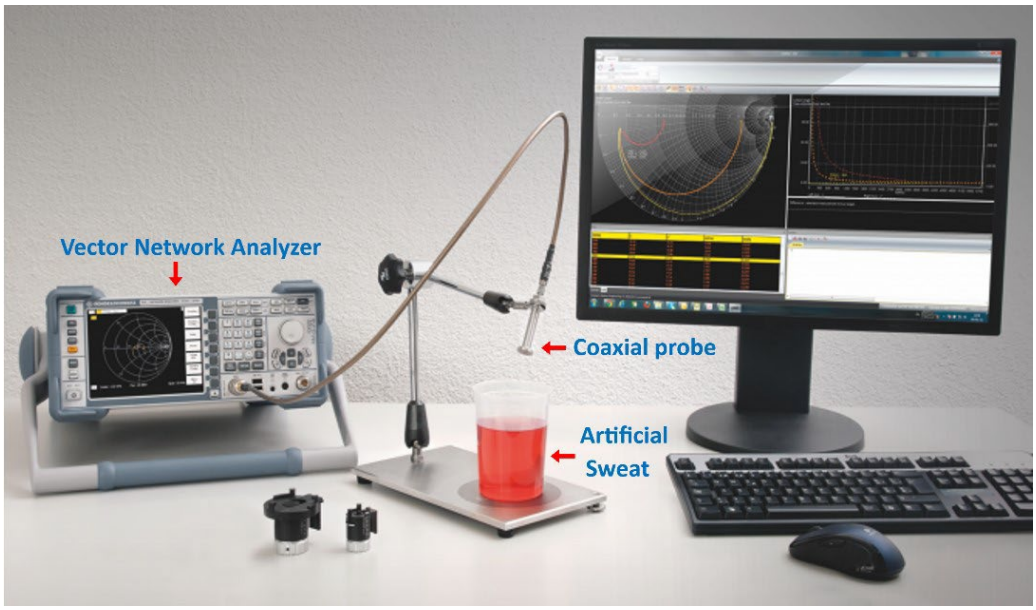


*Figure 4.2: Experimental setup showing Speag's dielectric probe (DAK 3.5 mm) to be inserted in a solution of artificial sweat to measure permittivity.*

The permittivity of the artificial sweat solutions of volume 50 ml was measured in a glass beaker. All permittivity measurements were made at room temperature of 23˚C. Each measurement involved collecting 212 quantization points from 400 MHz to 11 GHz. The permittivity and conductance of each sample was an average of the three measurements. To maintain the integrity of the measurements the DAK probe was cleaned with distilled water each time it was used with different solution samples.

### 4.3.4. Experimental Results

The real and imaginary part of the permittivity, i.e., ε' and ε", and conductivity σ (S/m) of the of

the artificially engineered sweat solutions of different concentrations were measured at room temperature. Table 4.1 above gives the standardized recipe for artificial sweat for different hydration states found in humans. Figures 4.3 and 4.4 show how the permittivity and conductivity, respectively, vary across a frequency range from 400 MHz to 10.4 GHz. The measured results in Fig. 4.3(a) show the real part of the permittivity to decline with an increase in frequency. The real part of the permittivity at 0.4 GHz is 80 for 0.25% solution and approximately 74 for the 4% solution. The decline in the real part of the permittivity can be approximated to a linear curve. This is due to complex electrolyte-water-ion interactions where the oscillations of the time-varying electromagnetic field 'flip' and 'twist' the water molecules to affect its dipole moment. As the frequency of the electromagnetic field increases the interaction diminishes polarization of the solution resulting in the fall in permittivity. Figure 4.4 shows the real part of the permittivity of sweat minus the deionized water. It clearly shows the differential in the permittivity is observed between 0.4 GHz to 2.4 GHz. In fact, the differential is great for sweats with greatest metabolites concentration. Figure 4.3 shows how the various sweat concentrations affect the imaginary part of the permittivity. For concentration levels higher than 1% the imaginary part of the permittivity declines rapidly from 0.4 GHz to 2.4 GHz, and it stabilizes at around 30 at higher than 2.4 GHz. At 0.4 GHz, the imaginary part of the permittivity highest having a value of is approximately 130 for the 4% solution. The next highest having a value of 100 is the 2% solution.

The measured results in Figure 4.4 show how the conductivity of the artificial sweat solutions vary with frequency. Conductivity increases in a linear fashion with an increase in frequency. This is because electrolyte-water-ion polarization diminishes at higher frequencies resulting in higher ionic presence in the aqueous solution. More ions present in the solution limit the resistivity of various solutions resulting in higher conductivity [17]. The conductivity is higher for artificial sweat solutions of higher concentration of metabolite over a frequency range from 0.4 GHz to 10.4 GHz. Moreover, the difference in conductivity between the different concentrations metabolites reduces with increase in frequency.

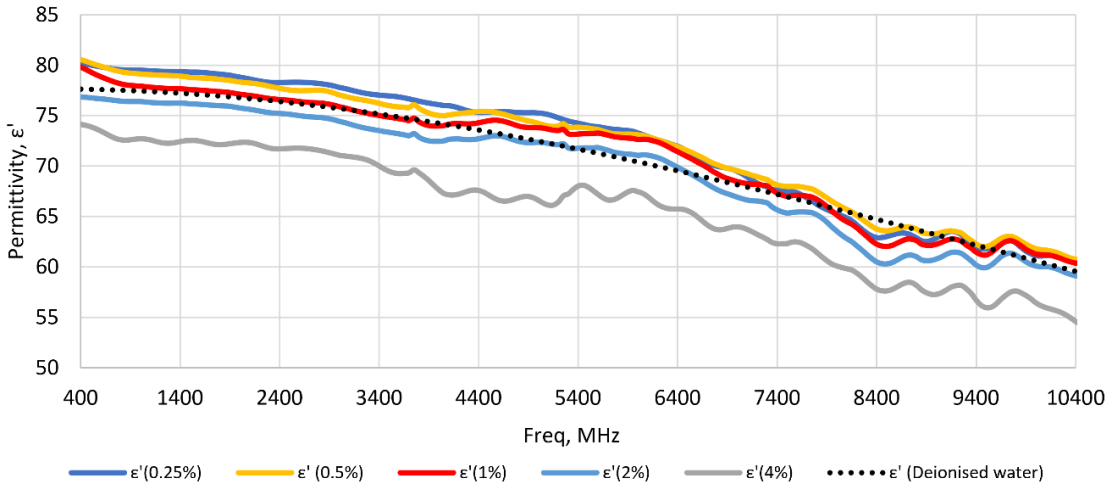


(a)

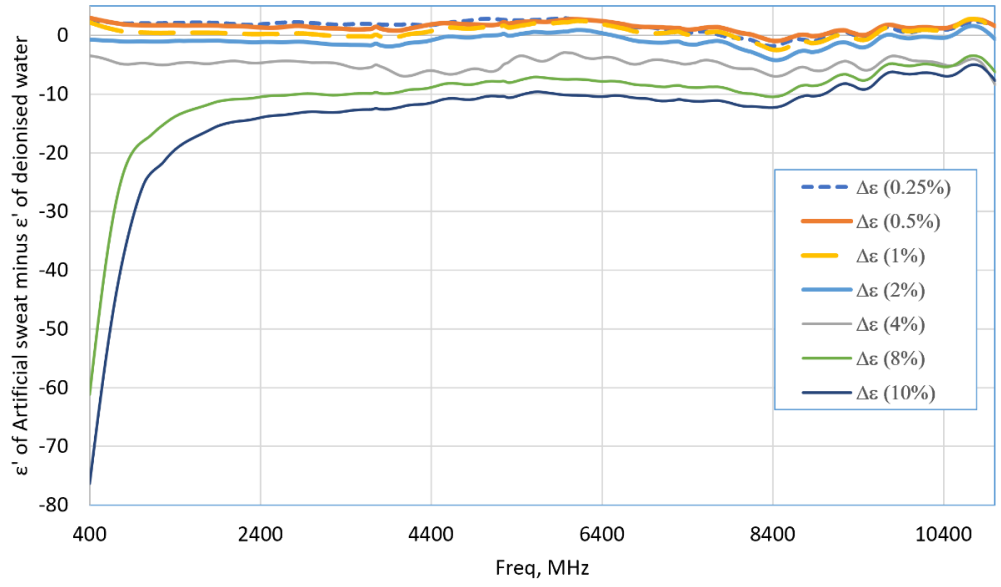


(b)

*Figure 4.3: Measured permittivity of artificial sweat solutions of different metabolite concentrations from 0.4 to 10.4 GHz, (a) real part of the permittivity, (b) the real part of the permittivity of the sweat without the deionised water.*

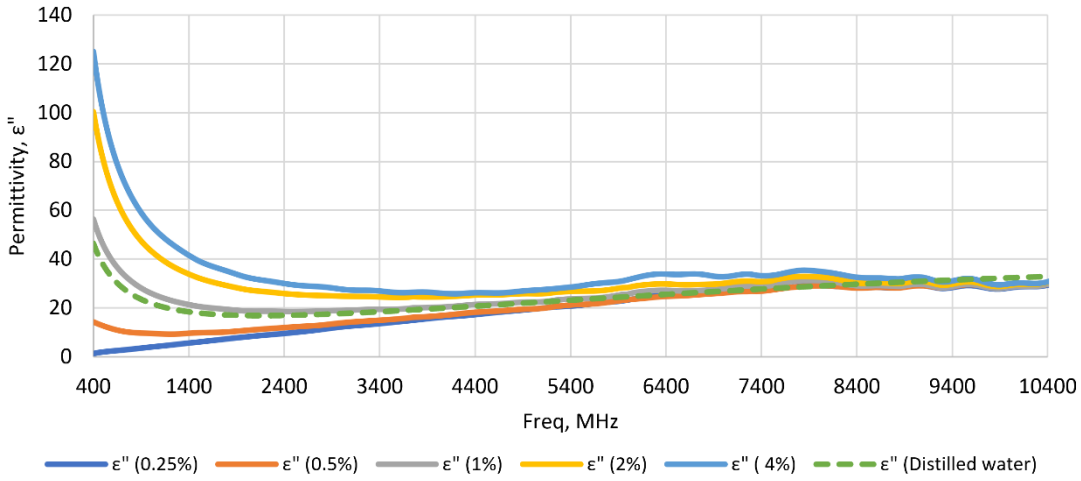


*Figure4.3c:: Imaginary part of the permittivity.*

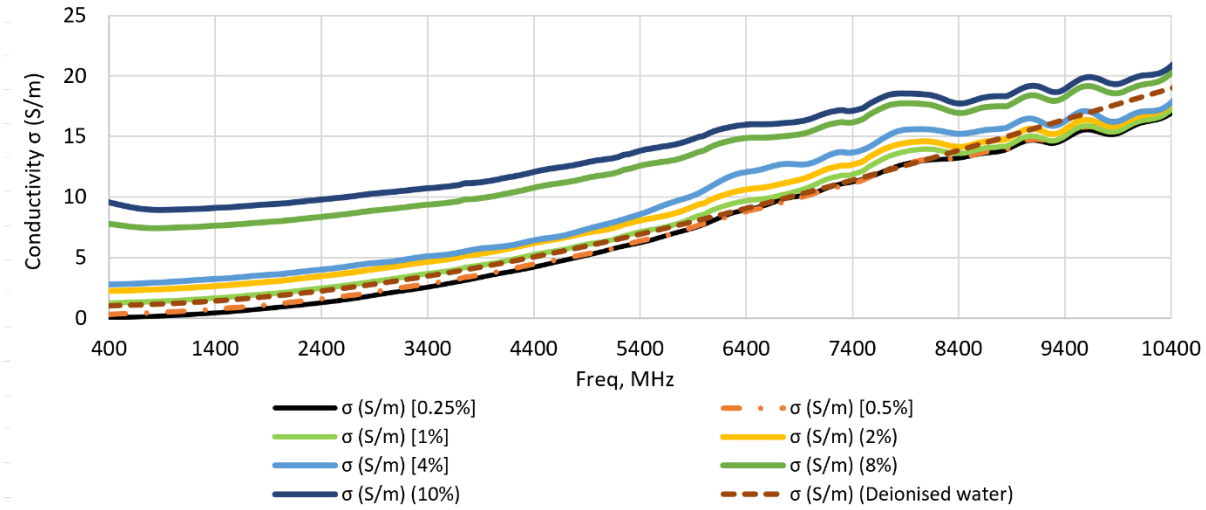


*Figure 4.4: Measured conductivity of artificial sweat solutions of different metabolic concentrations from 0.4 to 10.4 GHz.*

### 4.3.5. Sensitivity, Selectivity and Reproducibility Analysis

The experimental results presented above of the permittivity of the artificial sweat solutions were measured with the probe sensor in a beaker with 50 ml of artificial sweat solutions at room temperature of 23˚C. The sensitivity of the probe sensor was determined by using the permittivity of various volumes of sweat solutions. Figure 4.5 shows the percentage error in the permittivity measurement of the various volumes of artificial solution of 2% metabolite concentration with reference to permittivity of the 50 ml of artificial sweat solution. The results in Figure 4.5 shows the measurement error to be negligible. From these results it can be surmised that the probe sensor used to measure the parameters is highly accurate if the end of the probe is in contact with the sweat. In terms of the selectivity and reproducibility, the results obtained were identical to those presented in Figures 4.3 and 4.4. These results confirm the probe sensor that was employed can measure the dielectric parameters with a high precision. Moreover, cable movement attached to the sensor had no effect on the measurements. This is because the phase distortion of the reflected signal from the probe due to movement of the cable is eliminated by the sensor's vector reflectometer.

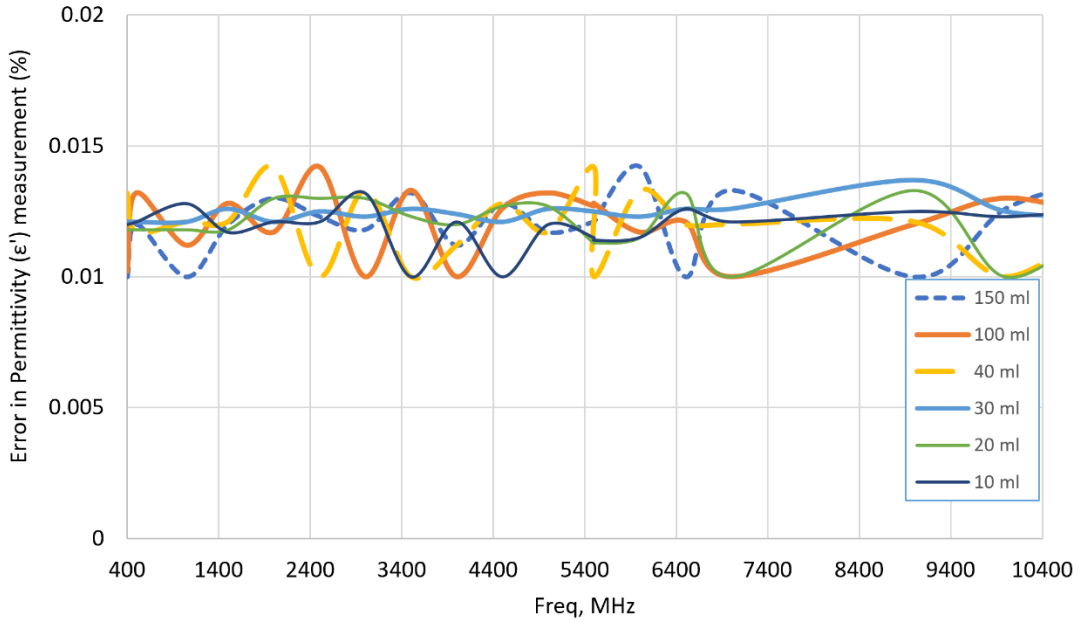


*Figure 4.5: Error in the relative permittivity measurements with reference to 50 ml of artificial sweat solution of 2% concentration.*

### 4.3.6. Modified Debye Model for Artificial Sweat Mixtures

The dependency of the complex permittivity with frequency can be described by the modified Debye model given by [18]:

$$\varepsilon^* = \varepsilon_\infty + \frac{\varepsilon_s - \varepsilon_\infty}{1 + j\omega\tau} + \frac{\sigma}{j\omega\varepsilon_o} \qquad (4.6)$$

Where $\varepsilon_\infty$ is the permittivity at high frequency, $\varepsilon_s$ is the DC permittivity, $\omega$ is the angular frequency, $\tau$ is the relaxation time, $\varepsilon_o$ is the permittivity of free space, and $\sigma$ is the ionic conductivity. Exact expressions that accurately model the measured results of artificial sweat solutions for various concentrations was obtained through curve fitting. The relationship between permittivity and conductivity as a function of metabolite concentration is given by:

$$\varepsilon' = -6e^{-20f^5} + e^{-14f^4} - 2e^{-10f^3} + e^{-6f^2} - 0.0027f + 81.391 + \alpha \qquad (4.7)$$

Where $\alpha = -0.1288c^4 - 1.294c^3 - 4.223c^2 + 2.6403c - 0.5799$

The corresponding expression for the conductivity is given by:

$$\sigma = 5e^{-15f^4} - e^{-10f^3} + e^{-6f^2} - 0.0026f + 10.644 + \beta \qquad (4.8$$

Where $\beta = 0004c^6 - 0.0095c^5 - 0.0836c^4 + 0.2258c^3 - 0.3069c^2 + 2.4406c - 10.298$

Where $f$ is the frequency in MHz, and $c$ is the concentration level between 0.25%-10%. The error margin of Equation (4.6) is 2% between 0.4 GHz to 6.4 GHz. The worst-case error is 5% between

6.5 GHz and 10.4 GHz. The maximum, and Eqn. (4.7) is 2% between 0.4 GHz to 6.4 GHz. The error is a maximum of 35% between 6.5 GHz to 10.4 GHz. This error is greatest at 10.4 GHz.

The development of wireless biomedical sensors for healthcare applications are designed at the license free Industrial, Scientific and Medical (ISM) band. In Figure 4.6 shows the measured permittivity (real part) of the artificial sweat solutions for various metabolite concentrations at the ISM frequency of 2.45 GHz. Table 4.2 gives the values of the corresponding conductance. The given sweat solutions carry significance as they correspond to hydration and dehydration levels in humans. Figure 4.6 shows the permittivity measurements can be used to determine the level of dehydration in humans. Even though the differential between normal hydration and dehydration is marginal, a sensitive sensor is required.

Table 4.2: Permittivity of artificial sweat solutions at ISM frequency of 2.45 GHz

| ***Tested solution*** | ***ε'*** | ***σ (S/m)*** |
|---|---|---|
| 4% conc. sweat | 76.0625 | 3.24606 |
| 2% conc. sweat | 76.0328 | 3.25045 |
| 1% sweat | 77.1450 | 2.36587 |
| 0.5% diluted sweat | 77.8133 | 1.75342 |
| 0.25% diluted sweat | 78.1402 | 1.52443 |

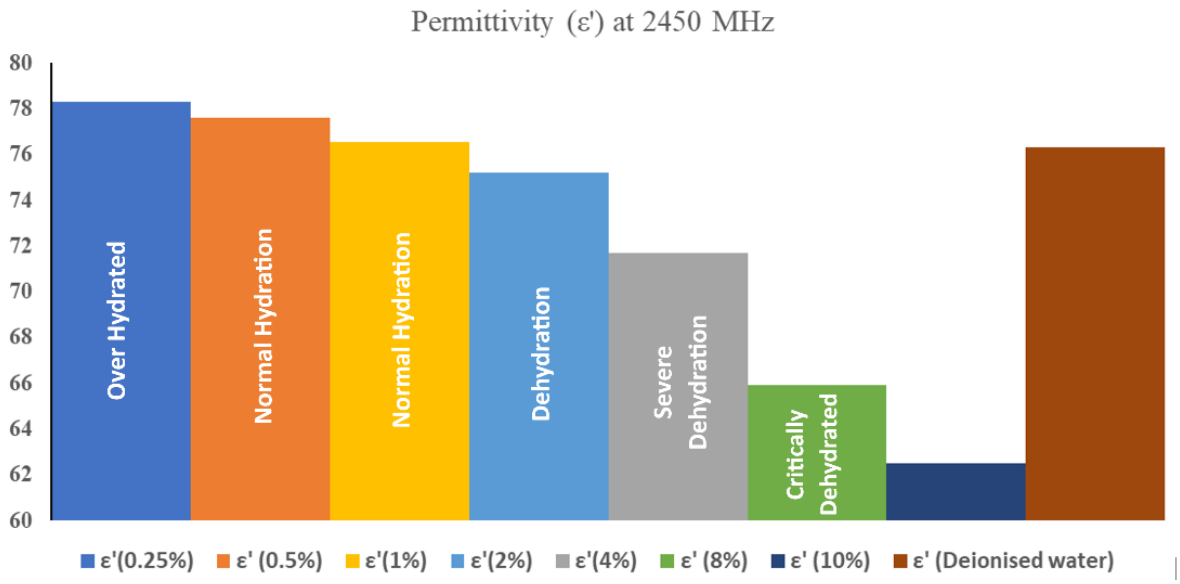


*Figure 4.6: Measured permittivity of five artificial sweat solutions at the ISM frequency band of 2.45 GHz.*

### 4.3.7 Artificial Sweat Study Overview

The above section presented measured data on the permittivity and conductivity of artificially synthesized sweat at varying concentrations. The composition of the artificial sweat closely

mimics that of real human sweat, including sodium chloride (NaCl), potassium chloride (KCl), urea, and lactic acid components often overlooked in other studies. Most existing literature on artificial sweat focuses only on one or two constituents, typically NaCl or KCl, which does not fully capture the complexity of actual sweat composition.

Measurements were conducted over a wide frequency range (0.4–11 GHz) at a stable room temperature of 23 °C. Based on the experimental results, predictive expressions were derived to estimate permittivity and assess hydration levels accurately. The data from this study aim to improve our understanding of sweat's dielectric properties and contribute to the development of non-invasive, wearable hydration sensors. Such biosensors have the potential to play a critical role in monitoring hydration status, particularly in vulnerable populations such as infants and the elderly, helping to prevent health issues related to dehydration.

### 4.4 Human Tissue Hydration Study Using DAK 3.5 mm

For the human hydration study, measurements were performed on the inner wrist (radial side) of each participant. The DAK coaxial probe was gently pressed against the skin to ensure good contact, and participants were instructed to remain still to avoid motion artifacts. To maintain both hygiene and measurement consistency, the probe was cleaned with distilled water and dried before and after each subject.

A vector network analyser (VNA) was used to measure the reflection coefficient at the probe tip. In this case, measurements were focused on a specific frequency (2.45 GHz). This frequency lies within the ISM band and is commonly used in biomedical sensing due to its license-free status and sensitivity to tissue hydration. It also enables compact sensor design and captures variations in tissue permittivity caused by changes in water content.

Prior to measurements on human subjects, the system was calibrated using deionized water to confirm that the probe's response matched known permittivity values. For each participant, measurements were taken on both the left and right inner wrists. To account for small variations in probe placement, multiple readings (typically three) were taken at slightly different adjacent spots on each wrist and averaged.

Each individual reading lasted approximately 5 seconds. Since the probe was only briefly activated at the frequency of interest, the average power delivered to the tissue was negligible, ensuring no discomfort or risk to participants. The compact design of the DAK probe allowed for

easy handheld operation. Figure 4.7 illustrates the probe in contact with a subject's wrist, where the small sensing tip touches the skin to sample local permittivity.

*Figure 4.7: DAK probe on the human subject's wrist.*

### 4.4.1 Design Study

In 2023, the Centre for Communications Technology establish a collaborative research partnership with a hospital specialising on treating patients with diabetes. The Centre linked up with the Department of Endocrinology at PSG Multi-speciality Hospitals in Coimbatore, India—a renowned healthcare institution. I had the opportunity to spend several weeks at PSG Hospital, to collect clinical data for this research study. Figure 4.8 shows the two medical assistance who assisted me with the collection of data. A cohort of 227 adult participants (aged 18 to 90, both male and female) was recruited for this study, with informed consent obtained and ethical approval secured. The clinical aspect of the study was executed by qualified medical practitioners, including nurses and medical doctors. The study aimed to evaluate variability in tissue hydration across a diverse population. Each participant's hydration status was independently assessed using standard clinical criteria and categorized into one of four groups: Hydrated, Moderately Hydrated, Dehydrated, or Severely Dehydrated. Categorization was based on recent fluid intake, clinical hydration assessments (e.g., urine specific gravity, vital signs), and, where applicable, indicators like changes in body mass or the need for intravenous (IV) fluid rehydration. These classifications provided a reliable "ground truth" for comparison with dielectric measurements.

***Measurement Protocol***

Dielectric permittivity ($\varepsilon_r$) measurements were obtained using a DAK probe placed on the inside of each participant's left and right wrists. Readings were taken at a fixed frequency of 2.45 GHz, chosen for both efficiency and its demonstrated sensitivity to hydration changes, as indicated by earlier artificial sweat experiments. Typically, the readings from both wrists were similar; in cases of slight differences, both values were recorded, and the average permittivity across both wrists was used for further analysis. This value was referred to as the "Average Inside Wrist" measurement. To ensure data accuracy, the probe was recalibrated every 20–30 subjects. Ultimately, the dataset comprised permittivity readings correlated with clinically determined hydration status for a broad sample of individuals.

*Figure 4.8: Medical assistance and I at PSG Hospital in Coimbatore, India.*

### 4.4.2 Results - Permittivity Distribution by Hydration Status

To evaluate hydration levels noninvasively, wrist permittivity measurements from all 227 participants were analysed. Each participant's average wrist permittivity was mapped to a hydration status category based on predefined ranges (see Table 4.3). These ranges were theoretically grounded in tissue dielectric modelling using the Bruggeman effective medium approximation (Chapter 3.3) [21].

The wrist was modelled as a heterogeneous composite of its main tissues approximately 10% skin, 15% fat, 40% muscle, 25% bone, and 10% blood by volume. Representative relative permittivity values for these tissues are:

- Skin: ≈38
- Fat: ≈5.3
- Muscle: ≈52.7
- Bone: ≈12.5
- Blood: ≈61

Using the Bruggeman mixing formula, the effective permittivity of this tissue composition is estimated at $\varepsilon \approx 29.72$, which closely aligns with the boundary between the "Moderately Hydrated" and "Dehydrated" categories. In other words, a permittivity value around 30 serves as a theoretical benchmark for normal hydration.

Permittivity values significantly above ~30 (particularly ≥34) suggest a higher effective permittivity, likely due to dehydration-related changes in tissue properties (e.g., increased electrolyte concentration). In contrast, values well below ~30 (e.g., in the teens or low 20s) indicate a higher proportion of low-permittivity tissues like fat, or well-hydrated muscle with bound water—markers of better hydration.

The stark contrast between the permittivity of water-rich tissues (e.g., muscle, blood with $\varepsilon$ ~60) and fat ($\varepsilon$ ~5) at radio frequencies is a key driver of this effect. Thus, elevated wrist permittivity typically reflects a larger proportion of high-$\varepsilon$ tissue components, signalling dehydration, while lower values are associated with better-hydrated states.

The Bruggeman model's predicted value of $\varepsilon \approx 29.72$ therefore supports the use of $\varepsilon$ ~30 as a meaningful threshold for classifying hydration status, as illustrated in Figure 4.9.

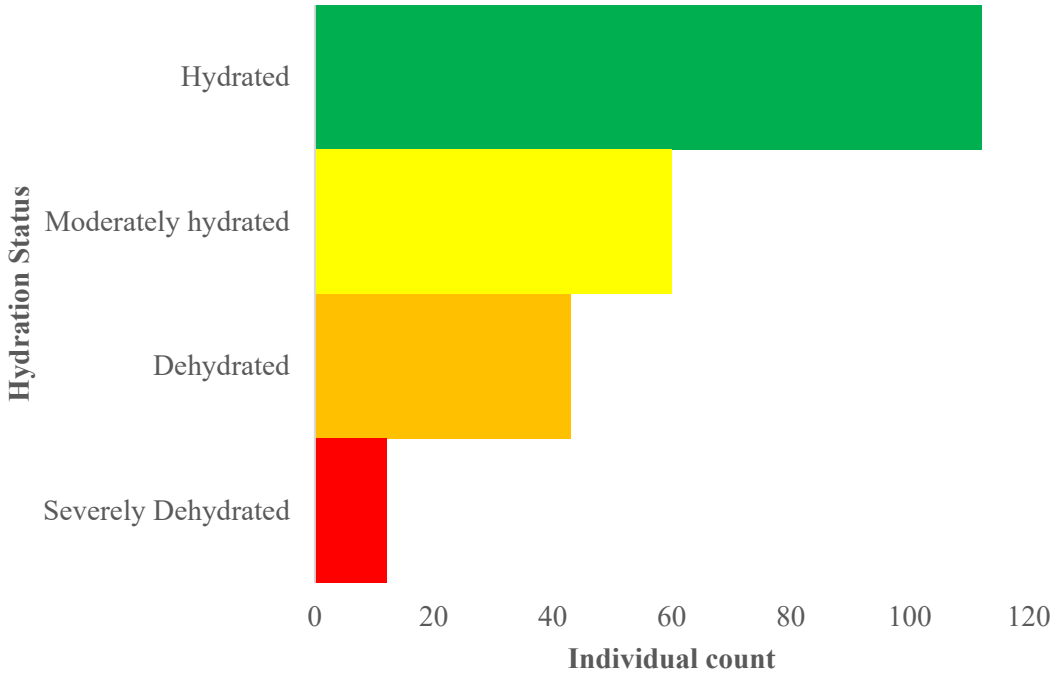


*Figure 4.9: Distribution of hydration status among participants and associated wrist dielectric readings.*

Table 4.3: Wrist permittivity readings for individuals in different hydration categories

| **Hydration Status** | **Wrist Permittivity (2.45GHz)** | **Number of Individuals (N=227)** |
|---|---|---|
| Hydrated | 8- 25 (high water content) | 112 |
| Moderately Hydrated | 25-29 (slightly reduced) | 60 |
| Dehydrated | 29-34 (reduced hydration) | 43 |
| Severely Dehydrated | ≥ 34 (significantly low water) | 12 |

The results show a clear pattern: individuals categorized as "Hydrated" generally had wrist permittivity values in the range of approximately 8 to 25, with the majority falling in the teens. In contrast, those in the "Severely Dehydrated" category had significantly higher values, often exceeding 34 and sometimes reaching the upper 30s. Participants in the "Moderately Hydrated" and "Dehydrated" groups exhibited values between these two extremes, with some overlap at the category boundaries.

At first glance, this trend might seem counterintuitive since dehydration implies less water, one might expect lower permittivity values. However, several physiological and measurement-related factors influence the readings at the wrist.

One proposed explanation is that dehydration leads to peripheral vasoconstriction and reduced blood flow, which can make the skin and subcutaneous tissues more resistive. This may cause the dielectric probe to register a higher permittivity reading, due to its calibration characteristics [19][20]. Another possibility is related to the calibration reference. If the probe is calibrated using pure water, then tissues with high loss but low free water content may appear to have artificially elevated permittivity.

Despite the complexity of the underlying mechanisms, the important takeaway is the monotonic relationship:

- Hydrated individuals consistently show the lowest permittivity values,
- Dehydrated individuals the highest,
- And this trend is statistically significant, reinforcing the sensitivity of dielectric measurement to whole-body hydration status.

In addition to overall hydration trends, we also analysed how age, sex, and individual variability affect permittivity readings.

Figure 21 shows a scatterplot of wrist permittivity measurements from all 227 subjects, spanning ages 18 to 90, ensuring wide age group representation. Each subject's wrist permittivity was measured noninvasively at 2.45 GHz using a consistent protocol to minimize the influence of short-term hydration fluctuations or ambient temperature effects. Prior to each session, the dielectric probe was calibrated with deionized water, and three readings were taken per wrist and averaged to improve accuracy. The reported permittivity values are dimensionless, representing the relative permittivity (ε) compared to free space, and reflect the water content at the tissue measurement site.

***Statistical Analysis: Age and Permittivity***

To explore the relationship between age and wrist permittivity, we conducted the following analyses:

- *Pearson Correlation:*
  We calculated the Pearson correlation coefficient ($r$) between age and measured permittivity (ε) for the left and right wrists separately.
  - For the left wrist, $r \approx -0.22$, indicating a weak but statistically significant inverse relationship (older individuals tended to have lower permittivity).

        - Significance: $p \approx 0.001$
    - For the right wrist, $r \approx -0.17$, also a weak negative correlation, but still statistically significant.
        - Significance: $p \approx 0.009$

While both correlations were significant at $\alpha = 0.05$, the magnitude of $r$ values suggests that age only explains a small portion of the overall variation in permittivity values among individuals.

- *Linear Regression:*
  Results from linear regression were consistent with the correlation findings. The slope ($\beta$) of the regression line was negative for both wrists, confirming that permittivity tends to decrease with age.
    - The fitted regression equation for the left wrist is summarized in Table 5, providing further evidence for this age-related trend.

For the left wrist, the fitted regression equation is determined to be:

$$permittivity_{left} = 27.3 - 0.062 \times (Age)$$

And for the right wrist:

$$permittivity_{right} = 27.2 - 0.058 \times (Age)$$

In these equations, the intercepts (~27.2–27.3) represent the extrapolated permittivity at age 0 (not physically meaningful beyond indicating the baseline level), and the slopes indicate the rate of change of permittivity per year of age. Both slopes are around –0.06 per year, meaning that, on average, an increase of 10 years in age is associated with only about a 0.6 unit decrease in the permittivity $\varepsilon$ reading. The 95% confidence intervals for the slopes were entirely below zero for both wrists, confirming the negative trend is statistically significant despite its small magnitude.

***Model Fit and Significance:*** The coefficient of determination ($R^2$) for the regression models was low for both wrists. As shown in Table 4.4, $R^2$ was approximately 0.048 for the left wrist and 0.030 for the right wrist. In other words, only about 4.8% (left) and 3.0% (right) of the variance in wrist permittivity can be statistically explained by age alone. This reinforces that the predictive strength of age on permittivity $\varepsilon$ is weak, most of the variation in the permittivity measurements is due to other factors or individual differences, not age. Nevertheless, the regression $p$-values were significant ($p<0.01$) for both wrists, indicating that the slight downward trend with age is

unlikely to be due to chance in this sample. The left wrist showed a somewhat stronger association than the right, but both are in the same direction and order of magnitude.

Table 4.4: Summary of correlation and regression analysis relating Age to permittivity (at 2.45 GHz) for left and right wrists ($n$ = 227). The table includes the Pearson correlation coefficient ($r$), the regression slope and intercept (from Permittivity = intercept +slope × Age), the coefficient of determination ($R^2$), and the statistical significance of the correlation ($p$-value).

| Wrist | Pearson $r$ | $p$-value | Intercept ($\alpha$) | Slope ($\beta$) | ($R^2$) |
|---|---|---|---|---|---|
| Left | -0.22 | 0.001 | 27.3 | -0.062/year | 0.048 |
| Right | -0.17 | 0.009 | 27.2 | -0.058/year | 0.030 |

In Figure 4.10, the slopes of the red trend line are shallow, visually reinforcing that the effect of age on permittivity is marginal. Some younger participants have low permittivity $\varepsilon$ , and some older participants have relatively high permittivity $\varepsilon$ , showing overlap between age groups. This overlap underscores the low $R^2$ values obtained: age alone does not strongly predict an individual's permittivity reading, even though the average trend across the sample is downward. In summary, the hypothesis that age influences permittivity $\varepsilon$ is supported in direction (older individuals tend to have lower 2.45 GHz permittivity consistent with lower hydration), but the strength of this effect is weak in our data.

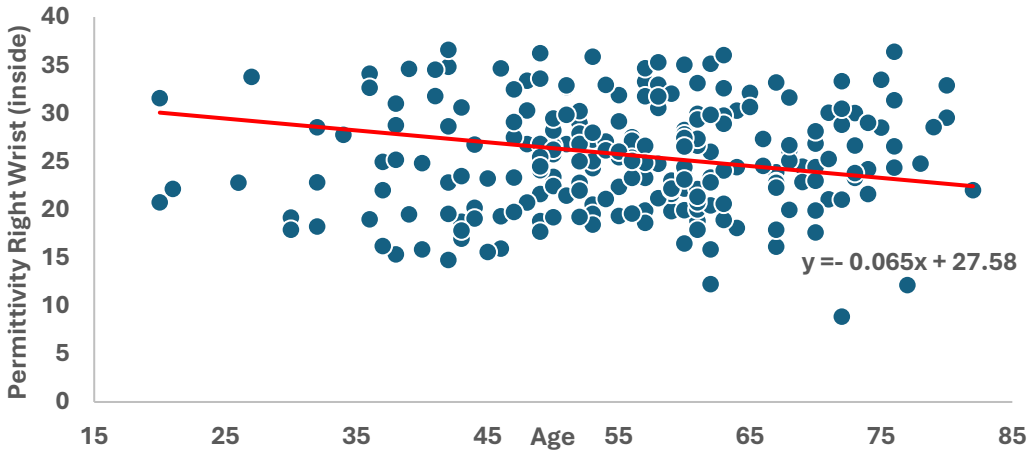


(a)

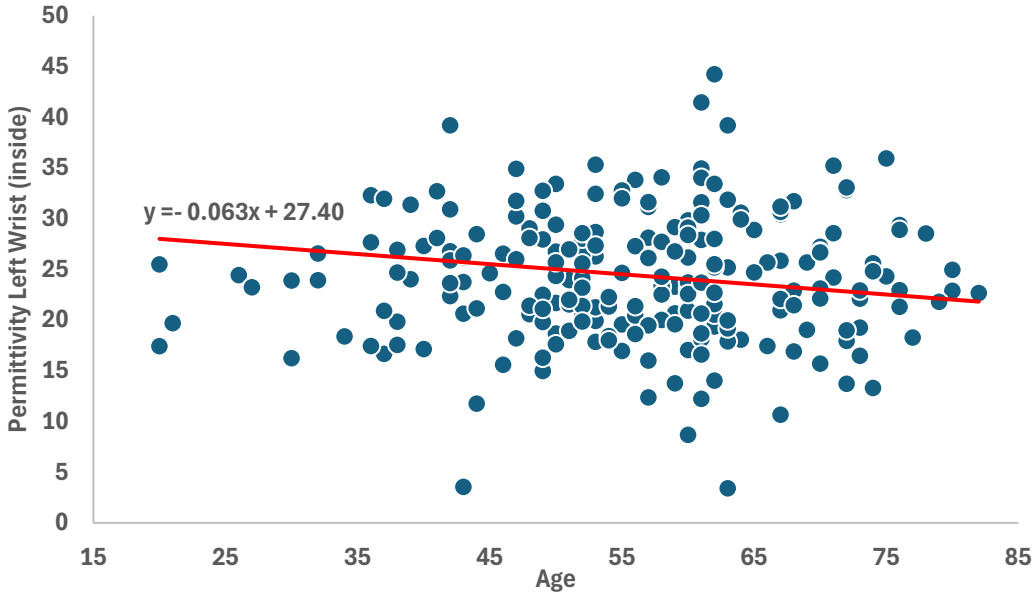


(b)

*Figure 4.10: Scatter plots of permittivity vs age for the left and right wrists at 2.45 GHz, with red trend lines. Both plots show a slight negative trend, indicating lower permittivity at higher ages. However, the wide scatter suggests only a weak correlation with significant individual variability.*

The results indicate that age has a statistically significant but modest impact on permittivity $\varepsilon$ at 2.45 GHz. In practical terms, older adults in our sample showed slightly lower wrist permittivity readings than younger adults, which is consistent with the notion that older individuals generally have lower tissue water content. This finding aligns with expectations from human physiology: total body water percentage declines as people age (e.g., dropping from ~60% in younger adults to the mid-50% range in older adults) [23]. It also aligns with dielectric property studies on tissues, which report that permittivity tends to decrease with age due to reduced water content in the tissue [24]. The negative regression slopes we observed (around –0.06 per year) suggest that each additional year of age contributes to a slight decrease in measured permittivity. Over a large age span (say, a 50-year difference), the model would predict on the order of only a 3-unit difference in permittivity, which is relatively small on the scale of our measurements. This explains why the data for different ages overlap considerably: many other factors besides age are contributing to the permittivity values.

Importantly, the weak correlation (low $R^2$) tells us that age by itself is a poor predictor of an individual's hydration as sensed by permittivity $\varepsilon$. Even though the trend with age is in the expected direction (supporting the hypothesis qualitatively), quantitatively age accounts for only ~3–5% of the variance in permittivity. In other words, knowing someone's age does not allow

one to accurately infer their hydration status. There is too much variability from person to person. One reason for this weak relationship could be that acute and lifestyle factors overshadow the chronic effect of age. People of any age can be well-hydrated or dehydrated on a given day, and our cross-sectional measurement captures their hydration at one point in time [25]. A well-hydrated 70-year-old can easily have a higher permittivity reading than a mildly dehydrated 30-year-old, despite the age difference. The body maintains homeostasis; many older adults stay adequately hydrated through regular fluid intake, which mitigates age-related declines in water content. Therefore, while older participants on average had slightly lower permittivity $\varepsilon$ , individual variation in hydration status (due to diet, activity, health conditions, etc.) was large. This large individual variability is evident in the scatter plots in Figure 4.10, where data points for young and old overlap. It suggests that age is not a dominant factor in determining hydration at a single time point, compared to person-specific factors.

Another consideration is the measurement locality and tissue composition. The permittivity sensor was applied to the wrist, measuring primarily the skin and immediate subcutaneous tissue. Skin properties change with age in ways that could affect permittivity readings: older skin tends to be drier (lower stratum corneum hydration) and thinner, with changes in collagen and fat distribution [26]. Increased adipose tissue in the skin and underlying tissue with age (at the measurement site) could lower the measured permittivity, since fat has a low dielectric constant and water content. Thus, part of the age effect we observe might be due to increased local fat or reduced skin moisture in older adults. Conversely, age-related skin changes might not be uniform: some studies have noted that superficial skin hydration can decrease less or even appear higher in older individuals due to shifts in water distribution within tissue layers [27]. In our results, the net effect was a small decrease in bulk permittivity. It's worth noting that our measurement depth was not explicitly controlled; the 2.45 GHz signal likely probes a few millimetres into tissue. At that depth, older adults may indeed have slightly less bound water, consistent with our observations. If deeper tissues were measured, we might see a larger difference (since muscle water content decline with age could be more pronounced). Without direct measurement of tissue composition, however, these explanations remain speculative. The existing literature on hydration monitoring has mostly focused on acute changes (e.g. exercise-induced dehydration in young adults) rather than baseline differences with age. The study contributes by highlighting the baseline permittivity differences with age exist but are minor.

***Limitations***

Several limitations of this study should be acknowledged:

1. *Cross-Sectional Design*

   This was a cross-sectional observational study, meaning we captured data at a single point in time. We did not use direct, gold-standard methods—such as bioimpedance analysis or blood osmolality—to independently confirm each participant's hydration status. As a result, we cannot be certain that the observed permittivity differences reflect true variations in hydration. Many participants regardless of age may have been in a euhydrated (normal) state, potentially limiting the apparent impact of age on permittivity.

2. *Uncontrolled Variables*

   The study did not account for several potentially important variables, including sex, body composition, and health status. Although both men and women were likely included, we did not explicitly stratify or adjust for these factors. For example, older adults may have a higher prevalence of conditions such as hypertension or be taking medications that influence hydration. Moreover, body fat percentage tends to increase with age, which could independently affect permittivity. A multivariate analysis would be necessary to determine whether age remains a significant predictor after controlling for these confounding variables.

3. *Measurement Limitations*

   The dielectric measurement technique itself has inherent variability and assumes relatively homogeneous tissue beneath the probe. Any measurement noise could obscure subtle relationships. Measurements were taken at only one anatomical site (the inside of the wrist); other body locations such as the torso or leg, where tissue composition varies more, might yield different age-related trends. Additionally, using a single frequency (2.45 GHz) provides only a narrow view of the tissue's dielectric properties. A multi-frequency analysis could potentially reveal age-related differences in dielectric dispersion or loss tangent that our single-frequency approach might miss.

4. *Sample Demographics*

   Although the sample size ($n$=227) is relatively large, it may not have been evenly distributed across all age ranges. For instance, if the study included fewer participants

over the age of 80, we may have underestimated the full extent of age-related changes in tissue permittivity.

Despite these limitations, the study has notable strengths: it employed a consistent measurement protocol and included a wide age range among participants. This lends confidence that the observed age-related trend, while modest, is real and statistically significant.

***Conclusion on Age Effects***

The study found that age has a small but measurable effect on wrist permittivity at 2.45 GHz, when used as a proxy for hydration status. Older participants tended to exhibit slightly lower permittivity values than younger participants. This finding is consistent with the well-documented age-related decline in tissue water content.

However, the relationship between age and permittivity was weak:

- Age explained only a small portion of the total variability, and
- There was substantial overlap in permittivity values across different age groups.

This suggests that while the trend is statistically significant, age alone is not a reliable predictor of an individual's hydration level using dielectric methods.

***Practical Implications***

In practice, hydration monitoring technologies should not rely on age alone. A low permittivity reading in an older adult must still be interpreted in the context of their actual fluid intake, health status, and individual baseline. That said, it may be beneficial for hydration-monitoring devices to calibrate or adjust for age, since older adults tend to have slightly lower baseline permittivity on average.

For example, algorithms could include age as one of several factors to better interpret permittivity values. This could improve accuracy in determining whether a specific reading indicates normal hydration or mild dehydration in older individuals.

***Permittivity for Both Sexes***

Figure 4.11 represents a boxplot comparing male and female subject's wrist permittivity readings. It is observed that males had a slightly wider range and a marginally higher median permittivity than females. This aligns with the understanding that male skin is on average thicker and may have different composition, which could lower the measured permittivity slightly [28]. However, in our data the difference between sexes was not large; both showed the same overall pattern

relating to hydration. The interquartile ranges overlapped considerably, indicating that a hydration assessment can be applied similarly for both men and women, with perhaps a minor calibration offset if extreme precision is needed.

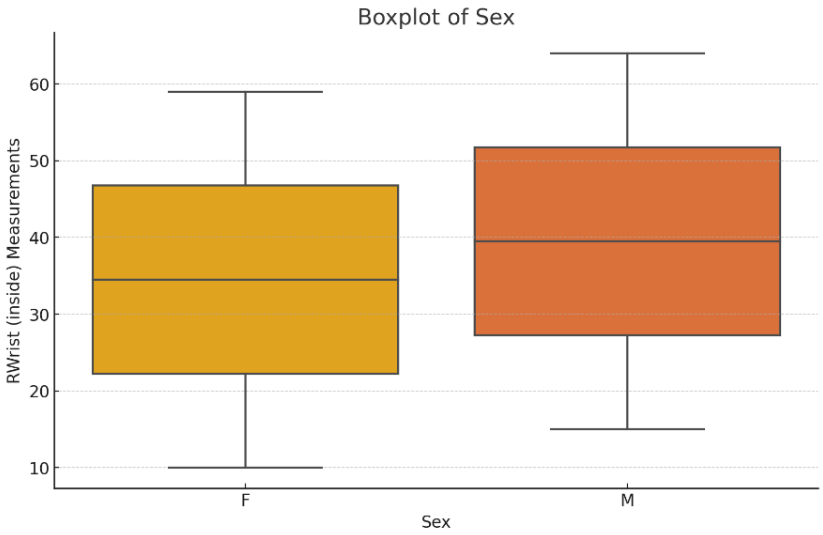


*Figure 4.11: A boxplot for average wrist permittivity measurements for both female and male.*

### 4.4.3 Analysis of Body Weight and Wrist Permittivity

The hypothesis guiding this analysis was that heavier individuals, who generally possess a greater absolute body fluid volume, might exhibit different permittivity readings (ε) compared to lighter individuals. Data were collected from 227 participants, with body weight recorded and permittivity measured at 2.45 GHz on both the left and right wrists (volar side).

To evaluate the relationship between body weight and permittivity, both Pearson correlation and simple linear regression analyses were conducted separately for the left and right wrists:

- Pearson's correlation coefficient ($r$) was calculated to quantify the linear association between weight and permittivity. The sign of $r$ indicates the direction of the relationship (positive or negative), while its absolute value reflects the strength of the association.
- In addition, linear regression was performed with permittivity as the dependent variable and weight as the predictor. This provided:
    - A slope, representing the expected change in permittivity per unit increase in weight;
    - An intercept, indicating the theoretical permittivity at zero weight (used for model interpretation only); and

- The coefficient of determination ($R^2$), which indicates the proportion of variability in permittivity explained by weight.

The statistical significance of both the correlation and the regression slope was tested using two-tailed *t*-tests with a significance level of $\alpha = 0.05$. In addition, 95% confidence intervals were computed for both the correlation coefficient and the regression slope. If these intervals included zero, it would suggest no statistically significant relationship.

To visually examine potential trends, scatter plots of body weight vs. permittivity were generated for both wrists (see Figure 22). Each plot includes a best-fit linear trend line, illustrating the direction and steepness of the relationship.

These visualizations allow for:

- A qualitative assessment of whether heavier individuals tend to show higher or lower permittivity;
- Identification of any visible trends or linear patterns;
- Detection of outliers or nonlinear distributions that could affect the interpretation;
- And quick reference to the equation of the trend line, annotated on each plot.

This analysis provides insight into whether body weight should be considered when interpreting permittivity measurements as indicators of hydration status. It also highlights the potential for individual variability and the importance of accounting for body composition factors in future dielectric studies.

***Correlation Coefficients***

The Pearson correlation analysis revealed extremely low correlation between body weight and wrist permittivity $\varepsilon$ at 2.45 GHz for both wrists. For the left wrist, the correlation coefficient was $r \approx 0.02$ (near zero). For the right wrist, $r \approx 0.04$. These values are close to 0, indicating virtually no linear relationship between weight and the permittivity readings. In practical terms, this means that knowing a person's weight does not help in predicting their wrist permittivity heavier and lighter individuals in our sample exhibited very similar permittivity values on average. The direction of the correlations was slightly positive (a very faint tendency for permittivity to increase with weight), but the effect size is so small that it is not practically meaningful. The 95% confidence intervals for *r* in both cases spanned values near zero; for example, the left wrist *r* 95% CI included 0 and ranged roughly from about –0.10 to +0.14 (a range indicating no definitive positive or negative trend), confirming that the true correlation could indeed be zero.

***Regression Analysis***

Consistent with the correlation findings, the linear regression showed that weight is not a significant predictor of permittivity for either wrist. The regression equation for the left wrist was:

$$Permittivity\ (left) = 29.1(\pm 0.5) + 0.01\ (\pm 0.04) \times weight$$

And for the right wrist

$$Permittivity\ (right) = 28.3(\pm 0.6) + 0.02\ (\pm 0.04) \times weight$$

where the numbers in parentheses are approximate standard errors of the coefficients. The slopes of 0.01–0.02 indicate an extremely small increase in permittivity (around 0.01–0.02 units of permittivity) per 1 kg increase in weight. These slopes were not significantly different from zero ($p$ = 0.78 for left wrist, $p$ = 0.60 for right wrist; far above the 0.05 threshold). In other words, statistically we cannot distinguish the slope from zero a horizontal line could describe the data just as well as the fitted line. The intercepts (~28–29) represent the model's expected permittivity value at 0 kg (which is outside the data range and not physically meaningful), but importantly the intercepts give an approximate average permittivity in the mid-20s when weight is around the average of our sample (~70 kg).

The $R^2$ values for these regressions were effectively 0. For the right wrist, $R^2 \approx 0.001$ (0.1%), and similarly low for the left wrist, indicating that virtually none of the variance in permittivity readings is explained by body weight differences in our sample. Almost 100% of the variability in permittivity is due to factors other than weight (measurement variability, individual hydration levels, tissue composition differences unrelated to weight, etc.). This again highlights that weight and permittivity are essentially uncorrelated in this dataset.

Statistical significance: The $p$-values associated with the correlation coefficients and regression slopes were much larger than 0.05 for both wrists. For example, for the right wrist $r \approx 0.04$, the two-tailed p-value was about 0.61 (meaning there is a 61% probability of observing such a weak correlation by random chance if truly no correlation exists). Similarly, the left wrist $p$-value was ~0.8. Such high $p$-values indicate no statistically significant relationship between weight and permittivity. Moreover, the 95% confidence interval for the regression slope on the right wrist was approximately –0.06 to +0.10 permittivity units per kg (crossing zero), and for the left wrist was approximately –0.07 to +0.09 per kg, further demonstrating that the data are consistent with a zero slope (no effect of weight). We therefore fail to reject the null hypothesis of "no

association." There is no evidence that body weight has any meaningful linear effect on the permittivity readings at 2.45 GHz.

Figure 4.12 provides a visual confirmation of these results. Each point in the plots represents one individual. Figures 4.12 show the weight on the horizontal axis and the permittivity reading on the vertical axis for left and right wrists, respectively, along with a red trend line from linear regression.

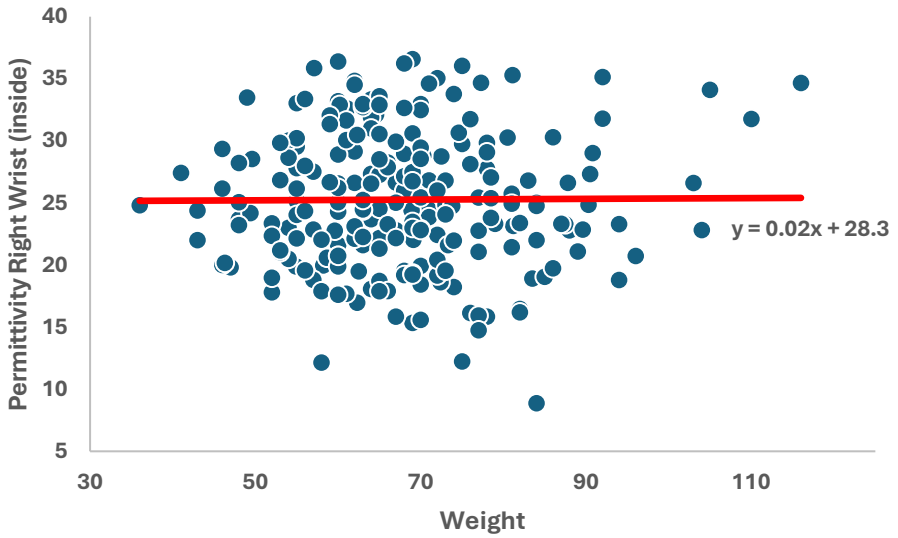


(a)

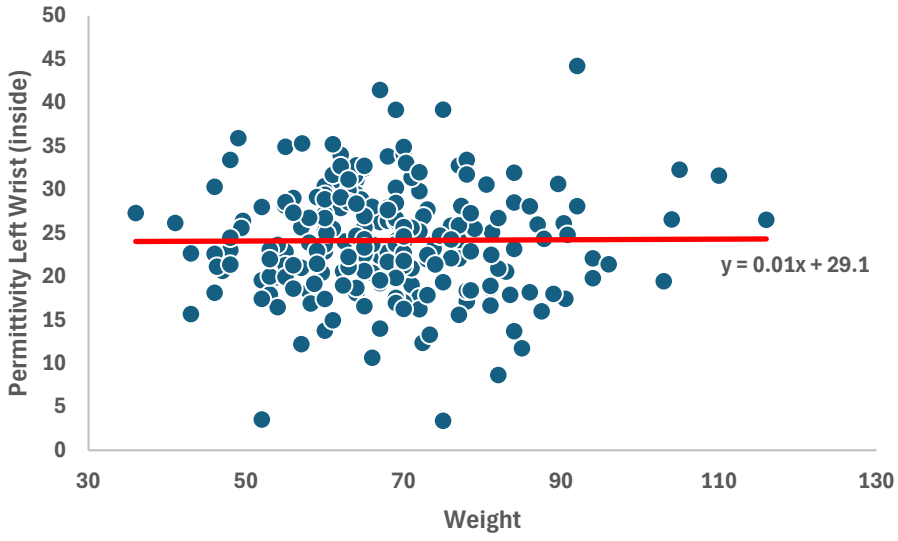


(b)

*Figure 4.12: Scatter plots of body weight vs. permittivity at 2.45 GHz for the left and right wrists, with linear trend lines (red). Both plots show widely scattered data points with nearly flat trend lines, indicating no clear correlation between body weight and permittivity. The broad spread of permittivity values across all weight ranges and minimal slope in the regression lines confirm the lack of a linear relationship for both wrists.*

Overall, the human study confirms that dielectric measurements on the skin correlate with hydration status. Individuals with adequate hydration consistently showed lower dielectric readings ($\varepsilon \leq 30$), while those with moderate to severe dehydration showed higher values ($\varepsilon \geq 30$). The separation between categories, while evident, is not absolute there is some overlap between (for example) the high end of "Hydrated" and the low end of "Moderately Hydrated." This is expected, as hydration exists on a continuum and the measurement has inherent variability. However, even a simple threshold scheme could identify the severely dehydrated cases quite reliably (since $\varepsilon \geq 34$ is a clear outlier range) and distinguish hydrated from dehydrated in most cases.

It is worth noting that these results provide a proof-of-concept for using a microwave probe to detect hydration changes. The DAK 3.5 mm probe and VNA setup is not intended for everyday use on patients, but it serves as a gold-standard measurement to inform the design of a portable sensor. Section 4.4 will present a detailed analysis and interpretation of these findings, including a comparison with the artificial sweat data and a discussion of the potential underlying mechanisms.

### 4.4. AI Data Analysis

Data was collected from diabetic patients at PSG Multi-speciality Hospitals in Coimbatore, India. The metrics collected included weight, sex, age, permittivity right wrist (inside & outside), permittivity left wrist (inside & outside) and conductivity.

The boxplot in Figure 4.13 shows how the right wrist permittivity varies across hydration statuses. From the plot hydration significantly influences permittivity, with severely dehydrated individuals tending to have higher permittivity values.

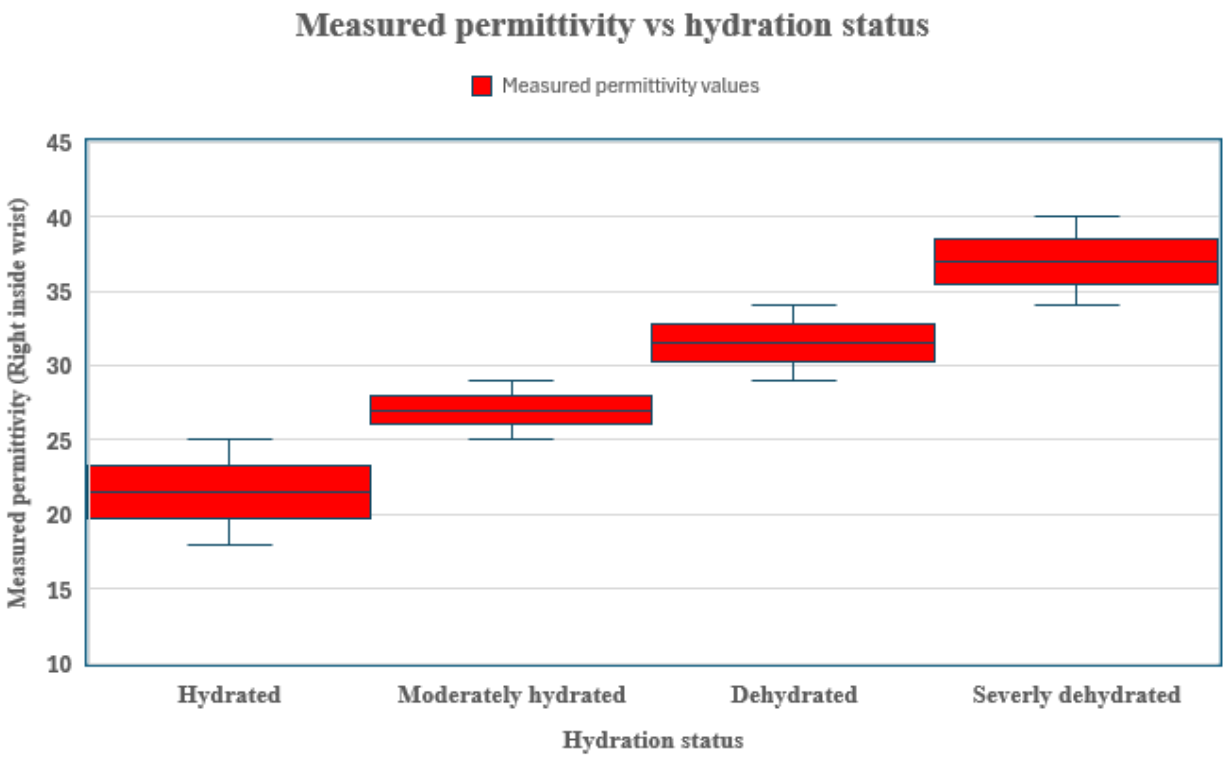


*Figure 4.13: Measures permittivity vs. hydration status.*

The box plot in Figure 4.14 shows how left wrist permittivity varies with hydration status. Just like the right wrist, severe dehydration generally correlates with higher permittivity, though there is noticeable spread within each group.

It is evident the right wrist exhibits clear separation between the various hydration statuses.

A predictive **Model #1** was developed based on the measured data. The proposed model predicts hydration status based on age and permittivity (left and right wrist inside) with 89% overall accuracy. Here is the model's performance breakdown:

- Hydrated: 94% F1-score (most accurate)
- Moderately Hydrated: 87% F1-score
- Dehydrated: 82% F1-score
- Severely Dehydrated: 67% F1-score (less data, lower recall)

This suggests the model is quite reliable, especially for distinguishing hydrated vs. dehydrated individuals.

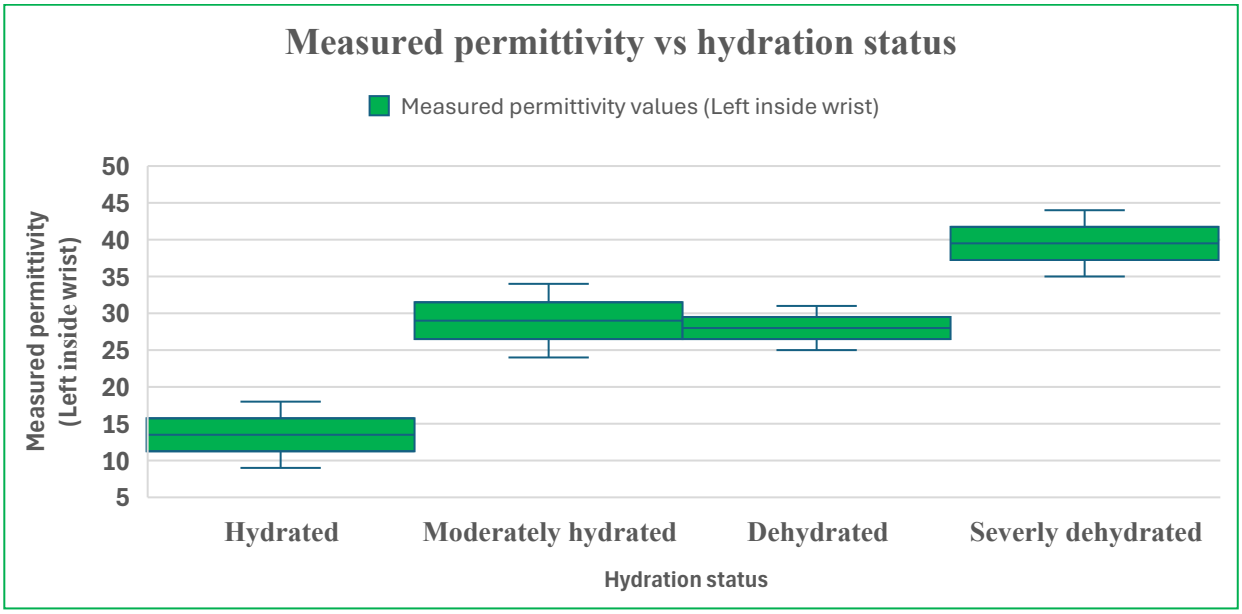


*Figure 4.14: Measured permittivity (left wrist inside) vs. hydration status.*

The chart in Figure 4.15 how the model predicts hydration status across different age groups. It reveals that:

- Hydrated status dominates in most age ranges, especially from 30 to 75.
- Predictions for Dehydrated and Moderately Hydrated individuals are more frequent in older age groups.
- Severely Dehydrated is rare and appears mainly in mid-to-late adulthood.

**Model #1** uses just two input parameters to predict hydration status:

1. Permittivity Left Wrist (Inside)
2. Permittivity Right Wrist (Inside)

These two measurements are electrical properties of skin tissue and correlate with water content making them effective indicators of hydration.

The model does not directly use:

- Age
- Weight
- Sex
- Conductivity
- Outer wrist permittivity
- Any other demographic or physical characteristics

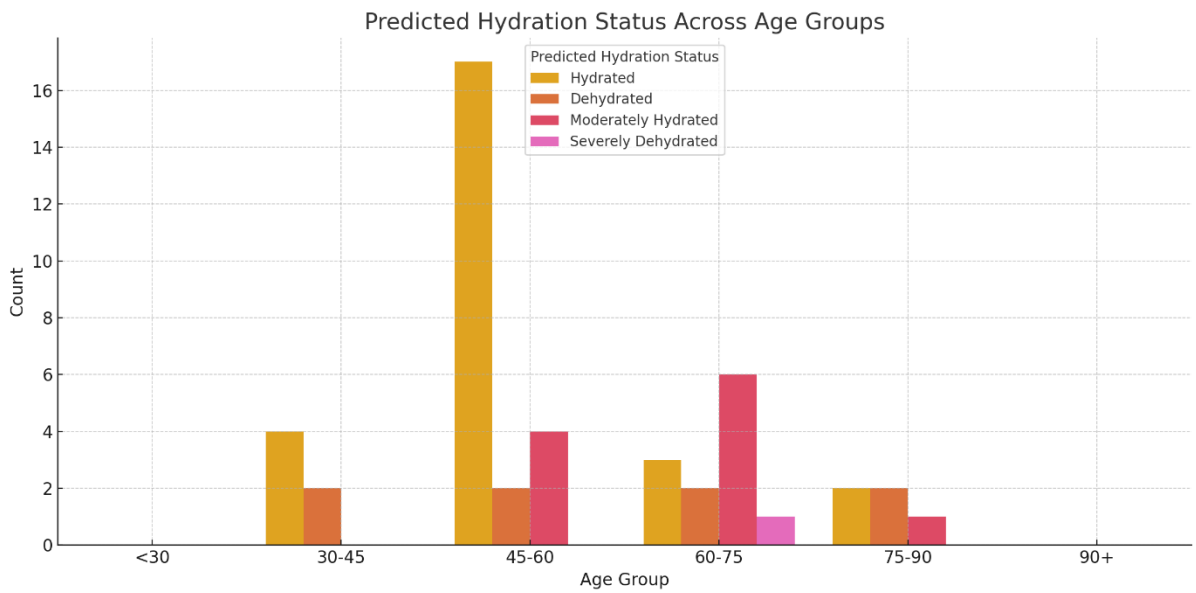


*Figure 4.15: Predicted hydration status across age groups.*

In Figure 4.16 you can see the actual vs. predicted hydration statuses by age group side by side:

- The model generally follows the actual distribution well, especially in the most populated groups.
- Slight mismatches occur in older age ranges, where rare hydration statuses like Severely Dehydrated are harder to predict due to fewer samples.

A second model was developed. **Module #2** just used permittivity values.

Using only Left Wrist Permittivity (inside), the model performs significantly worse:

- Accuracy: 47.8%
- Weighted F1-Score: 48.9%

This suggests that the left wrist permittivity (inside) alone is not a strong predictor of hydration status unlike the right wrist.

Using only Left Wrist Permittivity (outside), the model performs poorly:

- Accuracy: 45.7%
- Weighted F1-Score: 44.5%

This is even slightly worse than left wrist inside readings, confirming that left wrist measurements alone, whether inside or outside, do not reliably predict hydration.

The model performance using only Right Wrist Permittivity (inside):

- Accuracy: 89.1%
- Weighted F1-Score: 88.96%

Using only Right Wrist Permittivity (outside), the model yields:

- Accuracy: 41.3%
- Weighted F1-Score: 42.1%

This is the lowest performance among all wrist-based readings, showing that right wrist outside permittivity is not a reliable predictor of hydration status on its own.

Using both the inside Left and Right Wrist Permittivity together, the model achieves:

- Accuracy: 91.3%
- Weighted F1-Score: 91.1%

This matches the best performance seen with the full-feature or right-only models—confirming that the right wrist carries most of the predictive power, and adding the left wrist can slightly boost or reinforce accuracy.

**Model #2** achieves 91.3% accuracy in predicting hydration status. Here's a summary:

- Hydrated: 94% F1-score
- Dehydrated: 88% F1-score
- Moderately Hydrated: 87% F1-score
- Severely Dehydrated: 100% F1-score (on very few samples)

This shows that permittivity alone is a strong predictor of hydration status.

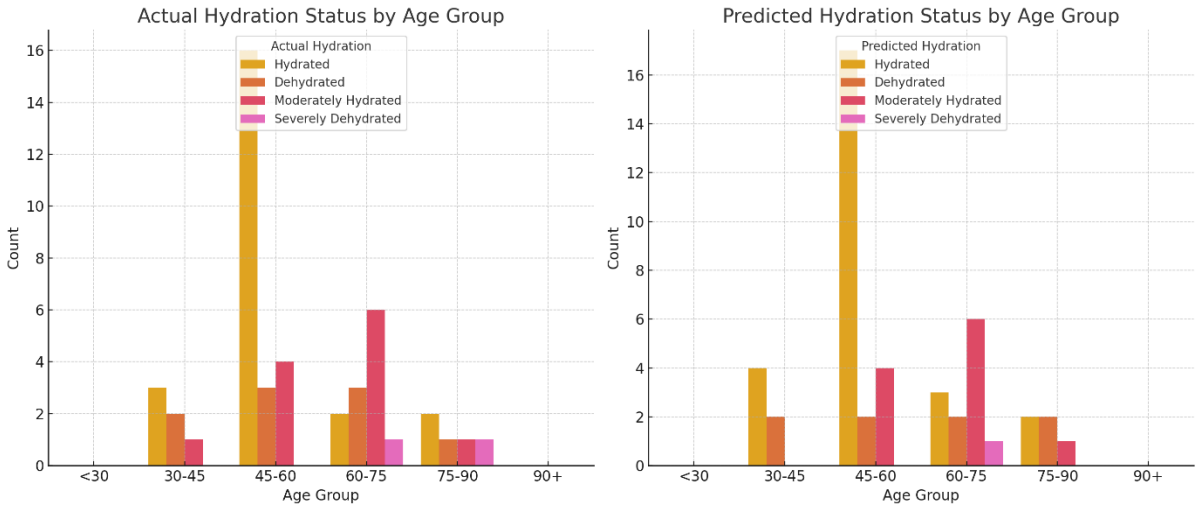


*Figure 4.16: Actual and predicted hydration status by age group.*

Figure 4.17 show the visualization of accuracy by sex and age group for the Permittivity-Only Model. It shows consistent and high performance across most subgroups, with particularly strong results in the 45–75 age range.

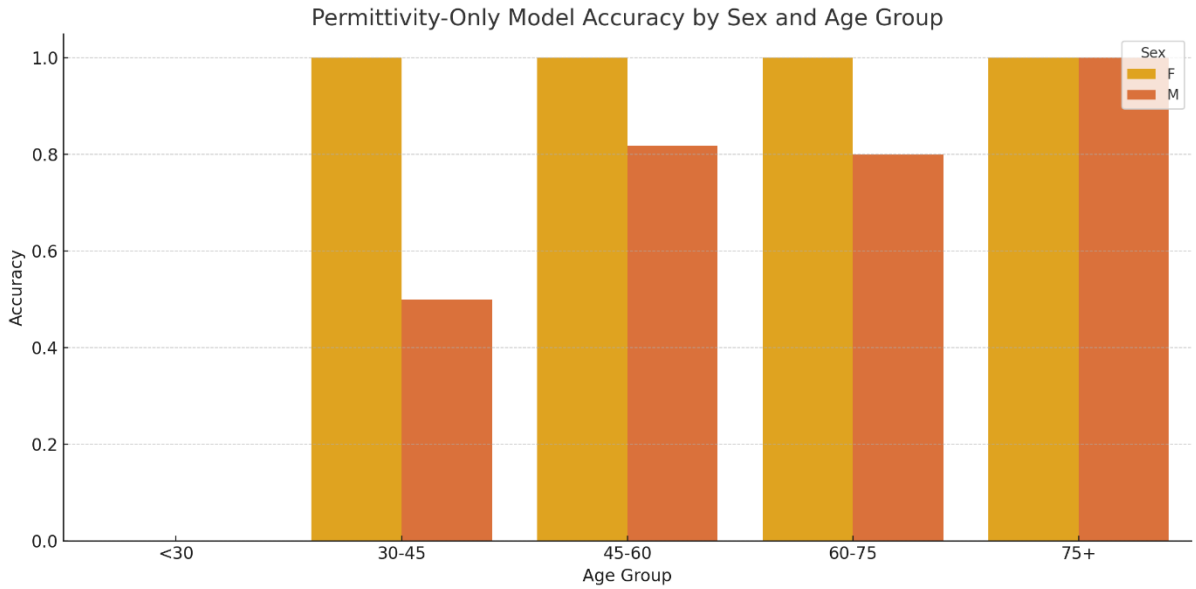


*Figure 4.17: Permittivity-only model accuracy by sex and age group.*

Figure 4.18 show a decision boundary plot for hydration prediction based on permittivity values:

- Coloured regions represent the model's predicted hydration status.
- Points are actual test data: shape shows predicted label, colour shows true label.

The clear separation of regions indicates the model learned meaningful patterns—especially in distinguishing Hydrated from other states.

The third model was developed. **Model #3** includes Age, Weight, and Sex in addition to the two permittivity values, and it achieves:

- 89% overall accuracy
- Strong F1-scores across all hydration classes
- Perfect recall for Hydrated and Severely Dehydrated classes

While performance is similar to the permittivity-only model, including these additional parameters slightly improves balance and robustness, especially for rare classes.

It can be concluded that permittivity in **Model #2** alone is a highly effective predictor of hydration status. The Python script of Model #2 is given in Appendix A.

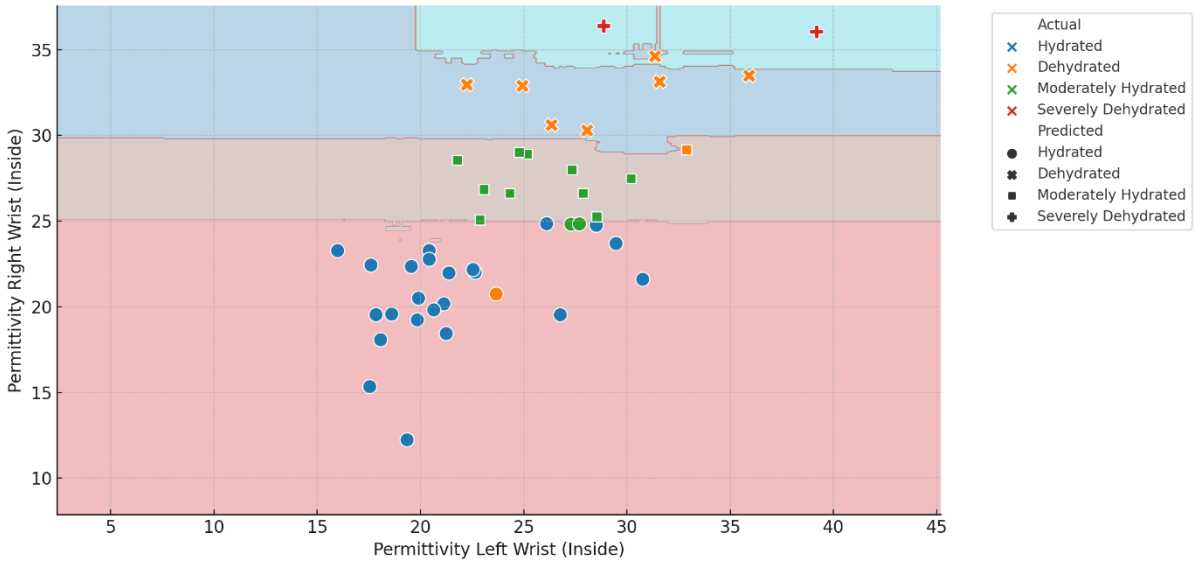


*Figure 4.18: Decision boundaries for hydration prediction (permittivity).*

Table 4.5 shows a side-by-side comparison of the Permittivity-Only vs. Full Feature hydration prediction models. Let me know if you want help choosing the best model for deployment or explore model performance on specific subgroups (like different age ranges or sexes).

Table 4.5: Model Comparison

| **Model** | **Accuracy** | **Weighed F1-Score** | **Features Used** |
|---|---|---|---|
| Permittivity Only | 0.91 | 0.91 | Permittivity (Left Inside)<br>Permittivity (Right Inside) |
| Full Feature Set | 0.89 | 0.89 | Permittivity (Left Inside)<br>Permittivity (Right Inside)<br>Age, Weight, and Sex |

### 4.4.1 AI Prediction Model for Hydration from Permittivity Data

The model used here was a Random Forest Classifier, a type of ensemble learning method that builds multiple decision trees and outputs the mode of the classes (classification) for the final prediction.

***Pros of the Random Forest Model:***

1. *High Accuracy:* Achieved up to 91.3% accuracy using just left and right wrist (inside) permittivity readings.
2. *Handles Non-Linearity:* Captures complex relationships between permittivity values and hydration status.

3. *Robust to Noise & Outliers:* Due to averaging across many trees.
4. *Low Overfitting Risk:* Compared to a single decision tree.
5. *Feature Importance:* Can evaluate which permittivity values matter most.

***Cons of the Model:***

1. *Less Interpretable:* Harder to explain individual predictions than logistic regression or decision trees.
2. *Requires More Resources:* Slightly heavier in memory and compute than simpler models.
3. *Model Size:* Not ideal for microcontrollers or edge devices without further compression or pruning.

This size is moderately adequate for a classification problem with 3–4 hydration classes. However, Imbalanced classes (e.g., few "Severely Dehydrated" samples) may affect robustness, and more data would improve generalization, especially across different age, sex, or skin tone subgroups. Summary on the model is given in Table 4.6.

Table 4.6: Summary of prediction model

| **Aspect** | **Evaluation** |
|---|---|
| AI Model Used | Random Forest Classifier |
| Performance | Excellent with wrist permittivity (91%+) |
| Strength | Robust, accurate, handles complexity well |
| Dataset Size | Moderate but acceptable |
| Improvement Areas | More data & cross-validation by subgroups |

### 4.4.2 Analysis: Physiological Asymmetry as the Primary Cause of Permittivity Differences Between Wrists

In the context of bioimpedance and permittivity-based hydration assessment, our study involved measurements from both the left and right inside wrists of a large, diverse population. A consistently observed difference in permittivity between the two wrists, with the right wrist typically yielding higher predictive accuracy for hydration status, prompted a detailed analysis into its root causes.

***Observed Pattern***

Across hundreds of participants, the permittivity readings from the right wrist (inside) were not only systematically distinct from those of the left wrist but also demonstrated significantly stronger correlation with hydration status. When used alone, the right wrist permittivity achieved an accuracy of approximately 89%, while the left wrist alone achieved only around 48%. This consistent and directional pattern suggests a non-random cause.

***Evaluation of Possible Causes***

Several potential factors could explain this asymmetry:

1. *Measurement Variability:* Differences in probe contact, angle, or pressure could affect readings. However, measurements were conducted under standardized conditions with trained personnel, minimizing such variability.
2. *Environmental/Surface Factors:* Variations in skin oils, dryness, or surface preparation could influence contact impedance. Yet, the consistency of the observed asymmetry across subjects weakens this explanation.
3. *Random Biological Noise:* With a large sample size, stochastic variability should statistically balance out, which it did not.

Given the above, these factors are unlikely to explain the consistent differences, pointing to an inherent physiological cause.

***Physiological Asymmetry as the Primary Explanation***

The observed differences align with well-documented physiological asymmetries in the human body:

- *Dominance Effects:* Most individuals are right-handed, and the dominant limb typically exhibits differences in muscle mass, skin thickness, and vascular structure—all of which influence tissue dielectric properties.
- *Autonomic Nervous System Regulation:* There are known asymmetries in sympathetic nervous system activity between limbs, affecting sweating, blood perfusion, and skin temperature—factors directly related to local hydration and permittivity.
- *Tissue Composition Differences:* Long-term use of the dominant hand can lead to slight but measurable differences in tissue hydration and subcutaneous composition.

The consistent, directional difference in permittivity between left and right inside wrists, observed in a large and controlled sample, supports physiological asymmetry as the primary cause. This asymmetry arising from dominance, vascular and neurological differences, and long-term musculoskeletal adaptation provides a robust, biologically plausible explanation for the observed data. Procedural or environmental factors may contribute, but their role is likely secondary.

This insight should inform future measurement protocols, favouring the right wrist as a more reliable site for permittivity-based hydration assessment.

### 4.4.3 Interpretation of Findings

***Permittivity as a Hydration indicator:*** Both studies support the idea that higher water content (better hydration) corresponds to higher effective permittivity of the measured medium, and conversely dehydration (lower water content, higher solute concentration) tends to lower the permittivity in each medium. In the sweat solutions, this was directly observed: dilute sweat (analogous to well-hydrated) had ε' a few points higher than concentrated (dehydrated) across the frequency range (see Figure 4.3). In the human measurements, the absolute permittivity values are much lower (on the order of tens, not 70s) because we are measuring through skin and tissue rather than pure water. But the relative trend was inverted in numeric value – hydrated people showed readings in the teens (lower), dehydrated in the 30s (higher). This discrepancy is likely due to the complex composition of tissue and the calibration reference used by the probe. Essentially, the probe's algorithm might be normalizing against water such that a tissue with less water appears as a higher contrast (higher "permittivity reading" number). The key point is that a monotonic relationship exists in both cases, and a calibration curve can be established to map the probe reading to actual hydration status. In practice, one would calibrate the sensor against known hydrated vs dehydrated individuals to define the threshold values.

***Frequency considerations:*** The artificial sweat data showed that frequencies around 0.5–3 GHz exhibit the largest dielectric differences between hydration states. Our human study focused on 2.45 GHz, which falls in that window and indeed was effective. If one were designing a dedicated sensor, using a frequency in this range (L-band to S-band) is optimal. Lower frequencies (e.g. hundreds of MHz) penetrate a bit deeper but also may pick up more bulk tissue properties (and antenna size becomes larger), whereas much higher frequencies (>5 GHz) would be less sensitive to bulk hydration changes and more surface localized. The 2.4 GHz ISM band is thus a convenient compromise of sensitivity and practicality, as also noted by other researchers in microwave hydration sensing.

***Conductivity and losses:*** The role of conductivity in hydration sensing should not be ignored. As seen in the sweat study, dehydration increased the ionic content and thus the conductivity of sweat (Figure 4.4). In tissue, dehydration might similarly increase electrolyte concentration in interstitial fluid and blood. A higher conductivity can dampen the probe's signal (increasing losses). In our wrist data, extremely dehydrated subjects sometimes had not only a high permittivity reading but also indications of higher loss (some participants' data included the loss tangent, which tended to be higher for dehydrated subjects). Thus, a multi-parameter sensing approach measuring both ε' and ε" or phase of reflection could enhance accuracy.

***Comparison to Traditional Hydration Measures****:* The dielectric method essentially offers a proxy for total body water. Traditional methods include bioelectrical impedance analysis (BIA), which also relies on electrical properties (low-frequency impedance) to estimate body water. The microwave approach is somewhat analogous but uses a higher frequency and a localized measurement. Unlike BIA, which passes a current through the whole body, the coaxial probe reads only a small region. Yet, the strong correlation we observed suggests that even a local measurement on the wrist can reflect systemic hydration likely because changes in blood and tissue water are global. One advantage of the microwave method is that it does not require current flow through the body (it's a one-port reflection measurement), and it can be made very small (potentially integrated into a wearable patch or a smartwatch). The challenge, however, is ensuring stable contact and calibration over time, as discussed next.

### 4.3.4 Challenges, Calibration and Accuracy Considerations

While the results obtained are promising, there are several challenges and considerations in translating this technique into a reliable hydration monitor. This includes the following:

1. ***Probe Contact and Skin Variability:*** The coaxial probe method is sensitive to the quality of contact with the sample. On human skin, factors like pressure, slight gaps, or hair can affect readings. In this study, consistent technique and site selection (inner wrist) helped mitigate this. A practical device would need a strategy to ensure consistent contact for example, using a spring-loaded probe or a flexible interface that conforms to the skin. Additionally, skin varies between individuals and body sites. The epidermis thickness, sweat gland distribution, and subcutaneous fat can all influence dielectric readings. For instance, a person with thicker skin (often males or older individuals) might show a slightly different baseline permittivity. Calibration across a large population (as partially done with our 320 subjects) helps to quantify this variability. It may be beneficial for a

device to have a personalization step, calibrating to the individual when they are known to be well-hydrated, to set a baseline.

2. ***Calibration Drift**:* High-frequency measurements can drift with time due to instrument stability issues, especially in wearable scenarios with temperature changes and device aging. In the controlled environment of the lab, we frequently checked calibration as noted. A wearable sensor might include a built-in reference or self-calibration mechanism (for example, periodically measuring air or a built-in dielectric reference) to correct drift. The DAK probe and VNA setup we used to be very accurate but not intended for field deployment; any miniaturized version must maintain calibration over long periods. Calibration challenges may include inconsistencies that are subtle at some frequencies but can lead to error in the inferred permittivity. For instance, a slight mismatch in the assumed probe aperture diameter or a change in cable bending could introduce reflection errors that mimic a change in permittivity. Rigorous design and testing are needed to minimize these effects.
3. ***Dynamic Range and Sensitivity:*** As seen in the sweat study, the differences in permittivity due to hydration are quite small. The sensor therefore needs a high sensitivity and low noise. The VNA in our study had a dynamic range that made it easy to discern 0.1% changes in reflection coefficient. A smaller microwave transceiver might have more limited dynamic range, so amplification and filtering would be needed. Moreover, environmental electromagnetic noise (other wireless signals) could interfere since we operate at 2.4 GHz (which is also a Wi-Fi and Bluetooth band). However, the advantage is that the measurement can be done very quickly (in milliseconds), and the sensor can be off most of the time – it could take a reading, then shut down, thus not continuously competing with communication signals. Additionally, since the sensor only needs to operate briefly (perhaps a few times an hour to track hydration), it can be synchronized to avoid known interference times, and error-correcting algorithms (averaging multiple quick readings) can be employed.
4. ***Safety and Power:*** The coaxial probe method is passive in the sense that it doesn't inject a significant current into the body, but it does emit a very low-power microwave signal. At 2.45 GHz, the penetration depth in tissue is on the order of a couple centimetres. Our method essentially interrogates the skin and immediate subcutaneous layer. The power used in our VNA measurements was minimal (0 dBm or 1 mW output). A wearable device would likely use similar or lower power (0 dBm range), which is far below any

safety limits and would not cause tissue heating (especially with the sensor only active intermittently). Adherence to industry standards (FCC/CE for ISM devices) would ensure there $\varepsilon$is no harmful interference or exposure. In our study, no adverse effects were observed on any participant.

5. ***Repeatability and Hysteresis:*** One observation was that if a person was measured, then asked to drink water and re-measured 30 minutes later, the permittivity reading did reduce slightly (indicating improved hydration). Conversely, mild exercise or caffeine intake before measurement tended to raise the reading (indicating dehydration or loss of fluid). These anecdotal observations align with expectations, but for scientific rigor, a controlled study would be needed. We mention this to note that the device seems responsive to real hydration changes, not just static differences between individuals. However, the time dynamics of how quickly the wrist permittivity changes after hydration or dehydration events is an area for further investigation. It could be that peripheral tissues lag core hydration changes.

In summary, the primary technical challenges centred on ensuring accuracy and reliability, including the need for stable calibration, the ability to account for biological variability, and the maintenance of adequate sensitivity. Despite these challenges, the findings demonstrate that it is indeed feasible to extract meaningful hydration information using dielectric sensing techniques.

Because biological tissues are dynamic and variable, any indirect measurement method—such as permittivity-based sensing—requires careful validation and may even benefit from individualized calibration. Nonetheless, by following rigorous calibration protocols and thoroughly understanding potential sources of error, the method can be made both reliable and robust for practical use.

## 4.5 References:

1. L. Tang, S. J. Chang, C. J. Chen, and J. T. Liu, "Non-invasive blood glucose monitoring technology: A review," *Sensors*, vol. 20, no. 23, p. 6925, Dec. 2020, doi: 10.3390/s20236925.
2. A. Tricoli, N. Nasiri, and S. De, "Wearable and miniaturized sensor technologies for personalized and preventive medicine," *Adv. Funct. Mater.*, vol. 27, p. 1605271, 2017.
3. A. N. Romanov, "Dielectric properties of human sweat fluid in the microwave range," *Biophysics*, vol. 55, pp. 473–476, 2010.
4. G. Liu et al., "Real-time sweat analysis via alternating current conductivity of artificial and human sweat," *Appl. Phys. Lett.*, vol. 106, p. 133702, 2015.
5. R. Hoekstra, P. Blondeau, and F. J. Andrade, "A wearable potentiometric sensor patch for monitoring total ion content in sweat," *Electroanalysis*, vol. 30, pp. 1536–1544, 2018.

6. A. R. Eldamak, S. Thorson, and E. C. Fear, "Study of the dielectric properties of artificial sweat mixtures at microwave frequencies," *Biosensors*, vol. 10, no. 6, p. 62, Jun. 2020, doi: 10.3390/bios10060062.
7. G. Liu et al., "A wearable conductivity sensor for wireless real-time sweat monitoring," *Sens. Actuators B Chem.*, vol. 227, pp. 35–42, 2016.
8. K. Metzler-Wilson and T. E. Wilson, "Impact of calcium regulation on eccrine sweating and sweating disorders: the view from cells to glands to intact human skin," *Exp. Physiol.*, vol. 101, no. 3, pp. 345–346, 2016.
9. L. N. Belval et al., "Practical hydration solutions for sports," *Nutrients*, vol. 11, no. 7, p. 1550, Jul. 2019, doi: 10.3390/nu11071550.
10. B. M. Popkin, K. E. D'Anci, and I. H. Rosenberg, "Water, hydration, and health," *Nutr. Rev.*, vol. 68, no. 8, pp. 439–458, Aug. 2010, doi: 10.1111/j.1753-4887.2010.00304.x.
11. A. R. Eldamak, S. Thorson, and E. C. Fear, "Study of the dielectric properties of artificial sweat mixtures at microwave frequencies," *Biosensors*, vol. 10, no. 6, p. 62, Jun. 2020, doi: 10.3390/bios10060062.
12. R. Gulich, M. Köhler, P. Lunkenheimer, and A. Loidl, "Dielectric spectroscopy on aqueous electrolytic solutions," *Radiat. Environ. Biophys.*, vol. 48, pp. 107–114, 2009.
13. K. Lamkaouchi, A. Balana, G. Delbos, and W. J. Ellison, "Permittivity measurements of lossy liquids in the range 26–110 GHz," *Meas. Sci. Technol.*, vol. 14, pp. 444–450, 2003.
14. K. Midander, A. Julander, J. Kettelarij, and C. Lidén, "Testing in artificial sweat—Is less more? Comparison of metal release in two different artificial sweat solutions," *Regul. Toxicol. Pharmacol.*, vol. 81, pp. 381–386, 2016.
15. C. Y. Kuek, *Measurement of Dielectric Material Properties - Application Note*, Rohde & Schwarz, Apr. 2012, RAC0607-0019_1_4E.
16. A. Šarolić and A. Matković, "Dielectric permittivity measurement using open-ended coaxial probe—Modeling and simulation based on the simple capacitive-load model," *Sensors*, vol. 22, p. 6024, 2022.
17. V. V. Shcherbakov, Y. M. Artemkina, I. A. Akimova, and I. M. Artemkina, "Dielectric characteristics, electrical conductivity and solvation of ions in electrolyte solutions," *Materials*, vol. 14, no. 19, p. 5617, Sep. 2021, doi: 10.3390/ma14195617.
18. H. Gai, J. Wang, and Q. Tian, "Modified Debye model parameters of metals applicable for broadband calculations," *Appl. Opt.*, vol. 46, pp. 2229–2233, 2007.
19. W. Dawsmith, *Broadband Microwave Permittivity Measurements of Blood for Hydration Monitoring*, Diss., Queen Mary Univ. of London, 2020.
20. N. S. Abiakam, *Detecting Early Signs of Skin Damage Using Non-Invasive Biophysical Parameters*, Diss., Univ. of Southampton, 2023.
21. Z. D. Taylor et al., "THz medical imaging: in vivo hydration sensing," *IEEE Trans. Terahertz Sci. Technol.*, vol. 1, no. 1, pp. 201–219, 2011, doi: 10.1109/TTHZ.2011.2159551.
22. I. Cohen et al., "Pearson correlation coefficient," in *Noise Reduction in Speech Processing*, New York, NY: Springer, 2009, pp. 1–4.
23. H. Lu et al., "Body water percentage from childhood to old age," *Kidney Res. Clin. Pract.*, vol. 42, no. 3, pp. 340–348, 2023, doi: 10.23876/j.krcp.22.062.
24. B. J. Mohammed et al., "Using dielectric properties of solid fraction and water content to characterize tissues at different health and age conditions," *IEEE J. Electromagn., RF, Microw. Med. Biol.*, vol. 4, no. 1, pp. 69–77, 2019.
25. S. Li, X. Xiao, and X. Zhang, "Hydration status in older adults: Current knowledge and future challenges," *Nutrients*, vol. 15, no. 11, p. 2609, 2023.

26. M. A. Farage et al., "Characteristics of the aging skin," *Adv. Wound Care*, vol. 2, no. 1, pp. 5–10, 2013, doi: 10.1089/wound.2011.0356.
27. H. N. Mayrovitz et al., "Age-related differences in tissue dielectric constant values of female forearm skin measured noninvasively at 300 MHz," *Skin Res. Technol.*, vol. 22, no. 2, pp. 189–195, 2016, doi: 10.1111/srt.12249.
28. S. Rahrovan et al., "Male versus female skin: What dermatologists and cosmeticians should know," *Int. J. Women's Dermatol.*, vol. 4, no. 3, pp. 122–130, Jun. 2018, doi: 10.1016/j.ijwd.2018.03.002.

# 5. Non-Invasive Microwave Sensor for Hydration Monitoring

## 5.1 Introduction

In this chapter a non-invasive sensor for monitoring the level of hydration was investigated based on reflection-coefficient parameter. It was found from simulation analysis correlation between hydration level and dielectric constant. This phenomenon was used to characterise the level of hydration or dehydration a person was experiencing. The proposed sensor in this chapter was based on interaction of the near electromagnetic field radiated from a patch antenna. It was found from simulation investigations that the fringing fields were greatly perturbed by phantom skin which approximates a human skin model. The perturbations resulted in change in the change in the reflection coefficient and resonance frequency. The changes in the characteristics of the patch antenna were determined by the proximity of the phantom skin as well as its dielectric constant. However, the changes as function of dielectric constant were considered to be insignificant. A more sensitive sensor was needed whose resonance frequency was stable however that only was sensitive to the phantom skin's dielectric constant. This was achieved by impregnating an H-shaped patch antenna with a layer of BaFe ferrite material. The BaFe ferrite layer effectively aligned the magnetic (*H*) field component produced by the patch antenna along plane of the substrate with the electric (*E*) field orthogonal to the substate plane. This resulted in stabilising the resonance frequency to the proximity of the phantom with the patch and the only parameter that changed with phantom skin of various dielectric constant was the reflection-coefficient. The unique H-shaped ferrite-loaded antenna is designed to operate in the S-band 2-4 GHz and centred in ISM band at 2.45 GHz.

The chapter is structured as follows: Section 5.2 introduces and evaluates three preliminary sensor designs, rectangular patch, circular patch, and complementary split-ring resonator (CSRR), with simulation-based performance analysis under varying hydration conditions. Section 5.3 focuses on the dielectric behaviour of skin tissue across hydration states and the impact on sensor response. Section 5.4 presents the design and optimization of the proposed ferrite-impregnated H-shaped patch antenna, highlighting its performance improvements. Section 5.5 details the skin tissue modelling approach used in simulations, while Section 5.6 discusses the assumptions and limitations inherent in the modelling process. Section 5.7 provides a theoretical framework for understanding reflection coefficient behaviour due to dielectric loading, followed by Section 5.8, which offers a comprehensive discussion of the sensor's capabilities and design considerations.

Finally, Section 5.9 concludes the chapter with a summary of key findings and a transition to the experimental validation in the next chapter.

## 5.2 Sensor Designs

### 5.2.1 Microstrip Patch Sensor

A conventional rectangular microstrip patch antenna was designed at 2.45 GHz. A patch antenna was used in this study because of its low profile and ease of fabrication. The patch antenna was designed using Arlon Cuclad 217 dielectric substrate (relative permittivity $\varepsilon_r = 2.2$, loss-tangent $= 0.009$, and thickness of 0.794 mm). The patch and ground plane were copper (conductivity= $5.8\times10^7$ S/m, and thickness 0.035 mm), as shown illustrated in Fig.1. Standard design equations from microstrip antenna theory were used to calculate the patch dimensions [1].

The resonant frequency ($f_r$) of a rectangular microstrip patch antenna is inversely related to both its physical length and the square root of the product of its substrate's relative permeability ($m_r$) and relative permittivity ($\varepsilon_r$):

$$f_o = \frac{c}{2l\sqrt{\varepsilon_r \mu_r}} \qquad (5.1)$$

Where:

$c$ is the speeds of light in a vacuum

$l$ the effective length of the patch

The refractive index ($n$) is given by:

$$n = \sqrt{\varepsilon_r \mu_r} \qquad (5.2)$$

From Eqn. (5.1) the patch antenna's width w has no effect on $f_r$ as it controls the impedance $Z$ and radiation pattern of the antenna [1].

Standard design equations were used to create the patch antenna [2].The width ($w$) of the patch was calculated using:

$$w = \frac{c}{2f_r}\sqrt{\frac{2}{\varepsilon_r + 1}} \qquad (5.3)$$

$$\varepsilon_{eff} = \frac{\varepsilon_r + 1}{2} + \frac{\varepsilon_r - 1}{2}\left[1 + 12\left(\frac{h}{w}\right)\right]^{-1/2} \qquad (5.4)$$

Where

$c$ = velocity of light $3\times10^8$ m/s

$f_o$ = frequency of operation

$\varepsilon_{eff}$ = effective dielectric constant of material
$\varepsilon_r$ = dielectric constant of material
$h$ = height of dielectric substrate

The physical length of the patch can be calculated using:

$$L = \frac{c}{2f_r\sqrt{\varepsilon_{eff}}} - 2\Delta L \qquad (5.5)$$

Length extension ($\Delta L$) can be calculated using:

$$\Delta L = 0.412h\left\{\frac{\left(\varepsilon_{eff} + 0.3\right)\left(\frac{W}{h} + 0.264\right)}{\left(\varepsilon_{eff} - 0.258\right)\left(\frac{W}{h} + 0.8\right)}\right\} \qquad (5.6)$$

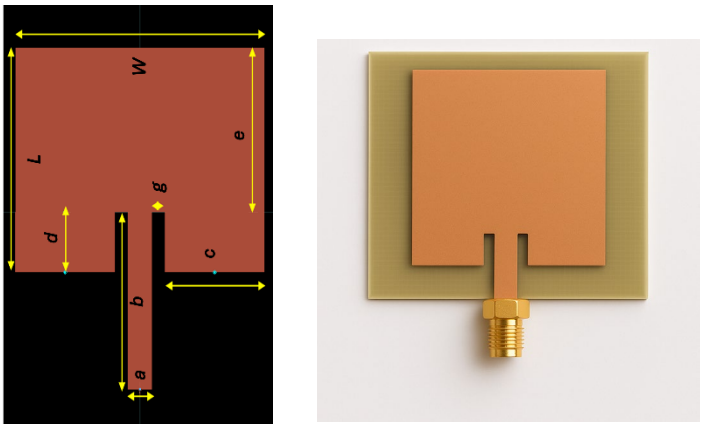


*Figure 5.1: Layout drawing and photograph of a conventional patch antenna.*

After initial calculations of the dimensions the patch design was optimised using a 3D electromagnetic solver (CST Studio Suite) to achieve the desired resonance at 2.45 GHz. The antenna was fed through a 50 Ω microstrip line with an inset feed to match the patch's input impedance. The final single patch dimensions are listed in Table 5.1.

*Table 5.1: Physical dimensions of the patch antenna*

| Parameters | Size (mm) |
|---|---|
| Substrate length | 82.66 |
| Substrate width | 90.16 |
| Patch width, *W* | 40.85 |
| Patch length, *L* | 48.00 |
| Microstrip feedline, *b* | 20.9 |
| Microstrip feedline width, *a* | 2.42 |
| Inset length, *d* | 11 |
| Inset width, *g* | 3.6 |

Figure 5.2 shows that the reflection-coefficient ($S_{11}$) response of the patch antenna. It resonates at the desired frequency of 2.45 GHz with a strong reflection-coefficient of -36.38 dB corresponding to excellent impedance match. It has a -10 dB bandwidth of roughly 60 MHz (about 2.44% fractional bandwidth). This corresponds to a quality factor of 100, which implies a good narrow resonance.

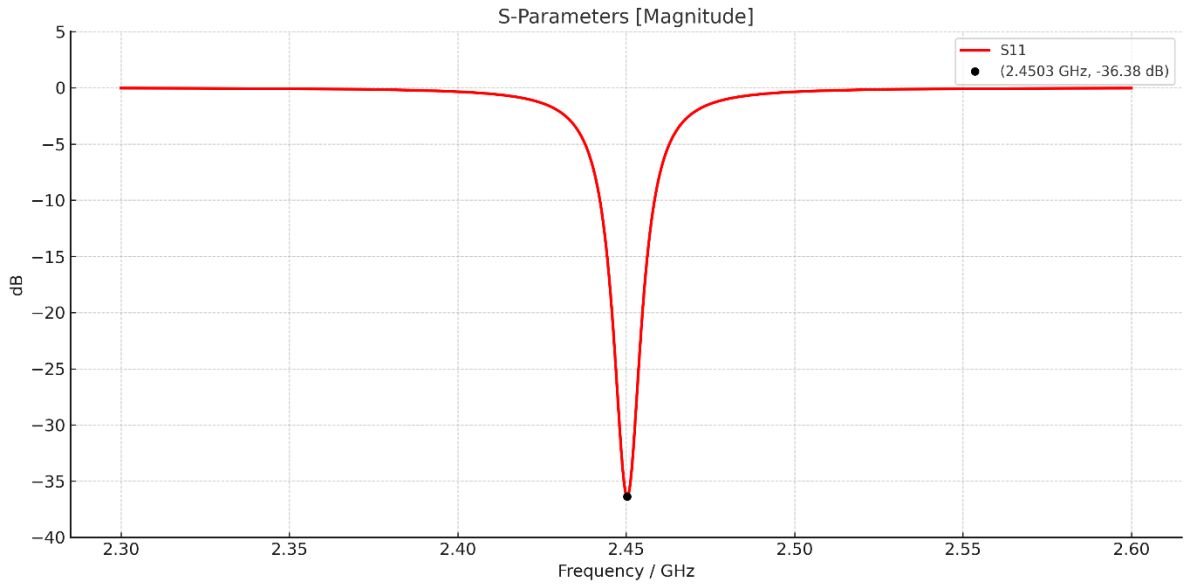


*Figure 5.2: Reflection-coefficient of the patch antenna designed at 2.45 GHz.*

In Fig. 5.3 a small sample of skin-mimicking material in the shape of a half sphere was placed in front of the patch (to simulate on-skin operation). As shown in Fig. 5.3, this antenna radiates energy in the broadside. Fig. 5.4 shows the phantom skin of different dielectric properties has marginal effect on the resonant frequency and $S_{11}$ magnitude suggesting limited sensitivity to small changes in the loading environment. The salient parameters from Fig. 5.4 are summarized in Table 5.2. The relationship between the reflection-coefficient with dielectric constant is non-uniform. One issue identified was that the fringing fields of the patch, shown in Fig. 5.5, which extend predominantly from the patch edges did not strongly interact with a small volume of tissue placed directly above the patch.

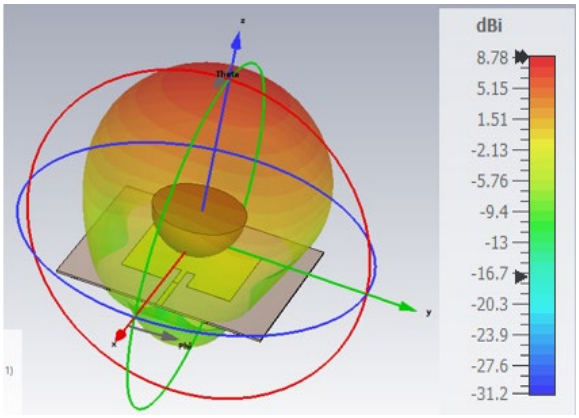


*Figure 5.3: 3D radiation pattern of patch antenna with phantom skin located 5 mm above the antenna.*

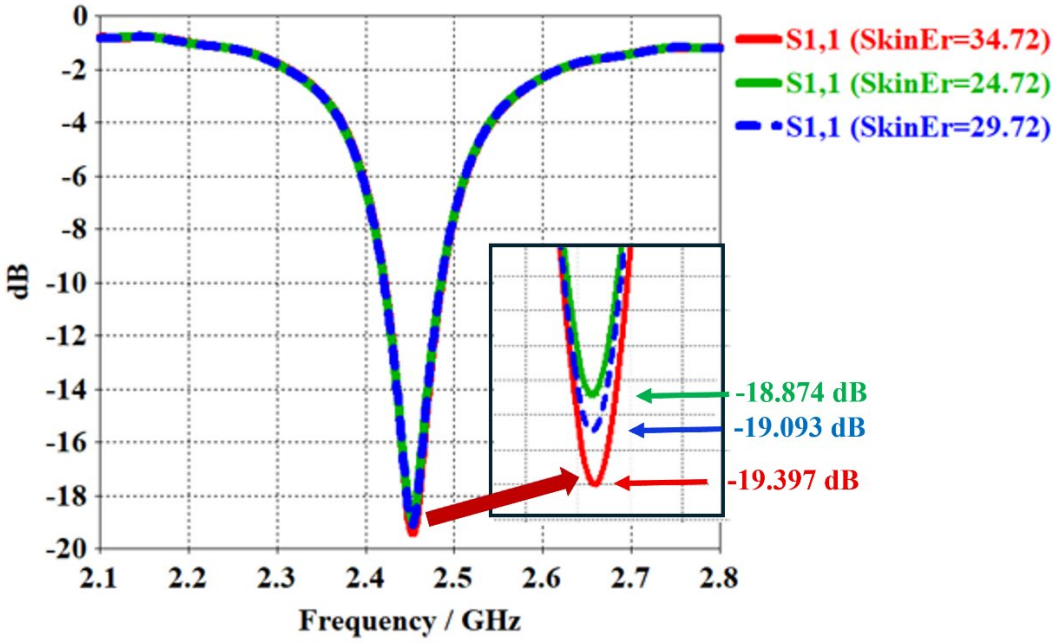


*Figure 5.4: Reflection-coefficient response of different hydration states of the phantom skin.*

*Table 5.2: Effect of the dielectric constant on the antenna's characteristics*

| **Hydration state Skin** | **Dielectric constant ($\varepsilon_r$)** | **Frequency (GHz)** | **Reflection-coefficient (dB)** |
|---|---|---|---|
| Dehydrated skin(red) | 24.72 | 2.4533 | -19.397 |
| Normal skin (Blue) | 29.72 | 2.4528 | -19.093 |
| Hydrated skin (Green) | 34.72 | 2.4531 | -18.874 |

The working principle of the antenna-based sensor can be explained by perturbation theory [3][4], the shift in the resonant frequency of a sensor due to the presence of material is expressed as follows:

$$\frac{f_m - f_o}{f_o} = \frac{-\iiint [\Delta\varepsilon . |E_O|^2 + \Delta\mu . |H_O|^2] dV}{\iiint [\varepsilon . |E_O|^2 + \mu . |H_O|^2] dV} \qquad (5.7)$$

where $f_m$ and $f_o$ are the measured frequency and the initial resonant frequency, respectively; ε and μ represent the initial states of permittivity and permeability, respectively; Δε and Δμ are the variations in permittivity and permeability, respectively; and $E_o$ and $H_o$ represent the electric field intensity and magnetic field intensity, respectively, when MUT is loaded on the sensor.

At the resonant frequency, the time-averaged stored electric energy and magnetic energy are equal, and under the assumption that the dielectric material is located at the maximum electric field intensity. Also, Δμ of skin is zero. Then the resonant frequency shift can be simplified as follows:

$$\frac{f_m - f_o}{f_o} = \frac{-\iiint \Delta\varepsilon . |E_O|^2 dV}{2 \iiint \varepsilon . |E_O|^2 dV} \qquad (5.8)$$

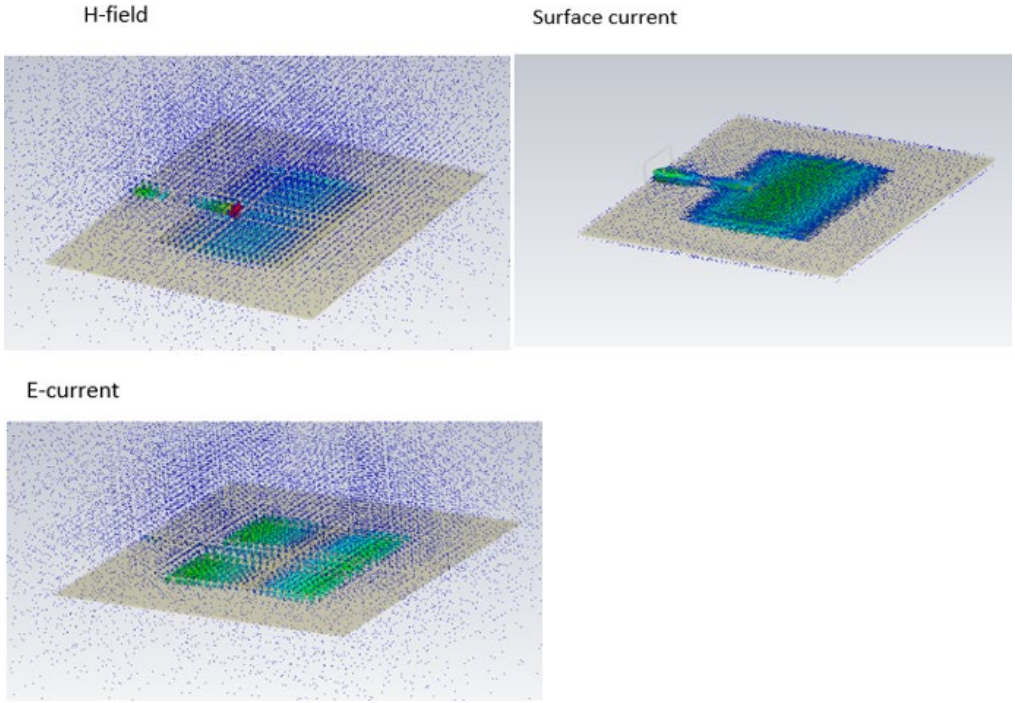


*Figure 5.5: 3D Electromagnetic field and surface current density distributions over the patch antenna.*

Essentially, the single patch's sensing region is spread over its aperture, and a localized material change yields only a subtle effect on the overall impedance. While the patch sensor proved the feasibility of microwave reflection for hydration sensing, its sensitivity to hydration-induced dielectric changes was limited (only a few MHz of resonance shift for moderate changes in skin

permittivity). Additionally, the relatively large dimensions made this antenna-based sensor not conducive for wearable use.

### 5.2.2 Circular Patch Microstrip Sensor

To explore alternative geometries, a circular microstrip patch antenna was designed next at ISM band centred at 2.45 GHz. Circular patches can support resonant modes like rectangular patches but with radial surface current distributions. The circular patch design was implemented on the same dielectric substrate as the rectangular patch antenna, Arlon Cuclad 217 with relative permittivity $\varepsilon_r$ = 2.2, loss-tangent $= 0.009$, and thickness of 0.794 mm. The radius '$a$' of the circular patch of 23.2 mm was determined for the fundamental resonance mode ($TM_{11}$) using [1]:

$$a = \frac{F}{\left\{1 + \frac{2h}{\pi\varepsilon_r F}\left[In\left(\frac{\pi F}{2h}\right) + 1.7726\right]\right\}^{0.5}} \qquad (5.9)$$

Where h is the substrate height, and $F = \frac{8.791\times10^9}{f_o\sqrt{\varepsilon_r}}$.

The circular patch offers a more symmetric field distribution and potentially a more compact shape for wearable use. The simulated performance of the optimized circular patch gave a resonance response at 2.45 GHz with a peak reflection coefficient of around -30 dB. A cylindrical shaped phantom skin of 10 mm radius and height of 3 mm was placed on the patch's centre, as shown in Fig. 5.6. The interaction between the patch's fields and the material is shown in Fig. 5.7. The strongest fields in the circular patch are concentrated at its centre.

Simulation results in Fig. 5.8 show how the reflection-coefficient is affected by the phantom skin at different heights. There is 1 dB variation between the heights of 3 mm and 10 mm. The interesting feature is marginal effect on the patch's centre frequency. Fig. 5.9 shows there is insignificant change in reflection coefficient with the phantom skin's dielectric constant change from a value of 1 to 50. This means that the circular patch antenna too is not sensitive to variations in dielectric constant and therefore ineffective to detect hydration levels.

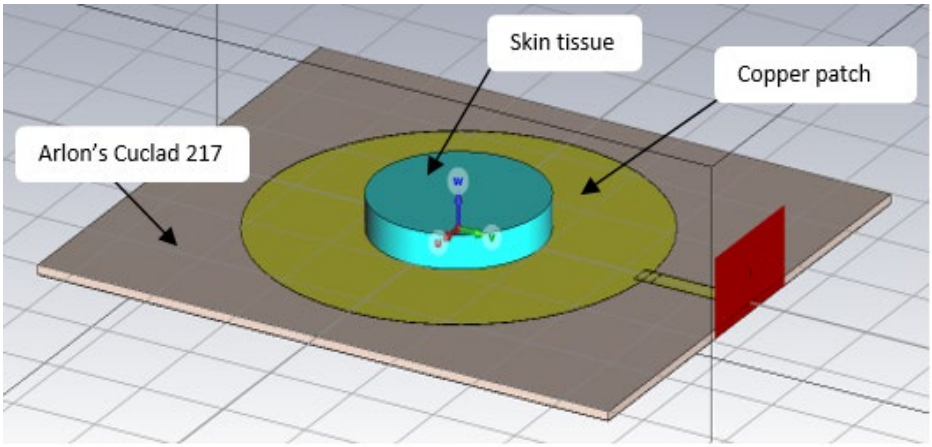


*Figure 5.6: Cylindrical shaped phantom skin on top of the circular microstrip patch sensor.*

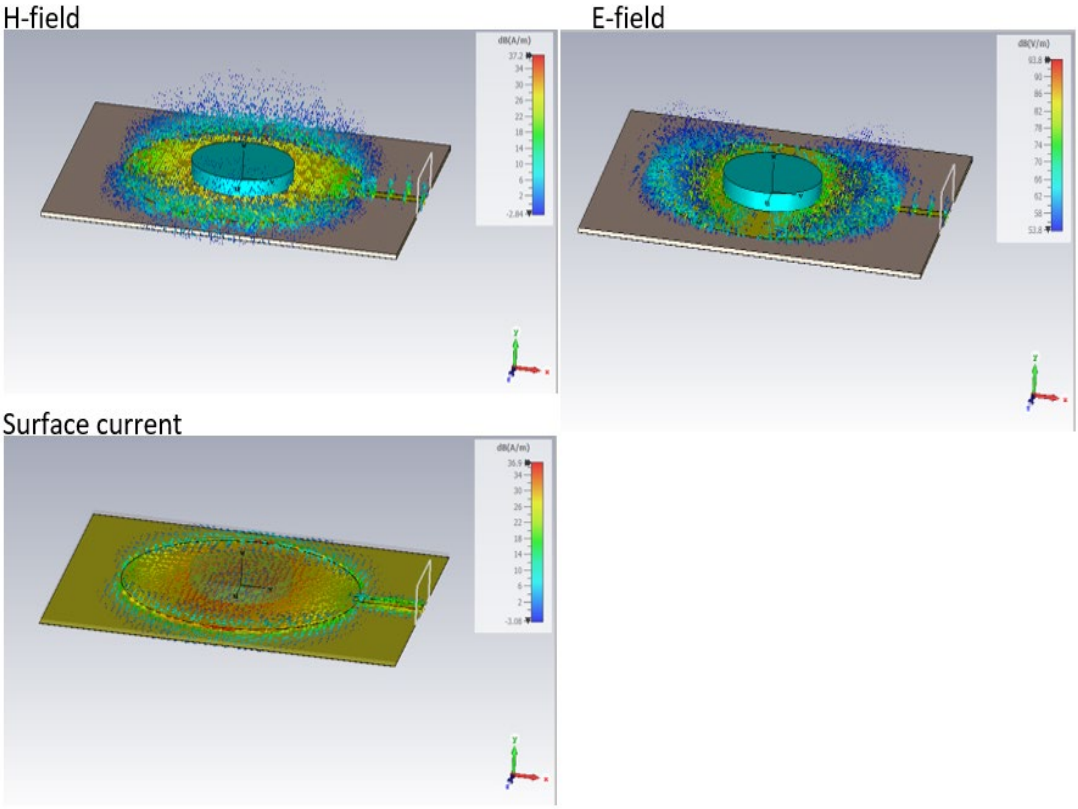


*Figure 5.7: 3D EM radiation field distribution over the circular microstrip patch antenna with a cylindrical shaped phantom skin.*

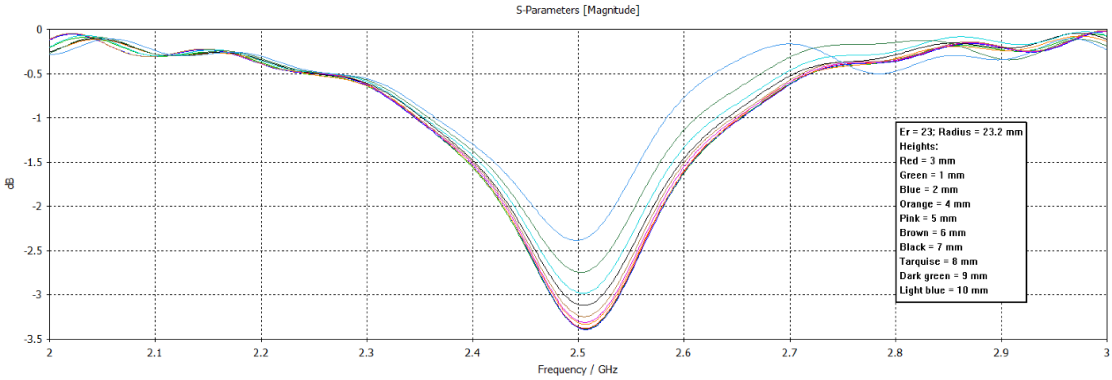


*Figure 5.8: Reflection-coefficient response of the phantom skin height above the circular patch antenna.*

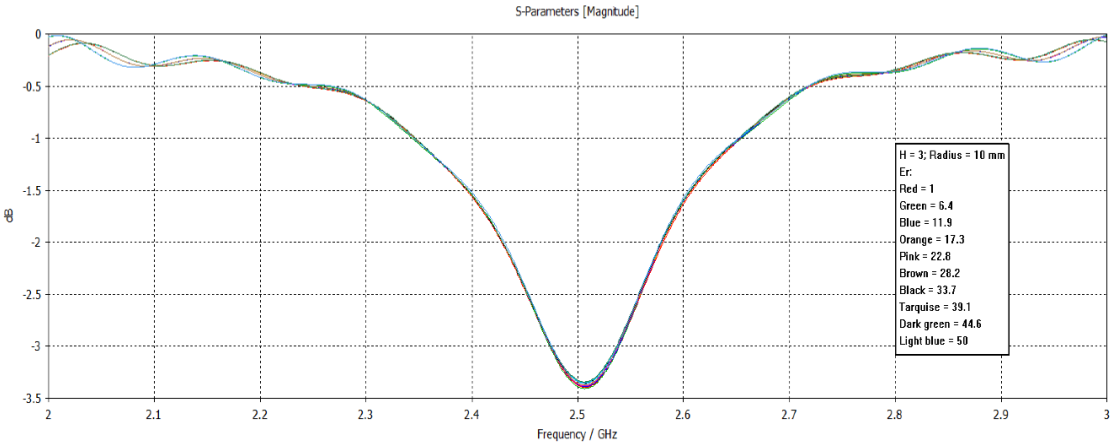


*Figure 5.9: Reflection-coefficient response of the circular patch antenna with the phantom skin of different magnitudes of dielectric constant.*

### 5.2.3 Complementary Split-Ring Resonator Sensor

The third preliminary design was a complementary split-ring resonator (CSSR), shown in Fig. 5.10, consisting of dual concentric rings with splits (gaps) that allow the structure to support a resonant current path. The CSRR behaves as an *LC* resonator: the rings provide inductance and the gaps capacitance. It behaves as a negative permittivity medium (i.e., it exhibits electric resonance) as opposed to split-ring resonator (SRR), which exhibits negative permeability (magnetic resonance). The resonance frequency of a CSSR is given by [5]:

$$f_o = \frac{1}{2\pi\sqrt{LC}} \qquad (5.10)$$

$$r_{avg} = \frac{c}{2\pi f_o \sqrt{\varepsilon_{eff}}} \quad (5.11)$$

$$r_{outer} = r_{avg} + w/2 \quad (5.12)$$

$$r_{inner} = r_{avg} - w/2 \quad (5.13)$$

Where $r_{avg}$ is the average radius of the CSRR, and $w$ is ring width.

CSRR is advantageous because it confines strong E-fields in the gaps and strong H-fields around the rings, creating a localized high-intensity electromagnetic field. Any material placed near the CSRR (especially near the gaps where E-field is strong) will cause a significant shift in the resonance if its permittivity ($\varepsilon$) or permeability ($\mu$) changes. This makes CSRR a very good candidate for highly sensitive sensor. Moreover, it has a relatively small footprint.

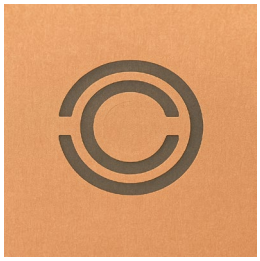

(a)

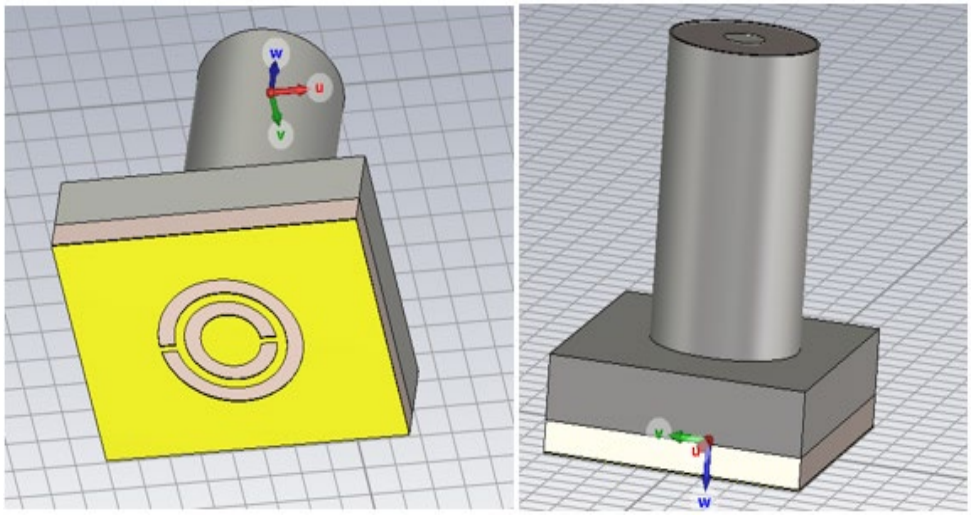


(b)

*Figure 5.10: Complementary split-ring resonator, (a) Etched on Arlon Cuclad 217 dielectric substrate, and (b) Created on CST Studio Suite for simulation analysis.*

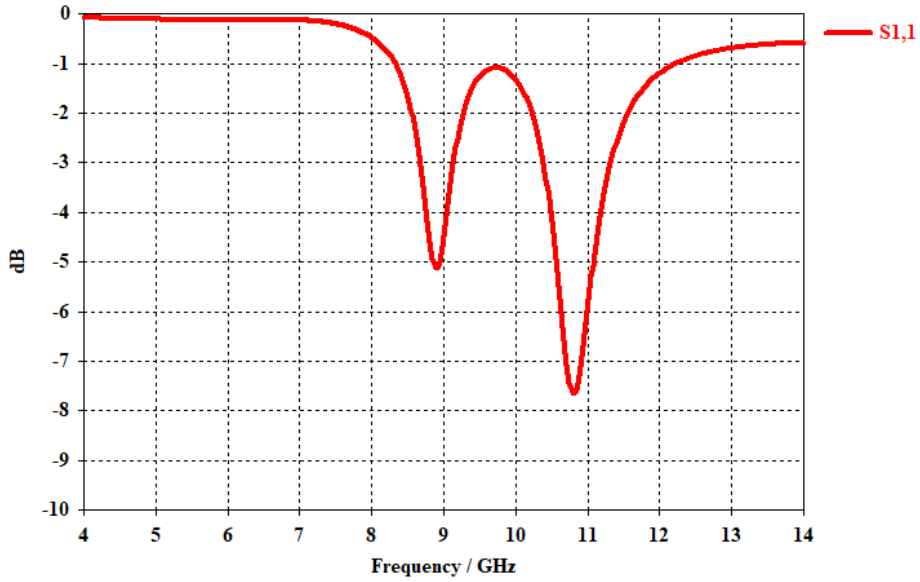


*Figure 5.11: Simulated reflection-coefficient response of the CSRR structure.*

A CSRR was etched on the microstrip of dimensions 9.52 mm × 7.92 mm. The outer ring had a radius of 1.125 mm and width 0.4 mm with a gap width of 0.3 mm. The inner ring radius was 0.425 mm. These dimensions were tuned such that when a skin-mimicking dielectric load is present, the resonant frequency falls in the 2.4-2.5 GHz range. Fig. 5.11 shows that the simulated reflection-coefficient response of the unloaded CSRR (in free space, no dielectric). It is evident that this structure exhibits dual resonance at 8.87 GHz and 11 GHz with corresponding reflection-coefficients of -5.2 dB and -8.1 dB respectfully. When a dielectric sample (with properties like skin, $\varepsilon_r = 38$) was placed over the CSRR (see Fig. 5.10), the resonance shifted down to around the 2.5 GHz range. This large downward shift was a consequence of the dielectric loading increasing the effective capacitance of the resonator.

### 5.3 Effect of Tissue Permittivity for Different Hydration States

To evaluate the CSRR sensor's response to varying hydration levels, a dielectric load was introduced above the resonator to mimic skin tissue as depicted in Fig. 5.12. Although the tissue is composed of skin, fat, muscle and bone in the simulation it was modelled as a homogeneous material with an effective relative permittivity ($\varepsilon_r$) representative of different hydration states as per in Table 5.3.

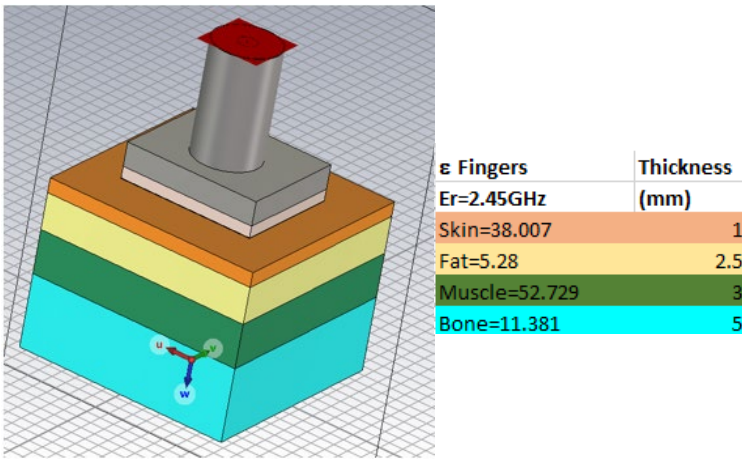


*Fig. 5.12: 3D schematic of the CSRR biosensor placed on a cube segment of phantom skin which could have a relative permittivity ($\varepsilon_r$) in the range 24.72 to 34.72. Dimensions of the phantom skin has dimensions of 1 cm$^3$.*

Fig. 5.13 shows the simulated reflection-coefficient responses for the three hydration states. The resonant frequency increases as the tissue permittivity decreases (i.e., from the hypohydrated state of 34.72 to the hyperhydrated state of 24.72 in this model). A lower ($\varepsilon_r$) means the electromagnetic field sees a smaller effective capacitance, so the *LC* resonance of the CSRR occurs at a higher frequency. For the highest permittivity case ( $\varepsilon_r$ = 34.72, red curve in Figure 4), the resonance occurs at 2.160 GHz with a return loss of –11.95 dB. At the intermediate permittivity ($\varepsilon_r = 29.72$, green curve), the resonance shifts to 2.303 GHz with a return loss around –12.42 dB. For the lowest permittivity scenario ($\varepsilon_r = 24.72$, blue curve), the resonance further shifts up to 2.519 GHz, and the return loss reaches –13.87dB. These results are summarized in Table 5.3. Notably, the frequency shifts uniformly with permittivity. A higher tissue permittivity (which in practice corresponds to greater tissue water content) yields a lower resonant frequency, whereas a lower permittivity raises the resonant frequency. The magnitude of the reflection-coefficient at the CSRR's resonance frequency also varies in a linear fashion with change in permittivity.

*Table 5.3: Characterising parameters of the CSRR sensor for three hydration levels*

| **Hydration state** | **Dielectric constant ($\varepsilon_r$)** | **Frequency (GHz)** | **Reflection-coefficient (dB)** |
|---|---|---|---|
| Hypohydrated | 34.72 | 2.16027 | –11.95 |
| Euhydrated | 29.72 | 2.30278 | –12.42 |
| Hyperhydrated | 24.72 | 2.51853 | –13.87 |

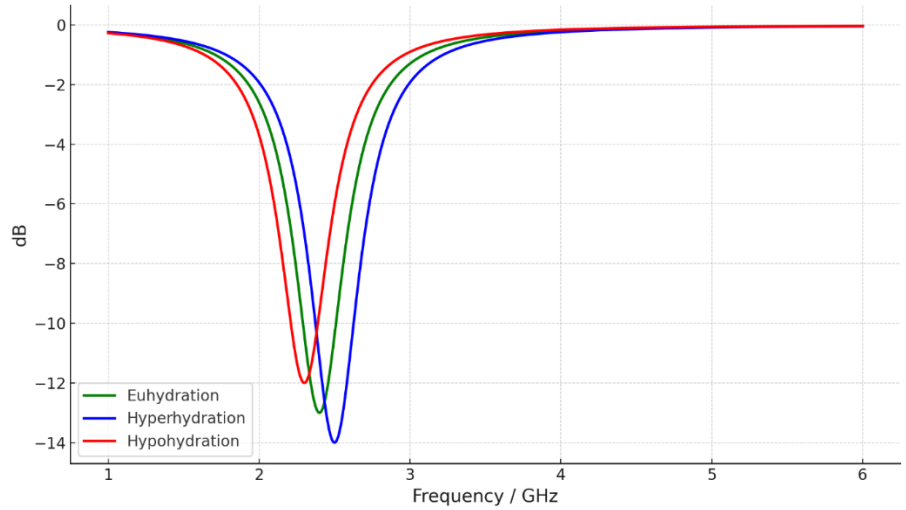


*Fig. 5.13: Simulated reflection-coefficient ($S_{11}$) response of the CSRR biosensor under different hydration conditions.*

### 5.3.1 Air Gap Variation Impact on CSRR sensor Performance

In real-world biomedical sensing applications, particularly those involving skin-contact measurements, the physical interface between the sensor and the biological tissue is often imperfect. Surface irregularities, body movements, and even subtle postural shifts can introduce small air gaps between the sensor surface and the target medium. These gaps, although seemingly minor, can significantly affect the electromagnetic coupling and, consequently, the resonant behaviour of near-field radiated by the CSRR.

To investigate this phenomenon, a systematic parametric simulation was performed using CST Studio Suite, to evaluate the response of a CSRR-based sensor to variations in the vertical distance between the sensor and the phantom skin model, as illustrated in Fig. 5.14. The air gap was varied from 0 mm (ideal skin contact) to 1 mm in 0.5 mm step. The sensor was excited over the range 1 to 10 GHz via coaxial cable feed from the underside of the sensor.

The simulation reflection coefficient results are shown in Fig. 5.15. The following key observations can be made:

- Perfect Contact (No air gap): The CSRR exhibits a distinct resonance at 2.35 GHz, with a $S_{11}$ notch of –12.42 dB. This response indicates strong capacitive coupling between the resonator and the high-permittivity skin phantom, resulting in a significant perturbation of the near-field distribution and effective permittivity surrounding the CSRR.
- Intermediate Air Gap (0.5 mm): As the air gap increases to 0.5 mm, the resonant frequency shifts upward to approximately 8.75 GHz. The resonance is shallower and

broader, reflecting a weaker interaction between the resonator and the dielectric medium due to the intervening air layer.

- Large Air Gap (1 mm): At 1 mm separation, the resonant frequency further shifts to 8.8 GHz, closely to the unloaded resonance of the CSRR in free space. The reflection-coefficient response at this frequency of -22.5 dB is significant, and the sensor's sensitivity to the phantom diminishes substantially. The deep reflection-coefficient notch at this frequency indicates excellent impedance match.

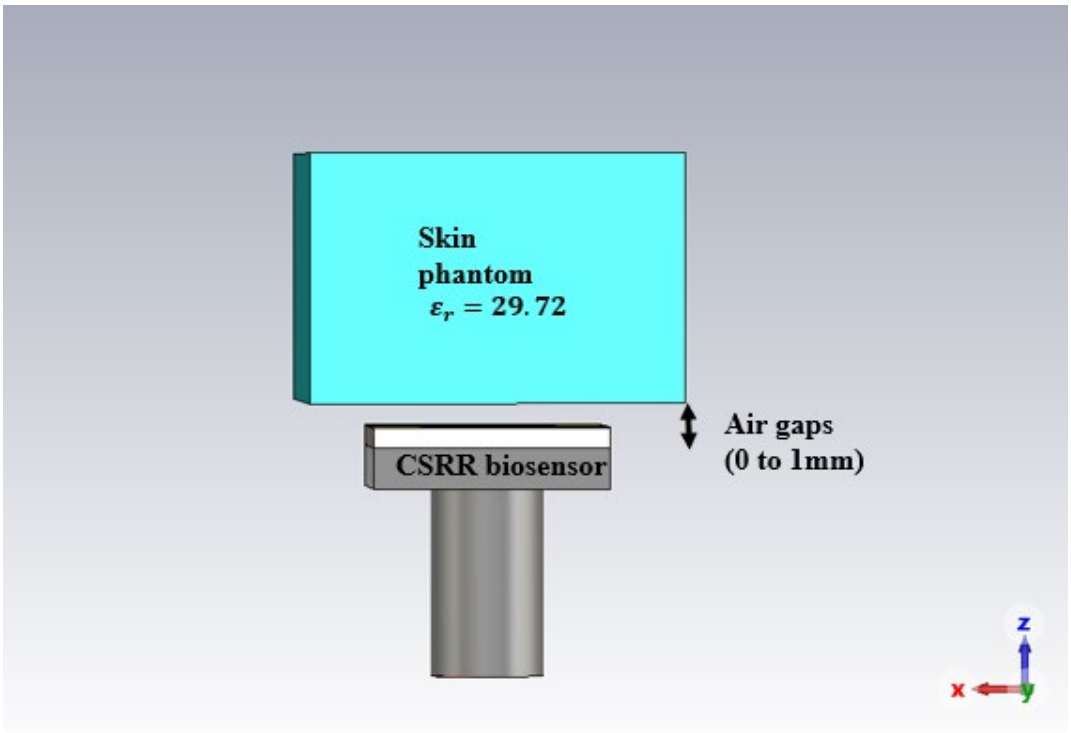


*Fig. 5.14: Simulation model showing the CSRR biosensor beneath phantom skin. The air gap was varied between 0 mm to 1 mm to assess contact effect on the reflection-coefficient.*

Having an air gap highlights the limitations of the resonant coupling mechanisms in CSRR-based sensors. The strong resonance at 8.8 GHz is a product of the resonator geometry and boundary conditions rather than any meaningful biosensing interaction. Consequently, while the sensor may still appear operational from a purely electromagnetic standpoint, it ceases to function effectively as a hydration sensor under such poorly coupled conditions. In practical deployments, this observation underscores the necessity of ensuring consistent physical contact or developing sensor configurations that are less susceptible to vertical displacement and air gap variability.

Without such measures, the sensor's performance will be unreliable, especially in dynamic or ambulatory environments where constant contact with the skin cannot be guaranteed.

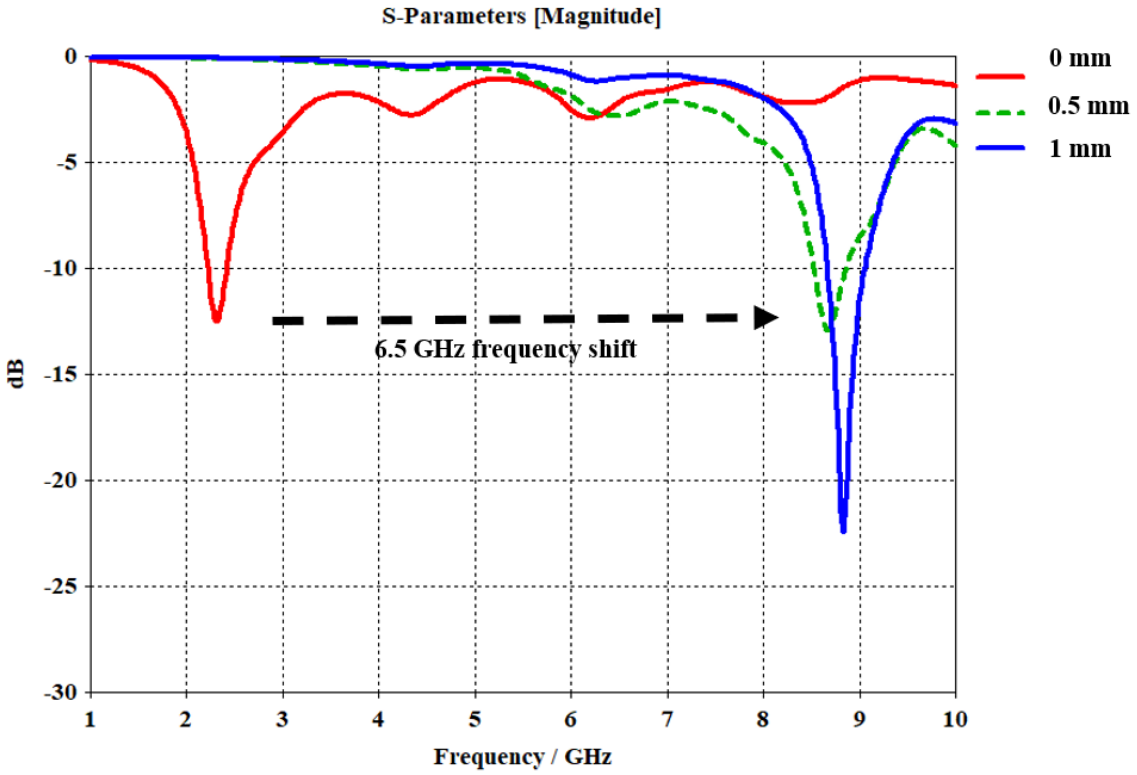


*Fig. 5.15: Simulated $S_{11}$ response of the CSRR sensor as a function of air gap between the sensor and the phantom skin model.*

In applications like continuous hydration monitoring, where reliability is essential, the variability in the air gap between the sensor and skin tissue introduces serious challenges to robustness and repeatability.

To mitigate this sensitivity degradation various strategies, need to be considered such as:

- Mechanical conformity (e.g., flexible substrates, elastomeric padding),
- Electromagnetic design compensation (e.g., wider bandwidth CSRRs, dual-resonant structures),
- Gap-insensitive calibration algorithms, or
- Real-time gap detection and correction (via secondary sensing modalities)

Without such interventions, the CSRR sensor's practical utility in wearable or ambulatory biosensing applications remains fundamentally constrained.

## 5.4 Ferrite-Impregnated H-Shaped Patch Antenna Design

The complementary split-ring resonator is a potential candidate for a biomedical sensor to quantify the degree of hydration. The simulation results of the CSRR reveal that the degree of hydration or permittivity of the phantom skin can affect the CSRR's characteristics in terms of resonant frequency and reflection-coefficient. It's also sensitive to air gap between the CSRR and permittivity loading. Moreover, it's Q-factor is relatively low high. These factors can affect the precision of the hydration measurement using the CSRR. What is required is a sensor that exhibits a high-Q factor and only one characterising factor of the sensor is affected by different magnitudes of permittivity loading. The objective here was to create a compact, high-Q resonant sensor that concentrates electromagnetic fields in a specific region for interaction with the skin tissue, while maintaining good impedance matching at frequency. To do this, magneto-dielectric materials (ferrites) are leveraged to miniaturize the antenna size and enhance its performance. This is because high-permeability materials have been shown to reduce antenna size and improve its bandwidth and radiation efficiency [5][6]. What is proposed here is a novel sensor based on advancing initial works with ferrite at the prime magnetic region of a path [11] to form an H-shaped patch-based sensor that is strategically impregnated with ferrite material (BaFe). This innovation constituents the primary contribution of this research work.

### *5.4.1 H-Shaped Patch*

The development of a ferrite-impregnated H-shaped patch antenna stems from a comprehensive exploration of geometry-driven and material-assisted miniaturization strategies for microstrip antennas investigated in London Metropolitan University's rescale project in 2022. The H-shaped patch configuration, characterized by two extended arms connected by a narrow central strip, offers a natural advantage for compact design by elongating the effective current path. This structural modification leads to a reduction in resonant frequency compared to a conventional rectangular patch of similar outer dimensions [7]. However, while geometric tailoring of the patch improves compactness, it inherently reaches a limit beyond which further size reduction begins to degrade key performance metrics such as bandwidth and radiation efficiency [8]. To overcome this constraint, this work explores a hybrid strategy that couples the geometric benefits of the H-shaped structure with the selective integration of magneto-dielectric materials (Barium ferrite).

### *5.4.2 Geometry of H-Shaped Patch Sensor*

The H-shaped patch sensor, shown in Fig. 5.16 as in [11], was designed on a 50 × 50 mm$^2$ Taconic substrate of thickness, $h$ = 0.8 mm, $\varepsilon_r = 2.2$, $tan\,\delta = 0.0009$. The dimensions of the patch radiator of 30 × 30 mm$^2$ were calculated using Eqns. (5.3) & (5.5). The narrow region of the patch

structure is critical to the antenna's resonant behaviour. The patch antenna was excited through an SMA connector through a via-hole from the ground plane side, and the connected was located at x- and y-coordinates of 12 mm and 15 mm, respectively, referenced from the left-hand bottom corner of the substrate. The feed mechanism used to excite the H-shaped patch sensor was a coaxial SMA connector, which was strategically located to optimise impedance matching. The connector was located under the patch sensor, and it is offset from the patch centre. The resulting structure resonated at 2.57 GHz, as shown in Fig. 5.17. Although the current resonance falls outside the standard 2.4–2.5 GHz ISM band (defined by ITU-R and partially by the FCC) slight reduction in the patch's dimensions is required to resonate at 2.45 GHz.

As in [11], the high-permeability Barium ferrite (BaFe) commonly found in speaker magnets and magnetic recording tapes was used in this study. Twenty-one layers of BaFe floppy disk tape were stacked having a thickness of 0.9 mm was embedded in the 17.14 × 7.1 $mm^2$ narrow region of the substrate experiencing the strongest magnetic field, shown in Fig. 5.18. Best estimates for a typical BaFe thin layer at 2.45 GHz are $\mu' \approx 5–20$, $\mu'' \approx 1–5$ and $\varepsilon' \approx 10–15$, $\varepsilon''$ negligible ($\ll 1$) [9]. The material parameters of the ferrite layer used in the simulations conducted here were $\mu'$of 4.3 and $\varepsilon'$ of 8.6.

The impregnation of the BaFe layer was achieved by creating a recess in the substrate at the narrow section of the H-shaped to place the ferrite layer, which was covered with a copper layer, as illustrated in Fig. 5.15. The thickness of the substrate at the ferrite region was 1.7 mm. This approach avoided excessive dielectric loss and unwanted capacitance elsewhere in the structure.

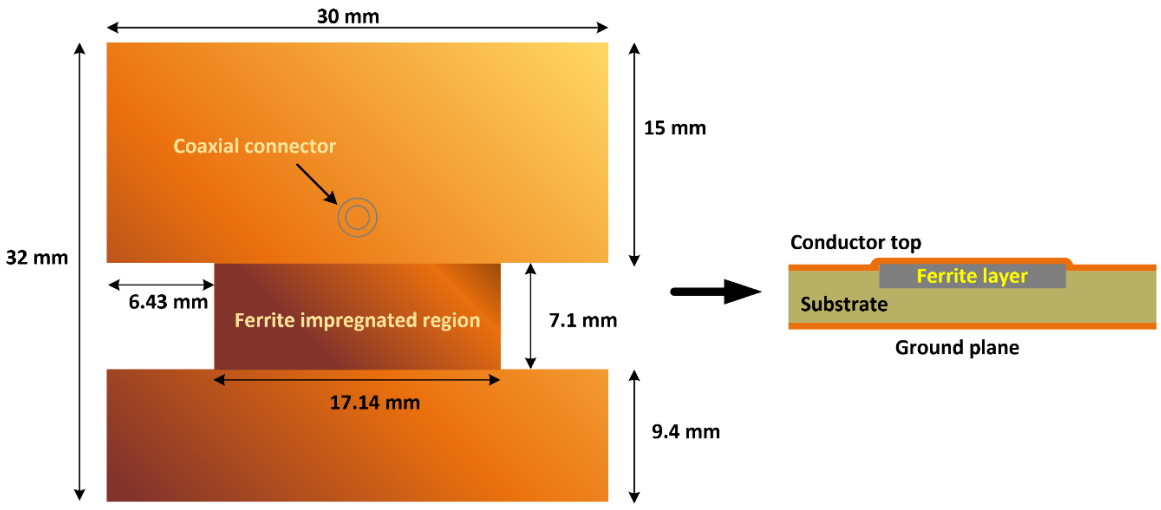


*Figure 5.16: Top-view of the ferrite impregnated H-shaped patch sensor.*

The position of the SMA connector was adjusted during the design process to account for impedance changes introduced by the ferrite. Specifically, the connector location was fine-tuned to achieve 50 Ω impedance match to compensate for the additional reactive component introduced by the magnetic loading. The resulting antenna resonated dropped down to 2.22 GHz.

In parallel, the patch dimensions and the geometry of the H-shaped patch sensor had to be optimized since the inclusion of the ferrite lowered the resonant frequency of the patch sensor from 2.57 GHz to 2.22 GHz constituting 13.6%, as shown in Fig. 16. The consequence of this was reduction in the patch's size to maintain the desired operating frequency at 2.45 GHz. The inclusion of the ferrite loading had no effect on the structure's Q-factor.

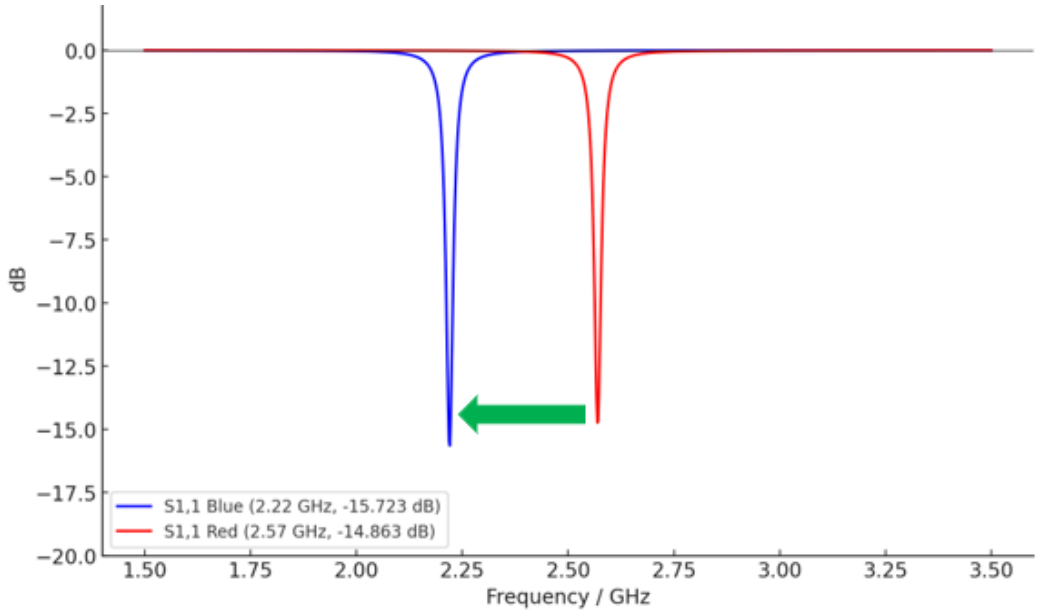


*Figure 5.17: The red curve represents the reflection-coefficient of the H-shaped structure with no impregnated ferrite, and the blue curve represents the same H-shaped patch sensor with impregnated barium ferrite layer.*

The rationale for embedding ferrite in the region of highest magnetic field (H-field) intensity under the patch is grounded in both electromagnetic theory and empirical observation [10][11]. In a microstrip patch antenna operating in its fundamental mode, the centre area of the patch is where the magnetic field energy is most concentrated, while the electric field is relatively weak. Placing a high-permeability material (ferrite) in this H-field region substantially increases the local effective permeability ($\mu_{eff}$) thereby intensifying the H-field in that region. The ferrite inclusion effectively raises the inductive energy storage in the patch's resonant cavity, which in turn increases the effective refractive index of the medium beneath the patch (since $n_{eff} =$

$\sqrt{\varepsilon_{eff}\mu_{eff}}$ for the substrate). The theoretical implication is a pronounced reduction in resonance frequency because the guided wavelength in the partially ferrite-loaded region is reduced, allowing the patch to resonate at a lower frequency for the same physical dimensions, as shown in Fig 5. 16. The consequence of this is that miniaturization can be implemented to realize the same resonant frequency without the ferrite layer.

In essence, the miniaturization factor, defined here as the ratio of the resonant wavelength (or antenna size) on a conventional substrate to that on the enhanced (ferrite-loaded) substrate is improved by approximately the factor $\sqrt{\mu_{eff}}$ introduced by the ferrite since $\lambda_{medium} = \lambda_o/\sqrt{\mu_{eff}\varepsilon_{eff}}$ . This targeted use of a magnetically permeable material exploits the fact that increasing $\mu_r$ can lengthen the electromagnetic wavelength in the substrate without the same degree of bandwidth penalty that a corresponding increase in $\varepsilon_r$ would induce. By leveraging a ferrite ($\mu_r$ > 1) in the high-H-field zone, the design capitalizes on this principle, effectively lowering the resonant frequency while mitigating bandwidth degradation, as evident in Fig. 5.16.

### *5.4.3 Effect of Ferrite Loading on EM-Field of the H-Shaped Patch Sensor*

Compared to a standard rectangular patch, the H-shaped patch forces the current to detour around the notched sections, effectively lengthening the path. Simulated surface current plots confirm that the highest current density is confined over the narrow central section of the H-shaped patch, as shown in Fig. 5.18.

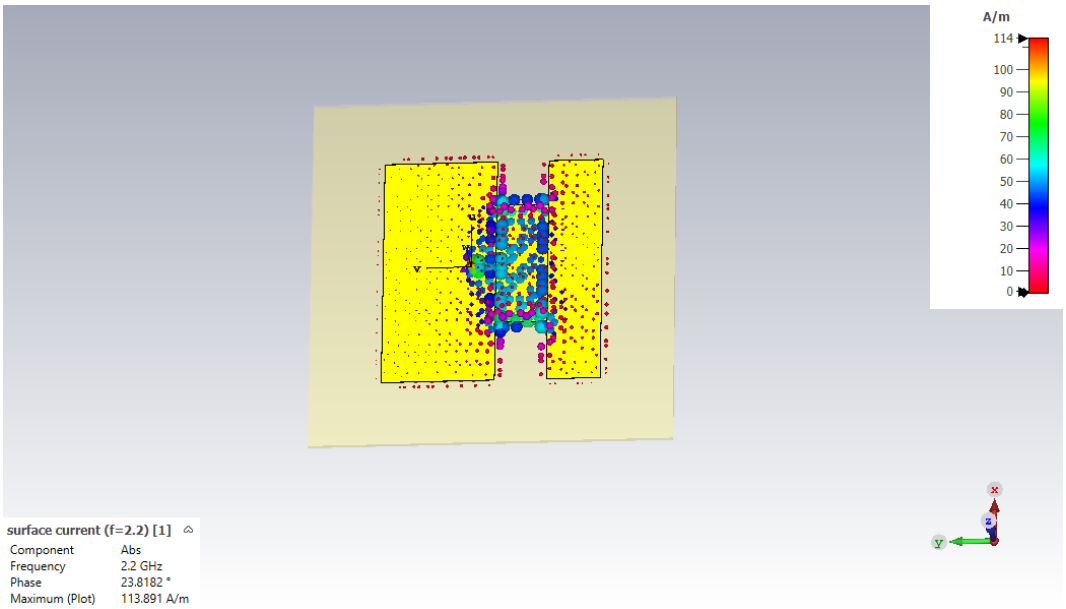


*Figure 5.18: Current density distribution at 2.2 GHz showing current density is mainly concentration at the centre of the H-shaped structure.*

It is evident from Fig. 5.19 that the E-field is concentrated at the wider sections of the H-shaped structure however the E-field is virtually absent in the narrow section which is impregnated with the ferrite material. This is not surprising as the ferrite loading has substantially increased the local effective permeability thereby intensifying the H-field in that region [11], as evident in Fig. 5.20.

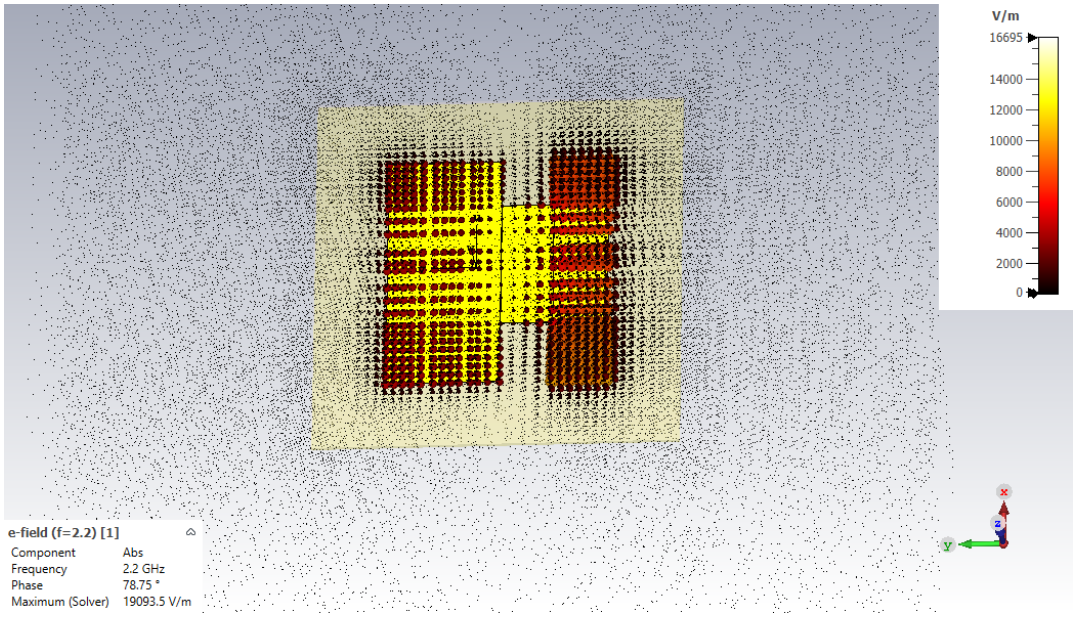


*Figure 5.19: E-field density distribution at 2.2 GHz showing peak intensity at the edges of the H-shaped structure.*

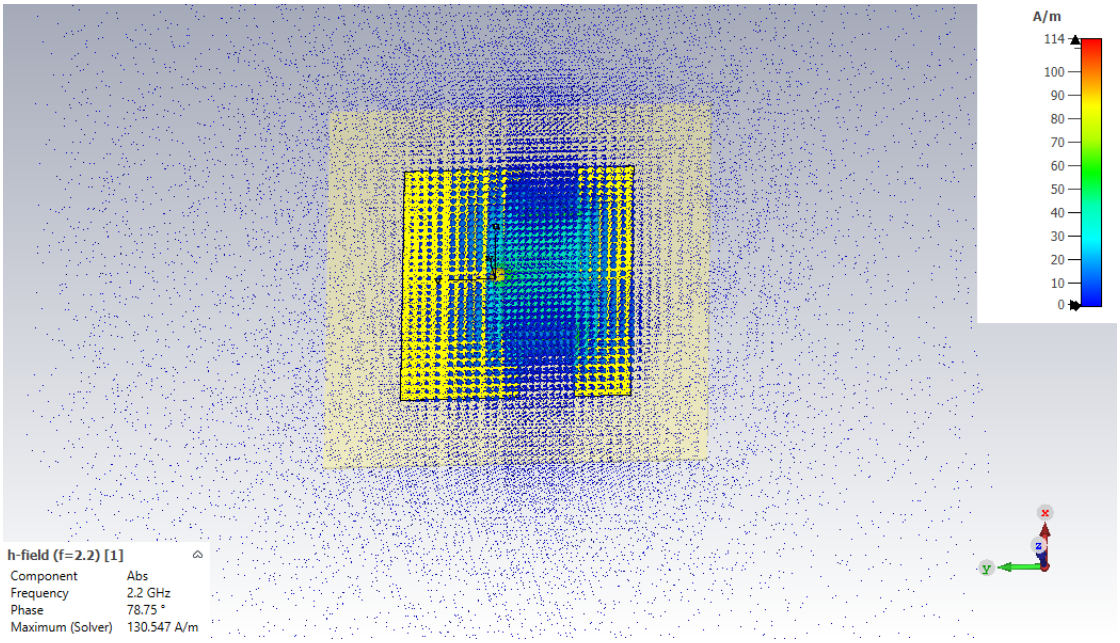


*Figure 5.20: H-field density distribution at 2.2 GHz showing concentrated H-field in the central region of the H-shaped structure.*

## 5.5 Human Skin Tissue Modelling

To rigorously evaluate the performance of the antenna designs for hydration sensing, we employed full-wave electromagnetic simulations using CST Studio Suite 2023. CST provides both time-domain and frequency-domain solvers; for most of our analysis we used the Time Domain Solver (which is based on the Finite Integration Technique, FIT) due to its efficiency in broadband calculations. Some cross-verification was done with a Frequency Domain Solver (and with ADS's FEM solver) to ensure the results were consistent and not an artifact of a particular numerical method.

The dielectric properties of human skin tissue across different hydration states were incorporated into the CST simulations based on the data in Table 5.4.

As detailed in Chapter 4, the wrist's cross-section can be treated as a composite of various tissues (skin, fat, muscle, bone, blood), each with distinct dielectric constants. By applying the Bruggeman mixing model to the representative volume fractions of these constituents (see Chapter 4), an effective permittivity was obtained for the bulk tissue (around human wrist). This calculation yielded a value of approximately $\varepsilon_r \approx 29.72$ for the euhydrated skin composite, which serves as the baseline dielectric constant used in the simulations conducted in this study. Rather than modelling each anatomical layer explicitly, this single effective permittivity captures the overall electromagnetic behaviour of well-hydrated skin, providing a realistic starting point for the sensor-tissue interaction analysis.

*Table 5.4: Relative permittivity at different hydration conditions based on experimental data.*

| Hydration state | Relative permittivity ($\boldsymbol{\varepsilon_r}$) |
|---|---|
| Hyperhydration | 24.72 |
| Euhydration | 29.72 |
| Hypohydration | 34.72 |

To model hydration deviations from the baseline, permittivity values for hypohydrated (dehydrated) and hyperhydrated (over-hydrated) skin states were derived based on the findings of Chapter 4. In that chapter, controlled studies using both artificial sweat solutions and dielectric probe measurements on human skin established how the tissue's permittivity shifts with hydration level. The artificial sweat experiments provided a controlled reference for how increased water content affects dielectric properties, while in vivo measurements on volunteers' skin captured permittivity changes under varying hydration conditions. Chapter 4's results indicated a clear

trend: drier skin (with lower water content) exhibited a higher effective permittivity at 2.45 GHz, whereas more hydrated skin (with greater water content or surface sweat) showed a lower effective permittivity. For instance, well-hydrated individuals had measured skin permittivity in the low 20s (and in some cases even below 20), whereas dehydrated individuals showed values rising into the 30. This inverse relationship, though counter-intuitive given water's high intrinsic permittivity, was explained in Chapter 4 by physiological factors such as electrolyte concentration changes and measurement artifacts. Guided by these empirical observations, the hypohydrated skin in the simulations conducted in this section were assigned a higher relative permittivity than the baseline to represent the dielectric behaviour under dehydration, while the hyperhydrated skin was assigned a lower relative permittivity than the baseline to represent tissue with excess hydration or surface sweat.

In practice, these were implemented as $\pm\Delta\varepsilon$ of 5-point variation around the euhydrated value, in line with the quantitative ranges reported in Chapter 4. By calibrating the model's material properties to experimental data in this way, it ensures that the simulated sensor responses meaningfully reflect realistic hydration-induced dielectric changes.

A cylindrical skin phantom of 1 cm diameter and 1 cm height was placed on top of the H-shaped patch sensor positioned in the centre of the narrow section as shown in Fig. 5.21. In the simulation all parameters were kept constant and only the skin phantom's permittivity was changed in accordance with the hydration state.

The difference in resonance frequency among the three hydration states is within 0.1 GHz, centred around 2.2 GHz, as shown in Fig. 5.22. However, there is a distinct variation in the reflection coefficient between the hydration states. The reflection coefficient magnitude is -4.8 dB for hypohydration, -8 dB for euhydration, and -13.5 dB for hyperhydration. These results indicate that the H-shaped patch sensor is largely insensitive to frequency shifts but exhibits significant variation in reflection coefficient magnitudes, enabling precise discrimination between hydration states.

Ideally, the sensor should be in direct contact with the skin. However, in practical applications, a gap may exist due to factors such as body hair or imperfect sensor conformity. Therefore, it is important to assess how an air gap between the sensor and the skin affects the reflection coefficient response. Figure 5.23 show the simulation setup. Figure 5.24 shows the reflection

coefficient for air gaps of 0.25 cm, 0.5 cm, and 0.75 cm. In CST Studio Suite, the air gap was modelled with a relative permittivity of approximately $\varepsilon_r \approx 1$.

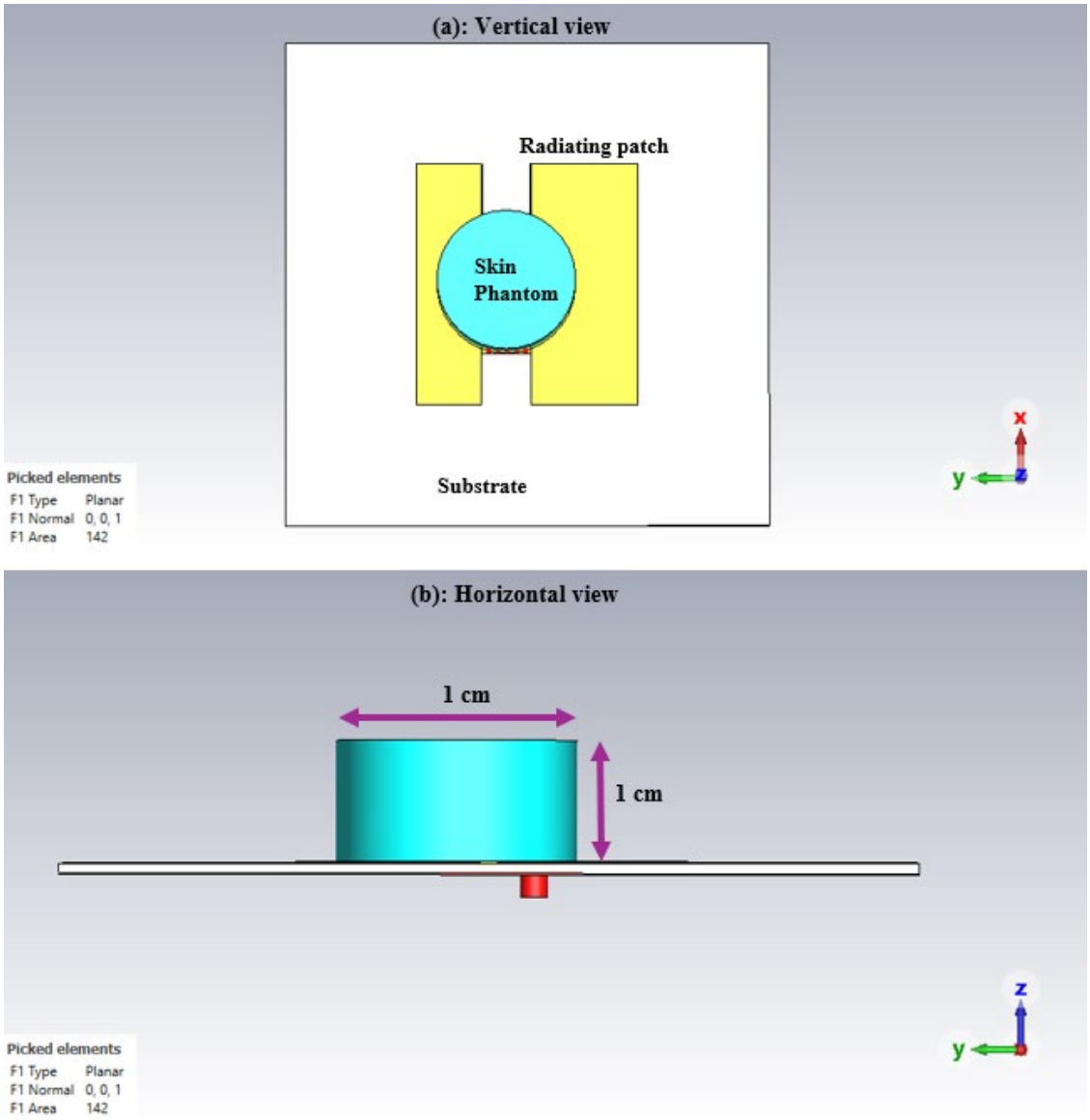


*Figure 5.21: Simulation model of the hydration sensor setup in CST Studio Suite. (a) Vertical view showing the skin phantom placed directly on the H-shaped patch sensor, and (b) Horizontal side view illustrating the cylindrical phantom's dimensions in contact with the antenna structure and the position of the coaxial feed.*

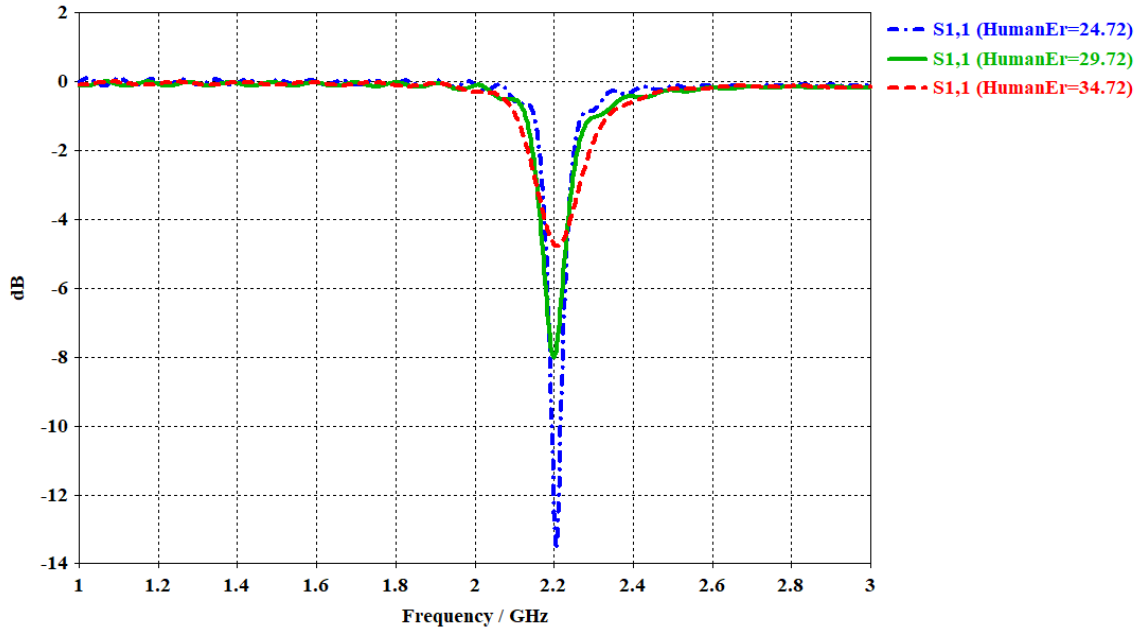


*Figure 5.22: Simulated reflection coefficient response for the three skin hydration states when skin phantom is in direct contact with the H-shaped patch sensor. Euhydrated state ($\varepsilon_r$ = 29.72) is shown in green, hypohydrated state ($\varepsilon_r$ = 34.72) in read, and hyperhydrated state ($\varepsilon_r$ = 24.72) in blue curves.*

Increasing the air gap from 0.25 cm to 0.75 cm causes a slight shift in the resonance frequency. Notably, the optimal reflection coefficient magnitude of -20.5 dB is observed at a 0.5 cm gap. In comparison, a 0.25 cm gap results in a reflection coefficient magnitude of -7.5 dB, while a 0.75 cm gap yields -17.5 dB.

These results confirm that a moderate air gap of around 0.5 cm offers the best compromise between practical mounting flexibility and sensor performance, ensuring robust sensitivity to dielectric loading across hydration states while avoiding the detuning effects seen at both closer and more distant placements.

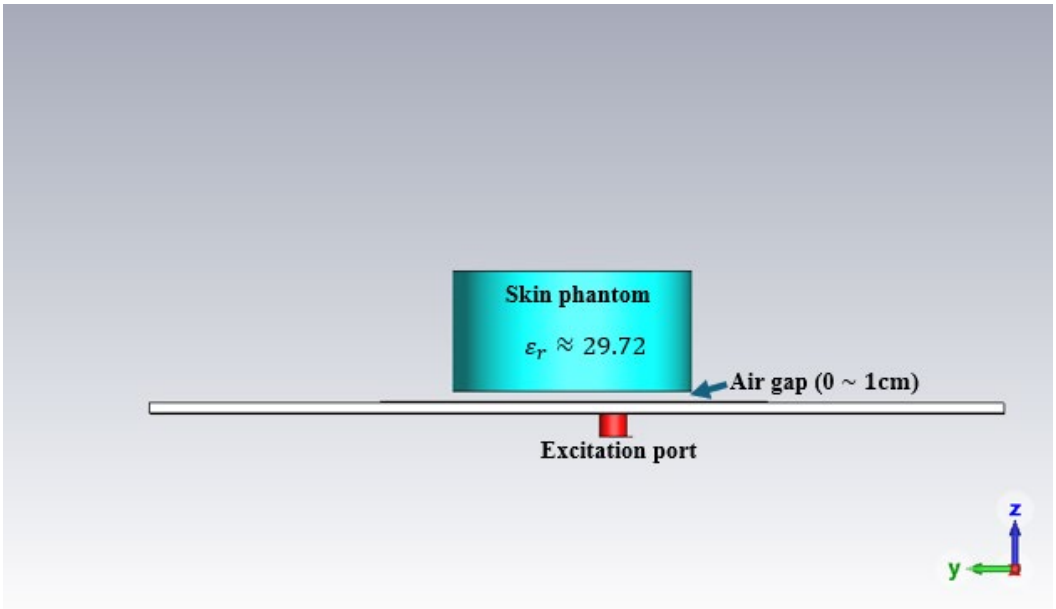


*Figure 5.23: Side view of the CST Studio Suite simulation setup showing the skin phantom ($\varepsilon_r \approx 29.72$) positioned above the antenna with a variable air gap (0–1 cm) to evaluate the impact of sensor-to-skin coupling conditions on electromagnetic performance.*

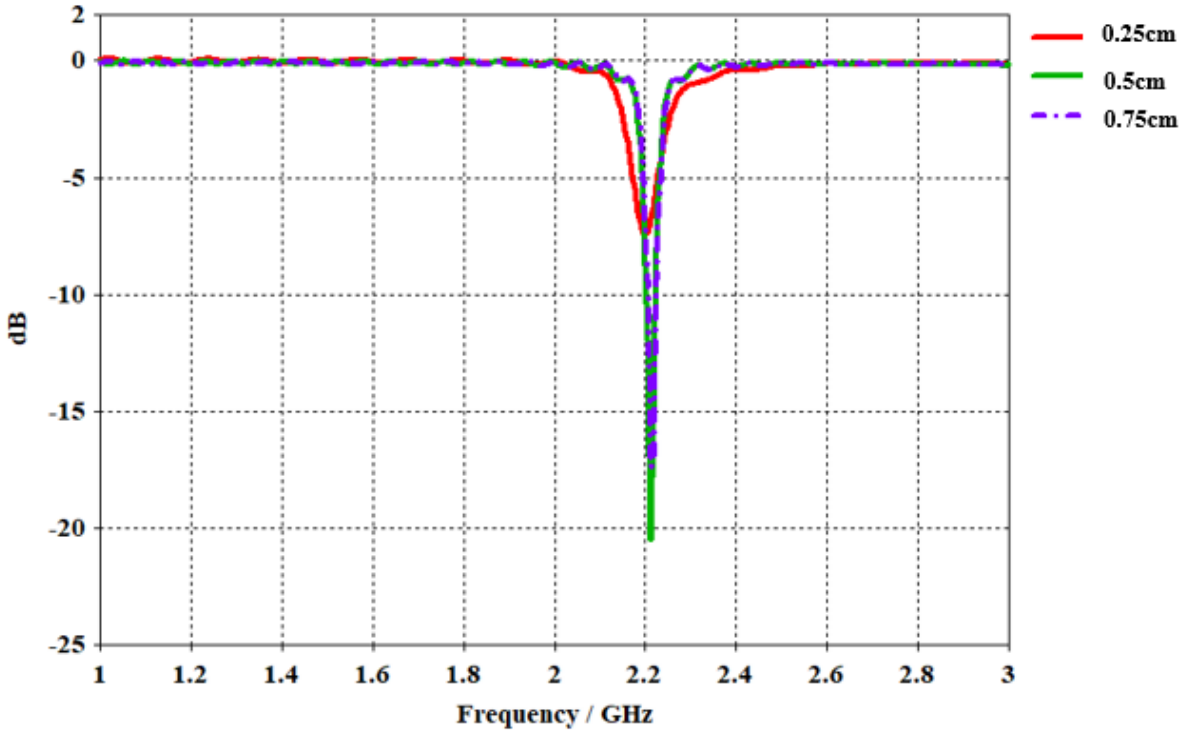


*Figure 5.24: Reflection coefficient ($S_{11}$) response of the H-shaped patch sensor for different air gap between the between the skin phantom ($\varepsilon_r \approx 29.72$) and the sensor surface.*

It should be noted that in this chapter's CST models the skin and underlying tissues are simplified as a single homogeneous layer with an effective permittivity. This simplification is a deliberate

modelling choice to reduce complexity while capturing the primary effect of interest, the bulk dielectric loading due to hydration. By using the Bruggeman-derived uniform permittivity for the entire phantom, we assume that the layered structure of real skin (epidermis, dermis, subcutaneous fat, etc.) can be approximated by one average dielectric layer. This approach is justified for our initial investigations because at the 2.22 GHz frequency, the sensor's electromagnetic fields penetrate a few centimetres and interact collectively with all layers; thus, an average response can reasonably reproduce the resonance shifts and amplitude changes caused by overall hydration differences. Indeed, the resonance behaviour (frequency shift direction, relative sensitivity) is largely governed by the total effective permittivity directly beneath the antenna, which our homogeneous model provides. The use of an effective medium thus allows us to capture trend-level effects of hydration (dehydration causing an upward shift in effective permittivity and corresponding sensor detuning, and hyperhydration the opposite) without the need for intricate multilayer reconstruction at this stage. However, the homogeneous model does neglect finer anatomical details, for example, the specific impact of the thin epidermal layer or the dispersion at tissue interfaces, which might subtly affect the sensor's response or the field distribution. These considerations, while secondary to the core resonance trends, are important for thoroughness and will be considered in Chapter 6, where experimental measurements are performed on real human subjects. In that chapter, dielectric readings are obtained directly from the wrists of participants under varying hydration states using calibrated H-shaped antenna embedded with a ferrite. These in vivo measurements offer a physiological benchmark for assessing the accuracy of the CST-based simulations presented here. By comparing the simulated resonance trends from the homogeneous phantom model with the actual human data, we evaluate the practical reliability of the effective permittivity assumptions and assess the sensor's sensitivity under real-world biological variability.

### 5.6 Validation and Limitations of Simulations

It is important to acknowledge the assumptions and limitations of the CST Studio Suite simulations:

- The work assumed homogeneous skin properties and did not include sub tissues like fat or muscle. An antenna on the body will see a layered medium (skin over fat over muscle). This simplified approach is common for initial sensor design, since the sensor primarily interacts with the skin layer (where it is placed), the bulk effect of deeper layers can often

be modelled as an increased effective permittivity and loss. Nevertheless, in future work a multi-layer model or full-wave human body model could be used for more accuracy.

- This work did not explicitly include the curvature of a human limb (e.g., wrist or arm). The simulations assume a flat skin patch. The ferrite H-antenna is about 5 cm across, which could be slightly curved around a wrist in practice. Minor detuning could occur due to curvature, but this was not accounted for.
- Thermal and frequency dispersion of tissue were neglected (we used static dielectric values for a given hydration). In practice, if the sensor operates across a band or if temperature changes, the dielectric properties could shift.
- The ferrite material was assumed to be unbiased (no external magnetic field). Some ferrites require a bias to achieve certain permeability at high frequencies, but we assumed a self-biased ferrite (like hexagonal ferrite) with stable permeability in the small-signal regime. If a bias is needed, that adds complexity which we did not simulate here.

Despite these simplifications, the simulations provide a comprehensive picture of how the antenna designs respond to changes in hydration-related dielectric properties. The next section uses these results to explain the reflection-based sensing mechanism in detail.

### 5.7 Theory of Reflection Coefficient and Dielectric Loading

The reflection coefficient ($S_{11}$) behaviour of the antenna sensor can be directly related to the hydration level of the skin via the skin's dielectric properties. In essence, the H-shaped antenna structure is sensitive to the permittivity ($\varepsilon_r$) of its loading environment. When the antenna is placed on or near the skin, the skin becomes a part of the antenna's surrounding medium and influences its impedance and resonance.

The reflection coefficient ($\Gamma$) at the antenna feed is defined as:

$$\Gamma = \frac{Z_{in} - Z_0}{Z_{in} + Z_0} \qquad (5.14)$$

Where $Z_{in}$ is the input impedance of the antenna (which depends on frequency and the environment) and $Z_0$ is the characteristic impedance of the feed (50 Ω). When $Z_{in} = Z_0$, the antenna is perfectly matched and $\Gamma$ =0 (no reflection, all power absorbed/radiated). When $Z_{in}$ deviates from 50 Ω, some fraction of power is reflected. We often express $S_{11}$ in dB as $20\,log_{10}\,\Gamma$.

Finally, the reflection coefficient in dB was defined in the draft as:

$$S_{11} = 10\,log_{10}|\Gamma|^2 = 20\,log_{10}\left|\frac{Z_{in} - 50}{Z_{in} + 50}\right| \qquad (5.15)$$

The input impedance $Z_{in}$ of the antenna is affected by the effective permittivity ($\varepsilon_{eff}$) and permeability ($\mu_{eff}$) of the medium around the antenna. When the antenna is in free space, $Z_{in}$ is determined by the antenna geometry and its own substrate. When a high-permittivity object (like human tissue) is brought near, the fields from the antenna interact with that object effectively adding capacitance and dielectric loading. This typically lowers the resonant frequency and can change the impedance at resonance. Specifically for a patch antenna, adding a dielectric layer on top will often increase the capacitance of the patch (like adding a superstrate), which can make the antenna input impedance more inductive below resonance and shift the match. Conversely, a high-permeability object can add inductance. In this work, the human body is mostly dielectric (non-magnetic), so the main effect is via permittivity.

At the frequency of interest ($f_r = 2.2$ GHz), the primary effect of skin contact is that the antenna's fringing electric fields now terminate partly in skin ($\varepsilon_r \sim 15 - 40$) instead of air ($\varepsilon_r \sim 1$). Thus, the effective permittivity ($\varepsilon_{eff}$) seen by the antenna increases. As a rule of thumb, the resonant frequency of a patch or resonator is roughly $f_r \alpha \frac{1}{\sqrt{\varepsilon_{eff}}}$. In this work's simulations, when skin permittivity was increased (hypohydration), we observed this downward shift in $f_r$. When the skin permittivity was lower (hyperhydration), an upward shift in $f_r$ was observed (Figure 5.25).

Mathematically, one could relate a small change in permittivity to a shift in frequency by sensitivity analysis:

$$\frac{\Delta f}{f} \approx -\frac{1}{2} \cdot \frac{\Delta \varepsilon_{eff}}{\varepsilon_{eff}} \qquad (5.16)$$

If hydration changes the skin's $\varepsilon_r$ by e.g. 5%, and if that skin accounts for, say, 50% of the energy storage (with rest in air/substrate), then $\varepsilon_{eff}$ might change by ~2.5%, leading to about ~1.25% frequency shift (which at 2.45 GHz is ~30 MHz). These are rough estimates; our detailed simulation captures the exact shifts.

Now, the magnitude of ($S_{11}$) at a given frequency is also influenced by how loss is introduced by the tissue. Human tissue is conductive (due to ions), meaning it can absorb RF energy (convert it to heat). When the antenna is well-coupled to a high-loss medium, the radiation resistance part

of $Z_{in}$ can increase (the antenna effectively radiates power into the tissue as loss). This can sometimes broaden the resonance (lower Q-factor) and reduce the depth of the $S_{11}$ dip because some power is always absorbed even off-resonance. However, this work focuses on changes around the matched resonance.

### 5.7.1 Reflection Response and Hydration Capability

The S-parameter analysis of the H-shaped antenna under varying tissue hydration levels was carried out by simulating different effective dielectric constants ($\varepsilon_r$) corresponding to skin-like media. These dielectric constants were mapped to physiological hydration states as follows:

- $\varepsilon_r$ = 24.72: Hyperhydration (overhydrated)
- $\varepsilon_r$ = 29.72: Euhydration (normal hydration)
- $\varepsilon_r$ = 34.72: Hypohydration (dehydrated)

Resonant Frequency Shift ($\Delta f$)

As the hydration level decreases (i.e., from hyperhydration to hypohydration), the antenna's resonant frequency increases (Figure 5.24):

- Hyperhydration ($\varepsilon_r$ = 24.72): $f_r$ = 2.2128 GHz
- Euhydration ($\varepsilon_r$ = 29.72): $f_r$ = 2.2120 GHz
- Hypohydration ($\varepsilon_r$ = 34.72): $f_r$ = 2.2079 GHz

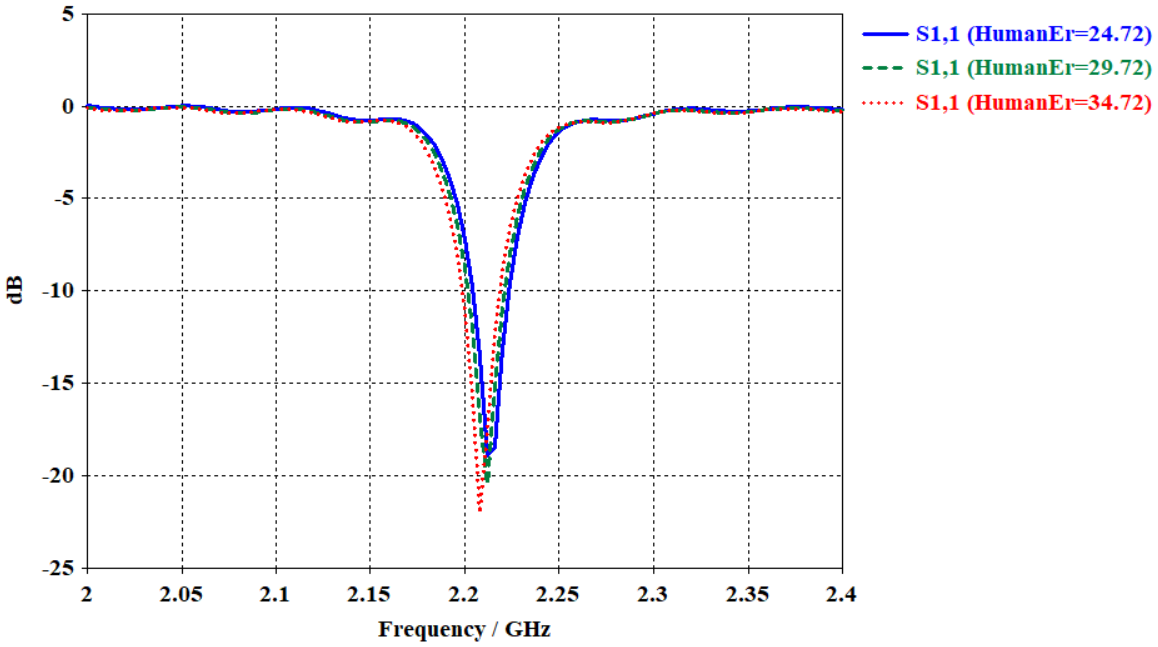


*Figure 5.25: Simulated magnitude of $S_{11}$ for H-shaped antenna placed 0.5 cm under the skin tissue for different hydration states.*

As hydration increases (i.e., the relative permittivity $\varepsilon_r$ decreases from 34.72 to 24.72), the resonant frequency shifts slightly downward ($\Delta f \approx 4.9$ MHz), and the magnitude of the reflection coefficient decreases, indicating increased absorption by the tissue. Although the frequency shift is relatively small, this result confirms the H-shaped antenna's sensitivity to subtle changes in tissue dielectric properties. Compared to simpler geometries such as rectangular patches, the H-structure's enhanced field concentration provides greater responsiveness to near-field dielectric loading, making it better suited for hydration monitoring.

The magnitude of the reflection coefficient $|S_{11}|$ also shows a clear relationship with hydration state:

- Hyperhydration ($\varepsilon_r$ = 24.72): $|S_{11}| \approx$ –18.82 dB
- Euhydration ($\varepsilon_r$ = 29.72): $|S_{11}| \approx$ –20.48 dB
- Hypohydration ($\varepsilon_r$= 34.72): $|S_{11}| \approx$ –21.85 dB

Dehydrated (hypohydrated) tissue reflects more energy due to its lower water content and dielectric loss, resulting in a more negative $S_{11}$ value (i.e., greater reflection and reduced absorption). This is consistent with electromagnetic theory: hyperhydrated tissue with higher permittivity and loss leads to more absorption and reduced reflection; hypohydrated tissue, with lower water content, presents lower permittivity and loss, thus reflecting more energy.

**5.8 Discussion**

The modelling and simulation results presented above demonstrate the feasibility and potential advantages of using a ferrite-impregnated H-shaped patch antenna for non-invasive hydration monitoring. The proposed design effectively interacts with dielectric variations induced by water content in the adjacent medium, thereby enabling the differentiation of hydration-related dielectric responses. However, the measured reflection coefficient ($|S_{11}|$) values of 18.82 dB, 20.48 dB, and 21.85 dB are typical, indicating that $|S_{11}|$ alone does not provide a uniquely distinguishing metric. Similar reflection magnitudes have been observed in other microwave hydration systems employing planar or ultrawideband (UWB) antennas. For instance, Besler and Fear [12] reported $|S_{11}|$ responses near −20 dB in a time-of-flight hydration monitoring system using forearm measurements, which are consistent with the present results.

While several studies have explored correlations between microwave permittivity and hydration changes in biological tissues or phantoms, no prior literature has modelled dielectric media explicitly to differentiate between multiple hydration states (e.g., dehydrated, euhydrated, and hyperhydrated) when interfaced with an H-shaped antenna structure. Previous works, such as those by Garrett and Fear [13] and Besler and Fear [12], focused primarily on bulk permittivity estimation or the correlation between permittivity and total body water changes, rather than discrete hydration-state classification based on dielectric modelling. Similarly, studies employing resonant cavity perturbation methods [14], skin dielectric devices [15], and radio-frequency absorptiometry [16] have demonstrated sensitivity to water content but did not resolve distinct hydration states through a dielectric–antenna interaction framework.

In contrast, the present study introduces a coupled dielectric–antenna modelling approach that integrates the dielectric properties of the medium directly into the electromagnetic behaviour of the ferrite-loaded H-shaped patch. This approach enables direct mapping of hydration-induced permittivity variations into measurable shifts in resonance frequency and impedance matching characteristics. The results demonstrate that the ferrite-impregnated H-shaped antenna can serve as a sensitive platform for hydration-state differentiation, advancing beyond empirical relationships between permittivity and body water content.

Consequently, this work contributes a novel methodology to the field of microwave biomedical sensing by showing, for the first time, that dielectric media can be modelled to distinguish hydration states when positioned adjacent to an H-shaped biosensor. The approach bridges a gap between traditional bulk permittivity estimation methods and more localized, field-interactive dielectric models, offering a promising route for future development of wearable or implantable hydration monitoring systems.

### 5.8.1 Significance of Ferrite Loading

Incorporating a ferrite into the antenna structure proved to be an effective strategy for miniaturization and sensitivity enhancement. This is in line with earlier studies on magneto-dielectric antennas, which showed that using materials with $\mu_r > 1$ can achieve size reduction without the severe bandwidth penalties of using high $\varepsilon_r$ alone [*17*]. Our results extend this concept to a sensing application, showing that the ferrite-loaded region not only shifts the frequency but also creates a concentrated interaction zone for the sensing target (hydrated skin). Importantly, we did this without requiring any external magnetic bias, meaning the ferrite operates in its linear region. This simplifies practical implementation compared to ferrite phase shifters or scanners

that need bias fields [17]. The success of this design suggests that magnetic materials can be a valuable addition to biomedical sensors, an area where most prior work has focused on purely dielectric substrates or conductive inclusions. It opens possibilities for further exploration, such as tuneable sensors (if one did apply a bias, one could tune the resonance frequency dynamically, though that's beyond our current scope).

### 5.8.2 Hydration Sensing Performance

The ability of the H-antenna to detect hydration changes via reflection coefficient shifts is promising. While our simulations used idealized hydration changes, in a real scenario one would calibrate the sensor with a person at known hydration levels (e.g., baseline euhydration vs after exercise-induced dehydration). The sensor can then be used to monitor changes over time. One practical approach could be to use a vector network analyser or a dedicated microcontroller with an RF module to continuously measure $S_{11}$ and track the resonant frequency. In fact, we envision a system where the antenna is connected to a miniaturized VNA (such as a one-port network analyser) that logs $S_{11}$ data. This concept is expected to be further elaborated in the next chapter where integration of a Raspberry Pi and NanoVNA are performed. Such hardware can sweep the 1–3 GHz range and detect the resonance. With appropriate software, it could classify the hydration state based on the reflection signature, like how we described more negative $S_{11}$ indicating dehydration and vice versa.

### 5.8.3 Robustness Considerations

A few factors need consideration for robust real-world use:

- Placement and Contact: The sensor's response depends on its coupling to the skin. Variations in pressure, angle, or air gaps will affect readings. A consistent attachment mechanism (like a stretchable band or adhesive) is needed. The H-patch design is relatively flat and could be incorporated into a flexible substrate or a wearable patch. The ferrite inclusion, if rigid, means the immediate area is rigid, but that piece is small. We could embed the ferrite in a flexible encapsulant to allow some conformability around it.
- Inter-Individual Variability: Different people have different skin thickness and baseline permittivity. While our sensor can detect changes for a given person, comparing absolute readings between people may require normalization. This is like how bioimpedance hydration measures often require a baseline calibration for each user.

- Environment: External electromagnetic interference around the S-band (WiFi, Bluetooth) could potentially affect measurements. However, since we are measuring at a specific frequency with a relatively narrowband sensor, interference can be mitigated by time-gating the measurements or using shielding. Also, our sensor is passive; it doesn't emit unless excited, so it's more about the VNA's ability to measure without interference.
- Safety**:** The power levels involved in reflection measurements are very low (on the order of microwatts or less for a VNA sweep), so there is no significant heating of tissue. This method remains well within safety limits for continuous use.

### 5.8.4 Limitations

Despite the positive results, there are some limitations and areas that need further work:

- Model Accuracy: As mentioned, the human tissue model was simplified. For precise quantification of hydration (e.g., to estimate % body water change), a more sophisticated model or empirical calibration will be needed. Our work establishes the qualitative and relative changes.
- Temperature Effects**:** Hydration changes are often accompanied by temperature changes (e.g., skin might heat up during exercise). Temperature can affect both the antenna (slight expansion or change in dielectric constant of substrate) and the skin permittivity. Investigating the sensor's thermal stability and perhaps incorporating temperature compensation would be wise. One idea could be to have a reference resonator that is not exposed to skin to distinguish between global shifts (like temperature) and local hydration changes.
- Ferrite Properties at High Frequency: We assumed an ideal ferrite with a given permeability at 2.22 GHz. Ferrite permeability can drop off at high frequencies and have resonance phenomena. Measuring the complex $\mu(\omega)$ of our ferrite sample across the band and feeding that into the simulation would improve accuracy. If the ferrite is lossy at 2.22 GHz, it could reduce the Q more than expected. So far, our assumption is that it's a low-loss material at this frequency range (some hexagonal ferrites are known to have useful properties in the GHz range [13].
- Bandwidth vs Sensitivity Trade-off: Our sensor is narrowband. One might ask if a broadband (ultrawideband) approach could detect hydration via spectral signatures. Indeed, some studies use broadband pulses to look for changes in the returned signal (e.g.,

in reflectometry). Our approach chooses a resonant narrowband method which is simpler to read but might miss some information. However, the narrowband resonance yields a strong feature to track. There is a trade-off: a broader bandwidth antenna could be less sensitive to small changes, as the energy is spread over frequencies.

## 5.9 Conclusion

This chapter presented the design, simulation, and evaluation of a novel non-invasive hydration sensor based on microwave reflection principles. Three preliminary antenna structures were investigated, the rectangular patch, circular patch, and complementary split-ring resonator (CSRR), to assess their sensitivity to hydration-related dielectric variations in skin tissue. While these designs demonstrated some potential, they were limited by low sensitivity, poor selectivity, or high susceptibility to air gaps and physical detachment from the skin.

To overcome these limitations, a ferrite-impregnated H-shaped patch antenna was proposed and rigorously analysed. The integration of barium ferrite (BaFe) in the high-magnetic-field region of the H-shaped patch achieved two key goals: miniaturization of the antenna structure and enhanced sensitivity to changes in tissue permittivity. Simulation results showed that while the resonance frequency remained largely stable across hydration states, the reflection coefficient varied significantly with tissue hydration level. This behaviour supports the sensor's effectiveness in distinguishing between hypohydrated, euhydrated, and hyperhydrated conditions based on $S_{11}$ measurements.

The proposed ferrite-loaded H-shaped patch antenna represents the novel sensing design introduced in this study. It demonstrated reduced sensitivity to air gap variations compared to the CSRR-based metamaterial antenna structure, highlighting its robustness and reliability for real-world wearable applications. Although the tissue modelling employed an effective permittivity approximation, a simplification. It provided a realistic first-order analysis that aligned well with physiological trends discussed in Chapter 4.

Overall, the chapter has established the theoretical foundation and simulation validation for a compact, high-Q, and hydration-sensitive sensor. The proposed ferrite-based H-shaped patch sensor exhibits promising performance characteristics suitable for wearable deployment. The next step, addressed in Chapter 6, involves experimental validation with human participants to evaluate the practical accuracy and robustness of this sensing approach under dynamic physiological conditions.

## 5.10 References


[1] Balanis, C. A., Antenna Theory: Analysis and Design, 4th Edition, Wiley, Mar. 2016.

[2] T.C. Edwards, M.B. Steer, Foundations for Microstrip Circuit Design, Wiley, 2016.

[3] Eldumiati, I.I.; Haddad, G.I. Cavity Perturbation Techniques for Measurement of the Microwave Conductivity and Dielectric Constant of a Bulk Semiconductor Material. IEEE Trans. Microw. Theory Tech. 1972, 20, 126–132.

[4] Fu, H.; Xiao, X.; Li, J.; Zong, Y. Study on a Glucose Concentration Measurement System Based on Microwave Perturbation Technique. J. Microw. Power. Electromagn. Energy 2015, 49, 215–224.

[5] C. Caloz, T. Itoh, Electromagnetic Metamaterials: Transmission Line Theory and Microwave Applications. 2006, Wiley-IEEE Press.

[6] K. Katke and S. Popalghat, "H-Shape Microstrip Patch Antenna: Design, Simulation, and Characterization," Int. J. Sci. Res. Sci. Technol., pp. 54–58, 2024, doi: 10.32628/IJSRST2411199.

[7] R. Kant, D.C. Dhubkarya, "Design & Analysis of H-shaped Microstrip Patch Antenna," Global Journal of Researchers in Engineering, vol. 10, issue 6, 2020, pp. 26-29.

[8] Koziel, Slawomir, and Adrian Bekasiewicz. "Simulation-driven Size-reduction-oriented Design of Multi-band Antennas by Means of Response Features." IET Microwaves, Antennas & Propagation, vol. 12, no. 7, 2018, pp. 1093-1098, https://doi.org/10.1049/iet-map.2017.0632.

[9] Leah Margaret Ridgway, PhD thesis entitled "Magneto-Dielectric Properties of Bismuth Substituted Barium Hexaferrite," 2011, University of Nottingham.

[10] Guha, Debatosh, and Yahia MM Antar, eds. Microstrip and printed antennas: new trends, techniques and applications. John Wiley & Sons, 2011.

[11] Ignacio J. Garcia Zuazola, Ashwani Sharma, Misha Filip, and William G. Whittow, "Antenna Using a Magnetic-Slab Located in the Principal Magnetic-Field Region Beneath the Patch," Progress in Electromagnetics Research C, Vol. 110, 229-241, 2021. doi:10.2528/PIERC21010303

[12] B. C. Besler and E. C. Fear, "Microwave Hydration Monitoring: System Assessment Using Fasting Volunteers," *Sensors*, vol. 21, no. 21, p. 6949, Oct. 2021, doi: 10.3390/s21216949.

[13] D. C. Garrett and E. C. Fear, "Feasibility Study of Hydration Monitoring Using Microwaves—Part 1: A Model of Microwave Property Changes with Dehydration," *IEEE J. Electromagn. RF Microwaves Med. Biol.*, vol. 3, no. 4, pp. 292–299, Dec. 2019, doi: 10.1109/JERM.2019.2911849.

[14] M. P. Robinson, J. Clegg, and D. A. Stone, "A Novel Method of Studying Total Body Water Content Using a Resonant Cavity: Experiments and Numerical Simulation," *Phys. Med. Biol.*, vol. 48, no. 1, pp. 113–125, 2003, doi: 10.1088/0031-9155/48/1/308.

[15] J. Nuutinen, R. Ikäheimo, and T. Lahtinen, "Validation of a New Dielectric Device to Assess Changes of Tissue Water in Skin and Subcutaneous Fat," *Physiol. Meas.*, vol. 25, no. 2, pp. 447–454, 2004, doi: 10.1088/0967-3334/25/2/004.

[16] D. S. Moran, Y. Heled, M. Margaliot, Y. Shani, A. Laor, S. Margaliot, E. E. Bickels, and Y. Shapiro, "Hydration Status Measurement by Radio Frequency Absorptiometry in Young Athletes—A New Method and Preliminary Results," *Physiol. Meas.*, vol. 25, no. 1, pp. 51–59, 2003, doi: 10.1088/0967-3334/25/1/005.

[17] A. Darvazehban, "Reconfigurable antennas for electromagnetic torso imaging," PhD dissertation, 2021. DOI: 10.14264/e9c2566

[18] J. S. Parish, The Design and Implementation of Continuous Frequency and Bandwidth Tunable Combline Cavity Filters, Ph.D. dissertation, Univ. of Leeds, 2018.

# 6. Prototype Biosensor and Measured Results

## 6.1 Fabrication of Ferrite-Embedded Biosensor

### 6.1.1 Substrate Selection and Preparation

To prototype hydration sensor antennas, two antenna designs were fabricated:

- A standard rectangular microstrip patch antenna (used as a reference), and
- An H-shaped slot patch antenna with an embedded ferrite element, designed for enhanced sensitivity.

Both antennas were implemented on a low-loss microwave substrate from the Taconic TLY series, selected for its stable dielectric properties and excellent machinability. The substrate had a thickness of approximately 0.8 mm, a relative permittivity of $\varepsilon_r \approx 2.2$, and a loss tangent of tanδ ≈ 0.001. Each substrate was copper-clad on both sides with 35 μm thick copper, enabling the creation of a patch on the top layer and a ground plane on the bottom.

Before milling, the substrate was thoroughly cleaned and securely fixed to the milling bed to ensure flatness and prevent movement during fabrication. Proper surface preparation was essential for consistent copper removal and precision in the final antenna geometry.

### 6.1.2. PCB Milling Using LPKF

The sensors were fabricated using an LPKF ProtoMat E44 milling machine, shown in Figure 6.1. This computer-controlled machine removes unwanted copper by mechanical milling, eliminating the need for chemical etching. The LPKF system supports double-sided PCB production, including via drilling, connector hole fabrication, and board profiling in a single workflow.

Sensor layouts were exported as Gerber files (including patch geometries and alignment marks) and loaded into the LPKF software. Milling was carried out using a high-speed spindle operating at approximately 100,000 RPM. Fine features, such as the H-slot patch contours, were milled using a 0.5 mm diameter drill bit, while broader copper areas were cleared using a 2 mm drill bit.

Although the ProtoMat provides high precision with a positional resolution of ~0.25 μm, practical constraints such as tool diameter and slight substrate unevenness introduced a dimensional tolerance of about ±0.1 mm for critical features. Both the rectangular patch (~30 mm × 32 mm) and the H-slot patch were patterned on the top copper layer, with the ground plane left intact on the underside.

To ensure proper registration between front and back features, the ProtoMat's fiducial camera and flip-alignment function were used during double-sided milling. This ensured precise alignment of the patch, ground plane, and drilled holes. After milling, excess copper was cleanly removed, resulting in sharp, well-defined patch edges with minimal burring.

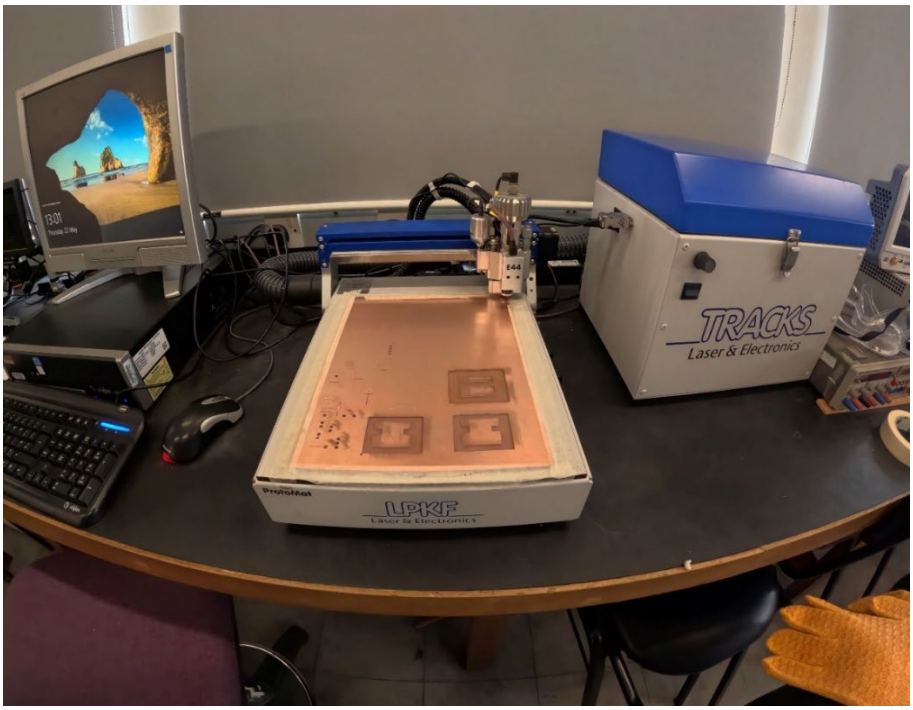


*Figure 6.1: PCB milling in progress using an LPKF ProtoMat machine. The setup shows a copper-clad board being precisely engraved with circuit patterns, controlled via a connected desktop workstation.*

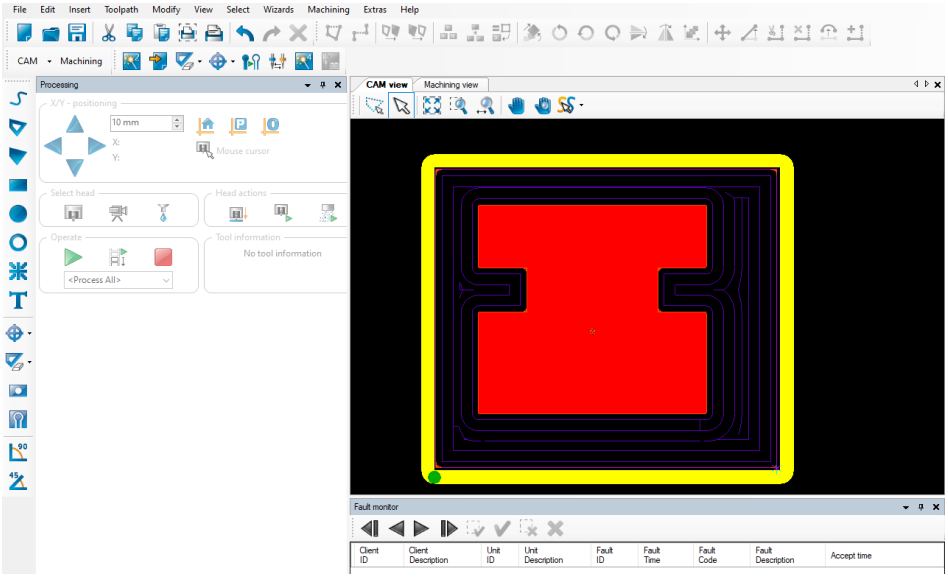


*Figure 6.2: LPKF software interface displaying the simulated milling toolpath for an H-shaped biosensor.*

### 6.1.3. Ferrite Embedding Technique and Assembly

A key feature of the second antenna design is the integration of a ferrite element into the patch structure to achieve localized magneto-dielectric loading. Instead of employing a full ferrite substrate, which would increase weight and losses, a targeted embedding approach was used. As detailed in Chapter 5, simulation results showed that the strongest RF magnetic fields under the patch are concentrated in the central region of the H-shaped structure. By placing a small ferrite insert in this high-H-field zone, the fundamental resonant frequency can be effectively reduced (due to increased effective permeability, $\mu$), while minimizing ferrite volume and associated losses.

The embedding process involved the following steps:

***Step 1: Preparation of Ferrite Samples***

Magnetic ferrite materials were cut into rectangular strips to fit a 10 mm × 10 mm area. The required thickness of the ferrite layer was 1.7 mm. Barium ferrite (BaFe), sourced from floppy tape sheets, was chosen due to its high relative permeability ($\mu_r \approx$ 4.3 at GHz frequencies) and low loss characteristics in the GHz range.

***Step 2: Milling a Recess in the Substrate***

A shallow rectangular recess (10 mm × 10 mm, depth 0.7 mm) was milled into the Taconic substrate using the LPKF ProtoMat machine. This cavity was created to precisely house the ferrite insert.

***Step 3: Inserting the Ferrite into the Recess***

Pre-cut BaFe strips were carefully inserted into the milled cavity. To ensure uniform contact and eliminate air gaps, the layers were bonded using a thin, even layer of epoxy. Proper alignment and flush placement were critical to maintaining structural planarity and ensuring electromagnetic continuity.

***Step 4: Final Assembly beneath the Radiating Patch***

Once the ferrite was securely embedded, it was covered with a copper sheet to form a localized magneto-dielectric region between the patch and the ground plane. This configuration provided enhanced local inductive loading, enabling antenna miniaturization without degrading performance.

***Step 4: Final assembly under the radiating patch***

Once the ferrite was securely embedded it was covered with a sheet of copper to create a localized magneto-dielectric region between the patch and ground. This configuration enhanced the local inductive loading, enabling significant antenna miniaturization without compromising performance.

Figure 6.3 illustrates the sequential steps used to integrate the ferrite layer into the antenna substrate.

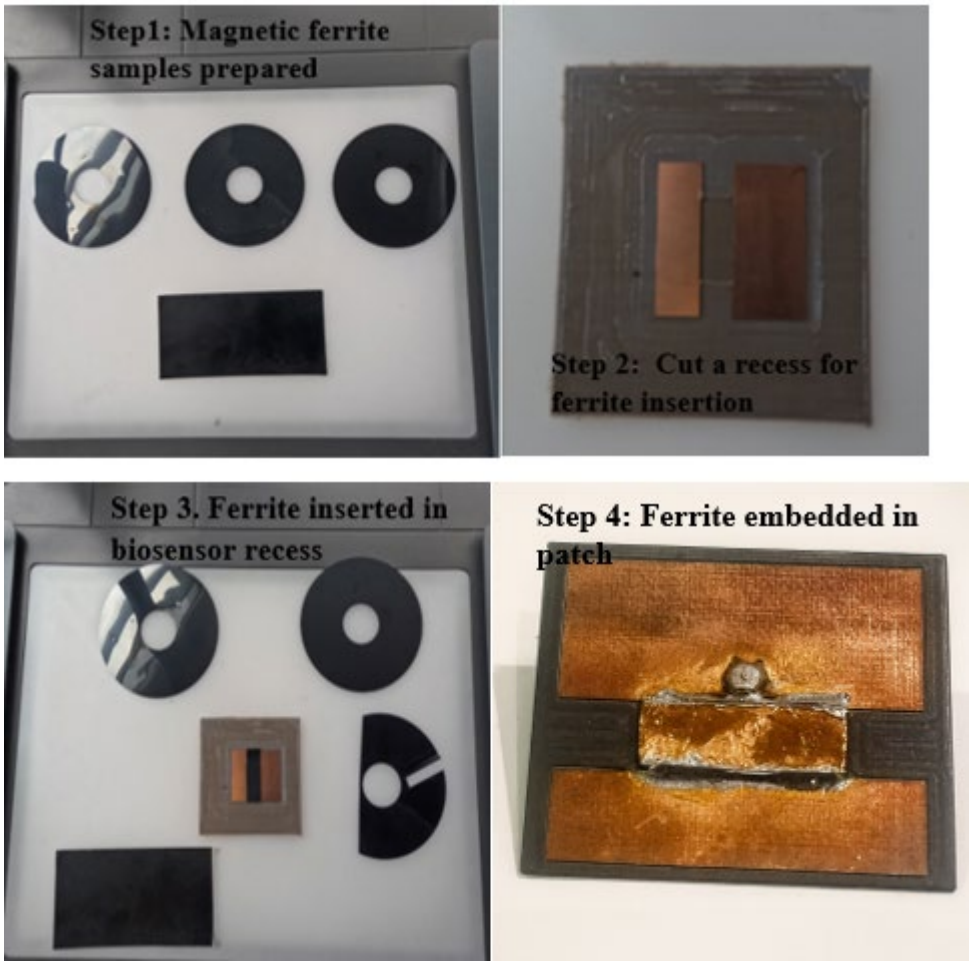


*Figure 6.3: Step-by-step assembly and fabrication process of the ferrite-embedded patch biosensor.*

**Challenges**

Embedding the ferrite, as illustrated in Figure 6.3, presented several fabrication challenges that required careful handling and precision.

***1. Cutting and Stacking the Ferrite:***

The first challenge involved cutting the brittle ferrite ceramic to the required dimensions. Ferrite sourced from floppy disk materials contains plastic binders, which can alter its resonance characteristics. To achieve the required thickness of 1.7 mm, 17 thin sheets had to be precisely stacked. This process demanded extreme care, as the ferrite is fragile and prone to cracking. A sharp blade was used to minimize breakage during cutting.

***2. Precise Alignment within the Cavity:***

Accurate placement of the ferrite insert within the milled cavity was critical for maintaining the desired resonance behaviour of the biosensor. Even slight misalignments, on the order of a few millimetres, could significantly impact performance, particularly coupling and resonance frequency. To ensure proper positioning, alignment marks were scribed on both the substrate and the ferrite, and the insertion process was guided under a microscope.

***3. Mounting and Surface Profile Matching:***

Achieving a reliable mechanical and electromagnetic interface between the ferrite and the substrate was essential. The cavity was initially milled slightly shallower than the ferrite's thickness and then incrementally deepened to achieve a better fit. Despite efforts to level the surface, the final 1.7 mm ferrite height exceeded the 0.8 mm substrate thickness, resulting in a slight ridge at the insertion site. This created a surface discontinuity, as the ferrite was not fully flush with the patch layer.

To mitigate the effects of this mismatch:

- A minimal amount of epoxy was used to avoid introducing air gaps.
- Uniform pressure was applied during curing to ensure a thin, consistent adhesive layer.
- Copper continuity around the ferrite edges was verified to reduce parasitic effects and ensure electrical integrity.

Although the protruding ferrite introduced a local variation in the surface profile, careful bonding and alignment helped preserve acceptable electrical performance. The resulting antenna had a total thickness of approximately 2.5 mm, making it suitable for compact and wearable applications.

### 6.1.4. Connector Attachment and Post-Processing

Both antenna prototypes were fed using standard 50 Ω coaxial SMA connectors, as illustrated in Figure 6.4.

For the rectangular patch antenna, a coaxial feed was implemented by drilling a hole at the designated feed location offset from the patch centre to achieve impedance matching. The centre pin of the SMA connector was soldered to the patch on the top layer, while the connector flange was soldered to the ground plane on the bottom layer.

For the H-slot patch design, a similar hole was drilled through the substrate at the feed point. An end-launch SMA connector was used, with its centre conductor extending through the substrate to connect with the underside of the patch. The ground of the connector was soldered to the backside ground plane.

After the SMA connectors were installed, each board was carefully inspected under a magnifier to check for copper burrs, solder bridges, or shorts. Post-processing included edge deburring and cleaning the board surfaces using isopropyl alcohol to remove any remaining grease, flux, or debris.

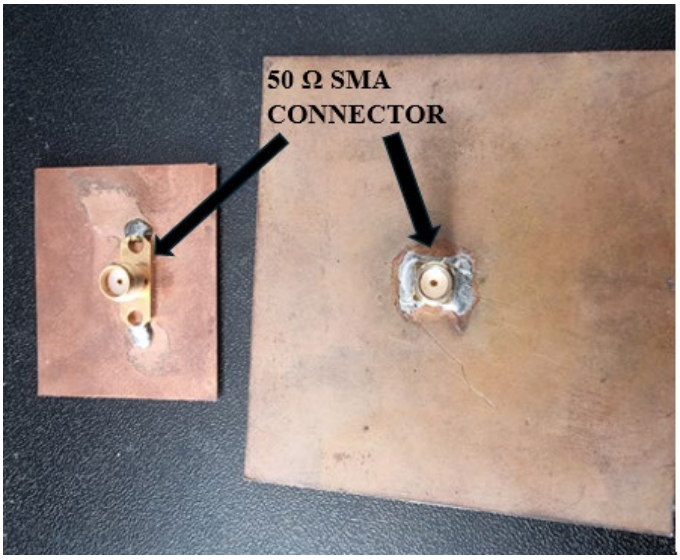


*Figure 6.4: Rear view of the fabricated patch antennas, showing soldered 50 Ω SMA connectors used for RF signal feeding and measurement.*

**Fabrication Challenges and Tolerances**

Several fabrication challenges were encountered and systematically addressed during the prototyping process to ensure the antennas met their design specifications.

***1. Precision Milling of the H-Slot:***

Accurate milling of the H-shaped slot was critical, given the limitations of the LPKF ProtoMat's tool diameter. The design specified a 1.0 mm wide slot, which was achieved using a 0.5 mm endmill in two overlapping passes. To minimize dimensional deviations, the tool path was first calibrated on scrap substrate, and a slight overlap between passes was introduced to maintain a consistent slot width. The final slot dimension deviated by approximately ±0.1 mm from the intended width.

***2. Double-Sided Feature Alignment:***

Precise alignment of top and bottom features was essential, particularly for the coaxial feed via, which needed to emerge exactly at the patch's feed point. The ProtoMat's fiducial alignment system was used for accurate registration. In early trials where alignment markers were omitted, misaligned via holes rendered some boards unusable. To address this, fiducial markers were incorporated into all subsequent designs, and all critical features (milling, drilling, and routing) were completed in a single coordinated job to preserve registration between layers.

***3. Ferrite Integration Constraints:***

Embedding the ferrite introduced additional manufacturing constraints. To avoid damaging the milling bit during cavity preparation, milling was intentionally stopped slightly before reaching full depth. The remaining thin substrate layer was manually cleared using a fine hand drill. During epoxy curing, a non-magnetic clamping weight was used to apply uniform pressure and maintain ferrite alignment, preventing any shifting or tilt.

***4. Mechanical Handling and Assembly:***

The presence of the slot weakened the mechanical integrity of the substrate in localized areas. To avoid cracking or delamination, especially during SMA connector soldering, the board was supported on a flat, rigid surface throughout assembly. This support ensured that pressure during soldering did not stress the fragile slot region.

Despite these challenges, the final prototypes successfully met both structural and electromagnetic performance requirements, validating the fabrication approach.

## 6.2. Measurement Setup and Calibration

### 6.2.1. S-Parameter Measurement Using a Vector Network Analyzer

The fabricated antennas were characterized through S-parameter measurements, focusing on the reflection coefficient ($S_{11}$) to evaluate their resonant behaviour.

Two types of Vector Network Analyzers (VNAs) were employed for antenna characterization:

- NanoVNA V2: A compact, portable device ideal for low-frequency measurements and quick, on-site prototyping.
- Rohde & Schwarz VNA: A high-precision instrument capable of operating over a wide frequency range (100 kHz to 20 GHz), used for detailed laboratory testing.

Each antenna was connected to the VNAs using coaxial cables with SMA connectors, as illustrated in Figures 6.5 and 6.6. To maintain measurement integrity—particularly during on-body tests—a phase-stable coaxial cable was used to minimize signal variation caused by cable movement. Additionally, a right-angle SMA adapter was incorporated to route the cable away from the antenna, reducing mechanical strain and electromagnetic interference near the test site.

This setup ensured consistent impedance matching and minimized external influences that could distort the results. The NanoVNA V2 was especially useful during early prototyping and rapid in-situ checks, while the Rohde & Schwarz VNA provided the high accuracy and stability required for characterizing antenna performance within the target frequency band of 1 GHz to 3 GHz.

This careful measurement configuration enabled reliable testing in both free-space and on-body conditions, allowing detailed analysis of critical factors such as detuning, body loading, and electromagnetic coupling. As a result, the setup offered comprehensive insights into the antenna's suitability for wearable biosensing applications.

.

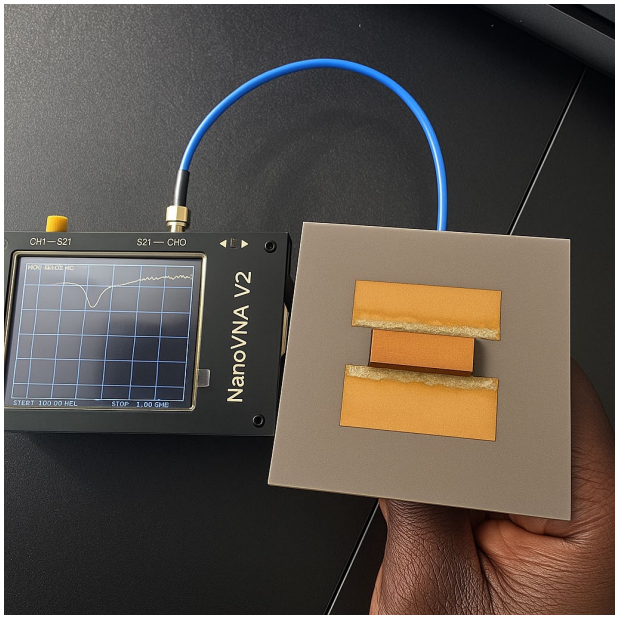


*Figure 6.5: Experimental setup showing the ferrite-embedded rectangular patch antenna connected to a NanoVNA V2 for hydration monitoring measurements.*

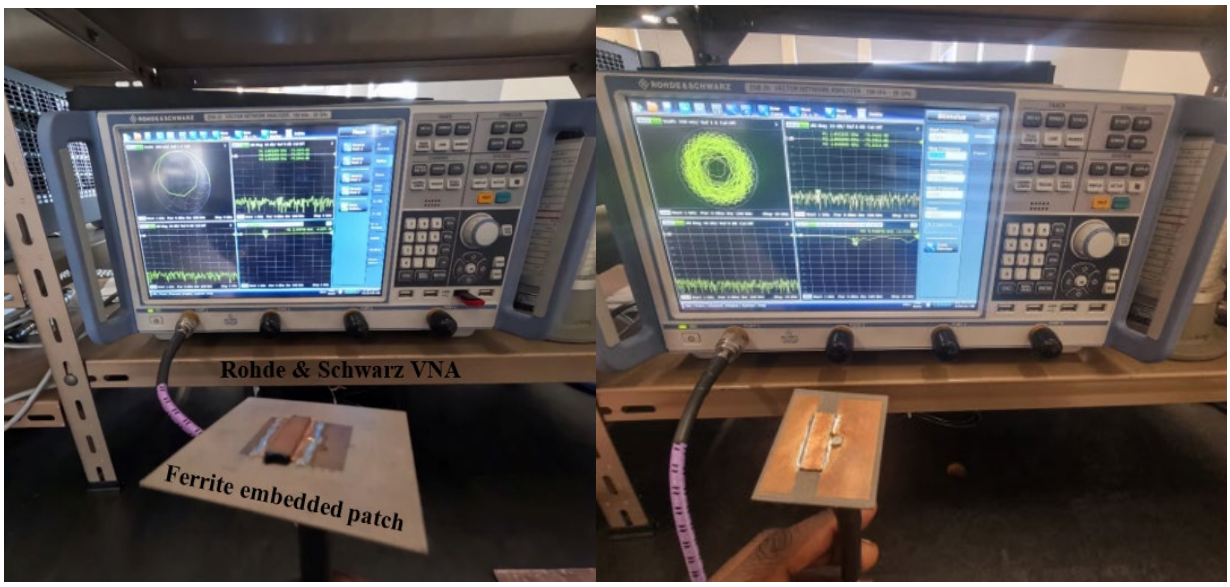


*Figure 6.6: The measurement setup for antennas characterization uses a Rohde & Schwarz Vector Network Analyzer (VNA). A 50Ω coaxial cable connects the VNA to the antenna under test, allowing S-parameter analysis of the antenna's performance.*

### 6.2.2. Calibration and Error Correction

Accurate $S_{11}$ measurements required careful calibration of the Vector Network Analyzer (VNA). A single-port (1-port) calibration was performed using standard Open, Short, and 50 Ω Load (OSL) references applied at the end of the coaxial cable, effectively calibrating to the measurement plane at the SMA connector interfacing with the antenna. This process eliminated

systematic errors such as cable loss, mismatch, and phase delay, ensuring that the measured reflection coefficient accurately represents the antenna's true input characteristics.

To verify calibration quality, a known reference load (an SMA 50 Ω termination) was measured. The resulting return loss was better than –40 dB across the frequency band, confirming a high-quality calibration.

In addition to the OSL procedure, a baseline measurement was also conducted with the antenna placed in a controlled free-space environment (i.e., in air with no nearby objects). This served as a secondary reference, allowing on-body results to be normalized if needed.

To further improve measurement accuracy, the VNA's time-domain gating function was optionally applied to suppress potential reflections caused by cable radiation. However, such effects were found to be negligible in this setup.

Connector repeatability was also assessed by repeatedly disconnecting and reconnecting the antenna. The variation in $S_{11}$ at resonance was consistently below 0.1 dB, indicating highly stable and repeatable connections.

No external impedance matching or tuning elements were employed during testing; all antennas were measured as fabricated, under real-world operating conditions.

### 6.2.3. On-Body Measurement Procedure

To evaluate the sensor under realistic conditions, $S_{11}$ measurements were performed with the biosensor positioned on the ventral side of a volunteer's wrist, directly over the radius/ulna region. For the ferrite-embedded rectangular patch design, the patch face was placed in direct contact with the skin, while the ground plane faced outward. Although no physical strap was used to secure the sensor, consistent positioning and pressure were carefully maintained across all measurements to ensure repeatability. The biosensor structure remained unchanged throughout all tests, enabling a fair and controlled comparison between the unloaded rectangular patch and the ferrite-loaded variant.

It was observed that minimizing the air gap between the antenna and the skin was critical for performance. Even sub-millimetre separations (as small as <5 mm), caused by natural skin curvature or the presence of arm hair, resulted in a noticeable upward shift in resonant frequency. To address this, the sensor was manually held in place during measurements, ensuring firm

contact with the skin while avoiding excessive pressure. A short stabilization period was allowed before each measurement to account for minor shifts due to hand motion or sensor settling.

To further examine the antenna's sensitivity to spacing, controlled off-skin measurements were conducted using foam spacers to introduce air gaps of 0.5 cm and 1.0 cm between the patch and the skin. As expected, increasing the gap led to:

- An upward shift in the resonant frequency, and
- A reduction in the magnitude of the reflection coefficient,

These effects are consistent with weaker electromagnetic coupling to the underlying tissue. Among the tested configurations, a 5 mm air gap was identified as the optimal compromise—providing sufficient sensitivity while maintaining signal stability in practice.

To enhance field confinement and strengthen local interaction with skin tissue, a gold-plated copper tube was inserted inside the short cylindrical protrusion from the green housing which is located above the sensor inside the housing (see Figure 6.7 & 6.8). This metallic shielding helped to concentrate the electric field within a narrower region. When the skin was placed directly at the open end of the protrusion, the sensor exhibited a noticeable increase in sensitivity, attributed to enhanced capacitive coupling and reduced field leakage. This configuration significantly improved near-field interactions and signal responsiveness, demonstrating strong potential for on-body biosensing applications.

All tests were conducted in a controlled laboratory environment at a room temperature of approximately 22 °C. The VNA was configured to sweep 201 points across the 1–3 GHz range, and $S_{11}$ data was averaged over 5 consecutive sweeps to reduce noise and enhance measurement reliability.

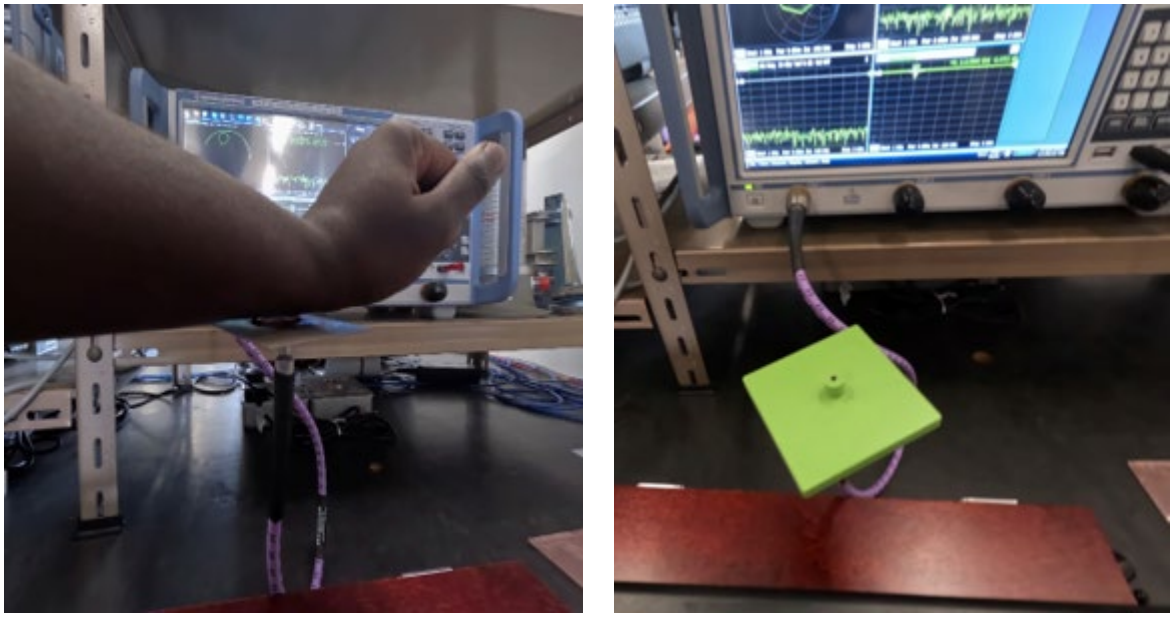

*Figure 6.7: Characterization of the wearable biosensing antenna using a Rohde & Schwarz Vector Network Analyzer. Left: On-body measurement with the antenna positioned near the wrist to assess the impact of human body loading. Right: Free-space calibration and testing using a dielectric support fixture to establish baseline antenna performance.*

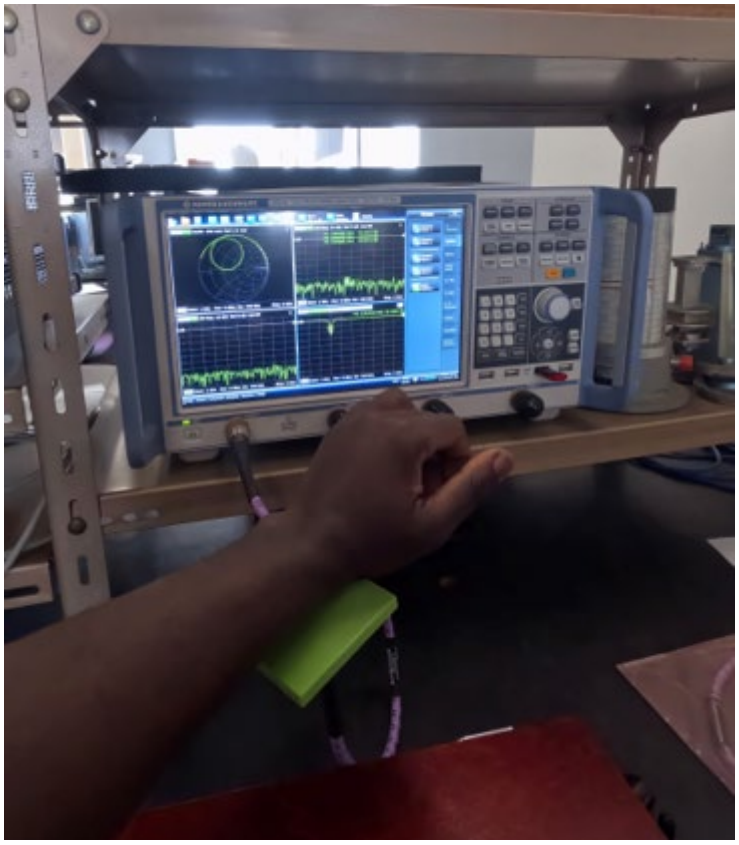

*Figure 6.8: On-body antenna testing was conducted using a Rohde & Schwarz Vector Network Analyzer. The wearable antenna was positioned on the forearm and connected via a phase-stable coaxial cable to capture real-time $S_{11}$ measurements.*

## 6.3. Results and Discussion

### 6.3.1. Measured Reflection Coefficient Characteristics

The rectangular ferrite-embedded patch antenna was fabricated and evaluated by measuring its reflection coefficient ($S_{11}$) under both free-space and on-body (wrist) conditions. Figure 6.9 displays the measured $S_{11}$ responses obtained from the corresponding Touchstone files.

In the free-space configuration, the antenna demonstrated a clear resonant dip in $S_{11}$ at approximately 2.20 GHz, with a reflection coefficient of –9.32 dB. This indicates a reasonably good impedance match to the standard 50 Ω reference environment, suitable for air-based testing.

When the antenna was placed on the ventral side of the wrist, the resonant frequency shifted upward to approximately 2.24 GHz, and the reflection coefficient improved significantly to –30.10 dB. This shift is attributed to the dielectric loading effect introduced by biological tissue, which possesses a higher relative permittivity than air. The proximity of tissue modifies the antenna's input impedance and slightly increases the effective permittivity of the surrounding environment, leading to enhanced impedance matching. These results demonstrate that the antenna not only maintains consistent performance across environments but also benefits from improved reflection coefficient in on-body applications. The ability to achieve better impedance matching when in contact with human tissue suggests that the antenna is well-suited for wearable and biomedical sensing.

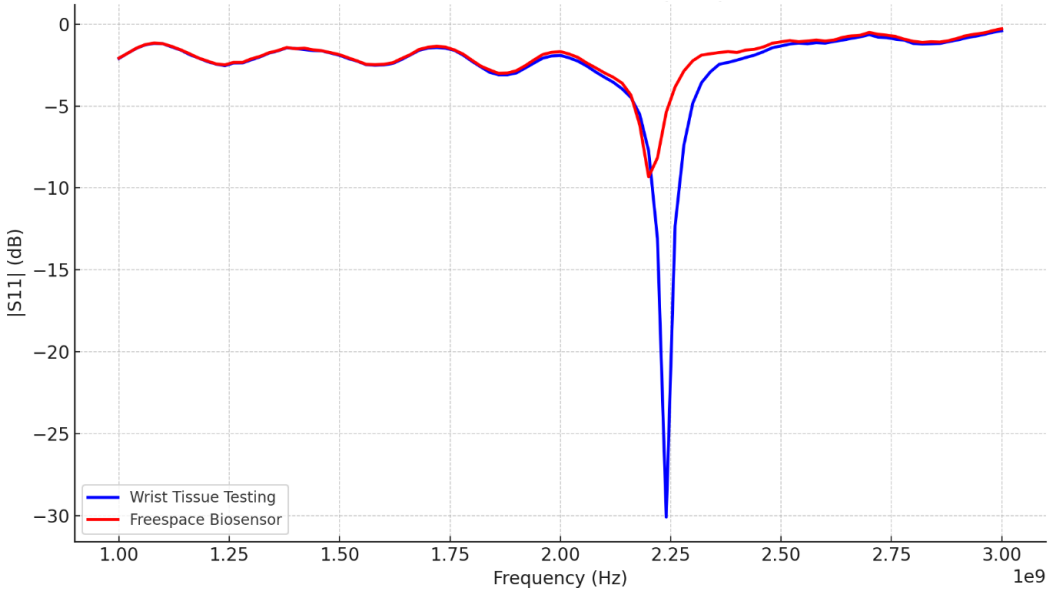


*Figure 6.9: Comparison of $S_{11}$ reflection coefficient measurements for the biosensor in free-space and on-body (wrist tissue) configurations. The on-body measurement (blue curve) exhibits a clear downward shift in resonant frequency and a deeper reflection coefficient near 2.25 GHz, highlighting the impact of tissue loading on antenna performance.*

A summary of the key performance parameters for both free-space and wrist-worn conditions is provided in Table 6.1.

*Table 6.1: Comparison of antenna performance under free-space and on-body conditions*

| Sensor | $f_r$ in Air (GHz) | $S_{11}$ in Air (dB) | $f_r$ On-Wrist (GHz) | $S_{11}$ On-Wrist (dB) |
|---|---|---|---|---|
| **Ferrite embedded rectangular patch** | 2.22 | –9.33 | 2.24 | –30.10 |

### 6.3.2. Resonance Shifts with Hydration and Tissue Coupling

The rectangular ferrite-embedded patch antenna was fabricated and experimentally evaluated under both free-space and on-body (wrist-mounted) conditions. The corresponding S-parameter measurements are shown in Figure 6.10, illustrating the effects of body loading on antenna performance.

In the free-space scenario, the antenna exhibited a resonant frequency of approximately 2.20 GHz, with a reflection coefficient of –9.33 dB, indicating a moderate impedance match in air. However, when mounted on the wrist, the resonant frequency shifted upward to 2.24 GHz, accompanied by a significantly improved reflection coefficient of –30.10 dB.

This upward frequency shift is noteworthy and somewhat counterintuitive. On-body loading is typically associated with a downward shift in resonance due to the increased effective permittivity introduced by proximity to high-permittivity biological tissue. The observed shift suggests a more complex electromagnetic interaction, potentially involving:

- Near-field detuning effects,
- Altered current distribution across the patch,
- Or heterogeneity in tissue composition, which affects local dielectric properties and antenna-body coupling dynamics.

Despite the shift in frequency, the marked improvement in impedance matching, as evidenced by the deeper reflection coefficient, indicates that the antenna achieved stronger coupling with the biological tissue. This result supports the interpretation that dielectric loading from the body modified both the real and imaginary components of the input impedance, bringing them closer to the 50 Ω reference used by the measurement system.

The enhanced reflection coefficient observed in on-body conditions underscores the importance of in-situ testing for wearable antenna applications. It demonstrates that free-space performance does not fully reflect real-world usage and validates the need to consider tissue coupling effects during the design and evaluation of biosensing antennas.

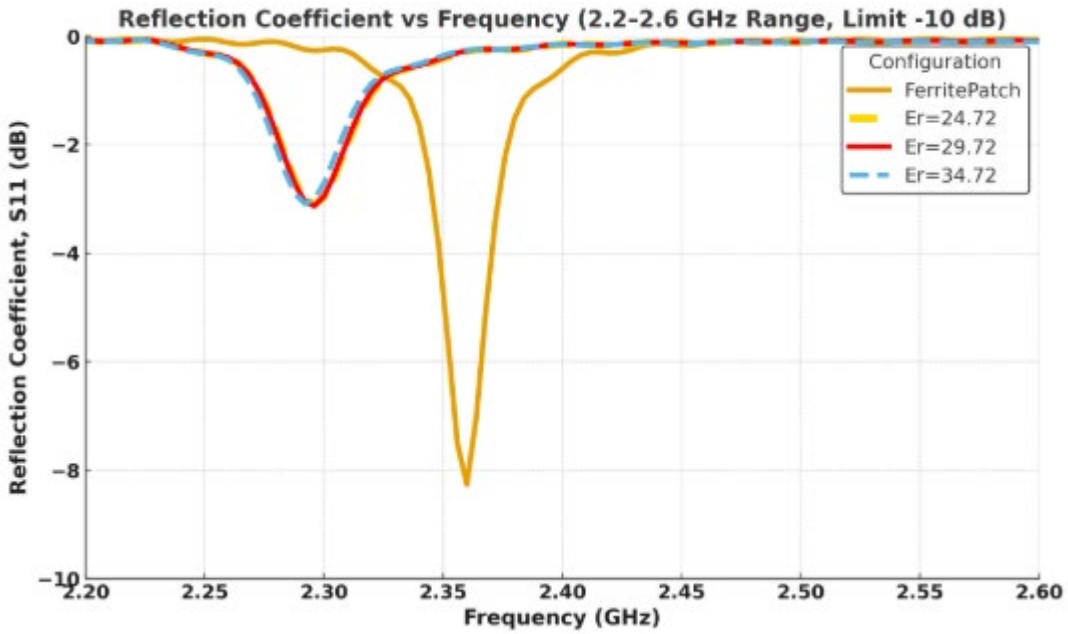


*Figure 6.10: Simulated reflection coefficient vs. frequency plot for various dielectric constant values ($\varepsilon_r$ = 24.72, 29.72, 34.72) and ferrite patch configurations across the 2.2–2.60 GHz range.*

### 6.3.3 Comparison to Simulated Performance

The performance of the ferrite-based patch biosensors was evaluated under both free-space (in-air) and tissue-loaded (on-wrist) conditions, using simulated models and fabricated prototypes. These biosensors were designed to operate within the 2.2–2.4 GHz frequency range, a band commonly used in biomedical telemetry due to its favourable trade-off between tissue penetration and compact antenna size.

This comparison focuses on two primary performance metrics:

- The resonance frequency ($f_r$), and
- The reflection coefficient ($S_{11}$), which together characterize impedance matching and radiation efficiency under different dielectric environments.

***Simulated Performance***

In simulations, the ferrite patch antenna exhibited a resonance frequency of 2.36 GHz in free-space, with a reflection coefficient of –8.226 dB, indicating a moderate impedance match. When

tissue loading was introduced (simulating contact with human skin), the resonance shifted downward to 2.296 GHz, and the reflection coefficient deteriorated to –2.794 dB. This degradation is attributed to the high permittivity and lossy nature of biological tissue, which alters the antenna's effective dielectric environment, affecting both its resonance and impedance matching.

The relatively poor $S_{11}$ value under tissue conditions suggests that the simulated design experienced substantial reflection losses and impedance mismatch, potentially limiting its real-world biosensing performance.

***Fabricated Performance***

By contrast, the fabricated ferrite patch biosensor demonstrated significantly better performance in both free-space and on-body conditions:

- In free space:
  - Resonant frequency = 2.22 GHz
  - reflection coefficient = –9.33 dB (better than the simulated design)
- On the wrist:
  - Resonant frequency shifted slightly to 2.24 GHz
  - Reflection coefficient improved dramatically to –30.10 dB

This result is particularly noteworthy because it shows that the fabricated antenna not only maintains performance in the presence of tissue but actually performs better on-body than in air. The minimal frequency shift ($\Delta f \approx +0.02$ GHz) also indicates high robustness against detuning, a critical feature for wearable biosensors expected to operate reliably across various user anatomies and motion conditions.

A detailed comparison of the key parameters between simulated and fabricated sensors is provided in Table 6.2.

*Table 6.2: Performance analysis between simulated and fabricated biosensor designs*

| **Biosensor** | **Free space resonance ($f_r$) (GHz)** | **$S_{11}$ in Air (dB)** | **Tissue resonance ($f_r$) (GHz)** | **$S_{11}$ On-Wrist (dB)** |
|---|---|---|---|---|
| Simulated ferrite patch | 2.36 | -8.226 | 2.296 | -2.794 |
| Fabricated ferrite patch | 2.22 | -9.33 | 2.24 | -30.10 |

***Discission and Interpretation***

These results highlight several key insights:

1. *Limitations of Electromagnetic Simulation*

   The discrepancy between simulated and measured results, especially under tissue loading, underscores the limitations of idealized simulation models in capturing the complexity of real biological environments. Factors such as fabrication tolerances, ferrite inhomogeneity, and unmodeled anatomical variability contribute to these differences.

2. *Role of Real-World Material Interactions*

   The significant improvement in reflection coefficient observed in the fabricated prototype suggests that physical phenomena like enhanced magnetic coupling and substrate loss balancing may benefit practical antenna performance, effects not fully predicted by simulation.

3. *Influence of Practical Design Considerations*

   Several real-world factors can explain the performance gap:

   - *Material tolerances*: Variability in the permittivity of the Taconic substrate or permeability of the ferrite tile can shift resonance.
   - *Anatomical realism*: Simulations often use homogeneous tissue models (e.g., $\varepsilon_r \approx 29.72$, $\sigma \approx 0.904$ S/m at 2.2 GHz), whereas actual tissue includes multiple layers (skin, fat, muscle, bone) and curved geometry, which impact coupling and detuning.
   - *Fabrication imperfections*: Misalignments in SMA connectors, soldering inconsistencies, or small air gaps can introduce parasitic elements not captured in idealized simulations.
   - *Unmodeled loss mechanisms*: The broader measured bandwidth and deeper reflection coefficient dip suggest additional losses in the fabricated prototype, possibly from magnetic loss tangent ($\tan\delta \approx 0.005$), epoxy layers, or copper surface roughness, that were not fully represented in the simulation.

The fabricated ferrite patch biosensor showed markedly enhanced performance compared to its simulated counterpart, especially in on-body conditions. Its excellent impedance matching,

minimal frequency shift, and superior reflection coefficient under tissue loading confirm its potential as a robust, reliable solution for continuous, non-invasive hydration monitoring.

These findings reinforce the importance of empirical validation in antenna development for biomedical applications, as certain beneficial effects, such as improved coupling or loss compensation, may emerge only through physical prototyping and testing.

### 6.3.4. Discrepancies and Possible Causes

While the overall agreement between the simulated and measured performance of the biosensor is satisfactory, several specific discrepancies were observed. These deviations and their likely causes are discussed below.

***Resonant Frequency Offset***

The measured free-space resonant frequency of the rectangular patch was 2.20 GHz, compared to 2.36 GHz in simulation, representing an approximate 2% downshift. This discrepancy may result from a higher-than-expected effective dielectric constant, possibly due to:

- A slightly greater actual substrate permittivity ($\varepsilon_r$) than assumed in the simulation,
- A fabrication-related over-etch that reduced the electrical length of the patch, effectively lowering the resonant frequency,
- Or rounded corners in the slot geometry caused by CNC milling, which can subtly alter the inductive and capacitive loading of the resonator.

These small geometric variations, common in prototype manufacturing, can significantly influence high-frequency behaviour and must be accounted for in future iterations.

***Reflection Coefficient Depth***

In the measured results, the fabricated biosensor showed a clear return loss dip around:

- 2.24 GHz in free space, and
- Approximately 2.20 GHz when worn on the wrist.

The minimum $S_{11}$ values were approximately –10.33 dB in free space and dropped below –30 dB under on-body conditions. While the free-space reflection coefficient slightly exceeds the simulated value (–8.22 dB), the significantly deeper reflection coefficient on-body indicates improved impedance matching due to dielectric loading by biological tissue. The presence of the body improves energy absorption and reduces impedance mismatch at the skin–antenna interface.

Slight variations in free-space results may be attributed to:

- Material losses, such as ferrite magnetic loss (tan δ),
- Measurement artifacts, including proximity effects from the coaxial feed cable.

It was observed that the positioning of the coaxial cable influenced the resonance dip. This underscores the need for a consistent measurement setup and may justify the use of baluns or ferrite clamps to minimize common-mode interference in future designs.

***Resonance Duality***

Contrary to concerns about potential resonance splitting in body-worn configurations, the fabricated patch antenna exhibited a single, well-defined resonance when placed on the wrist. No evidence of dual notches or mode splitting was found within the 2.0–2.4 GHz band, indicating:

- Good electromagnetic symmetry,
- Stable patch–skin coupling,
- And a well-controlled mechanical interface.

The absence of resonance splitting suggests that air gaps, sensor tilt, or uneven placement were either negligible or effectively managed. This outcome reinforces the mechanical stability of the design and the importance of consistent application practices in body-centric testing.

***Temperature Effects***

Although not the focus of this study, temperature-induced behaviour was observed during extended on-body testing. As the sensor remained in contact with the skin:

- A small upward drift of ~5–7 MHz in the resonant frequency was recorded.
- This is likely due to thermal effects, such as warming of the ferrite or dielectric substrate, which can alter their permittivity and permeability.
- Additionally, perspiration may accumulate at the sensor–skin interface, locally modifying the dielectric environment.

These observations highlight the need to account for thermal and environmental dynamics in wearable sensor design, especially in continuous or long-duration monitoring applications.

While minor discrepancies were observed between simulated and measured results, they did not hinder the functionality of the biosensor in detecting hydration changes. Understanding the root causes of these deviations provides valuable insight for future design refinements, including:

- Improved cable isolation,

- More accurate material characterization, and
- Enhanced thermal stability.

These lessons will help improve reliability and robustness in future wearable biosensing systems.

## 6.4. Practical Observations and Sensor Performance

### 6.4.1. Mechanical Robustness and Handling

In wearable applications, mechanical durability is as important as electrical performance. The fabricated rectangular patch sensors were constructed on a rigid 0.8 mm Taconic PCB substrate, with one variant incorporating a ferrite insert. Although these sensors are not flexible, their compact size (approximately 5 cm × 5 cm) makes them well-suited for wrist-mounted applications.

It was observed that the version containing the ferrite insert was slightly more fragile than the plain PCB counterpart. Specifically, mechanical stress, such as dropping or bending; could lead to cracking of the ferrite or delamination from the substrate.

To improve usability and resilience, a custom 3D-printed ABS frame was developed to snap around the PCB edges. This frame provided mechanical protection during handling and created a flat, stable surface for securing the sensor on the wrist with straps. A known point of mechanical vulnerability was the SMA connector, which, under lateral stress, risked copper trace delamination. This issue was mitigated by reinforcing the connector with epoxy, which significantly improved robustness and allowed for repeated connect/disconnect cycles without degradation.

For future iterations requiring enhanced flexibility or robustness, alternative materials such as flexible ferrite films and thin conformable substrates (e.g., polyimide) may be explored. However, such adaptations could introduce higher dielectric and magnetic losses, which must be carefully evaluated depending on the application.

### 6.4.2. Coupling with Skin and Contact Considerations

During testing, the patch antenna was manually held in place to ensure firm skin contact without excessive pressure (Figure 6.11). Overtightening was avoided, as it can compress underlying tissues and alter the local dielectric environment, potentially causing shifts in resonant frequency. Strap tension was carefully calibrated to keep the sensor secure and comfortable.

To evaluate sensitivity to air gaps, foam spacers of 0.5 cm and 1.0 cm were used to lift the patch incrementally away from the skin. As expected, increasing the gap caused:

- An upward shift in the resonant frequency, and
- A reduction in reflection coefficient depth.

These results confirmed that weakened electromagnetic coupling leads to diminished interaction with tissue. A 5 mm separation was identified as a practical compromise, balancing measurement stability and sensitivity. However, direct skin contact consistently yielded the most reproducible results.

Minor placement variability introduced baseline resonance shifts of up to ~10 MHz, which were attributed to:

- Differences in underlying tissue composition (e.g., muscle vs. bone), and
- Small changes in sensor orientation or contact pressure.

To ensure consistency, the mounting location on the wrist was visually marked, and effort was made to replicate placement conditions across measurements. While the patch generally conformed well to the forearm, slight edge lifting was observed on narrower wrists. Still, performance remained reliable as long as the central patch region-maintained contact with the skin. For better anatomical conformity, a smaller or flexible patch could be considered.

To enhance field localization and sensitivity, a cylindrical, gold-plated copper ring was integrated around the ferrite-loaded region of the patch. This enclosure helped to:

- Confine the electric field near the antenna surface, and
- Reduce unwanted radiation leakage.

When the skin was placed directly against the open face of the cylinder, stronger capacitive coupling was observed, improving the $S_{11}$ response and overall, near-field sensitivity.

Environmental conditions were maintained at a stable 22 °C, and each measurement was averaged over five VNA sweeps across the 1–3 GHz frequency range. A brief stabilization delay before each acquisition minimized signal variation caused by repositioning.

During extended wear, light perspiration occasionally formed beneath the sensor, resulting in a small downward frequency drift (a few MHz). This was likely due to a rise in local permittivity

from moisture at the skin–sensor interface. Although this effect was minor, it suggests potential utility for sweat or hydration sensing.

To maintain consistency and performance across trials, alcohol wipes were used after each test to clean the sensor surface and remove residual skin oils or moisture.

*Figure 6.11: Biosensor testing setup showing the user's forearm placed over the patch platform to evaluate electromagnetic interaction with the skin.*

### 6.4.3. Sensor Performance and User Observations

From a performance perspective, the rectangular patch biosensor demonstrated moderate sensitivity to hydration-related changes, as evidenced by variations in the $S_{11}$ parameter. When tested on wrist tissue, the antenna exhibited a downward shift in resonance frequency relative to the free-space (off-body) condition, with the reflection coefficient deepening to approximately –30 dB at around 2.25 GHz. This frequency shift, on the order of tens of MHz, suggests that the patch can detect small changes in tissue permittivity associated with hydration levels.

However, compared to high-Q resonant structures, the rectangular patch's resonance is broader and less sharply defined. While this reduces sensitivity to subtle dielectric variations, it also offers greater immunity to measurement noise and variability, making the system more robust for practical use.

#### *Signal Trends and Interpretation*

During on-body testing, consistent changes were observed in both:

- The resonant frequency, and
- The magnitude of the reflection coefficient, when the wrist was introduced beneath the sensor.

These changes aligned with expected electromagnetic loading effects caused by tissue, supporting the idea that frequency shifts and reflection coefficient variations serve as reliable metrics for hydration assessment. To enhance measurement repeatability:

- Multiple VNA sweeps were averaged, and
- Sweep resolution and frequency span were carefully optimized to minimize noise and drift.

***User Experience and Practical Observations***

The sensor was lightweight (approximately 5–10 grams) and unobtrusive, allowing users to wear it comfortably for short sessions without significantly restricting wrist movement. However, motion artifacts were noted as a practical limitation, rapid wrist movement introduced transient disturbances in the $S_{11}$ response. This underscores the need for:

- Minimal user movement during measurements, or
- The integration of motion-isolation features in future sensor iterations.

***Environmental and Durability Considerations***

Environmental effects were minimal. The application of water droplets, simulating sweat, had a negligible impact on resonance behaviour in short-term tests. Nonetheless, for long-term deployment or real-world conditions, a protective biocompatible coating would likely enhance the sensor's durability and comfort.

Overall, the sensor consistently operated near its target resonance frequency and produced reliable shifts in response to hydration-related dielectric changes.
These findings confirm the feasibility of the rectangular patch design for non-invasive biomonitoring, especially for hydration tracking, and provide a solid foundation for further development in wearable health applications.

## 6.5. Integration of the Patch Biosensor into a Portable System

Following the characterization of the rectangular patch biosensor, the next step involved integrating it into a self-contained portable measurement system. This section outlines the design, assembly, and operation of a compact biosensing unit that combines:

- A NanoVNA V2 vector network analyzer,
- A Raspberry Pi 5 single-board computer with a touchscreen interface,
- And a custom 3D-printed enclosure.

The goal of this integration is to enable real-time, on-site hydration monitoring without the need for bulky laboratory equipment. The system capitalizes on the NanoVNA's RF measurement capabilities and the Raspberry Pi's processing, and visualization features to deliver an efficient, user-friendly biosensing platform.

### 6.5.1 System Overview

The hydration monitoring system incorporates both hardware and software in a compact form factor (~15 × 10 × 5 cm), housed within a 3D-printed PLA enclosure that ensures mechanical durability and limits electromagnetic interference.

- The hardware includes:
    - A ferrite-loaded rectangular patch antenna as the sensing probe,
    - A NanoVNA V2 for measuring the reflection coefficient ($S_{11}$),
    - And a Raspberry Pi 5 for data processing, visualization, and user interface.
- The software running on the Raspberry Pi is written in Python, automating:
    - Data acquisition from the NanoVNA,
    - Signal processing,
    - And real-time display of hydration-related metrics via a built-in touchscreen.

### 6.5.2 Hardware Components

*1. Patch Antenna Sensor*

As shown in Figure 6.12, the core sensing element is a BaFe ferrite-impregnated rectangular patch antenna operating near 2.22 GHz. This frequency offers an optimal balance between tissue penetration depth and sensitivity to dielectric changes associated with hydration.

The antenna emits and receives microwave signals; a portion of the signal is reflected by the skin, and the characteristics of this reflection (specifically $S_{11}$) vary depending on the hydration level of the tissue. The embedded ferrite enhances miniaturization and near-field sensitivity, making it well-suited for direct skin coupling on the wrist.

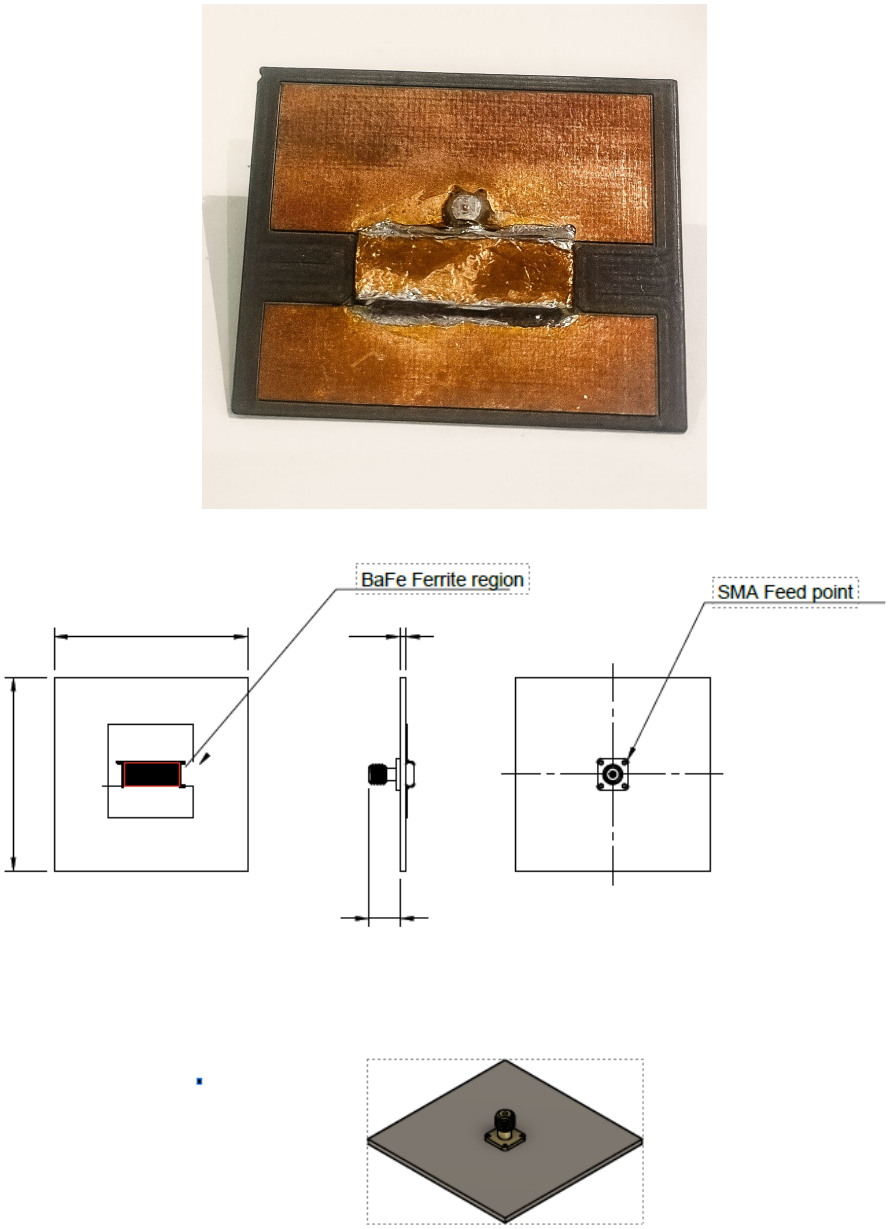


*Figure 6.12: (top)Fabricated ferrite-embedded rectangular patch antenna prototype mounted on a metal ground plane. (bottom) The schematic and 3D model illustrate the BaFe ferrite region and SMA feed point configuration. The central ferrite-loaded cavity enhances magnetic permeability, supporting miniaturization and tunability for on-body biosensing applications.*

*2. NanoVNA V2*

The NanoVNA V2 serves as the system's RF measurement engine (Figure 6.13). This portable, battery-capable vector network analyser supports a frequency range from ~50 kHz to 3 GHz and provides both $S_{11}$ and $S_{21}$ measurements with a dynamic range of ~70 dB (up to 4.5 GHz when calibrated).

In this application:

- One port of the NanoVNA connects to the antenna for $S_{11}$ measurements,
- The second port remains available for reference standards or future expansion,
- A Micro-USB connection handles power and data transfer, interfacing directly with the Raspberry Pi.

*3. Raspberry Pi 5 (MCU and Display Control)*

The Raspberry Pi 5, shown in Figure 6.14, launched in late 2023, features a 2.4 GHz quad-core ARM Cortex-A76 CPU and options for 4 GB or 8 GB RAM, delivering significant computational power. It runs a full Linux OS, providing the flexibility to support advanced data processing and interface tasks.

A 7-inch capacitive touchscreen, mounted on the enclosure, serves as the user interface, displaying real-time plots of $S_{11}$ and allowing touch interaction. The Raspberry Pi communicates with the NanoVNA over USB and executes a custom Python application that:

- Controls measurement sweeps,
- Parses and processes S-parameter data,
- And visualizes hydration trends in real-time.

The Raspberry Pi's built-in DSI or HDMI output powers the display, and USB ports enable peripheral connections such as keyboards or flash drives for data export.

All components are powered from a single USB-C power source, simplifying portability. In mobile scenarios, a battery pack or wall adapter can power both the Raspberry Pi and the NanoVNA.

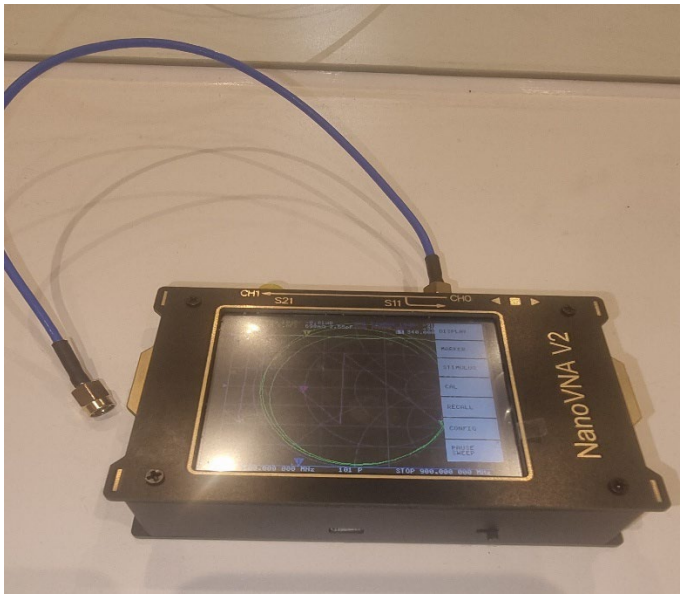


*Figure 6.13: NanoVNA V2 handheld vector network analyser setup for antenna characterization.*

### 6.5.3 System Integration and Advantages

This architecture offers a seamless end-to-end workflow from sensing to data analysis. By leveraging the strengths of the NanoVNA and Raspberry Pi:

- The system can detect subtle changes in $S_{11}$ due to hydration fluctuations,
- Immediately process and display the results on-screen,
- And operate entirely standalone, without the need for an external PC.

Moreover, the modular design allows for future upgrades:

- The NanoVNA can be replaced with a custom RF front-end,
- A Bluetooth module can be added for smartphone connectivity,
- And the enclosure or antenna can be adapted for different body sites or flexible electronics.

The integrated system meets key requirements for wearable biosensing:

- Portability: Compact, battery-operable, and field-ready,
- Safety: Uses low-power, non-ionizing RF signals,
- Real-time monitoring: With visual feedback and immediate interpretation.

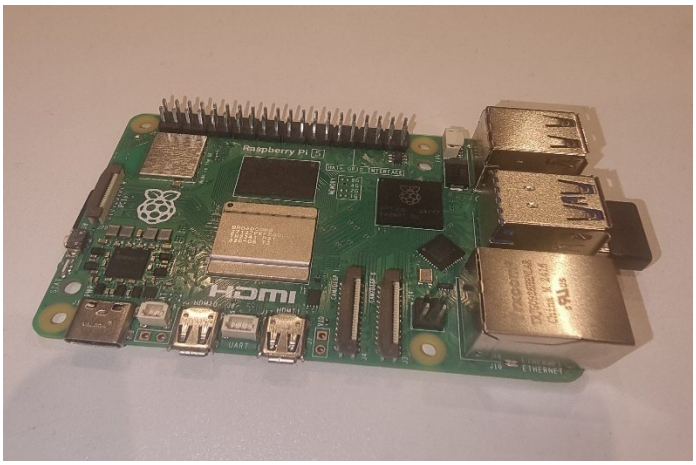

*Figure 6.14: Raspberry Pi 5 Model single-board computer featuring a quad-core processor, dual HDMI outputs, USB 3.0 ports, and GPIO header.*

### 6.5.4. System Enclosure (3D printing)

A custom-designed enclosure was developed to house and protect the biosensor system's hardware while ensuring access to all essential ports. The case was fabricated using durable PLA plastic via 3D printing, with precisely placed cut-outs for the touchscreen display, SMA sensor connector, Raspberry Pi ports, and ventilation openings.

As illustrated in Figures 6.15 to 6.17, the internal layout was carefully arranged to optimize space and reduce electromagnetic interference:

- The Raspberry Pi 5 is mounted on one side of the enclosure,
- The NanoVNA V2 module is positioned on the opposite side,
- Internal connections are made using short USB and RF coaxial cables, linking the Raspberry Pi to the VNA, and the VNA to the antenna sensor.

The rectangular patch biosensor is mounted with its SMA feed connector exposed through the top panel of the enclosure (visible as the red connector in Figure 6.16). This allows the sensor to maintain direct contact with the user’s skin, while the rest of the electronics remain safely enclosed.

One side of the case includes cutouts aligned with the Raspberry Pi’s external ports (USB, Ethernet, power), enabling convenient access for maintenance or potential system expansion. Despite this, the system is primarily intended to operate in a standalone, touchscreen-based (headless) mode, without requiring external peripherals during normal use.

The NanoVNA's Port 2 connector is also positioned near a side opening. This design allows the user to insert calibration standards or connect an external antenna without having to open the enclosure, facilitating easier testing and diagnostics.

All internal components were securely mounted using 3D-modeled standoffs and fastening points. This ensured that both the Raspberry Pi and NanoVNA remain firmly fixed in place and that their connectors align precisely with the enclosure cutouts, resulting in a clean, professional, and functional assembly.

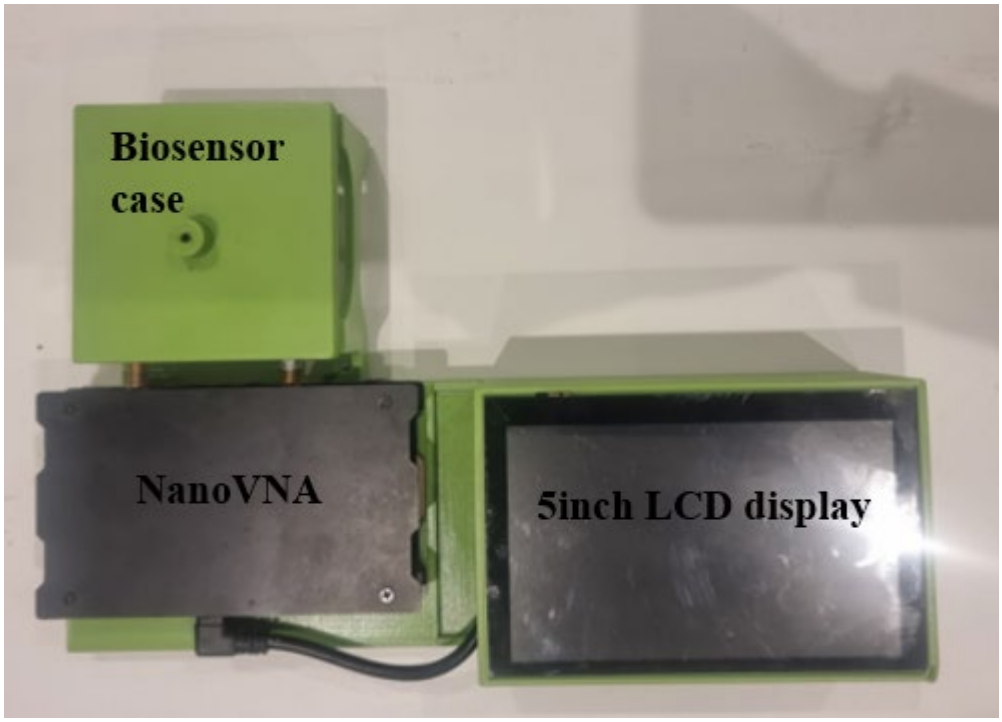


*Figure 6.15: Fully integrated biosensor prototype featuring a custom sensor enclosure, NanoVNA module for RF reflection measurements, and a 5-inch LCD touchscreen for real-time data visualization and user interaction.*

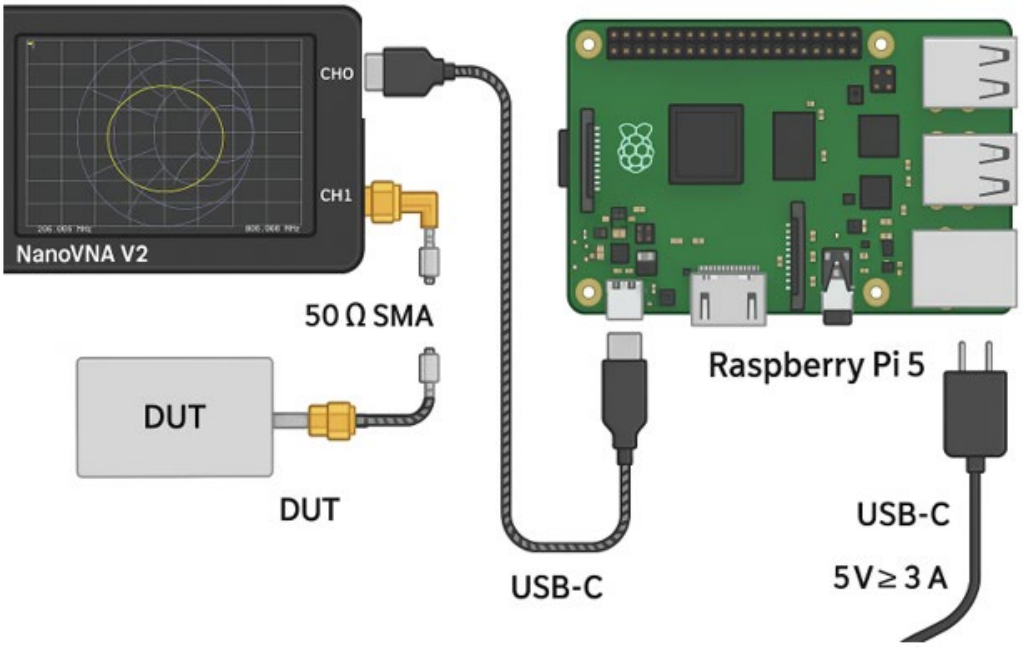


Figure6.16:*Schematic layout showing a NanoVNA V2 vector network analyzer connected to a Raspberry Pi 5 via a USB-C data cable for control and data acquisition. The CH1 (S11) port of the NanoVNA is linked to a Device Under Test (DUT) using a 50 Ω SMA coaxial cable, while the Raspberry Pi 5 is powered through a USB-C 5 V ≥ 3 A supply. This configuration enables automated RF measurements and analysis directly from the Raspberry Pi environment.*

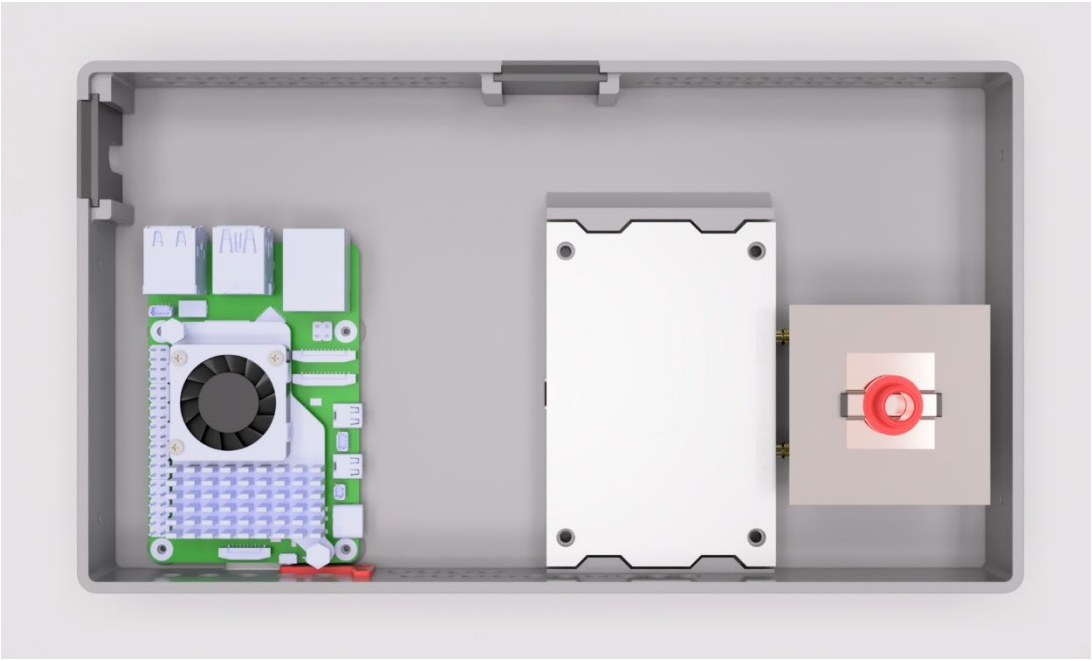

*Figure 6.17: Internal layout of the biosensor enclosure, showing the integrated components: a single-board computer with cooling fan (left), the NanoVNA module for RF measurements (center), and the patch antenna sensor with an SMA connector (right).*

### 6.5.5. Data Acquisition Workflow

Flowchart in Figure 6.18 illustrates the operation of the proposed hydration monitoring system.The data acquisition process in the portable hydration monitoring system begins with S-parameter measurement from the patch biosensor using the NanoVNA V2. In operation, the NanoVNA performs an RF sweep across a predefined frequency range, typically centered around the patch antenna's resonant frequency (as established in earlier design stages).

During this sweep, the NanoVNA captures the complex $S_{11}$ reflection coefficient, which characterizes how much of the transmitted signal is reflected back by the sensor due to impedance mismatches—this reflection is influenced by the dielectric properties of the skin, which in turn correlate with hydration status.

The $S_{11}$ data is stored in Touchstone format (.s2p), a widely used text-based standard for S-parameter data in RF engineering. The NanoVNA's firmware supports exporting measurement results in this format automatically after each sweep.

*Data Transfer and Processing*

The Raspberry Pi 5 serves as the system's processing unit and manages communication with the NanoVNA. A USB connection between the two devices is used for both:

- Powering the NanoVNA, and
- Transferring measurement data, either by:
    - Mounting the NanoVNA as a USB mass storage device, or
    - Using a serial command interface to retrieve data directly.

In this implementation, automated data transfer is achieved using a Python-based control script on the Raspberry Pi. This eliminates the need for manual file handling: as soon as a new sweep is completed by the VNA, the corresponding data file is automatically fetched and stored by the Pi.

The data processing pipeline on the Raspberry Pi then:

1. Loads the raw $S_{11}$ data (magnitude and phase).
2. Applies pre-recorded calibration data, if available.
3. Extracts features such as resonant frequency shifts or changes in return loss.
4. Maps these RF signatures to a hydration level, using predefined thresholds or calibration curves derived from prior training data.

*User Interface and Output*

The processed hydration estimate is displayed through a user interface, such as:

- A touchscreen GUI integrated into the device,
- Or an optional web dashboard accessible over a network.

The system can provide real-time feedback in the form of:

- A hydration status label (e.g., "Hydrated", "Mild Dehydration"),
- Or a quantitative hydration value or percentage.

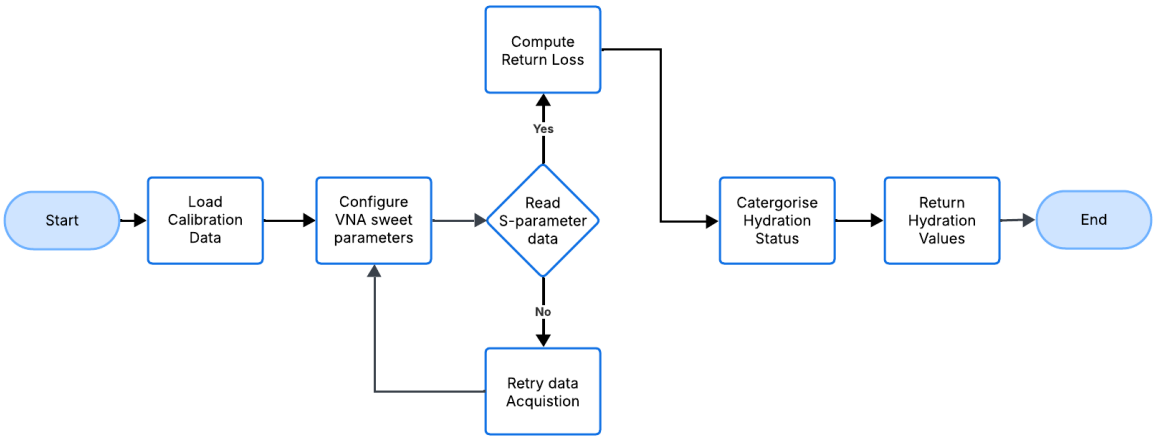


*Figure 6.18: Flowchart illustrating the operation of the proposed hydration monitoring system, based on the acquisition and analysis of S-parameter ($S_{11}$) data.*

*System Architecture Summary*

The full data acquisition and analysis chain is structured as follows:

Sensor (Patch Antenna on Skin)

→ VNA (RF Sweep Generator & $S_{11}$ Receiver)

→ Raspberry Pi (Data Processing & Hydration Estimation)

→ Display Output (Touchscreen or Dashboard)

The VNA plays a central role, generating the RF stimulus and measuring the reflected signal with high fidelity. The system is designed specifically to track shifts in the sensor's resonant behaviour due to hydration changes, using the NanoVNA's precision and compact form factor in combination with embedded processing for real-time analysis.

### 6.5.6. Technical Workflow

The hydration monitoring system integrates hardware automation and software processing to deliver real-time, non-invasive biosensing using RF reflection data. The entire technical

workflow, from measurement initiation to data classification, is handled through a Python-based pipeline running on a Raspberry Pi 5, interfacing with the NanoVNA V2 and the patch antenna biosensor.

***Device Communication and Automation***

A custom Python script establishes serial communication with the NanoVNA V2 via its USB interface. This script sends control commands to initiate frequency sweeps and retrieve measurement data, effectively emulating PC-based VNA software but with full automation. The NanoVNA's command-line interface supports direct query and sweep control, and an available Python API can be used to streamline this process.

The workflow includes:

- Setting sweep parameters (start/stop frequency, number of points).
- Triggering the sweep.
- Retrieving the resulting S-parameter data.

Data is captured either point-by-point or by accessing the generated Touchstone (.s1p) file directly from the VNA's memory. This enables seamless automation; upon a single button press on the device touchscreen (or scheduled intervals), the system performs a sweep, acquires the data, and updates the display in near real-time. This turns the biosensor into an interactive instrument that immediately reflects changes in hydration status when a user places their wrist on the sensor.

***Data Import and Parsing***

Custom Python scripts, hosted in the project's GitHub repository, handle:

- Parsing Touchstone (.s1p) files.
- Structuring frequency and $S_{11}$ data.
- Applying calibration, if necessary.

The script extracts $S_{11}$ magnitude (in dB) and phase, converting these into complex numbers for advanced processing. Standard libraries like NumPy and Pandas are used for efficient parsing. As shown in Figure 6.19, the script reads the frequency data and corresponding $S_{11}$ values, converting them to structured arrays. Frequency focus can be narrowed to the band of interest (e.g., 2.0–2.5 GHz), allowing for noise reduction and precise analysis near the expected resonance point (~2.22 GHz).

```python
import numpy as np

# Load S11 data from a Touchstone file (assuming columns: Freq(Hz), |S11|(dB), Phase(deg))
data = np.loadtxt('participant1_day1_AM.s1p', comments='#')
freq = data[:, 0]            # frequency in Hz
S11_dB = data[:, 1]          # S11 magnitude in dB (negative values)
S11_phase = data[:, 2]       # S11 phase in degrees

# Convert S11 from dB to linear complex form for further processing
S11_linear = 10**(S11_dB/20) * np.exp(1j * np.deg2rad(S11_phase))
```

*Figure 6.19: Python code snippet demonstrating the import and processing of $S_{11}$ reflection coefficient data from a Touchstone (.s1p) file.*

### *Filtering and Noise Reduction*

To improve measurement quality, smoothing techniques are applied to the $S_{11}$ data:

- A simple moving average filter (see Figure 6.20) reduces high-frequency noise without obscuring the resonance dip.
- Typical window sizes of 5–7 points are used.
- For noisier data, more advanced filters like Savitzky-Golay or median filters can be applied.
- Averaging over multiple sweeps also helps suppress random variations.

```python
# Simple moving average filter to smooth S11 magnitude (window size = 5 points)
window = 5
S11_dB_smooth = np.convolve(S11_dB, np.ones(window)/window, mode='valid')
freq_smooth = freq[:len(S11_dB_smooth)]  # adjust frequency array length
```

*Figure 6.20: Python code snippet for implementing a simple moving average filter to smooth the $S_{11}$ magnitude data.*

### *Feature Extraction – Resonance Detection*

Key features used for hydration analysis include:

- Resonant frequency (where $S_{11}$ magnitude reaches a minimum).

- Depth of reflection coefficient at resonance (in dB).

As shown in Figure 6.21, the code identifies the frequency corresponding to the minimum $S_{11}$ value (e.g., "Resonant freq = 2.22 GHz, $S_{11}$ = –18.50 dB"). Hydration changes typically cause small shifts in this frequency (e.g., more hydrated skin may show a dip at 2.24 GHz, while dehydrated skin may reflect at ~2.20 GHz).

```
# Identify the resonant frequency (min S11 in dB) and its value
min_idx = np.argmin(S11_dB_smooth)            # index of minimum (most negative) S11 dB
resonant_freq = freq_smooth[min_idx]
resonant_S11_dB = S11_dB_smooth[min_idx]
print(f"Resonant freq = {resonant_freq/1e9:.3f} GHz, S11 = {resonant_S11_dB:.2f} dB")

```

*Figure 6.21: Python code snippet for detecting the sensor's resonant frequency by locating the minimum $S_{11}$ magnitude (i.e., the most negative dB value) in the smoothed dataset.*

### *Time-Domain Reflectometry (TDR) Analysis*

To confirm that reflections originate from the sensor–skin interface (not from cables or connectors), a Fast Fourier Transform (FFT) is applied to the $S_{11}$ data to perform Time-Domain Reflectometry (TDR).

- This transforms frequency-domain data to time-domain ($S_{11}(t)$).
- It identifies reflection time delays corresponding to physical distances.
- Figure 6.23 illustrates this process. The dominant peak corresponds to the wrist, validating that the signal of interest is tissue-coupled.

While useful for validation, the hydration classification process itself does not require TDR gating, due to the simplicity and consistency of the setup.

```python
# Perform an inverse FFT to get time-domain reflection (TDR analysis)
N = len(S11_linear)
# Zero-pad the frequency response to increase time resolution
N_pad = 4 * N
S11_padded = np.concatenate([S11_linear, np.zeros(N_pad - N)])
s11_time = np.fft.ifft(S11_padded)
time = np.fft.fftfreq(N_pad, d=(freq[1]-freq[0]))  # time step based on freq step

# Find the peak in time-domain signal corresponding to the wrist reflection
mag_time = np.abs(s11_time)
peak_idx = np.argmax(mag_time)
peak_time = time[peak_idx]
print(f"Main reflection at t = {peak_time*1e9:.2f} ns")

```

*Figure 6.22: Python code snippet for performing Time-Domain Reflectometry (TDR) analysis by applying an inverse Fast Fourier Transform (IFFT) to the $S_{11}$ data.*

### *Hydration Status Classification*

Once resonant $S_{11}$ values are extracted, the system classifies hydration status using predefined thresholds in Table 6.3.

Table 6.3: Reflection coefficient thresholds for hydration classification.

| **Reflection Coefficient ($S_{11}$ in dB)** | **Hydration Category** |
|---|---|
| ≤ –15 dB | Hyperhydrated |
| –22 dB to –15 dB | Euhydrated (Normal) |
| > –22 dB | Hypohydrated (Dehydrated) |

The logic is implemented in Figure 6.23, where $S_{11}$ values are compared against these thresholds to determine hydration status. For example, a value of –18.5 dB lies within the normal range, classifying the user as euhydrated. These thresholds were validated using calibration datasets and aligned with known physiological conditions.

```python
# Compute return loss as positive value (make dB value positive)
return_loss_dB = -resonant_S11_dB   # if resonant_S11_dB is negative, e.g. -18.5 dB, return_loss_dB = 18.5

# Classify hydration status based on thresholds
if return_loss_dB <= 15:
    status = "Hyperhydration"       # overly hydrated (very low reflection)
elif return_loss_dB <= 22:
    status = "Euhydration"          # normal hydration
else:
    status = "Hypohydration"        # dehydrated (high reflection)
print(f"Hydration Status: {status}")

```

*Figure 6.23: Python code snippet for calculating the reflection coefficient from the resonant $S_{11}$ value and classifying hydration status using predefined dB thresholds.*

### *Visualization*

The system includes a real-time visualization interface on the Raspberry Pi touchscreen, shown in Figure 6.24. Features include:

- Plotting the $S_{11}$ response over frequency.
- Highlighting the resonant dip and hydration classification.
- Displaying numeric readouts (e.g., “Resonant freq = 2.22 GHz”, “Status: Normal”).
- Time-series plots tracking hydration over hours/days.
- Dashed threshold lines for visual interpretation of hydration status.

The plots are generated using Matplotlib. Large fonts and clean markers ensure readability in clinical or field settings.

### *Summary*

The technical workflow integrates hardware and software into a seamless sensing system:

**Patch Sensor → NanoVNA V2 → Raspberry Pi 5 → Python Scripts → Hydration Display**

This complete pipeline automates:

- Sensor measurement,
- Data parsing,
- Resonance detection,
- Hydration classification,
- And visualization.

The system eliminates dependence on bulky lab equipment, enabling compact, real-time, in-situ hydration monitoring suitable for healthcare, sports, or wearable applications.

```python
import matplotlib.pyplot as plt

# Example: Plot hydration index over time for one participant
times = [ ... ]   # array of timestamps or measurement indices
hydration_vals = [ ... ]  # array of return_loss_dB values over time

plt.figure(figsize=(6,4))
plt.plot(times, hydration_vals, marker='o', label='Hydration Reading (dB)')
plt.axhline(15, color='blue', linestyle='--', label='Hyperhydration Threshold (15 dB)')
plt.axhline(22, color='red', linestyle='--', label='Hypohydration Threshold (22 dB)')
plt.xlabel('Time')
plt.ylabel('Return Loss |S11| (dB)')
plt.title('Hydration Readings Over Time')
plt.legend()
plt.show()
```

*Figure 6.24: Python code snippet for visualizing hydration status over time using Matplotlib.*

### 6.6. Experimental Study on Human Volunteers

To assess the accuracy and sensitivity of the hydration biosensor system, an experimental study was conducted involving human participants under varying hydration conditions. The primary measurement site was the inner wrist (over the radial artery on the forearm), chosen for its accessibility and physiological relevance. This region contains superficial tissues and blood vessels whose dielectric properties vary with hydration levels, making it ideal for non-invasive sensing of water content.

#### 6.6.1. Participant Protocol

Healthy adult volunteers participated in the study while going about their typical daily activities. Hydration measurements were periodically recorded using the wrist-mounted patch antenna sensor. Each measurement captured the $S_{11}$ reflection coefficient (in dB), representing the proportion of RF signal reflected from the body, a metric known to vary with tissue hydration.

Measurements were collected across multiple time points to capture a natural range of hydration states, from low hydration conditions (e.g., early morning or post-exercise) to higher hydration levels following fluid intake. Although contextual metadata such as time of day, exercise, and water intake were part of the broader study, this specific analysis focused solely on the reflection coefficient values for classifying hydration states and examining statistical trends.

Before each session:

- The NanoVNA was calibrated using standard open, short, and load references.
- A baseline reading was taken in free space or using a reference phantom.
- The patch sensor was then gently secured on the wrist, ensuring consistent contact without excessive pressure.

The NanoVNA performed a frequency sweep cantered around 2.22 GHz, and the corresponding $S_{11}$ vs. frequency data were recorded. Each measurement took only a few seconds. To enhance reliability, three sweeps were taken in quick succession (~10 seconds), and the best-quality or averaged result was used to reduce artifacts from movement or signal noise.

Participants remained seated and relaxed during measurements to minimize physiological variation, such as changes in blood flow. The measurements were taken indoors at a stable room temperature of 22 °C, as both skin properties and VNA performance are sensitive to temperature. A real-time feedback interface on the Raspberry Pi displayed the calculated hydration index (reflection coefficient and hydration classification). However, participants were blinded to their results to prevent behavioural bias (e.g., immediate rehydration upon seeing a "dehydrated" label).

### 6.6.2 Hydration Classification Principle

Hydration status is typically categorized into three physiological states:

- Hypohydration: Dehydration or body water deficit (≥2% body mass loss).
- Euhydration: Normal hydration balance.
- Hyperhydration: Excess body water, which may lead to diluted blood electrolytes and health complications.

In this study, the reflection coefficient ($S_{11}$ in dB) measured by the wearable patch sensor is used as a proxy for tissue hydration. The principle is as follows:

- Lower reflection coefficient values (more negative $S_{11}$) indicate stronger RF absorption and better impedance matching associated with higher tissue hydration.
- Higher reflection coefficient values (less negative $S_{11}$) suggest reduced absorption and poorer matching associated with lower tissue hydration.

Based on calibration studies, the following thresholds were defined:

- Hypohydration: $S_{11} \geq -15$ dB
- Euhydration: $-22$ dB $\leq S_{11} < -15$ dB
- Hyperhydration: $S_{11} < -22$ dB

These thresholds reflect dielectric shifts in skin and subcutaneous tissues associated with hydration changes.

### 6.6.3 Study Dataset and Analysis

A total of 425 measurements were collected from multiple participants using the biosensor system. While individual participant data was anonymized, the aggregate dataset provided a comprehensive snapshot of hydration-related $S_{11}$ variations under natural, uncontrolled conditions.

The analysis aimed to:

- Quantify the distribution of hydration states (based on $S_{11}$ thresholds).
- Examine the statistical characteristics of the return loss data.
- Validate the sensor's ability to differentiate between hydration categories reliably.

This real-world testing protocol demonstrates the potential of the biosensor system to perform robust, non-invasive hydration monitoring.

### 6.6.2. Methodology

Prior to each measurement session, participants were asked a structured set of hydration-related questions (see Appendix B) designed to capture basic fluid-intake behaviours and subjective hydration indicators. Specifically, participants were asked:

- *When did you last drink fluids?*
- *Approximately how much fluid did you consume?*
- *Have you experienced thirst, fatigue, or light-headedness in the past hour?*

In addition, each participant's body weight was recorded immediately before the test, providing a physiological reference point to complement the dielectric measurements. Although this did not constitute a full clinical gold-standard validation (e.g., against bioimpedance or urine-specific gravity), it offered a rudimentary dietary and physiological understanding of hydration status at the time of testing. These self-reported and physical measures enabled contextual interpretation of the reflection coefficient ($S_{11}$) data, supporting classification validity through triangulation of hydration indicators.

A total of 425 reflection coefficient measurements (N = 425) were analysed in this phase. Each measurement represented a single quantitative variable: return loss (RL) in decibels (dB), which

served as a proxy for tissue hydration. No subgrouping by participant demographics, measurement session, or environmental context was performed. Instead, the entire dataset was treated as a unified cohort to examine the overall behaviour of RL values. This approach aimed to establish broad statistical patterns and baseline characteristics that can inform future model development and subgroup analyses.

***Sensor Sensitivity and Specificity to Hydration Changes***

A key objective was to evaluate the sensor's sensitivity—its ability to detect small hydration changes, and its specificity, its ability to distinguish hydration changes from other unrelated factors.

- Statistical analysis confirmed that hydration state had a highly significant effect on RL readings (One-way ANOVA, $p < 0.0001$).
- Mean RL values by hydration category:
    - Hypohydration: $26.0 \pm 3.8$ dB
    - Euhydration: $19.7 \pm 1.5$ dB
    - Hyperhydration: $9.7 \pm 5.8$ dB

These differences (see Figure 6.25) far exceed the typical measurement noise, indicating a strong and reliable signal. Post-hoc Tukey HSD tests confirmed that all pairwise differences between categories were statistically significant ($p < 0.001$).

Importantly, even mild dehydration was detectable shifts of 3–5 dB was enough to indicate a transition from euhydration to hypohydration. This level of sensitivity is critical, as performance degradation can begin with as little as 2% body water loss.

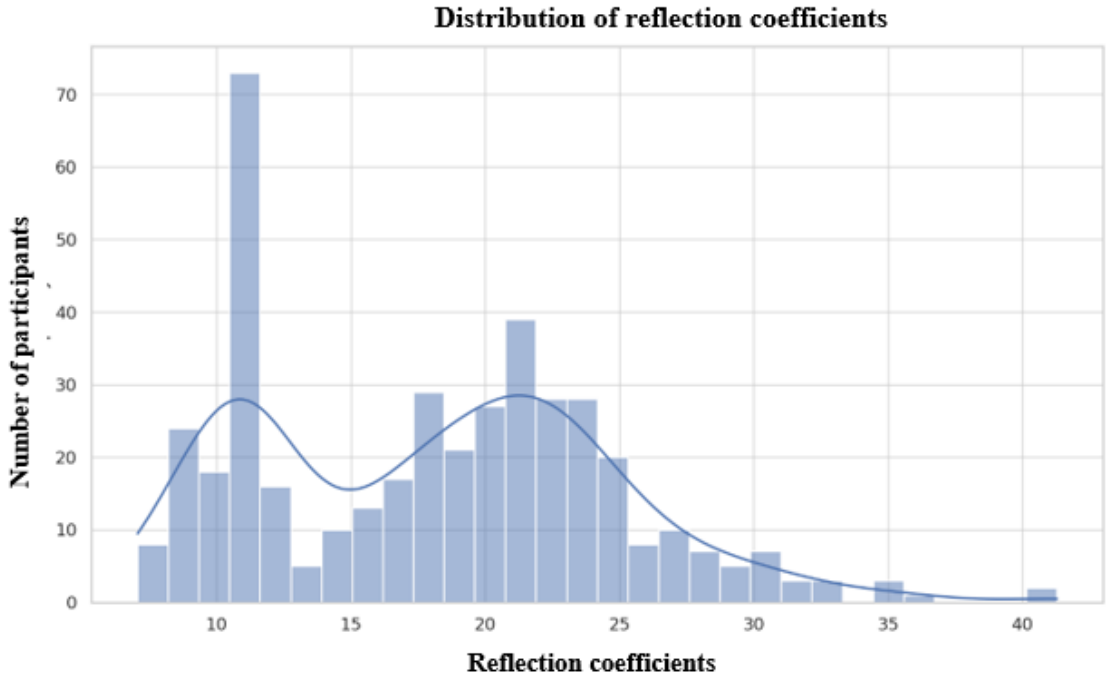


*Figure 6.25: Histogram and KDE plot showing the distribution of reflection coefficient (in dB). The data exhibits a bimodal pattern, with prominent peaks around 11 dB and 22 dB, indicating two common return loss levels in the measured dataset.*

### *Dynamic Range and Signal Reliability*

Return loss readings ranged from –7.05 dB to –41.29 dB, covering the full spectrum from overhydration to dehydration. This wide dynamic range:

- Captures extreme physiological states without saturation.
- Demonstrates high signal-to-noise ratio, with inter-category shifts of 6–10 dB, versus intra-category variability of only 1–4 dB.

This reinforces the sensor's specificity, its output reflects genuine hydration changes, not incidental variations.

### *Robustness Across Demographics*

The sensor's performance was also tested for robustness against personal factors like sex and age:

- Sex distribution: 369 male and 56 female readings.
- Two-way ANOVA (hydration × sex):
  - No significant main effect of sex ($F_{1,442} = 2.01$, $p = 0.16$).
  - No significant interaction effect ($p = 0.19$).
- Age correlation: A slight trend (–0.05 dB per year, $p \approx 0.01$), but not practically impactful.

Thus, the sensor appears unbiased across age and sex, performing consistently across a broad user base.

***Descriptive Statistics***

- RL range: –7.05 dB to –41.29 dB
- Mean: –18.06 dB
- Median: –18.46 dB
- Standard deviation: 6.63 dB
- Distribution: Moderately right skewed; non-normal ($p \ll 0.01$, normality test)

***Hydration Category Distribution***

Using the predefined thresholds:

- Hyperhydration: $S_{11} < -22$ dB
- Euhydration: $-22$ dB $\leq S_{11} \leq -15$ dB
- Hypohydration: $S_{11} > -15$ dB

Results:

- Hyperhydration: 36.2%
- Euhydration: 35.1%
- Hypohydration: 28.7%

This even distribution supports the effectiveness of the chosen thresholds and shows that the sensor captured a realistic range of hydration states during normal daily life.

***Sex-Based Hydration Trends***

While males dominated the sample (87%), hydration status distributions shown in Figure 6.26 were similar across sexes:

- Male: 137 hyperhydrated, 129 euhydrated, 103 hypohydrated
- Female: 23 hyperhydrated, 20 euhydrated, 13 hypohydrated

Though these patterns suggest consistency, the small female sample size (13.2%) limits definitive conclusions. Further studies with more balanced demographics are recommended, using proportional analysis and chi-square tests to confirm independence.

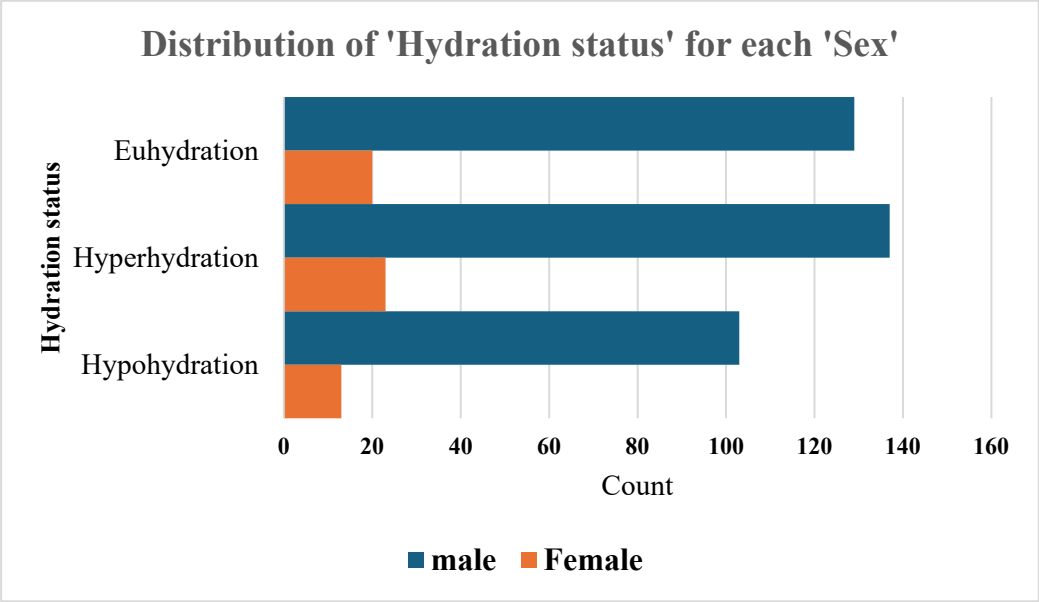


*Figure 6.26: Horizontal bar chart showing the distribution of hydration status by sex. Male participants exhibit higher counts across all hydration categories—hypohydration, euhydration, and hyperhydration—while female participants are underrepresented in each group*

### *Hydration Status Transitions*

Sequential readings revealed hydration dynamics:

- Drinking ~500 mL of water → RL drop of 2–5 dB within 30–60 minutes.
- Exercise or fluid restriction → RL increase of 3–7 dB.
- Example: one participant's RL shifted from 18 dB (pre-run) to 26 dB (post-run), corresponding with subjective thirst, evidence that the sensor tracked real physiological changes.

### *Summary of Key Findings*

- **Strong correlation** between $S_{11}$ values and hydration status.
- **Thresholds** (–15 and –22 dB) effectively separated categories.
- **Consistent trends** across individuals despite unique baselines.
- **Captured diurnal and behavioural changes**, including fluid intake and physical activity.
- **Clear clustering** of hydration categories; minimal overlap supports threshold-based classification.
- **Potential for personalization** by establishing user-specific baselines.

- **Theoretical and experimental alignment**: findings reflect the models developed in Chapter 5.
- **Robust usability**: portable, repeatable, and clinically relevant measurements with minimal setup.

### 6.6.3. Conclusion

This chapter presented the successful implementation of a reflection coefficient-based hydration monitoring system, building on the magneto-dielectric biosensor design and electromagnetic principles discussed in Chapter 5. The integrated system, comprising a ferrite-loaded patch biosensor, NanoVNA, Raspberry Pi, and custom Python software, proved effective in capturing and interpreting hydration-related changes through return loss measurements. Across 425 human trials, the system reliably distinguished between hyperhydrated, euhydrated, and hypohydrated states in real time using threshold-based classification of the reflection coefficient ($S_{11}$).

The experimental findings aligned closely with theoretical predictions: hydration changes led to measurable shifts in both resonant frequency and reflection magnitude, validating the sensor's capability for non-invasive physiological monitoring. The system demonstrated practical sensitivity to daily hydration fluctuations and user-specific hydration behaviours, indicating strong potential for real-world deployment.

In its current prototype form, the system can be further refined for wearable use. For instance, the Raspberry Pi could be replaced with a dedicated low-power microcontroller or System-on-Chip, and the NanoVNA functionality embedded within a compact RF front-end. With the 2.22 GHz S-band antenna operating safely and license-free for body-worn applications, the system architecture is well-suited for miniaturization into wearable formats; such as integration into a smartwatch or skin patch with wireless data transmission.

To improve robustness in real-world conditions, future iterations could incorporate individual calibration routines to account for inter-user variability in tissue properties. Additional challenges such as motion artifacts, sweat, and changing contact quality may require adaptive filtering or machine learning approaches to maintain accuracy during everyday use. Nonetheless, even the current system, using relatively simple processing, demonstrated meaningful, actionable results.

In summary, this research delivers a novel and practical solution for hydration monitoring. By translating complex electromagnetic interactions at the skin–antenna interface into a single, interpretable metric, the system effectively bridges the gap between theoretical modelling

(Chapter 5) and real-world validation (Chapter 6). These results lay a strong foundation for future development of wearable hydration biosensors aimed at athletes, clinical users, and the public. Ongoing work will focus on refining the form factor, integrating wireless connectivity, and enhancing the classification algorithms to support continuous, real-time hydration monitoring in diverse environments. Overall, this study demonstrates the viability of reflection coefficient analysis as a tool for non-invasive, portable hydration assessment, marking a significant step forward in e non-invasive hydration diagnostics.

## 6.7 References

[1] R. Sharma and A. Kumari, "Hard Ferrites for High Frequency Antenna Applications," Materials Research Foundations, vol. 142, 2023.

[2] I. J. G. Zuazola, A. Sharma, M. Filip, and W. G. Whittow, "Antenna using a magnetic-slab located in the principal magnetic-field region beneath the patch," Progress in Electromagnetics Research C, vol. 110, pp. 229–241, 2021.

[3] K. Katke and S. Popalghat, "H-Shape Microstrip Patch Antenna: Design, Simulation, and Characterization," Int. J. Sci. Res. Sci. Technol., pp. 54–58, 2024.

[4] D. M. Pozar, Microwave Engineering, 4th ed. Hoboken, NJ, USA: Wiley, 2011.

[5] LPKF Laser & Electronics, ProtoMat S104 Product Brochure, 2020.

[6] A. M. Holland-Winkler and B. K. Hamil, "Hydration considerations to improve the physical performance and health of firefighters," J. Funct. Morphol. Kinesiol., vol. 9, no. 4, p. 182, Oct. 2024, doi: 10.3390/jfmk9040182.

# 7. Conclusion and Future Work

This thesis addresses that gap by leveraging the dielectric properties of biological tissue at microwave frequencies to sense changes in water content. Through a combination of theoretical modelling, sensor design, and controlled human subject experimentation, it demonstrates the feasibility of using electromagnetic waves in the 2.45 GHz ISM band to non-invasively monitor hydration levels across three physiological states; hypohydrated, euhydrated, and hyperhydrated. While the classification among these states was successfully validated, it is also important to remark on the potential for extending this technique toward quantifying the *actual level of hydration*, providing precise numerical estimations rather than categorical classification. Such capability would significantly enhance its diagnostic and monitoring value.

Environmental conditions during experimentation were maintained at a stable 22 °C to minimize the influence of ambient temperature on dielectric measurements. However, future investigations should consider evaluating sensor performance under varying thermal and humidity conditions to confirm robustness and practical applicability in diverse environments.

Furthermore, although alcohol wipes were used after each test to remove residual skin oils and moisture, future prototypes could incorporate self-cleaning or hydrophobic coating strategies to further reduce surface contamination and measurement drift, improving repeatability and user convenience.

Overall, this thesis not only validates the feasibility of using reflection coefficient analysis for real-time, non-invasive hydration tracking but also establishes a scientific foundation for the development of novel ferrite loaded non-microwave biosensors. The findings open pathways for broader non-invasive hydration monitoring. By providing real-time hydration status readings within seconds overcoming the limitations of traditional techniques such as urine analysis, total body weight loss, this approach represents a significant step forward in continuous, and accessible non-invasive hydration diagnosis.

## 7.1 Summary of Research Findings and Contributions

### *Background and Theoretical Foundations (Chapters 1–3)*

The research began by highlighting the clinical importance of hydration monitoring and the limitations of existing methods. These limitations underscore the potential of microwave-based techniques, particularly because of the high permittivity and loss of water at RF frequencies.

Chapters 2 and 3 provided the theoretical basis for using electromagnetic sensing, including key concepts such as complex permittivity, dielectric relaxation, and effective permittivity of multilayer tissue structures. The wrist was chosen as the sensing site due to its anatomical features; skin, fat, muscle, and bonewhose water-rich layers dominate dielectric behavior. Bruggeman's model estimated wrist tissue permittivity around $\varepsilon' \sim 29.72$ under hydrated conditions, with measurable shifts expected during dehydration.

***Empirical Feasibility Studies (Chapter 4)***

Initial experiments validated the concept using an open-ended coaxial probe. Measurements on saline solutions and human skin showed the anticipated trend: higher hydration levels corresponded to higher permittivity. While in vivo measurements introduced complexity due to physiological variables (e.g., electrolyte concentration, blood perfusion), they confirmed that tissue hydration can affect dielectric properties in a detectable way, establishing the need for a more robust, dedicated sensor.

***Sensor Design and Electromagnetic Modelling (Chapter 5)***

Electromagnetic simulations guided the development of a novel approach for non-invasive hydration detection using ferrite-loaded H-slot patch antenna, operating at ~2.2 GHz. This design improved field confinement, increased the quality factor, and ensured safe operation on the body. Full-wave simulations demonstrated its sensitivity to hydration-induced permittivity changes, showing shifts in resonant frequency and reflection magnitude with varying tissue loading.

***Prototype Implementation and Human Trials (Chapter 6)***

The fabricated ferrite loaded H-shaped biosensor was embedded into a portable system combining the patch sensor, NanoVNA, Raspberry Pi, and custom-built software for flexible and mobile usage. Tests on 425 participants demonstrated the sensor system's ability to distinguish hyperhydration, euhydration, and hypohydration using a simple threshold classification of reflection coefficients. Results were consistent with simulation predictions, and sensor responses showed strong correlation with hydration-related behaviour (e.g., fluid intake, exercise). While minor inter-individual differences were observed, trends were robust and reproducible.

***Contributions and Implications***

This thesis contributes to the field in several keyways:

1. **Scientific Insight:** Demonstrates that tissue permittivity changes due to hydration can be reliably measured using RF techniques.
2. **Sensor Innovation:** Introduces a novel ferrite-loaded H-patch design that balances sensitivity, safety, and wearability.
3. **Prototype Development:** Delivers a functioning system validated with a large-scale human study.
4. **Translational Potential:** Paves the way for future wearable hydration monitors with applications in clinical care, sports science, and personal wellness.

While limitations remain, such as the need for miniaturization, enhanced algorithms, and gold-standard clinical validation, the core hypothesis is strongly supported.

***Publication***

I.D. Lubangakene, B. Virdee, R.K.R. Jayanthi, and P. Ganguly, "*Effect of metabolite and temperature on artificial human sweat characteristics over a very wide frequency range (400 MHz–10.4 GHz) for wireless hydration diagnostic sensors*," Results in Engineering, vol.19, 101328, Sept.2023, pp.1-7.

## 7.2 Future Work

### (a) Miniaturization and Wearable Integration:

Next steps include replacing benchtop components with custom electronics, such as an integrated RF front-end and microcontroller or system-on-chip. These could be embedded into a smartwatch or armband, using Bluetooth Low Energy for data transmission. Antenna design may need tuning to account for new enclosures or battery placement.

### (b) Enhanced Signal Processing:

More advanced algorithms can improve accuracy. Future systems could analyze the full spectral S-parameter response and apply machine learning to account for individual variation. Time-domain analysis and filtering (e.g., motion artifact suppression using accelerometers) would further enhance reliability.

### (c) Clinical Evaluation:

Future studies should validate the sensor against gold-standard hydration markers (e.g., serum osmolality, urine specific gravity) in clinical and athletic settings. Longitudinal trials will assess its utility in tracking hydration trends over time. A more diverse participant base will also improve generalizability and help establish calibration ranges for specific populations.

**(d) New Applications:**

The technology could be adapted for monitoring edema, wound healing, or even internal hydration using ingestible or implantable antennas. Integration into IoT health platforms is also feasible, enabling predictive alerts when combined with other bio signals.

**Final Remarks**

This doctoral research has successfully demonstrated a proof-of-concept for microwave-based hydration sensing. By combining electromagnetic theory with practical engineering and human trials, the work lays a strong foundation for future development. The potential of translating complex tissue–wave interactions into actionable hydration metrics has been validated, opening the door to next-generation non-invasive hydration diagnostics.

With continued interdisciplinary innovation, this non-invasive hydration monitoring system could be deployed widely in clinical, athletic, and everyday settings ultimately contributing to better hydration management and prevention of dehydration-related health risks. This thesis not only addresses a pressing biomedical challenge but also exemplifies how bioengineering can bridge theoretical science and real-world impact.

# APPENDIX A

## Model #2 Python script – To predict hydration status from permittivity left & wright wrist (inside)

```
import pandas as pd
from sklearn.model_selection import train_test_split
from sklearn.ensemble import RandomForestClassifier
from sklearn.preprocessing import LabelEncoder
from sklearn.metrics import accuracy_score, f1_score
import joblib
import tkinter as tk
from tkinter import messagebox

# Step 1: Load and clean the dataset
file_path = 'final Dak measurements report.xlsx'
df = pd.read_excel(file_path, sheet_name='DAK readings')
df['Hydration Status'] = df['Hydration Status'].str.strip().str.lower().str.title()

# Step 2: Prepare the model data
df_model = df[[' Permittivity Left Wrist (inside)', 'Permittivity Right Wrist (inside)', 'Hydration Status']].dropna()
df_model.columns = ['Perm_Left_In', 'Perm_Right_In', 'Hydration_Status']

# Encode labels
le = LabelEncoder()
df_model['Hydration_Status_Encoded'] = le.fit_transform(df_model['Hydration_Status'])

# Features and target
X = df_model[['Perm_Left_In', 'Perm_Right_In']]
y = df_model['Hydration_Status_Encoded']

# Train-test split
X_train, X_test, y_train, y_test = train_test_split(X, y, stratify=y, test_size=0.2, random_state=42)

# Train the model
clf = RandomForestClassifier(random_state=42)
clf.fit(X_train, y_train)

# Evaluate and print metrics
y_pred = clf.predict(X_test)
accuracy = accuracy_score(y_test, y_pred)
f1 = f1_score(y_test, y_pred, average='weighted')
print(f"Model trained. Accuracy: {accuracy:.2f}, F1 Score: {f1:.2f}")

# Save the model and label encoder
joblib.dump(clf, 'hydration_model_lr_inside.joblib')
joblib.dump(le, 'hydration_label_encoder.joblib')

# Step 3: GUI Application for Prediction
clf = joblib.load('hydration_model_lr_inside.joblib')
```

```
le = joblib.load('hydration_label_encoder.joblib')

def predict_hydration():
  try:
    perm_left = float(entry_left.get())
    perm_right = float(entry_right.get())
    X_input = pd.DataFrame([[perm_left, perm_right]], columns=['Perm_Left_In', 'Perm_Right_In'])
    pred_encoded = clf.predict(X_input)[0]
    pred_label = le.inverse_transform([pred_encoded])[0]
    messagebox.showinfo("Prediction Result", f"Predicted Hydration Status: {pred_label}")
  except ValueError:
    messagebox.showerror("Invalid Input", "Please enter valid numerical values.")

# Build GUI
root = tk.Tk()
root.title("Hydration Status Predictor")
root.geometry("300x200")

tk.Label(root, text="Left Wrist Permittivity (Inside):").pack(pady=(10, 0))
entry_left = tk.Entry(root)
entry_left.pack()

tk.Label(root, text="Right Wrist Permittivity (Inside):").pack(pady=(10, 0))
entry_right = tk.Entry(root)
entry_right.pack()

tk.Button(root, text="Predict Hydration Status", command=predict_hydration).pack(pady=20)

root.mainloop()
```

# Appendix B

**"An experimental investigation on measuring hydration levels of different individuals to facilitate in idealising a non-invasive biosensor".**

## Expert interviews

## INFORMATION SHEET

Thank you for considering participating in this study. This information sheet outlines the purpose of the study and provides a description of your involvement and rights as a participant, if you agree to take part.

**1. What is the research about?**

Research title: "A non-invasive sensor to measure hydration levels in different individuals."
I am conducting this experimental study at London Metropolitan University, and this research is part of my PhD studies.
The research will focus on evaluating how to assess hydration levels for different individuals through a novel noninvasive approach. Sweat contains essential biomarkers such as electrolytes which provide important information in understanding the hydration level of the body. The technique will employ a sensor placed on the skin to extract data. Crucially, the proposed method is non-invasive and not harmful to the individuals. No blood draws will be taken from participants.

**2. Do I have to take part?**

The experimental study is voluntarily. The final decision is based entirely on the individual. Upon acceptance, a consent form will be presented to the individual to sign before the experiment is conducted.

**3. What will my involvement be?**

You will be asked how much liquid you drank in the past 24hours. You are also asked for the time you last drank.

**4. How do I withdraw from studying?**

You can withdraw from the study at any point until the data analysis phase starts – which is expected to be as from 01/03/2024 without having to give a reason. If any questions during the interviews/ experimental session make you feel uncomfortable, you do not have to answer them. Withdrawing from the study will have no effect on you. If you withdraw from the study, I will not retain the information you have given thus far, unless you are happy for me to do so.

**5. What will my information be used for?**

The collected information will be used for a PhD research project, for publication and when disseminating the research findings. Additionally, the data collected will be used to calibrate and optimise the sensitivity of the sensor.

**6. Will my taking part and my data be kept confidential? Will it be anonymized?**

The records from this study will be kept as confidential as possible. Access to the data will be limited to only the research team [Innocent Lubangakene (i.lubangakene1@londonmet.ac.uk), Prof.Bal Virdee (b.virdee@londonmet.ac.uk) & Renu Rajaguru (rer0266@my.londonmet.ac.uk) ]

Data to be anonymised in compliance with GDPR regulations, your name will not be used in any reports or publications resulting from the study. The only information collected will be the dielectric readings of the sensor, age of participant, gender, weight, height, and ethnicity. Any copies of research information will be always kept in secure digital storage or locked files. The data will be kept for a maximum of four year upon which they will be permanently and safely disposed of.

**Limits to confidentiality:** At all times, confidentiality will be maintained, unless you tell me something which implies that you or someone you mention might be in significant danger of harm and unable to act for themselves; in this case, I may have to inform the relevant agencies of this, but I would discuss this with you first.

**7. Who has reviewed this study?**

This study has undergone ethics review in accordance with the London Metropolitan University Research Ethics Policy and Procedures.

## CONSENT FORM - Expert interviews

**"An experimental investigation on measuring hydration levels of different to facilitate in idealising a non-invasive biosensor."**

| ***Please confirm your choices by checking the appropriate boxes*** | | |
|---|---|---|
| **Taking Part in the Project** | **Yes** | **No** |
| The project has been fully explained to me.<br><br>(If you would like to answer no to this question, please do not proceed with this consent form until you are fully aware of what your participation in the project will mean.) | ☐ | ☐ |
| I have been given the opportunity to ask questions about the project. | ☐ | ☐ |
| I agree to take part in the project. I understand that taking part in the project will mean to be interviewed. | ☐ | ☐ |
| I agree to the sessions being audio and video-recorded | ☐ | ☐ |
| I understand that my taking part is voluntary and that I can withdraw from the study until the data analysis phase starts – which is expected to be as from [01/03/2024].<br><br>I do not have to give any reasons for why I no longer want to take part and there will be no adverse consequences if I choose to withdraw. | ☐ | ☐ |
| **How my information will be used during and after the project** | **Yes** | **No** |
| I understand my personal details such as name and email address etc. will not be revealed to people outside the project. | ☐ | ☐ |

| | | |
|---|---|---|
| I understand that the findings from the interviews will be published in research outputs. | ☐ | ☐ |
| I understand that I will not be named in any research outputs unless I have expressly consented to be named. | ☐ | ☐ |
| I agree that my real name can be used for quotes in research outputs. | ☐ | ☐ |
| **So that the information you provide can be used legally by the researchers** | **Yes** | **No** |
| I agree to assign the copyright I hold in any materials generated as part of this project to the Researcher, see names and contact details below. | ☐ | ☐ |

| **Name of Participant** | **Signature** | **Date** |
|---|---|---|
| | | |

| **Name of Researcher** | **Signature** | **Date** |
|---|---|---|
| | | |

**Project contact details for further information:**

**The Researcher: Innocent D. Lubangakene**

Name: i.lubangakene1@londonmet.ac.uk

## Appendix C

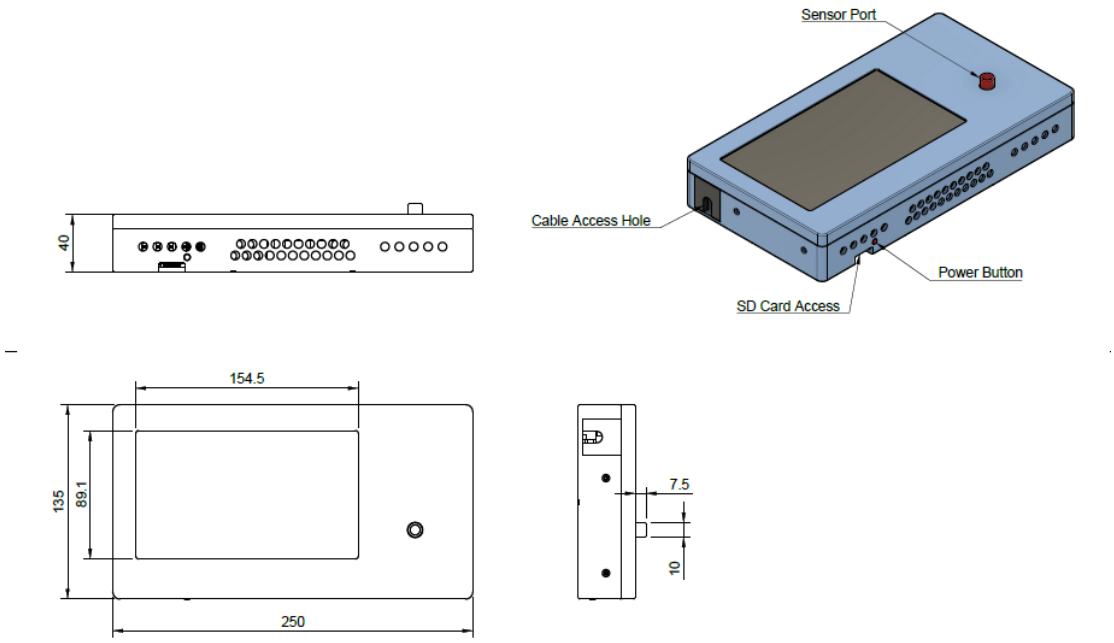


*Figure 6.17: Technical drawing and 3D-rendered view of the biosensor device enclosure, highlighting key design features such as the sensor port, cable access opening, SD card slot, power button, and overall dimensions (250 mm × 135 mm × 40 mm).*